

**Dissertation zur Erlangung des Doktorgrades
der Fakultät für Chemie und Pharmazie
der Ludwig-Maximilians-Universität München**

**DNA origami based tools
for the investigation of biomolecular interactions**

Lennart Grabenhorst

**aus
Wolfenbüttel, Deutschland**

2024

Erklärung

Diese Dissertation wurde im Sinne von § 7 der Promotionsordnung vom 28. November 2011 von Herrn Prof. Dr. Philip Tinnefeld betreut.

Eidesstattliche Versicherung

Diese Dissertation wurde eigenständig und ohne unerlaubte Hilfe erarbeitet.

Lennart Grabenhorst
München, 12.01.2024

Dissertation eingereicht am: 15.01.2024

1. Gutachter: Prof. Dr. Philip Tinnefeld

2. Gutachter: PD Dr. Jan Vogelsang

Mündliche Prüfung am: 27.02.2024

Abstract

The ability to visualize and interact with nanoscale objects is of great importance for biology, as many biological phenomena can ultimately be broken down to processes on these length-scales. In this context, fluorescence microscopy and especially the distance dependent fluorescence resonance energy transfer (FRET) between two fluorescent labels have developed into valuable tools, because they allow for the elucidation of biomolecular dynamics with low invasiveness, at near physiological conditions and at the single-molecule level. Recent developments in the bottom-up self assembly of DNA nanostructures have now also made it possible to construct nanoscale components that can perform designed tasks and enabled many new applications. In this thesis, I utilized the nanoscale arranging capabilities offered by DNA nanotechnology to construct new tools for the visualization of biomolecular interactions with single molecule FRET.

In the first part, I developed a new generation of DNA origami nanoantennas, which are self-assembling nanophotonic devices comprising two gold or silver nanoparticles. In the zeptoliter volume between the two nanoparticles, plasmonic effects increase the electric field intensity by orders of magnitude. The DNA origami structure here serves as a positioning device, selectively immobilizing molecular entities in this volume of highest enhancement. The increased electric field strongly increases the fluorescence intensity of fluorophores, while simultaneously making them more resistant to photobleaching. In this thesis, I made these plasmonic hotspots accessible for larger molecules such as diagnostic assays and proteins. I showed that the fluorescence intensity in single molecule FRET experiments can be increased by approximately an order of magnitude, which increases the time resolution and facilitates the observation of ultrafast processes such as the diffusive barrier crossing events between two potential energy minima, e.g. in the coupled folding and binding of two intrinsically disordered proteins.

In the second part, I developed a DNA origami based tunable and modular biosensing platform. A problem that is often encountered in the field of biosensing is that on the one hand, it is difficult to determine whether a small molecule such as a metabolite has bound to a receptor, because the conformational change upon binding is too small to be directly read out with methods such as FRET. On the other hand, the sensitive concentration range of these interactions is dictated by the thermodynamics of the binding reaction and cannot easily be adjusted in the case that the concentrations of interest are not falling within this range. The platform I developed opens up new strategies to overcome these challenges by arranging the sensor components on a DNA origami scaffold. This enables the spatial decoupling of the

sensing interaction from the signalling element, meaning that the signal contrast is not any longer defined by the conformational change that the ligand binding causes at its receptor binding site, but rather by the larger conformational change of the DNA origami scaffold that is a consequence of the binding. Furthermore, the DNA origami technique and its nanometer precise positioning capabilities open up the possibility to arrange several sensing elements on the same backbone, which enables the tuning of the sensors response window and even can give rise to cooperative responses.

In summary, this thesis adds new tools to the repertoire of fluorescence based single-molecule biophysics and hopefully opens up new research directions for the more detailed understanding of biomolecular interactions.

Contents

1	Introduction	1
1.1	DNA origami nanoantennas	3
1.2	Engineering single-molecule sensors with the help of DNA origami	6
2	Theoretical Background	9
2.1	Single-molecule fluorescence	9
2.1.1	Fluorescence	10
2.1.2	Limitations of fluorescent dyes	11
2.1.3	Resonance energy transfer	13
2.1.4	Plasmonic fluorescence enhancement	15
2.2	DNA nanotechnology	17
2.2.1	DNA as a building material	19
2.2.2	Dynamic DNA nanostructures	20
2.3	Biomolecular binding reactions	21
2.3.1	Allostery	23
2.3.2	Transition paths	25
3	Materials and Methods	27
3.1	Microscopy setups	27
3.2	Design and production of DNA origami nanostructures	29
3.3	Sample preparation	30
3.4	Data analysis	30
4	Fluorescence enhancement with DNA origami nanoantennas	31
4.1	Associated Publication 1	31
4.2	Associated Publication 2	33
4.3	Associated Publication 3	35
4.4	Associated Publication 4	37

5	Decoupling signal transduction from recognition in DNA origami biosensors	39
5.1	Associated Publication 5	39
6	Conclusions and Outlook	41
6.1	DNA origami nanoantennas for single-molecule biophysics	41
6.2	Modular and tunable single molecule biosensors	44
7	Bibliography	47
8	List of publications	61
9	Acknowledgements	64
10	Appendix	66

1 Introduction

The development of new tools has been a driver for progress throughout the history of humanity and constantly improved the quality of life on earth, be it by creating machines that help in performing physical work such as the steam engine or by providing means to “make the invisible visible”, such as a microscope or telescope. Scientific progress, therefore, has always been tightly linked to developments of new instruments and measurement techniques – maybe even more so in recent years, as our models and theories become more and more detailed and testing them requires distinguishing smaller and smaller differences. For example, new staining methods as well as improvements in the manufacturing of microscopes directly led to the discovery of bacteria as a major pathogen and subsequently helped curing diseases like anthrax or tuberculosis (Figure 1.1a [1–3]). A more recent example is the development of fluorescent tags based on the green fluorescent protein (GFP [4]) which among many other applications enabled the visualization of cancer processes in vivo and led to a new understanding of this complex disease (Figure 1.1b [5]). With access to more advanced microscopy techniques provided by the scientific progress, new tools are required in order to not only visualize but also interact with objects on very small scales. However, the construction of useful tools on the nanoscale is a very challenging task, because it is hard to directly and specifically manipulate larger objects to fabricate tools of these dimensions from the “top down”. Another problem is often referred to as “fat and sticky fingers”: on the one hand, it is difficult to specifically pick up a molecule without picking up a lot of other surrounding molecules, because the smallest entity that can be imagined to work as the “finger” would be an atom, which still is similar in size to the molecule that is to be moved. On the other hand, once a molecule is picked up using, for example, coulombic interactions, it is hard (though not impossible) to let go of it again when it is placed at the desired location (Figure 1.1c [7, 8]). These points were raised in a public controversy in the early 2000s, discussing whether it would ever be possible to construct sophisticated nanoscale molecular machines [9].

A more successful strategy for the construction of such tools therefore does not rely on direct manipulation of the components but leverages fundamental physical properties for the programmed self-assembly of these structures from the “bottom up”. Deoxyribonucleic acid

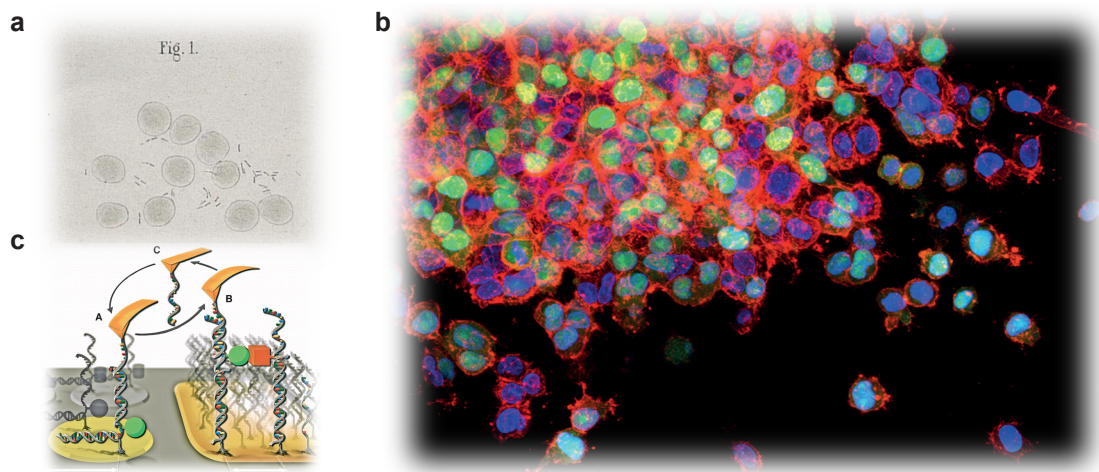


Figure 1.1: The development of new tools drives scientific progress. **(a)** The introduction of new microscopes led to the discovery of *Bacillus anthracis* as the pathogen responsible for anthrax [1]. **(b)** Green fluorescent protein (GFP) and its colourful derivatives helped in the understanding of cancer processes. Here, a fluorescence microscope image of GFP expressing lung cancer cells (green) invading a tissue is shown. Image created by S. Wilkinson and A. Marcus, National Cancer Institute [6]. **(c)** Single-molecule cut-and-paste: an example of direct interaction with nanoscale components. An atomic force microscope's cantilever was used to selectively transport single-stranded DNA molecules from a reservoir to a target site. From [7]. Reprinted with permission from AAAS.

(DNA) is an ideal material for this approach because of its regular, well defined features as well as the fact that two single strands will only form a stable double helix if the sequence of their nucleobases are matched. The detailed knowledge of the DNA sequences can be utilized to construct complex structures without the need for symmetry, which significantly increases the design options when compared to many other self-assembly methods. This has been realized in the 1980s by Seeman [10] and a clever revamping of the synthesis strategy by Rothemund in 2006 [11] made this technology so robust that even non-experts are now able to create nano-objects in a matter of hours. In early days of the technique termed "DNA origami", the structures that were created were not of much real use other than to showcase the impressive control over the features of the structures, but researchers from many different fields quickly realized the potential of DNA origami to become a valuable scheme for the construction of nanoscale tools. Examples include the development of a DNA origami nanopore [12], a nanorobot that can transport cargo to specific cells [13], a calibration standard for superresolution microscopes [14] or a DNA origami adapter for the deterministic positioning of molecules on a surface [15].

Single-molecule fluorescence microscopy is a method that exquisitely complements the DNA origami technique [16]. On the one hand, it enables the visualization of nanoscale dynamics,

for example via the distance dependent Fluorescence Resonance Energy Transfer (FRET [17]). On the other hand, the DNA origami technique allows for easy, selective and nanometer precise arrangement of functional components such as fluorescent dyes, metallic nanoparticles, proteins and other chemical modifications, opening the door to very complex experimental setups. This synergy is the foundation for this thesis, in which I applied the DNA origami technique to two different challenges that can be addressed by the precise arrangement of different components on the nanoscale.

1.1 DNA origami nanoantennas

In the first part, I developed a new generation of DNA origami nanoantennas, which are nanostructures comprising a DNA origami backbone and two metallic nanoparticles. Generally, an antenna is a structure that enables the coupling of electromagnetic radiation to an emitter or receiver. For the case of radio-frequency radiation – with wavelengths on the order of mm to m – antennas make it possible to transmit signals over very large distances. This is exemplified by the space probe *Voyager 1* (Figure 1.2a), which is currently¹ 24.345.840.227 km away from earth and still can transmit and receive data to and from the NASA Deep Space Network using its 3.7 m diameter Cassegrain antenna [18]. As a rule of thumb, the characteristic distance for the size of the antenna is the wavelength of the electromagnetic radiation. Interestingly, for visible light (wavelengths of ca. 400 – 700 nm), an analogous function emerges if the antenna size matches this length scale. Then, light can get focussed to very small areas, and furthermore, the emission of a fluorescent molecule can be enhanced significantly (Figure 1.2b). The fabrication of these optical antennas has conventionally been achieved top-down with methods such as electron-beam milling (Figure 1.2c). The drawback of this method is that it offers no room for parallelization, i.e. every antenna needs to be fabricated separately. An even greater problem is the fact that there is no straightforward way to selectively place molecules such as fluorophores into the antenna, and the researcher mostly has to rely on “luck”, that is, the fact that in a large enough sample there will be some molecules that are randomly deposited in the desired location. To overcome these limitations, the DNA origami approach has been employed successfully for many years [20, 22]. Here, the components forming the optical antenna (metallic nanoparticles) are held in the desired orientation by the DNA origami nanostructure which simultaneously is used to immobilize a fluorescent molecule in the small gap between the nanoparticles and immobilize the assembled nanoantenna on a glass coverslip (Figure 1.2d). The effect of these so-called plasmonic hotspots on fluorescence

¹As of December 5th, 2023.

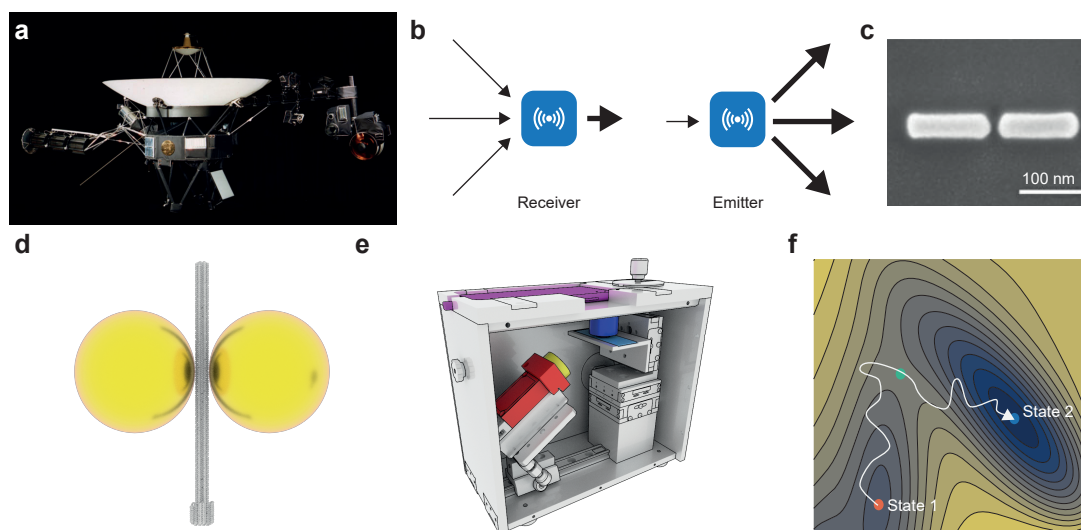


Figure 1.2: (a) The space probe *Voyager 1* with its directional antenna. (b) Scheme showing the two functions of an antenna: help receive weak input signals (left) and help transmit weak output signals (right). (c) An example for an optical antenna fabricated with focussed ion-beam milling. Reproduced with permission from Springer Nature [19]. (d) Illustration showing the first optical antenna self-assembled via the DNA origami technique [20]. (e) The smartphone microscope used for mobile detection of diagnostically relevant DNA with the help of DNA nanoantennas [21]. (f) Schematic representation of diffusion over a potential energy surface (blue $\hat{=}$ lower potential energy) taking a system from state 1 to state 2. The time needed for this diffusion is called transition path time.

was characterized thoroughly [20, 23–25], in some cases reaching enhancement factors of over 3 orders of magnitude [23, 26]. The key steps in the development of DNA origami nanoantennas are reviewed in the associated publication 1 in chapter 4.1. Altogether, the strongly increased brightness of fluorescent molecules placed in plasmonic hotspots *via* DNA origami nanoantennas opened up several interesting applications.

In the field of biosensing, where the detection of disease specific molecules in a complex mixture of analytes is usually aggravated by high background signal, e.g. from autofluorescence of blood, this serves as a mechanism to “highlight” the target molecule, facilitating its detection. Conceptually, the antenna in this case offers an amplification mechanism based on a physical phenomenon. In contrast to molecular amplification mechanisms, such as the polymerase chain reaction (PCR), the amplification is instantaneous, which significantly reduces the time to result and circumvents the introduction of possible errors during the amplification. Furthermore, the high fluorescence intensity of targets captured in the hotspot enables the detection of pathogens with low-tech instruments, which is attractive for the use in settings where expensive diagnostic devices are not available. To accomplish these goals, a challenge

that had to be overcome was the fact that DNA origami designs thus far blocked most of the plasmonic hotspot regions with the construction material and it was therefore not possible to immobilize larger entities such as diagnostic assays or proteins directly into the hotspot region [27]. Therefore, in the associated publication 2 in chapter 4.2, a new antenna design was introduced which was capable of hosting much larger units than previous designs while maintaining the high fluorescence enhancement factors. This is exemplified by carrying out a diagnostic assay for the detection of antibiotic resistance in *Klebsiella pneumoniae* using a portable microscope constructed with a smartphone camera, a cheap objective, and a laser running on a USB power bank (Figure 1.2e).

In single-molecule biophysical experiments, the same amplification mechanism would be of use for conducting experiments at higher concentrations of labelled species. A typical observation volume in single-molecule fluorescence microscopy is on the order of approximately one femtoliter. To ensure that only one molecule is observed at the same time, the concentration of labelled species thus is limited to the low nanomolar range. However, many biological interactions occur with micromolar affinity constants, making them very hard to observe with conventional methods. In contrast, the zeptoliter plasmonic hotspot would still only be occupied by less than 1 molecule at these concentrations [28]. Beyond that, plasmonic hotspots can also be used to boost the performance of fluorophores in single molecule FRET experiments. The observation of ultrafast (submillisecond) biomolecular reactions thus far has been limited to reactions in which both educt and product states are occupied significant amounts of time, enabling the use of statistical methods such as nanosecond fluorescence correlation spectroscopy [29]. This is due to the fact that the required time resolution for such observations on the single-molecule level thus far was out of reach: even the best labels photobleach within a few milliseconds under strong irradiation, and at the same time also only emit around 1000 photons per millisecond, a count rate that is hardly enough to examine the many biologically relevant processes on the microsecond timescale such as protein folding [30, 31].

Plasmonic hotspots have been shown to increase the photostability [32] and decrease saturation effects [33, 34] of fluorescent labels at high excitation intensities and thus could be used to facilitate these types of experiments. In the associated publication 3 in chapter 4.3, we studied the effects of such high excitation intensities on different classes of fluorophores and quenchers and found that certain fluorophores like ATTO 647N exhibit pronounced dark state formation. This severely hampers their photon output, while cyanine based fluorophores like AlexaFluor 647 do not suffer from this problem as much, but are instead limited by increased blinking on ms – μ s timescales due to photoisomerization reactions [35]. With the

help of these findings, in the associated publication 4 in chapter 4.4, we were able to carry out biologically relevant single-molecule FRET experiments in a plasmonic hotspot. More specifically, we observed the binding of two intrinsically disordered proteins to one another. This coupled binding and folding was shown to occur *via* an intermediate encounter complex with lifetimes on the order of 100 μs [36], which we were able to confirm with our experiments, underlining the compatibility of the plasmonic hotspot with biological reactions. In a second set of experiments, we then observed the hybridization reaction of two single-stranded DNAs with photon count rates of up to > 10 MHz and found mean transition path times – the average time for the diffusion on the free energy surface between two minima (Figure 1.2f) – on the order of ≈ 17 μs .

1.2 Engineering single-molecule sensors with the help of DNA origami

In the second part, I applied the toolkit provided by the DNA origami technology to the construction of modular biosensors. A biosensor is a structure that can bind a target molecule, such as a pathogen marker or a metabolite, with high specificity and selectivity and simultaneously translates the binding event into a measurable signal change. As such, it enables the diagnosis of diseases or the elucidation of cellular processes. With the exception of *de novo* engineered proteins and aptamers, generally, a naturally occurring biointeraction is used as a sensing element. Then, if the binding of the target induces a sufficient conformational change, translating the binding event into a signal change can be achieved by simply labelling the binder with a FRET pair comprising two fluorophores at suitable positions. However, the oftentimes subnanometer conformational changes severely limit the signal contrast of these types of sensors (Figure 1.3a) and more generally, most natural binders do not even undergo large enough conformational changes upon binding at all [37]. This problem fueled intense research efforts, and several strategies to overcome this issue have been devised. For example, by linking the binding of the ligand to the binding site to a larger conformational change, *e.g.* the connection of two split proteins which then form a functional luciferase [38] or the displacement of a fluorescently labelled tethered ligand from the binding site [37], it became possible to translate the binding of small molecules into a large signal change.

A further problem, that has so far only been addressed in a few specific examples [39] originates from the thermodynamics of binding to a single site receptor, which will always result in a dose-response curve with a certain mid-point and steepness (Figure 1.3b). These parameters,

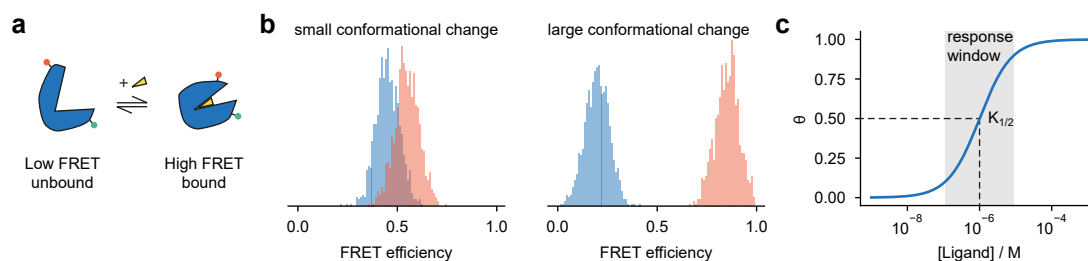


Figure 1.3: (a) In order to visualize the binding of a target molecule to a receptor with fluorescence microscopy, positions for the labels need to be found at which the receptor undergoes a large enough conformational change. (b) Illustration of the ramifications of the labelling position on the FRET contrast. For the case of too small differences in fluorophore separation (left) it becomes hard to distinguish the bound from the unbound state. If the conformational change is large enough (right), the populations can be readily distinguished. (c) Exemplary dose-response curve for a ligand binding to a receptor. The target concentration resulting in half-occupation of the receptor ($K_{1/2}$) as well as the curve steepness defining the response window are values that are dictated by the thermodynamics of the ligand binding reaction.

termed $K_{1/2}$ and n_H (or “Hill coefficient”) are fundamental properties of the receptor-ligand interaction. Changing $K_{1/2}$ traditionally would involve the perturbation of this interaction, *e.g.* by the introduction of point mutations in the binding site that reduce or increase the interaction strength. Of note, this could bring with it potentially unwanted changes to substrate specificity [40] as well as requires knowledge of the full mechanism of target binding – or alternatively the trial of several positions by brute force.

To change the steepness of the response, however, it is not enough to change the interaction strength and strategies of coupling two or more binding events are required. In nature, there are several examples of such strategies. The prime example is binding of O_2 to hemoglobin. Although the complete mechanism of action is still not entirely understood [41], it is known that hemoglobin is a heterotetramer with four equivalent heme groups which each can bind one O_2 molecule. Upon binding of the first O_2 , the hemoglobin undergoes a conformational change which facilitates the binding of the next O_2 molecule to the next heme group *etc.*, resulting in a much steeper dose-response than in single-site binding [42]. This phenomenon termed “cooperativity” enables the efficient uptake and release of oxygen despite the fact that venous and arterial O_2 concentrations only vary by around threefold [43, 44]. In the context of biosensing, a cooperative system would thus be of use in situations where the analyte concentrations vary only slightly, but unambiguous diagnostic answers are needed. This is the case, *e.g.* when overseeing the glucose levels in the blood of diabetic persons [45], or monitoring the concentrations of therapeutic drugs [46]. However, achieving cooperative responses in synthetic biosensors is challenging [39], and most of the strategies developed

for the design of modular sensors do not offer the possibility to have multiple biorecognition elements interacting with each other.

The DNA origami approach has the potential to synthesize these strategies into a modular system that is easily adoptable to new targets, offers mechanisms of tuning the biosensor's dose-response behavior while simultaneously serving as an interface to several possible signal readout mechanisms. To do so, it is pivotal to understand the interplay of multivalent interactions in artificial sensors. To this end, I set out to develop a biosensing platform based on a dynamic DNA origami with a large, controllable conformational change [47]. Using reversible DNA-DNA interactions as a model for receptor-ligand binding, we studied the effects of multivalency, allosteric control and mechanical strain on the binding properties of the sensor and found several potentially generalizable mechanisms for tuning of the response window. This project is described in the associated publication 5 in chapter 5.1.

2 Theoretical Background

2.1 Single-molecule fluorescence

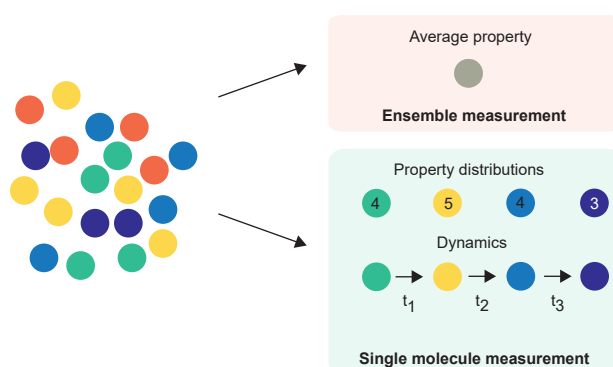


Figure 2.1: Illustrating the advantages of single molecule experiments: while ensemble measurements give quick access to the average parameters describing a mixture, the underlying properties such as distributions of properties or the dynamics of interconversions between different states can only be observed when single molecules can be distinguished.

Given the enormous size difference between our perceivable reality and the fundamental building blocks of life, it may come as no surprise that the macroscopic properties we experience are usually the result of a complex interplay of different agents forming a complex ensemble. What we observe are usually property averages, although the underlying property distribution might actually be quite heterogeneous or dynamically interchanging. To learn about this property distribution and potential kinetic heterogeneities (Figure 2.1), it is pivotal to be able to observe single molecules “at work”, a task that has been achieved for the first time with methods such as scanning tunneling microscopy [48] and the related technique of atomic force microscopy [49] in the early 1980s and which has been expanded to the much less invasive field of optical microscopy in 1989 for molecules at cryogenic temperatures [50]. With the next evolution step of optical single molecule detection in biologically relevant conditions (i.e. in aqueous solution and at room temperature [51]), the technique has rapidly developed into a valuable tool in all domains of natural science which was recognized with a Nobel

prize in Chemistry in 2014 [52]. The physical phenomenon of fluorescence is very important for optical single-molecule detection. As fluorescence photons are always less energetic than excitation photons, the excitation light can simply be filtered out in the detection channel and only the fluorescence can be observed – which results in comparably high signal-to-background ratios when compared to methods that use elastically scattered light [53].

2.1.1 Fluorescence

Fluorescence is a process by which a molecule in an excited state – which is induced by absorption of an excitation photon of a certain energy given by the product of Planck's constant h with the frequency of the light wave f – returns to the ground state and emits a photon of lower energy and thus higher wavelength. The absorption of the excitation photon only occurs when its energy exactly matches the energy difference between the fluorophore's ground state S_0 and one of the vibrational microstates ν_N of an excited state S_N . Since the absorption process is much faster than the reorganization time of the nucleus, the excitation usually occurs not to the vibrational ground state of the excited state but to the vibrational microstate which has a maximum of the wave function at the same nuclear coordinates as the ground state [54] (Franck-Condon principle, Figure 2.2a). The rate of this process is determined by the intensity of the incident field and the absorption cross section of the molecule.

The processes following the absorption of a photon can be illustrated in a Jabłoński diagram [55] (Figure 2.2b): typically, the excitation occurs not to the vibrational ground state but to a higher microstate. Then, on the timescale of picoseconds, the molecule relaxes to the vibrational ground state of the S_1 excited state, giving off heat in the process (internal conversion and vibrational relaxation) [56]. From the S_1 state, the system can relax in multiple different ways: energy can be dissipated non-radiatively with the rate k_{nr} or via emission of a photon (fluorescence, k_{fl}). Another possibility is the conversion of the system to a triplet excited state T_N (intersystem crossing, k_{isc}). This $S-T$ transition, however, is spin-forbidden and thus occurs with much lower probability. Analogously, triplet excited states can then decay to the singlet ground state via non-radiative pathways or also with emission of a photon (phosphorescence, k_{ph}). The probability of observing a fluorescence photon after excitation of the molecule is called fluorescence quantum yield Φ_{fl} :

$$\Phi_{fl} = \frac{k_{fl}}{k_{fl} + k_{nr} + k_{isc}} \quad (2.1)$$

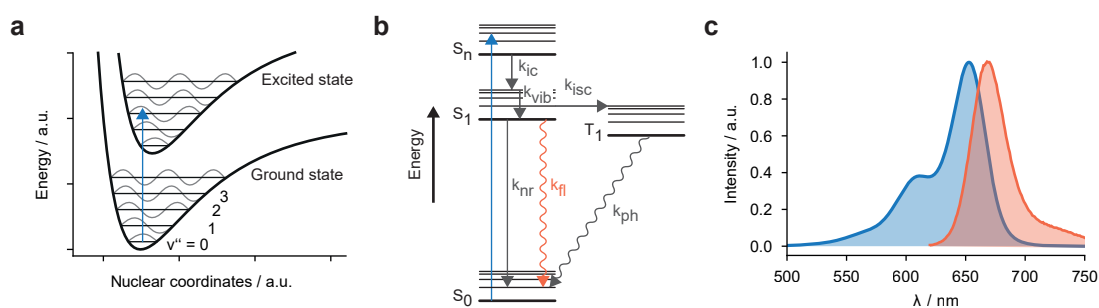


Figure 2.2: Physical processes in fluorescence: **(a)** Illustration of the Franck-Condon principle: excitation by a molecule usually occurs from the ground state to an excited vibronic microstate ν_n with a maximum of the wave function at the same distance to the nucleus. **(b)** Jablonski diagram showing the different processes occurring after excitation of a molecule from its ground state S_0 to an excited state S_N with suitable energy (blue). Typically the molecule very quickly relaxes to the vibrational ground state of the S_1 state by energy dissipation to the environment via internal conversion (ic) or vibrational relaxation (vib). From there, it can return to the ground state via nonradiative (nr) or radiative processes (fluorescence, fl). Another process that can occur, with usually lower likelihood, is the intersystem crossing (isc) to a triplet excited state (T_N). The return to the ground state then analogously occurs via nonradiative or radiative (phosphorescence, ph) pathways. **(c)** Absorption (blue) and emission (orange) spectrum of the commonly used fluorophore AlexaFluor 647. The emission is red shifted from the absorption.

and the average time spent in the S_1 state before emission of a fluorescence photon is called fluorescence lifetime τ_{fl} :

$$\tau_{fl} = \frac{1}{k_{fl} + k_{nr} + k_{isc}} \quad (2.2)$$

Analogously, the intersystem crossing quantum yield Φ_{isc} and the triplet lifetime τ_{tr} are given by

$$\Phi_{isc} = \frac{k_{isc}}{k_{fl} + k_{nr} + k_{isc}} \quad \text{and} \quad \tau_{tr} = \frac{1}{k_{ph}} \quad (2.3)$$

For organic fluorophores, fluorescence quantum yields can be as high as 70% and fluorescence lifetimes typically are on the order of a few ns. Intersystem crossing yields are usually below 5% [35, 57], and unquenched triplet lifetimes are on the order of 100 μ s.

2.1.2 Limitations of fluorescent dyes

Despite great advances in the last quarter of a decade, organic fluorophores are far away from being perfect emitters without limitations and especially in highly demanding applications, such as single-molecule studies, they often are the major bottleneck in the success of an experiment [58, 59].

On the one hand, this is due to the problem of photoblinking and photobleaching: whenever the fluorophore populates long lived excited states – with lifetimes on the order of μs to ms – such as the triplet state or photoisomers, it is not available for fluorescence emission. The highly energetic excited states can react with surrounding molecules and form long-lived non emitting intermediates or even irreversibly convert to non-fluorescing species (photobleaching). Generally, triplet states are more prone to these side reactions than singlet states because of their orders-of-magnitude higher lifetimes. The most common pathway for this is the reaction of the triplet excited state with ambient oxygen, in which the fluorophore transfers its energy to the oxygen resulting in the formation of singlet oxygen or other highly reactive oxygen species (ROS). By using enzymatic systems that consume oxygen, such as glucose oxidase/catalase, the probability of these side reactions can be reduced. However, since oxygen also acts as a triplet quencher, the removal of oxygen leads to increased triplet and radical blinking. This can in turn be mitigated by other additives that serve as triplet quenchers, such as the reducing and oxidizing system (ROXS [60]), e.g. trolox/troloxquinone or methyl viologen/ascorbic acid or physical triplet quenchers such as cyclooctatetraene [61] (COT) or Ni^{2+} [62].

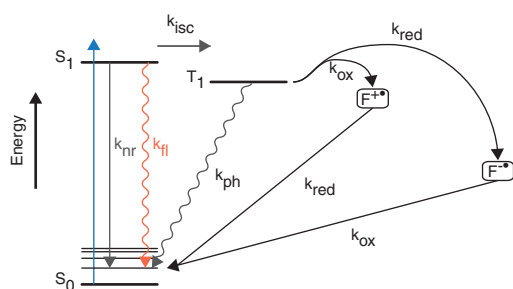


Figure 2.3: Jabłoński diagram of the ROXS mechanism. After intersystem crossing into the triplet state, the fluorophore can be either reduced or oxidized by additives in solution forming radical anion or radical cation species. From there, the complementary reduction or oxidation, respectively, can recover the singlet ground state. The rate of these reactions is dependent on the concentrations of the additives and can be faster than the “native” recovery of the ground state via phosphorescence.

In this thesis, only the ROXS approach was employed. It can be illustrated with a Jabłoński diagram (Figure 2.3): if an additive with matching redox potential collides with a molecule in the triplet state, electron transfer reactions occur, leading to formation of a radical anion for the case of a reducing agent and to the formation of a radical cation for the case of an oxidizing agent. From these dark intermediate states, the ground state can be recovered by the subsequent reaction with the complementary reaction partner (e.g. the reduction of the radical cation) [63]. If the concentration of these additives is high enough (typically mM), both of these reactions will occur within hundreds of microseconds which leads to dark times

of the fluorophore on almost the same timescale as the triplet lifetimes in ambient oxygen – but without the generation of harmful ROS.

On the other hand, the finite lifetimes of the excited states themselves pose a fundamental limit to the obtainable photon output per unit time: even if the ROXS system is used to depopulate the triplet state, since the mechanism requires a collision of the fluorophore with both the reductant and the oxidant in the correct order, the speed of this process is limited by the concentration of the additives in the solution. At very high concentrations, however, photoinduced electron transfer reactions of the singlet excited state [64] occur, leading to quenching of the fluorescence. These two factors have to be weighed against each other, which limits the dark times to the low microsecond timescale. The same low microsecond timescale limit is also hit by photoinduced isomerization reactions between bright and dark states of fluorophores from the class of cyanines, which poses an additional limitation for these kinds of fluorophores [35].

2.1.3 Resonance energy transfer

If a fluorophore in an excited state is in close proximity to a second electronic system, such as another fluorophore or a quencher, another relaxation pathway becomes feasible. In this case, energy can be transferred non-radiatively from the excited state of the first molecule to the second molecule, which in turn enters an excited state from which it can then relax following the aforementioned pathways. The rate of this Fluorescence Resonance Energy Transfer (FRET), k_{FRET} , between a donor and an acceptor system separated by distance r is given by the equation [56]

$$k_{\text{FRET}}(r) = \frac{\Phi_{\text{D}}\kappa^2}{\tau_{\text{D}}r^6} \left(\frac{9000(\ln 10)}{128\pi^5 N_{\text{A}}n^4} \right) \int_0^{\infty} F_{\text{D}}(\lambda)\epsilon_{\text{A}}(\lambda)\lambda^4 d\lambda \quad (2.4)$$

and is dependent on several parameters, which are briefly explained below (N_{A} = Avogadro's number).

Firstly, since FRET is a dipole-dipole interaction, the efficiency of the process scales with $1/r^6$. When the electronic systems get too close to each other (approx. < 2 nm), other types of energy transfer, such as photoinduced electron transfer or direct electron exchange interactions dominate the behavior, while FRET typically is the dominating process at intermediate distances around 3–10 nm (commonly characterized by the distance at which the energy transfer efficiency is 50%, the so-called “Förster radius”, R_0 , Figure 2.4a).

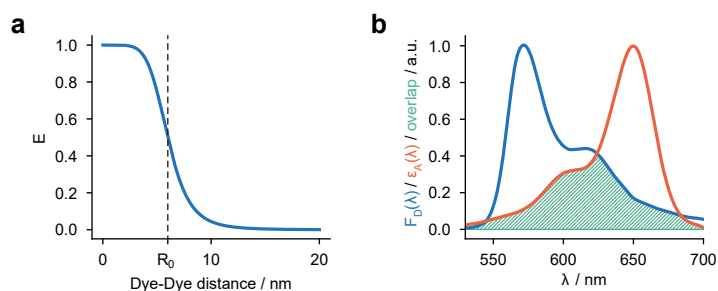


Figure 2.4: (a) Dependency of the FRET efficiency E on the dye-dye distance r : at $r = R_0$, the efficiency is 50%. (b) Exemplary emission spectrum of Cy3B (blue), absorption spectrum of AF647 (orange) as well as their spectral overlap (green) in arbitrary units. The efficiency of the energy transfer increases with the spectral overlap.

Secondly, the (photo-)physical properties of donor and acceptor dyes as well as the medium. This includes the refractive index n , the quantum yield Φ_D and fluorescence lifetime τ_D of the donor in absence of the acceptor, but also the overlap integral J

$$J = \int_0^{\infty} F_D(\lambda)\epsilon_A(\lambda)\lambda^4 d\lambda \quad (2.5)$$

of the emission spectrum of the donor $F_D(\lambda)$ with the acceptor absorption spectrum $\epsilon_A(\lambda)$ (Figure 2.4b): it is necessary that there is a transition from the ground state of the acceptor to an excited state with an energy difference that matches the energy of the excited state of the donor for efficient energy transfer to occur.

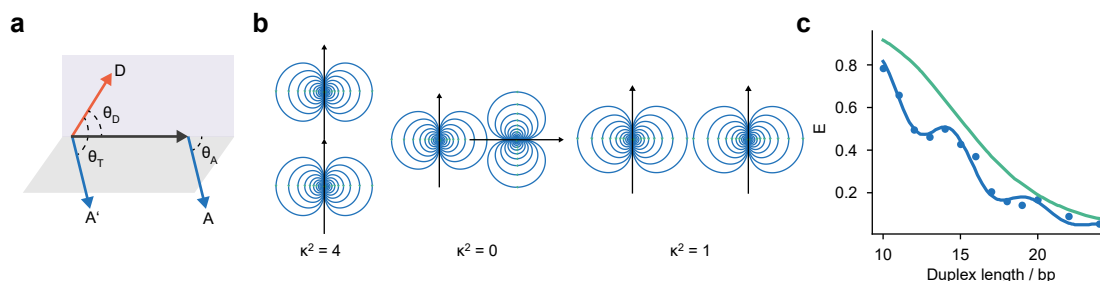


Figure 2.5: Influence of the orientations of the transition dipole moment of the donor and acceptor in FRET experiments. (a) Depiction of the nomenclature of the angles and distances between donor (D) and acceptor (A). (b) If the rotations of the fluorophores are hindered, the orientation of the transition dipole moments of the donor and the acceptor dye can influence the overall rate of FRET. For the extreme case of orthogonal moments, FRET can theoretically vanish completely. (c) A real-world example of this intricacy was shown in [65], where the sticking of the dye molecules to a DNA backbone hindered their rotation and resulted in a deviation of the measured FRET efficiency (blue) from the theoretical prediction (green). Copyright 2008 National Academy of Sciences.

Lastly, the extent of FRET depends on the relative orientation of the two electronic systems

to each other, encoded by the orientation factor κ^2 :

$$\kappa^2 = (\cos(\theta_T) - 3 \cos(\theta_D) \cos(\theta_A))^2 \quad (2.6)$$

Usually, both fluorophores can be assumed to rotate freely, which leads to an averaging of the value for κ^2 to $\frac{2}{3}$. However, if their rotation is hindered, e.g. by sticking of the dyes to their surroundings, κ^2 can be as high as 4 for head-to-tail aligned transition dipole moments and as low as 0 for orthogonal transition dipole moments (Figure 2.5a and b). In this extreme case, FRET can theoretically completely vanish. A nice illustration of this dependence of FRET on the orientation of the dyes to one another was shown in [65], where sticking of the Cy3 and Cy5 fluorophores to a DNA backbone prevented their free rotation and led to deviations of the observed FRET efficiency from the expected values assuming $\kappa^2 = \frac{2}{3}$ (Figure 2.5c).

FRET has become an extremely important tool in the investigation of biomolecular dynamics [17, 30, 66], which stems from the fact that the sensitive distance range of FRET of ca. 2–10 nm nicely overlaps with the dimensions of biomolecules such as proteins and nucleic acids. Furthermore, the time resolution that is offered by this method (milliseconds to minutes) is highly relevant for many biological processes, and the labelling and imaging conditions are generally compatible with in vitro and even in vivo studies.

2.1.4 Plasmonic fluorescence enhancement

Similar to other dipoles, the electromagnetic field itself can also affect the fluorescence properties of a molecule. A special case of this interaction involves the generation of locally enhanced electromagnetic fields with the use of specifically arranged metallic nanoparticles. To understand why these strong fields are generated, it is beneficial to first consider what happens to a metallic nanoparticle as it is irradiated with light. Metallic nanoparticles show non-localized conduction band electrons which in the Drude-Sommerfeld theory [68, 69] are approximated as an ideal electron gas. This gas responds to changes in the local electric field like a damped harmonic oscillator (without a restoring force) damped by collisions between the electrons with frequency γ and with a characteristic mass m :

$$m\ddot{x} + m\gamma\dot{x} = -eE(t) \quad (2.7)$$

For the case of light, where the electric field intensity oscillates with a certain frequency ω perpendicular to the propagation direction of the wave (Figure 2.6a), the displacement of the

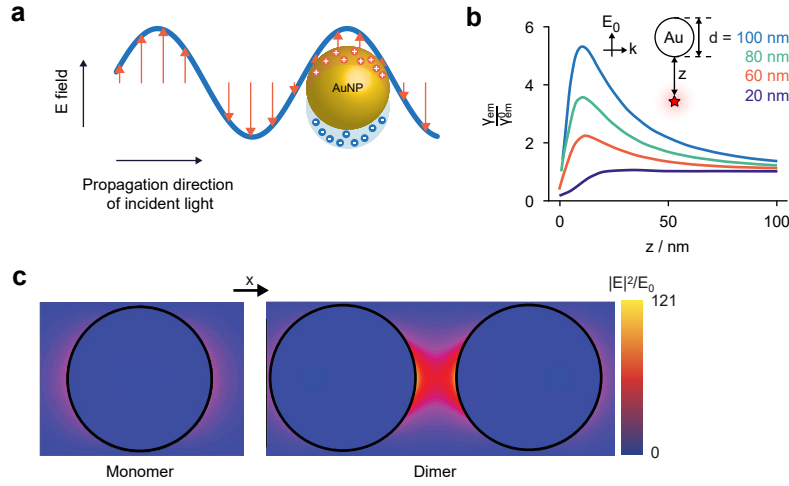


Figure 2.6: (a) Illustration of the behavior of a plasmonic nanoparticle upon irradiation with light: the electromagnetic field leads to a charge separation inside of the metal and induces a dipole moment. (b) Simulations of the dependency of the emission rate γ_{em} of a fluorescent molecule on the distance z to a gold nanoparticle of diameter d compared to the free space emission rate γ_{em}^0 . Reproduced figure with permission from [67]. Copyright 2023 by the American Physical Society. (c) Simulations of the electric field around a monomer (left) as well as a dimer with a 23 nm interparticle spacing (right) of 80 nm AuNPs. From [20]. Reprinted with permission from AAAS.

electron gas is given by

$$x(t) = \frac{e}{m(\omega^2 + i\gamma\omega)} E(t) \quad (2.8)$$

and the electric dipole moment per unit volume P of the nanoparticle is given by

$$P = -\frac{ne^2}{m(\omega^2 + i\gamma\omega)} E(t) \quad (2.9)$$

which can in turn be used to calculate the dielectric displacement D via

$$D = \epsilon_0 \left(1 - \frac{\omega_p^2}{\omega^2 + i\gamma\omega} \right) E = \epsilon_0 \epsilon E \quad (2.10)$$

with $\omega_p^2 = \frac{ne^2}{\epsilon_0 m}$ as the plasma frequency of the electron gas and ϵ_0 as the electric permittivity of the vacuum. From this expression, it follows that the dielectric constant of the nanoparticle is frequency dependent:

$$\epsilon(\omega) = 1 - \frac{\omega_p^2}{\omega^2 + i\gamma\omega} \quad (2.11)$$

With this, it is possible to calculate the dipole moment p of the nanoparticle:

$$p = 4\pi\epsilon_0\epsilon_m a^3 \frac{\epsilon_s - \epsilon_m}{\epsilon_s + 2\epsilon_m} E_0 \quad (2.12)$$

This implies a maximum at $\epsilon_s(\omega) = -2\epsilon_m$ (“Fröhlich condition”) and the effect of the incident light on the dipole moment of the nanoparticle is maximal at this frequency, which is called the plasmon resonance frequency [70]. This frequency usually is in the visible range, for gold nanoparticles with a diameter of 100 nm for example, it lies at approx. 620 nm [71]. The electromagnetic field influences the properties of fluorescent molecules, firstly by increase of the excitation rate, which is proportional to the product of the transition dipole μ of the fluorophore and the electric field E [72]:

$$k_{\text{exc}} \propto |\mu E|^2 \quad (2.13)$$

Secondly, the relaxation pathways from the excited state are modified by the vicinity of the nanoparticles: there are additional routes for non-radiative decay, where the energy is dissipated into the nanoparticle [73]. Furthermore, the radiative decay rate (the emission of a fluorescence photon) is accelerated by the electric field (also called the Purcell effect [74, 75]). Whether radiative or non-radiative decay pathways are more pronounced is dependent on the distance of the fluorescent molecule to the nanoparticle: at shorter distances, the non-radiative decay is dominating, which leads to quenching of the fluorescence, while at intermediate distances there is an overall increase of the emission rate, because the radiative decay is accelerated the most (Figure 2.6b).

When two of these nanoparticles are in close proximity, the induced dipole moments can interact and couple to each other, forming so called plasmonic hotspots – zeptoliter volumes in which the electric field can be several orders of magnitude stronger than the incident electric field [72, 76] (Figure 2.6c). These plasmonic nanostructures were first constructed using lithographic methods [19, 72, 77], but more recently, the DNA origami technology has emerged as a promising alternative method for their construction [20, 22, 78].

2.2 DNA nanotechnology

The determination of the crystal structure of B-Form deoxyribonucleic acid (DNA) [79, 80] in the 1950s was a cornerstone for the biological revolution in the following decades. Being able to relate the physical structure of DNA to the way in which genetic information is passed on

between living organisms was crucial for a deeper understanding of life in general, but also enabled the development of new diagnostic and therapeutic methods – the swiftness of the development of diagnostic tests and vaccines to fight the global SARS-CoV2 pandemic in the years 2020–2023 [81] was an impressive demonstration of the power of modern biology.

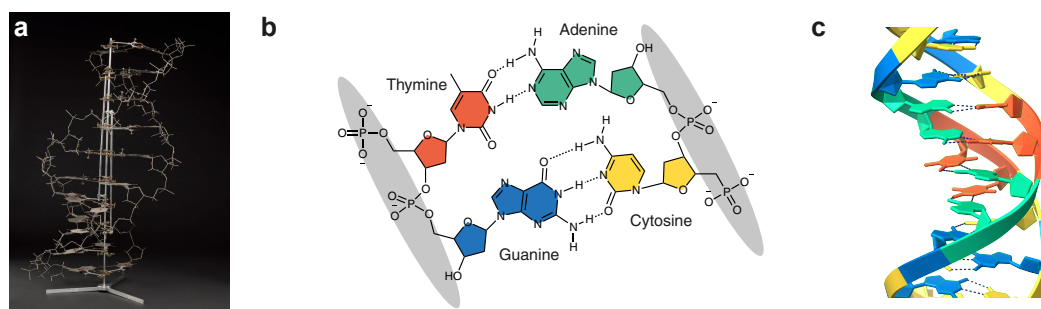


Figure 2.7: The molecular structure of DNA. **(a)** Original model proposed by Watson and Crick in 1953 [79] (CC-BY, The Science Museum). **(b)** Molecular structure of the four fundamental building blocks of dsDNA: in antiparallel alignment, the nucleobase thymine can form two hydrogen bonds with adenine while guanine can form three hydrogen bonds with cytosine. **(c)** Crystal structure of double stranded DNA [82] showing how the nucleobases align in space.

DNA is a biopolymer consisting of four different building blocks, the nucleotides adenine, thymine, guanine and cytosine (Figure 2.7). One strand of several of these nucleotides covalently linked via phosphodiester bonds can antiparallely interweave (hybridize) with a second single strand of DNA, given that the sequence of bases follows a certain pattern: due to the chemical structure of each nucleobase, the energetically most favourable alignment is reached when an adenine base is met with a thymine base on the other strand and when a guanine base is met with a cytosine base on the other strand, and *vice versa*, permitting hydrogen bridges between the two bases and forming a regular, double helical structure. This double-stranded DNA (dsDNA) is the central storage unit for genetic information, which is given by the sequence of the nucleobases.

To read, write and copy information to and from dsDNA, living systems developed a toolshed of DNA processing enzymes such as DNA helicases, which split a double stranded DNA into two single strands [83], or DNA topoisomerases, which can relax supercoiled dsDNA (dsDNA with higher-order secondary structure resulting from over- or underwinding [84]) by transiently breaking a DNA strand and passing the other strand through the gap [85]. In some of these processes, the dsDNA forms a so-called replicational junction, in which the parent dsDNA splits up and forms two new dsDNA strands. When exchanging information between two copies of DNA, as it is done during the recombination phase of the cellular cycle, the strands also form so-called Holliday junctions [86] – junctions with a four-way intersection. It is these

secondary structures that inspired researchers to think of DNA not only as a means of storing genetic information but also as a nanoscale construction material [10]. Since the way in which single DNA strands align with each other can be pre-programmed by their sequences it became conceivable to form 3D nanostructures with ever growing complexity.

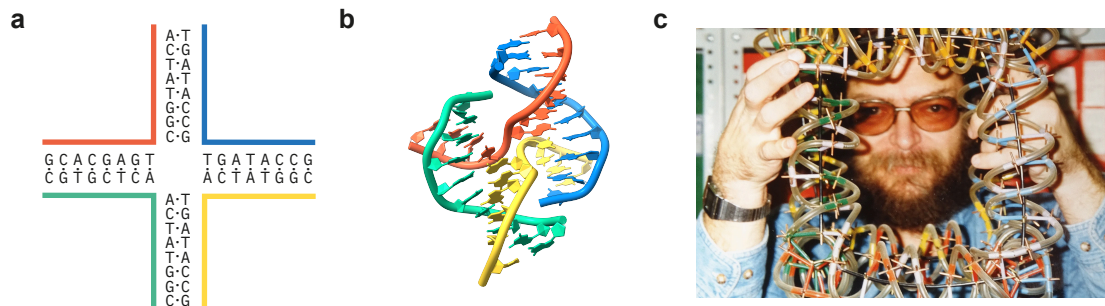


Figure 2.8: Some structural considerations for building DNA nanostructures: **(a)** the basic inspirational element of DNA nanostructures, an immobilized version of a Holliday junction. **(b)** Crystal structure of the junction shown in a) [87]. **(c)** One of the pioneers of DNA nanotechnology, Ned Seeman, presenting a model of the first synthetic nanostructure made with DNA: a cube with an edge length of ≈ 7 nm [88]. From [89]. Reproduced with permission from Springer Nature.

2.2.1 DNA as a building material

The key step in using DNA as a building material for 3D nanostructures was the creation of immobile junctions [90] – junctions between DNA strands that do not spontaneously resolve themselves due to the process of branch migration but remain “trapped” in the junction state (Figure 2.8a and b) and thus serve as a stable joint. Using these immobile junctions, researchers managed to create nanostructures such as a DNA cube [88] (Figure 2.8c), in which a total of ten ssDNAs were combined in a specific manner. However, the synthesis remained challenging, since it involved several steps of purification, and yields were relatively low.

This changed in 2006, when a new method for the creation of DNA nanostructures [11] was introduced. This method – termed “DNA origami” – uses a long (ca. 8k nucleotides) ssDNA as a scaffold strand to which shorter ssDNA strands hybridize and thereby join distal parts, forming a well-defined 2D structure. Since the sequence of the scaffold strand is known, the exact way in which the shorter strands will hybridize can be programmed. The advantage in terms of simplicity of this method is that exact stoichiometric ratios are not necessary for the formation of a structure and there are also no intermediate purification steps required. The scaffold and the staple strands are simply combined in a reaction tube,

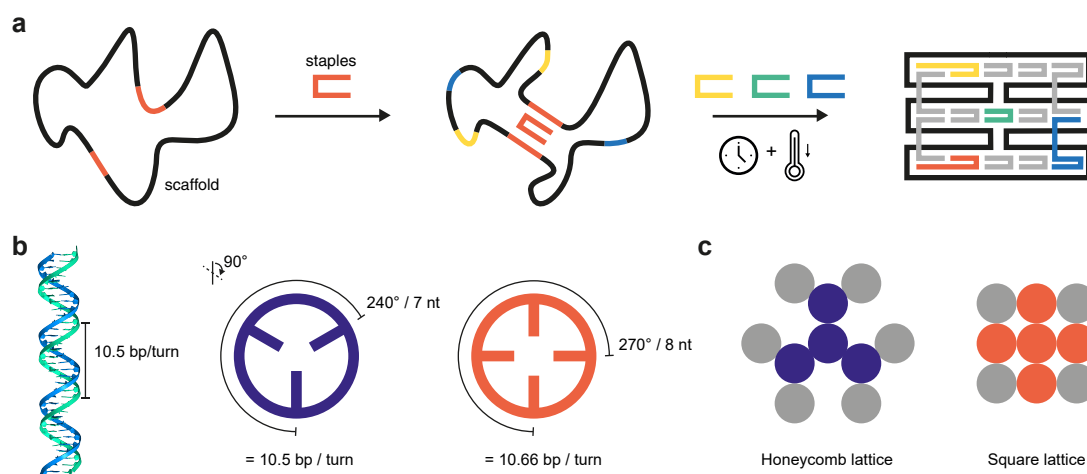


Figure 2.9: The DNA origami technique. **(a)** Illustration of the general approach: a long, single stranded scaffold strand is mixed with ca. 100–200 short staple strands. After denaturation at high temperature and slow cooling to room temperature, the staples connect distal parts of the scaffold strand to form a nanostructure. **(b)** The natural helicity of dsDNA imposes certain rules on the spacing of crossovers to other helices. A threefold symmetry (violet) is suited the best as it matches the natural helicity. A fourfold symmetry (orange) is also possible, but may lead to twists in the structure due to slight underwinding [91, 92]. **(c)** Depiction of the two most common approaches to form 3-dimensional DNA origami structures (each circle represents a DNA double helix).

denatured with a high temperature and then slowly cooled down to room temperature to allow the thermodynamically most stable configuration to form (Figure 2.9a). With this, the development of new structures was accelerated significantly and soon after was extended to three dimensions, which was done by placing crossovers between helices at non-integer multiples of full helix turns [93] (Figure 2.9b and c). Because of its ease of use and the endless possibilities with which the staple strands – at positions known *a priori* – can be modified with fluorescent dyes, reactive groups such as thiols or click-chemistry functionalites and other molecules, the DNA origami technique has become widely used as a nanoscale molecular breadboard [94–97] and tool to construct functional components on the nanoscale [13, 98].

2.2.2 Dynamic DNA nanostructures

With the ability to precisely construct nanostructures of almost arbitrary shape and complexity, the goal of many researchers was to transform these structures from passive units into structures that can perform actions on the nanoscale. One of the first examples of such structures was the “molecular tweezer structure” designed by Turberfield, Yurke and co-workers [99]. The critical point for their system was the realization that they can displace

one strand of dsDNA with another incumbent ssDNA by branch migration. This “toehold-mediated strand displacement” (Figure 2.10) works as long as the incumbent strand is able to form a more stable complex with the parent strand than the strand that is to be displaced. To a certain extent, this even works if the incumbent strand is forming a less stable complex with the parent strand, if the concentration of the incumbent strand is much higher [100].

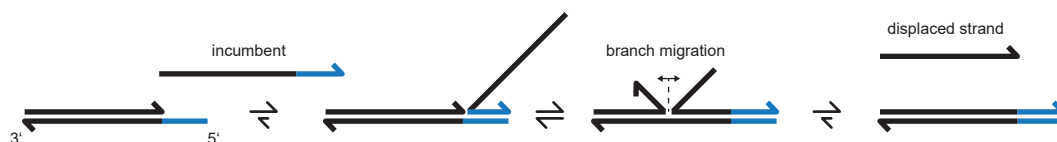


Figure 2.10: Toehold mediated strand displacement. An incumbent strand can displace one strand of the double stranded DNA by branch migration. Because the incumbent strand has a part of the opposing DNA to which it can bind exclusively, it will win the “tug-of-war” with the displaced strand: once the branch migration reaches a point where this strand is not stably bound to its partner anymore it will dissociate and diffuse away, leaving no chance for retaliation.

Another straightforward way to introduce dynamic behavior is to intentionally leave some regions of the nanostructure single stranded. Single stranded DNA is much more flexible than dsDNA — its persistence length was found to be 1.98 nm [101] as compared to ca. 50 nm for the case of dsDNA. Using these two strategies as the starting point, researchers soon were able to design structures that can adopt multiple conformations, such as a structures that could open and release cargo upon addition of trigger strands [13, 102] or nanoscale joints and hinges [47]. Recently, other examples of dynamic DNA nanostructures were shown by the combination of several stiff components into a ratchet motor [103] and a DNA turbine powered by an ion gradient [104].

2.3 Biomolecular binding reactions

One could make the point that the non-covalent binding of one molecule to a partner is the most fundamental process of biology, and indeed there are countless examples. In glycolysis, a central process of aerobic respiration, the metabolite glucose is sequentially bound and enzymatically reacted by not less than 10 different enzymes to yield pyruvate [105]. The reversible binding of DNA and RNA processing enzymes to the nucleic acid is central to replication and translation. The transport of proteins to the different subcellular compartments such as the endoplasmic reticulum is mediated by transient interactions of signal recognition particles with specific signal peptides [106, 107]. Furthermore, almost all sensory processes, e.g. the perception of umami taste [108], involve the binding of a ligand to a receptor, which

then triggers downstream signalling pathways. Conceptually, the binding of two molecules a

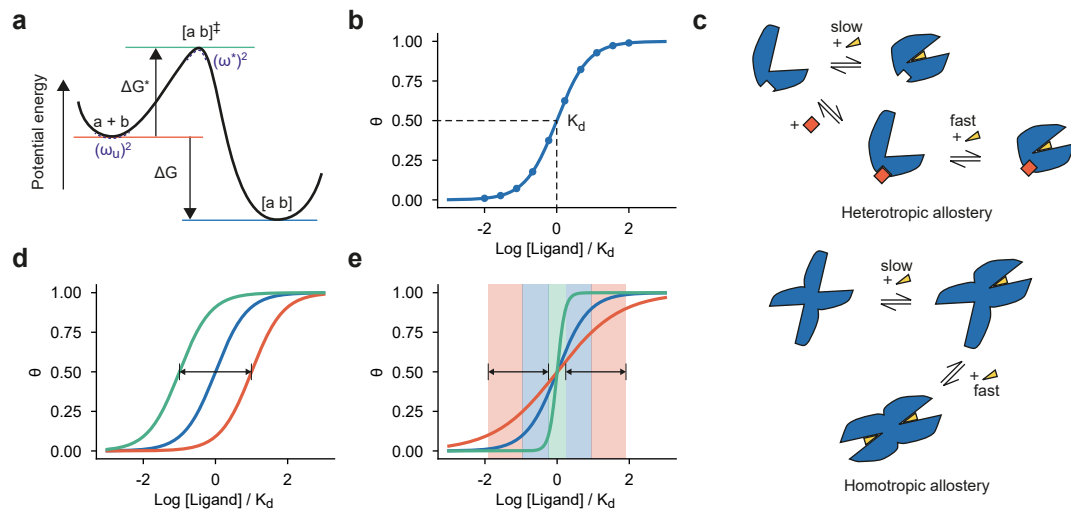


Figure 2.11: Biomolecular binding reactions. **(a)** Potential energy diagram of the complex formation of compounds a and b . The curvature of the energy surface is shown by ω . ΔG shows the difference in potential energy between the states. **(b)** The dissociation constant, which is the concentration at which half of the receptor is occupied, of a binding reaction can be determined by titration with one of the partners while monitoring the complex concentration. **(c)** Top: Heterotropic allostery, in which an effector molecule that is structurally different from the ligand influences the binding reaction, is one of the strategies used by living systems for the regulation of enzyme activities. Bottom: The other strategy, in which the ligand simultaneously acts as effector, can lead to cooperative or anticooperative behavior. **(d)** Effect of heterotropic allosteric regulation on the dose-response curve of a biological binding reaction. Binding of the effector can shift the dissociation constant to higher or lower values. **(e)** Homotropic allosteric regulation, or cooperativity, furthermore, can have an effect on the steepness of the curve, leading to potentially very sensitive responses to a ligand or a very broad response window (indicated by the colored areas).

and b to form a complex ab is driven by a favorable change in free energy $\Delta G < 0$, which in turn results from the combination of entropic effects, where the reduction in degrees of freedom of the two binding partners is opposing the increase in degrees of freedom of the solvent, and enthalpic effects through e.g. the formation of new hydrogen bonds [109] (Figure 2.11a). Experimentally, usually the association or dissociation constants K_a or K_d can be determined, which are related to ΔG via

$$\Delta G = -k_B T \ln K \quad (2.14)$$

where k_B is Boltzmann's constant and T is the temperature. This is typically done by adding a known concentration of one of the binding partners to the other binding partner and monitoring the resulting change in occupancy ("titration", Figure 2.11b). According to the

law of mass action, the dissociation constant is given by

$$K_d = \frac{[a][b]}{[ab]} \quad (2.15)$$

However, typically only the initially added amount of a and b are known, which separate into bound and unbound fractions:

$$[a]_0 = [a] + [ab] \quad \text{and} \quad [b]_0 = [b] + [ab] \quad (2.16)$$

Substitution of this expression for $[a]$ into Eq. 2.15 allows to retrieve the dissociation constant from known parameters:

$$[ab] = \frac{[a]_0[b]}{K_d + [b]} \quad (2.17)$$

which can be further divided by $[a]_0$ to yield the fractional saturation/occupancy

$$\theta = \frac{[ab]}{[a]_0} = \frac{[b]}{K_d + [b]} \quad (2.18)$$

It is important to note that the known parameter in a titration experiment is usually the total added amount $[b]_0$, which means that the extraction of K_d with this expression assumes

$$[b] \approx [b]_0 \quad \text{i.e.} \quad [a] \ll K_d \quad (2.19)$$

which has to be validated before the experiment [110]. Most binding constants lie in the micromolar regime [28] but in some cases, they can be as low as femtomolar [111]. The dissociation constant K_d on the molecular level can be understood as a measure for the strength of the interaction or a probability for a spontaneous dissociation event and is a fundamental property for any given pair of receptor and ligand. For a single-site receptor, the window in which the receptor occupancy can be translated to a ligand concentration, traditionally the window between 10% and 90% occupancy, spans an 81-fold change in ligand concentration.

2.3.1 Allostery

As mentioned above, the binding of a ligand to its partner can have huge effects, e.g. by the subsequent triggering of a signalling cascade. Yet, the binding to a single site will always follow a sigmoidal dose-response curve with fixed mid-point and steepness (Figure 2.11b). It is therefore important for living systems to be able to modulate this behavior, in order

to ensure that they can react dynamically to e.g. environmental changes. Several of these modulation mechanisms have been discovered, which involve the modulation either by a different modulator molecule (heterotropic allostery) or by the ligand itself (homotropic allostery [112]).

In heterotropic allostery, the modulator molecule, which can be as small as a sodium ion [113], binds to the protein and leads to a change in its conformation [114] or structural dynamics [115] which in turn changes ΔG of the binding interaction and thus the dissociation constant (Figure 2.11c and d).

In homotropic allostery, the modulator is the ligand itself, and thus this mechanism can only occur in multivalent systems. Here, the binding of the first ligand leads to structural rearrangements of the system resulting in an altered affinity of the binding of the next ligand to the next site (Figure 2.11c) which can in turn result in a steepening or flattening of the dose-response curve (Figure 2.11e). Often also termed “cooperativity”, this behavior is extremely important for efficient transport and sensing of molecules with smaller or larger differences in concentrations. The mechanisms of cooperativity are still not completely understood [41, 116], however, there are models that describe the behavior quite well. A relatively simple model was presented by Hill [117]: for the case of n ligands binding to one receptor, he defined the dissociation constant according to the law of mass action as [118]

$$K_d = \frac{[a][b]^n}{[ab_n]} \quad (2.20)$$

which can be rearranged in an analogous way to Eq. 2.17 to yield

$$\theta = \frac{[b]^n}{K_d + [b]^n} \quad (2.21)$$

with the exponent n as the “Hill coefficient”, often also denoted n_H . Hill’s equation describes cooperative binding reasonably well, but failed at retrieving the total number of binding sites of hemoglobin, which was the original goal. This is due to the fact that the model only assumes simultaneous binding of all ligands and does not account for intermediate binding steps, which is only true in the edge case of infinitely strong cooperativity [118]. Adair [119] therefore derived a more realistic equation, where each binding step is assigned its own binding constant:

$$\theta = \frac{[ab] + 2[ab_2] + 3[ab_3] + \dots + n[ab_n]}{[a] + [ab] + [ab_2] + \dots + [ab_n]} \quad (2.22)$$

which results in a binding curve whose steepness depends on the difference between the

individual binding constants for each subsequent step: for the case that the individual binding constants are equal, the steepness of the binding curve becomes 1, indicating non-cooperative binding behavior. The higher the difference between the individual steps, the more the steepness will approach its maximum value of n . The Hill coefficient n_H thus is a relative measure of how cooperative the binding reaction is, rather than a concrete measure for the number of binding sites.

2.3.2 Transition paths

While the macroscopic behavior of the binding interaction is sufficiently characterized by the thermodynamic parameters ΔG and K_d , many of the mechanistic insights are contained in the kinetics of the transition of the unbound to the bound state or generally between two conformational states. Specifically, informations on the shape of the free energy barrier between the two states as well as potential trap states or short-lived intermediates [120–122] along the reaction coordinate can be obtained, possibly leading to new druggable targets and a deepening of the understanding of processes such as protein aggregation or misfolding. By analyzing the Brownian motion of a particle with diffusion coefficient $D^* = \frac{k_B T}{\zeta^*}$ (Einstein-Smoluchowski equation) – in which ζ^* is the friction coefficient which is related to the viscosity of the solution [123] – in a potential energy surface with two wells and a transition barrier with barrier height ΔG^* and curvatures of the energy surface in the educt state and at the transition state $(\omega_u)^2$ and $(\omega^*)^2$ connecting them (Figure 2.11a), Kramers [123–125] derived an expression for the rate k of the reaction:

$$k = \frac{D^* \omega^* \omega_u}{2\pi k_B T} \exp\left(\frac{-\Delta G^*}{k_B T}\right) \quad (2.23)$$

Interestingly, unlike the macroscopic rate of the reaction, which is exponentially sensitive to the height of the free energy barrier, the mean transition path time $\langle \tau_{tp} \rangle$ is only logarithmically sensitive to the barrier height, as was shown by Szabo [125–127]:

$$\langle \tau_{tp} \rangle = \frac{k_B T}{D^* (\omega^*)^2} \ln\left(\frac{2 \exp(\gamma) \Delta G^*}{k_B T}\right) \quad (2.24)$$

with γ as Euler's constant. This theoretical prediction was also confirmed experimentally [128] by comparing transition path times for a fast-folding and a slow-folding protein. In general, the simple description of the process as one dimensional diffusion over the potential energy surface is remarkably successful at explaining experimental observations [129, 130].

Measurements of transition path times require single molecule methods, because the barrier crossing event is a rare process that can not be synchronized. However, as these times are typically on the order of a few microseconds, extreme sensitivity and time resolution is needed. This is why the most detailed measurements of these processes so far have been done with optical tweezers [131, 132]. Single molecule FRET experiments also have been used for the determination of transition path times [36, 125, 128, 133, 134], but so far the time resolution of these experiments does not permit direct observation of the transition paths but relies on statistic analysis using a Maximum Likelihood estimator [128, 135]. This method explicitly imposes a certain shape of the transition path (usually a step function) on the data and thus might under- or overestimate the transition path times [136].

3 Materials and Methods

3.1 Microscopy setups

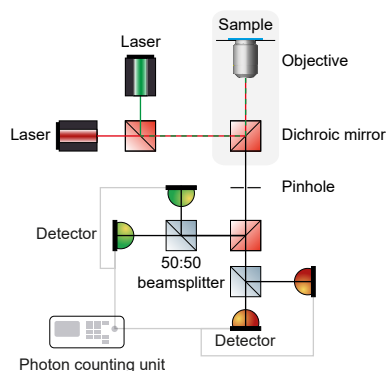


Figure 3.1: Schematic drawing showing the setup of the confocal microscopes.

Setup 1

Data was acquired on a home-built setup based on an Olympus IX-71 microscope body. A LDH-D-C-640 laser (636 nm) and optionally a LDH-P-FA-530B laser (532 nm) were focussed to a diffraction-limited spot and sent through a linear polarizer (LPVISE100-A, Thorlabs GmbH) and a $\lambda/4$ plate (AQWP05M-600, Thorlabs GmbH) for circularly polarized light. An oil-immersion objective (UPLSAPO100XO, NA1.40, Olympus Deutschland GmbH) was employed to focus the light onto the sample. A piezo stage (P-517.3CD, Physik Instrumente GmbH & Co. KG) and a piezo controller (E-727.3CDA, Physik Instrumente GmbH & Co. KG) was used to scan the sample. Fluorescence was separated from the excitation light with a dichroic beam splitter (zt488/543/635/730rpc or zt532/640rpc, Chroma Technologies) and focussed on a pinhole (50 μm diameter, Thorlabs GmbH). The fluorescence was then split between the red and infrared or red and green channel using a beam splitter (HC BS 749 SP or 640 LPXR, Chroma Technologies). The red fluorescence was sent to one APD

(SPCM-AQRH-14-TR, Excelitas Technologies GmbH & Co. KG, Germany) or distributed to 2 APDs (SPCM-AQRH-14-TR and SPCM-AQR-15, Excelitas Technologies GmbH & Co. KG, Germany) using a nonpolarizing 50:50 beam splitter (CCM1-BS013/M, Thorlabs GmbH). The green or infrared channel was sent to one APD (SPCM-AQRH-14-TR, Excelitas Technologies GmbH & Co. KG, Germany) or distributed to 2 APDs (SPCM-AQRH-14-TR and SPCM-AQR-15, Excelitas Technologies GmbH & Co. KG, Germany) using a nonpolarizing 50:50 beam splitter (CCM1-BS014/M, Thorlabs GmbH). Events were registered by a multichannel picosecond event timer (HydraHarp 400, PicoQuant GmbH) and the hardware was controlled using a commercial software (SymPhoTime 64, PicoQuant GmbH).

Setup 2

Data was acquired on a home-built confocal microscope based on an Olympus IX-83 body (Japan). A supercontinuum white light laser pulsed at 78 MHz (SuperK Extreme, NKT Photonics, Denmark) was used for excitation of the samples. The appropriate wavelengths were selected by using an acousto-optically tunable filter (SuperK Dual AOTF, NKT Photonics, Denmark) controlled with a digital controller (AODS 20160 8R, Crystal Technology, USA). Optionally, a second acousto-optically tunable filter (AA.AOTF.ns:TN, AA Opto-Electronic, France) controlled with a home-written LabVIEW (National Instruments, USA) program was used to alternate between two wavelengths. A neutral density filter, a linear polarizer and a $\lambda/4$ plate were used to achieve circularly polarized excitation light of the desired intensity. The excitation light was sent to the sample through an oil immersion objective (UPlanSApo 100 \times , NA=1.4, WD=0.12 mm, Olympus, Japan) via a dichroic beam splitter (zt532/640rpc, Chroma, USA). A piezo stage (P-517.3CL, E-501.00, Physik Instrumente GmbH & Co. KG, Germany) was used to move the sample in X-Y. The fluorescence light was collected with the same objective and separated from the excitation light with the dichroic. Then, the fluorescence light was sent through a 50 μm pinhole, the two emission channels were split using another beam splitter (640DCXR, AHF Analysetechnik AG, Germany) and focused onto the single photon detectors (SPCM, AQR 14, PerkinElmer, USA).

3.2 Design and production of DNA origami nanostructures

Design of DNA origamis

DNA origami nanostructures were designed in caDNA_{no} [137] and iteratively optimized with the simulation tools CanDo [138, 139] and oxDNA [140–144]. For the analysis and optimization of the folding, as well as the purification of the origamis, protocols inspired by [145] were used:

Agarose gel electrophoresis

50 mL TAE buffer with 10 mM MgCl₂ were mixed with 0.75 g agarose. After heating the mixture in a microwave to dissolve the agarose, it was poured in a gel tray with large combs. If staining of the DNA was needed, 1 µL of ROTI[®] GelStain (Carl Roth GmbH & Co. KG, Germany) was added beforehand. The gel was placed into the gel chamber and submerged in the same TAE buffer. 50 µL of the DNA origami sample was mixed with 5 µL of 10× BlueJuice[™] (Thermo Fisher Scientific, USA) and loaded into the gel well. The gel chamber was placed into an ice bath and then run at 70 V for at least 3 hours. Afterwards, the gel was placed in a gel documentation system (Fusion FX, Vilber Deutschland GmbH, Germany) to identify the bands with the DNA origami structures. The respective bands were cut out of the gel with a scalpel and placed on a Parafilm surface, where the samples were squeezed out of the gel using a glass slide that was also covered in Parafilm.

Filter purification

For filter purification of DNA origami structures, Amicon[®] Ultra 0.5 mL centrifugal filters with 100 kDa molecular weight cut-off were used. The filters were washed by filling them with 450 µL of FoB5 buffer (10 mM TRIS, 5 mM MgCl₂, 5 mM NaCl, 1 mM EDTA) and centrifuging at 10 krcf for 7 minutes. Then, 50 µL of unpurified DNA origami solution and 450 µL of FoB5 buffer were filled into the filter tubes and the mixture was centrifuged for 12:30 minutes at 7 krcf. The filtrate was discarded and the procedure was repeated for 3 times. Then, the filter was placed upside down into a new centrifuge tube and the purified origami mixture was recovered by centrifuging for 3 minutes at 7 krcf.

3.3 Sample preparation

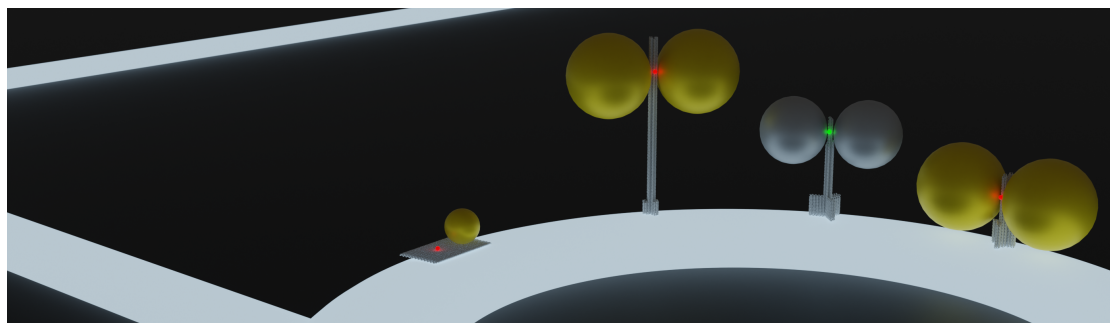
Microscopy slides (24 mm × 60 mm size and 170 μm thickness (Carl Roth GmbH, Germany)) were cleaned at 100 °C for 30 mins in an ozonator (PSD-UV4, Novascan Technologies, USA). Then, 2 CoverWell™ Perfusion Chamber gaskets (9 mm diameter, 0.5 mm deep, Grace Bio-Labs, USA) were glued on the microscopy slides and the glue was activated by shortly (30 seconds) placing the slide on a 100 °C heating plate. Surfaces were cleaned by incubating with 1 M KOH for 10 minutes. The chambers were washed with PBS (4 times). The surfaces then were passivated with BSA-Biotin (1 mg/mL in 10 mM TRIS, 1 mM EDTA, 50 mM NaCl, Sigma Aldrich, USA) for 10 minutes. The chambers were then washed with PBS (3 times). Then, the chambers were incubated with NeutrAvidin™ (0.25 mg/mL in PBS, freshly diluted from a 1 mg/mL stock in ultrapure H₂O, Thermo Fisher Scientific, USA) for 10 minutes. After washing with PBS another 3 times, the chambers were ready for use. If photostabilization required sealing the slides off from ambient air, or the sample needed to be protected from evaporation, the chambers were closed with adhesive seal tabs (Grace Bio-Labs, USA).

3.4 Data analysis

Data was analysed using custom Python and C++ code. To import time correlated single photon counting data, the module `phconvert` [146] was used. Further modules that were used for data analysis and visualization purposes were `NumPy` [147], `Matplotlib` [148], `SciPy` [149] and `Eigen` [150].

4 Fluorescence enhancement with DNA origami nanoantennas

4.1 Associated Publication 1



DNA origami nanoantennas for fluorescence enhancement

Viktorija Glembockyte*, [Lennart Grabenhorst*](#), Kateryna Trofymchuk* and Philip Tinnefeld

*equal contribution

Accounts of Chemical Research **54**, 17, 3338–3348 (2021). doi: 10.1021/acs.accounts.1c00307

(open access)

The DNA origami method has proven extremely valuable for the field of nanophotonics. The possibility of selectively immobilizing molecules in nanophotonic devices such as plasmonic nanoantennas offers unprecedented flexibility in experimental setups and has great potential for fields such as biosensing and biophysics. In this review article, we summarize the developmental steps for DNA origami nanoantennas from the first measurements of fluorescence quenching by single gold nanoparticles on a flat 2D DNA origami to the successful incorporation of complex diagnostic assays into plasmonic hotspots, enabling the detection of DNA relevant

to antibiotic resistance genes in *Klebsiella pneumonia* with a cheap and portable smartphone microscope.

In the first section, we review fundamental aspects of the interaction of fluorophores with plasmonic nanoparticles. Briefly, for smaller nanoparticles, the non-radiative decay is the only photophysical rate that is affected while for larger (> 20 nm) nanoparticles, also the excitation and radiative decay are accelerated.

The second section focusses on the key developments that helped maximize fluorescence enhancement and optimize the DNA origami nanoantennas for the use with fluorophores covering a broader range of the visible spectrum as well as making the plasmonic more accessible for the use in various applications.

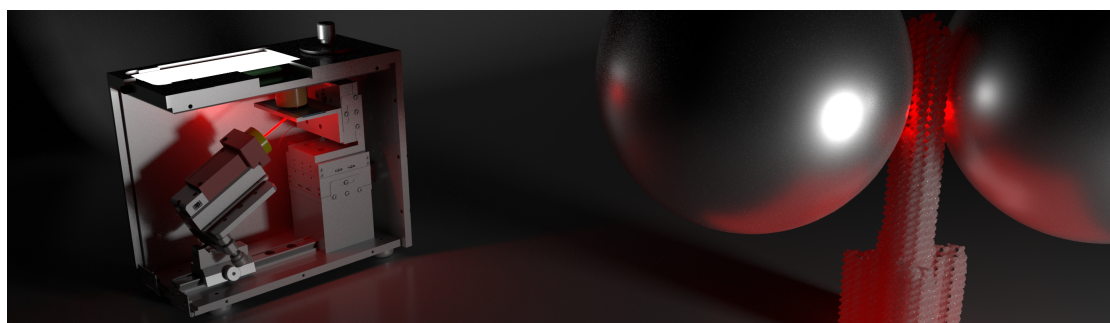
In the third section, we highlight the potential of DNA origami nanoantennas to be used in single molecule biophysics. Here, we expand on three key advantages we identified, namely the ability to work at higher background concentrations of labelled molecules, the possibility of increasing the photon count rate for better time resolution as well as the beneficial effects of the plasmonic hotspot on fluorophore photostability.

In the last section, the potential of DNA origami nanoantennas for diagnostics is showcased, which originates from its function as a physical amplification mechanism. Unlike biological amplification strategies such as the polymerase chain reaction, which usually needs some time as well as equipment, the nanoantenna can in principle amplify the signal *in situ*, leading to an instant result which could be detected with a low-tech camera.

Author contributions

For this publication, I gathered the data of previous publications, wrote parts of the manuscript (“Introduction”, “DNA origami nanoantennas for single molecule biophysics” and “Conclusions and Outlook”) and designed all 5 figures as well as the ToC figure and a cover figure.

4.2 Associated Publication 2



Addressable nanoantennas with cleared hotspots for single-molecule detection on a portable smartphone microscope

Kateryna Trofymchuk*, Viktorija Glembockyte*, [Lennart Grabenhorst](#), Florian Steiner, Carolin Vietz, Cindy Close, Martina Pfeiffer, Lars Richter, Max L. Schütte, Florian Selbach, Renukka Yaadav, Jonas Zähringer, Qingshan Wei, Aydogan Ozcan, Birka Lalkens, Guillermo P. Acuna and Philip Tinnefeld

*equal contribution

Nature Communications **12**, 950 (2021). doi: 10.1038/s41467-021-21238-9

(open access)

The use of DNA origami nanoantennas for diagnostic purposes was severely limited by the fact that the volume of highest fluorescence enhancement was mostly blocked by the DNA origami nanostructures, which resulted in problems when larger entities – such as diagnostic assays – were supposed to be immobilized in the plasmonic hotspot. As a consequence, only moderate fluorescence enhancement values were obtained, which prevented the further use of these structures for diagnostic applications.

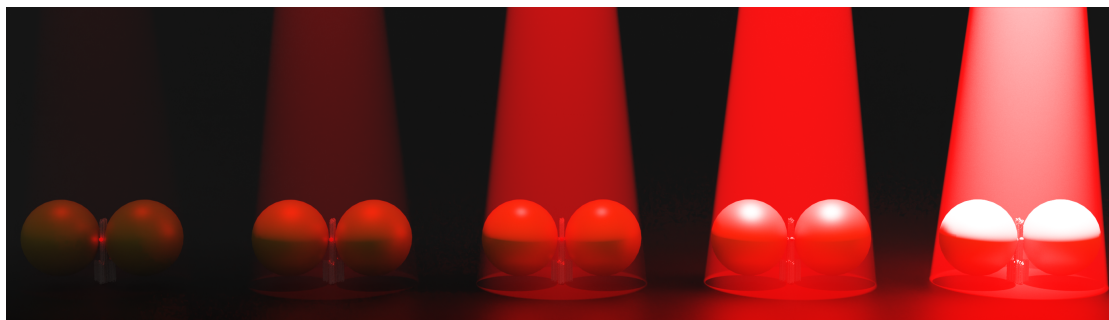
In this contribution, we sought to solve this problem with a new DNA origami design. Here, the attachment sites for the plasmonic nanoparticles were distributed to two pillars instead of one, resulting in precise placement of the plasmonic hotspot to the region exactly between these two pillars. This “cleared hotspot” was now available for the placement of a complex diagnostic sandwich assay for the detection of DNA specific to antibiotic resistance genes in *Klebsiella pneumoniae*. With the large fluorescence enhancement values provided by the new

design, it then became possible to carry out this diagnostic assay on a portable smartphone microscope with all required power provided by a USB power bank. This new design thus paved the way for many follow-up projects in which larger biomolecules such as proteins could be placed in plasmonic hotspots.

Author contributions

P.T., A.O. and G.P.A. conceived the project, L.G. and B.L. developed the DNA origami structure, K.T., V.G. and M.P. optimized the solution synthesis procedure, F.Se. performed the TEM measurements, K.T., V.G., C.C., M.P. and R.Y. developed the sandwich assay and prepared samples, performed and analyzed the measurements on the confocal microscope, C.V., L.R., M.L.S., Q.W., A.O. and G.P.A. worked on an earlier version of the smartphone microscope, K.T., V.G., F.St. and J.Z. constructed the portable smartphone microscope, K.T., V.G. and F.St. performed and analyzed the measurements on the smartphone microscope, K.T., V.G., L.G., F.St. and P.T. wrote the manuscript.

4.3 Associated Publication 3



Fluorophore photostability and saturation in the hotspot of DNA origami nanoantennas

Lennart Grabenhorst*, Kateryna Trofymchuk*, Florian Steiner, Viktorija Glembockyte and Philip Tinnefeld

*equal contribution

Methods and Applications in Fluorescence **8**, 024003 (2020). doi: 10.1088/2050-6120/ab6ac8

(open access)

During the development of the new DNA origami nanoantenna presented in Publication 4.2, many details on the effects of fluorescence enhancement on the photophysical properties of fluorescent dyes and quenchers were discovered, which we summarized in this publication. It is well-known that the increased electric field in the plasmonic hotspot leads to acceleration of the excitation rate as well as the non-radiative and radiative decay rates from the singlet excited state. We confirm previous studies showing that this has beneficial effects on the stability of fluorescent labels: even the most photostable fluorescent dye, ATTO 647N, emitted an average of approximately ten times more photons before photobleaching, even though the excitation power was ≈ 5.6 times lower. However, at these drastically changed excitation and emission rates, new photophysical processes start to appear, which have to be accounted for in the design of an experiment.

Firstly, we discovered that dyes from several different classes start to show reversible or irreversible transformations to less emissive states, which we hypothesized could be due to formation of spectrally shifted forms of the dyes. Importantly, it is sometimes difficult

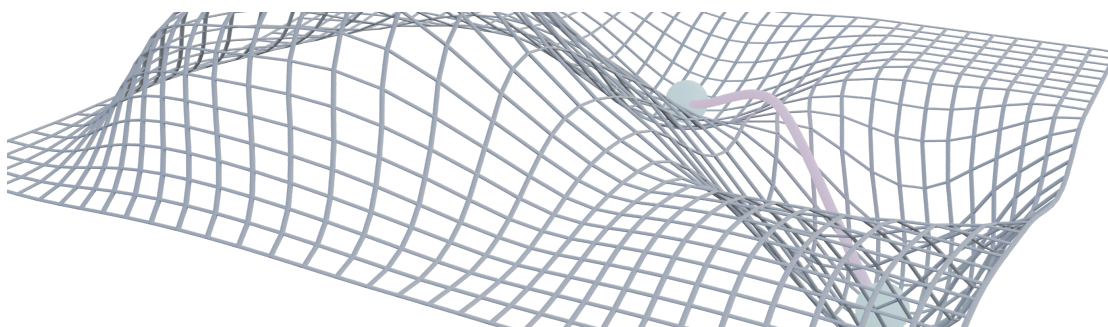
to tell whether such rearrangement has happened, which might lead to underestimation of fluorescence enhancement values. We also highlight that saturation of the fluorescence becomes noticeable at higher excitation powers, which is most pronounced in dyes where additional power-dependent processes such as photoisomerization take place. Lastly, we also demonstrate that also fluorescence quenchers are influenced by the strong excitation intensities. These molecules can photobleach prematurely, leading to possible false positives in diagnostic essays.

Altogether, in this contribution we summarize key aspects of working with fluorescent dyes at elevated excitation intensities as they can be found in plasmonic hotspots. Our findings pave the way towards high-concentration experiments, e.g. for studying biological interactions (as it will be shown in Publication 4).

Author contributions

For this publication, I designed research with Philip Tinnefeld, Viktorija Glembockyte, Kateryna Trofymchuk and Florian Steiner. For the FCS data I prepared samples and acquired and analysed the data, discussed all data and wrote the manuscript with Philip Tinnefeld, Viktorija Glembockyte, Kateryna Trofymchuk and Florian Steiner.

4.4 Associated Publication 4



Single-molecule FRET at 10 MHz count rates

Lennart Grabenhorst, Flurin Sturzenegger, Moa Hasler, Benjamin Schuler and Philip Tinnefeld

bioRxiv (2023). doi: 10.1101/2023.12.08.570755

Single molecule FRET experiments are important for the understanding of biomolecular dynamics. Many interesting processes, however, occur on timescales that are hard to access with conventional fluorescent labels because of their limited photostability. In this publication, we show that plasmonic hotspots can be used to increase photon count rates and fluorophore photostabilities in these types of experiments. We use a well-studied pair of intrinsically disordered proteins (IDPs) which form a short-lived encounter complex upon binding as a model system for biomolecular reactions. One of the IDPs was immobilized in the plasmonic hotspot and binding of the other IDP was observed at high illumination intensities. Analysis of the binding events yielded lifetimes consistent with previous results, affirming the biocompatibility of our system.

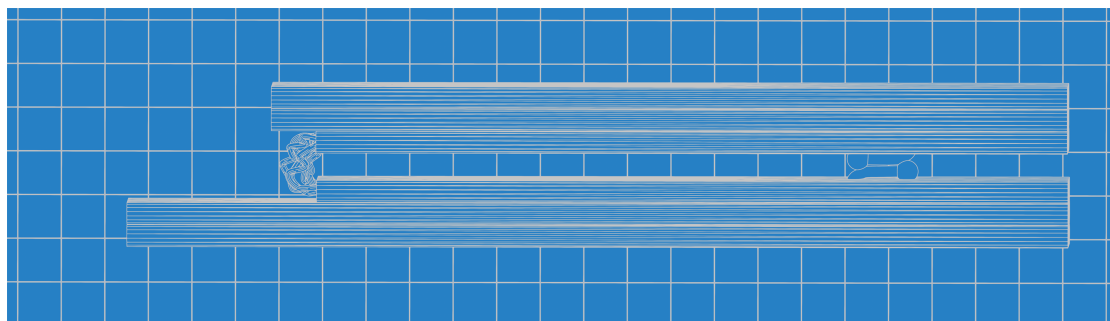
We then observed the hybridization of a short ssDNA to a ssDNA docking site in the plasmonic hotspot. Here we achieved maximum photon count rates of > 10 MHz, which enabled us to reveal a transition path time for the hybridization reaction of ≈ 17 μ s. This shows that DNA origami nanoantennas can be of use in biophysical experiments, and could potentially help gain new insights on ultrafast biological processes such as protein folding.

Author contributions

For this publication, I designed the research with Philip Tinnefeld, Benjamin Schuler and Flurin Sturzenegger, prepared all samples, acquired and analysed all data, wrote the manuscript with Philip Tinnefeld and Benjamin Schuler and designed all figures.

5 Decoupling signal transduction from recognition in DNA origami biosensors

5.1 Associated Publication 5



Engineering modular and tunable single-molecule sensors by decoupling sensing from signal output

Lennart Grabenhorst*, Martina Pfeiffer*, Thea Schinkel, Mirjam Kümmerlin, Jasmin B. Maglic, Gereon A. Brüggenthies, Florian Selbach, Alexander T. Murr, Philip Tinnefeld and Viktorija Glembockyte

bioRxiv (2023). doi: 10.1101/2023.11.06.565795

*equal contribution

The binding of a molecule a to another molecule b is arguably the most fundamental form of biological information transfer. While living systems can process this information directly, we as researchers have to find ways to visualize this information transfer in order to have access to the full picture of cellular processes and diseases. The difficulty in this lies in the fact that especially small molecules like hormones, neurotransmitters or metabolites most often

only lead to miniscule conformational changes in the binding molecule, which are extremely hard to detect with any *in vivo* or *in vitro* method. This typically results in the need for tedious optimization of the signal (typically FRET), which slows down the development of new sensors. The second challenge then is of thermodynamic origin: given that the analyte concentration range of interest is far away from the dissociation constant of the biological interaction, or the change of concentrations we are interested in is smaller than the two orders of magnitude dictated by the binding curve, how do we find out whether something has changed? In this publication, we developed a modular sensor platform in an effort to tackle these problems.

By arranging the sensor components on a dynamic DNA origami that is able to undergo large conformational changes, we spatially decoupled the signal transduction unit from the sensing unit. This ensured a large FRET contrast between the bound and the unbound state, independent of the biointeraction that we used. We then used a DNA-DNA interaction as a model for reversible ligand binding to demonstrate several strategies for the tuning of the sensor's response window (given by $K_{1/2}$ and n_H). We then demonstrated the modularity of this platform by adapting it to a range of different biomolecular targets such as antibodies and nucleases, without the need for re-engineering the signalling unit and under retention of the high FRET contrast. Altogether, this work is a starting point for the development of many new biosensors with tunable response windows and highlights key strategies for the tuning of a sensor's response window.

Author contributions

V.G. and P.T. conceived the idea and directed the project. V.G., P.T., L.G. and M.P. further conceptualized the research. L.G. designed the DNA origami sensor and performed oxDNA simulations. L.G., V.G., M.K., and J.M. tested and optimized the design of the sensor and the signal transduction element. F.S. and G.A.B. performed TEM measurements. L.G. and V.G. implemented the sensor tuning strategies and carried out and analyzed single molecule titration experiments with the help of G.A.B. and A.T.M.; T.S. and V.G. designed and carried out the sensor specificity studies. M.P. carried out and analyzed antibody, nuclease detection, multiplexed detection assays. L.G. wrote the code for single-molecule data analysis. L.G. and V.G. prepared figures. V.G., L.G. and P.T. wrote the manuscript with additional input from M.P.

6 Conclusions and Outlook

The DNA origami technique is a powerful method for the construction of higher-order nanoscale assemblies. The ease at which complex molecular arrangements can be realized offers unprecedented possibilities for single molecule experiments, two of which I realized in this thesis.

6.1 DNA origami nanoantennas for single-molecule biophysics

The successful redesign of the DNA origami nanostructure used in plasmonic nanoantennas for fluorescence enhancement opened up many new applications and avenues of research. The option to incorporate larger molecular entities not only enabled the first portable diagnostic assay based on fluorescence with a portable microscope (chapter 4.2), but also already made it possible to detect another diagnostic target, namely antibodies, using this setup [151]. This is a big step towards the realization of a point-of-care diagnostic device that can be used in settings without access to stable power supply and trained personnel or in areas far away from diagnostic laboratories. In this thesis, the focus was put on developing DNA origami nanoantennas to the point where they can be useful in biophysical FRET experiments, specifically in increasing the attainable photon count rates when observing single FRET pairs, an application that has long been anticipated [20, 28]. To this end, a thorough characterization of the effects of high excitation intensities on the photophysics of fluorescent dyes was carried out (chapter 4.3), and several key points were identified. It was shown that most fluorophores exhibit pronounced dim state formation, which makes them less suitable for the use in these conditions. However, for cyanine dyes this dim state formation occurred less frequently, which generally allowed for longer observation times at high count rates. Furthermore, higher fluorescence intensities were obtained when a FRET pair covering the red and near IR wavelength regions was used, as opposed to a FRET pair covering the more commonly used green and red spectral regions.

The successful incorporation of the ACTR protein into the plasmonic hotspot, as well as the fact that the binding reaction with NCBD could be observed at photon count rates much higher than it was possible without the plasmonic fluorescence enhancement, shows the promises of this approach for single molecule FRET experiments. However, the much lower average observation times as well as the much lower average photon count rates in comparison to the experiment with the labelled DNA shows that there still is room for improvement. As hypothesized in chapter 4.4, a plausible explanation for this discrepancy is the proximity of the thioether group [152] due to our linking chemistry, which relies on cysteine labelling via Michael addition of dye-maleimides [153]. An obvious next step thus would involve either changing the linking strategies to labelling of amines, or the use of unnatural amino acids and click-chemistry [154]. Furthermore, the submicrosecond blinking of the dyes used in this study still aggravate the analysis, and ways to improve these characteristics are of particular interest. It can be assumed that the main source of submicrosecond blinking is either ROXS-induced radical blinking or triplet blinking, with the additional possibility of blinking caused by photoisomerization reactions in cyanines. Therefore, these experiments would greatly benefit from new fluorescent labels, which show less blinking at these timescales [155, 156] and from new photostabilization strategies that circumvent long lived intermediates (e.g., efficient triplet energy transfer or geminate recombination [62, 157]). Ideally, these improvements would then enable the direct visualization of even the faster transitions without the need for a maximum likelihood analysis.

As the previously determined lifetimes for the encounter complex of the two proteins [36] were also obtained in these experiments, there is good reason to believe that the general biological reaction is not significantly influenced by the crowded nanoantenna environment. In the case that even larger biomolecules should be placed in the hotspot region, newer designs have already been developed that retain the attainable fluorescence enhancement while offering even more room for the molecules of interest [158]. As mentioned in chapter 4.4, it would be interesting to study the transition path times of DNA hybridization reactions in more detail (Figure 6.1a). The effect of a single nucleotide mismatch has been glimpsed at, but more data is needed to corroborate these findings. Beyond that, other influences could be studied. How does the transition path time change with G/C-content? How does it change in the case of an ssRNA as one of the binding partners? Does the transition get influenced by overlapping strands that block parts of the available hybridization site?

As a next possible step, the investigation of protein folding processes could be of interest. By immobilizing a protein in the plasmonic hotspot and increasing denaturant (such as guanidinium chloride or urea) concentration, a state of reversible folding and unfolding can be

reached. It then should become possible to observe several folding and unfolding transitions on a single protein (Figure 6.1b), which would significantly increase the number of transitions that can be extracted and analysed – currently, several thousand single molecules have to be analysed in order to be able to observe enough transitions for statistical significance [128]. The information obtained from the observation of these folding transition paths could lead to new insights on folding and misfolding of proteins [31] and close the gap towards molecular dynamics simulations, where they would serve as valuable observables for the assessment of the quality of the simulations [159, 160].

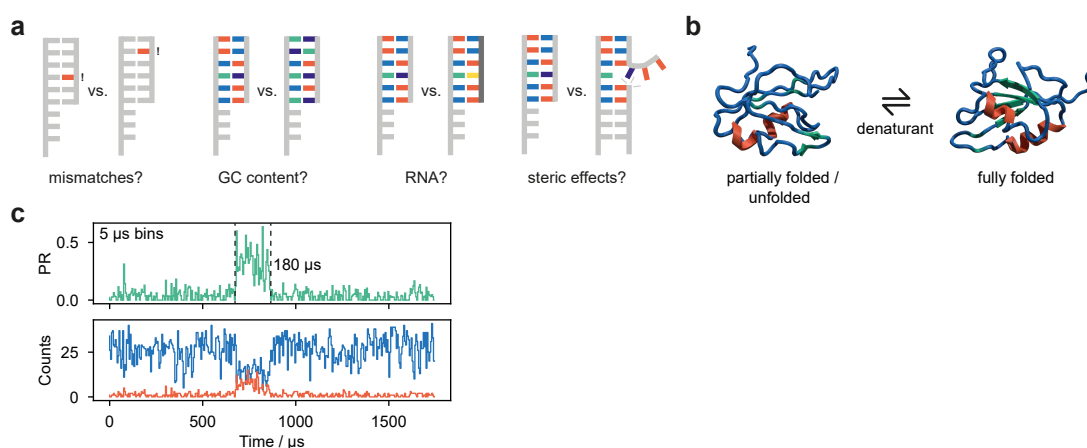


Figure 6.1: (a) More detailed studies on nucleic acid hybridization reactions can be envisioned. For example, the impact of mismatches or blocking strands could be investigated. (b) At high count rates, the transition path times of protein folding processes could become accessible, and reveal potential trap states or intermediates [161]. (c) Visualization of short lived bound states: here, the binding of a 6 nt ssDNA including an AT mismatch to a docking site is shown (estimated [162] $K_d \approx 200 \mu\text{M}$, blue: donor (AlexaFluor 647) fluorescence, red: acceptor (ATTO740) fluorescence, green: proximity ratio).

Apart from the measurement of transition path times, there are many other biomolecular processes where the higher photon count rates provided by the DNA origami nanoantenna could be beneficial for the experiment. A longstanding goal is the real-time observation of the synthesis of a new DNA strand by a DNA polymerase, where the zeptoliter sized plasmonic hotspot could reduce the observation volume and make it possible to work at labelled nucleotide concentrations in the micromolar range, in a similar way as it is done with zero-mode waveguides in commercial systems [163]. Going beyond that, the possibility to work at these concentrations makes accessible the world of low-affinity biointeractions: interactions that are essential for the functioning of cells but are very difficult to detect and study on the single molecule level [164]. For example, the dissociation constants between cell-surface molecules of leukocytes, which are important parameters in the investigation of

tumor mechanisms and for judging the efficacy of anti-cancer drugs, can be as high as several hundred micromolar [165], translating to submillisecond lifetimes of the bound states [166], which is impossible to measure with conventional smFRET based methods. However, with the decreased excitation volume and the fluorescence enhancement provided by the DNA origami nanoantenna, these short lived states can be identified (Figure 6.1c).

6.2 Modular and tunable single molecule biosensors

The modular biosensor platform presented in this work (chapter 5.1) can potentially solve many of the issues that slow down the speed at which new biosensors are developed. By spatially decoupling the signal recognition from the signal transduction, the large FRET signal contrast is retained even when the recognition element is changed to adapt to a completely new target and recognition mechanism. More importantly, it was shown that the parameters that describe the dose-response of the biosensor, namely $K_{1/2}$ and n_H , can be tuned without interfering with the recognition interaction itself, e.g. by introducing changes to the DNA origami backbone or by arranging multiple recognition sites on the same backbone. The latter added the additional possibility of introducing cooperative behavior, which has been challenging to implement in biosensors thus far [39] and significantly enhanced the selectivity of the sensor when facing structurally/energetically different off-targets when compared to the single binding interaction. While cooperativity in *de novo* designed protein has recently been demonstrated [167], whether or not these proteins can be converted to useful biosensors will ultimately depend on the conformational change upon the last binding event that can be achieved in these systems.

The combination of the arranging capabilities of the DNA origami approach and the tuning options offered by this method with other biological interactions such as e.g. glucose binding by the glucose binding protein or even *de novo* designed binder proteins [38, 168, 169] is a promising route to versatile biosensors. By harnessing the multiplexing options not only offered by the possibility to arrange multiple sensing units on one DNA nanosensor, but also by the possibility to selectively immobilize DNA origami nanostructures to specific locations [170] on e.g. a DNA chip, a universal point-of-care sensor can be envisioned. In this sensor (Figure 6.2a), a plethora of different analytes can be tested for in the same ultralow sample volume. At the same time, the high signal contrast and the possibility to tune the sharpness of the response could allow for high-confidence and easily understandable test results. Furthermore, several other readout mechanisms such as an electrochemical readout [171] or a readout

based on graphene-based fluorescence quenching [172, 173] could be readily implemented in the system. Another target of particular interest in this context would be proteases – proteins which cleave polypeptides at sequence specific cleavage sites. Closing the hinge with a polypeptide, in the same way as it has already been achieved with DNA strands, presents a straightforward way to construct protease sensors. The multiplexing capabilities would allow testing for several different protease activities in the same sample, which is necessary in many diagnostic settings: proteases are involved in cancer, Alzheimer's disease, diabetes and other disorders [174, 175].

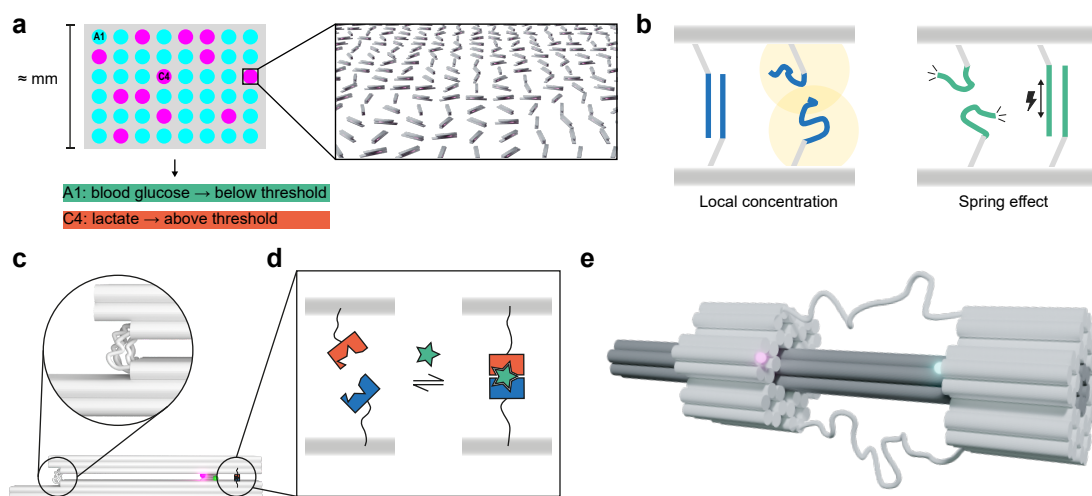


Figure 6.2: (a) The modularity of the DNA origami approach in combination with the ability to immobilize these origamis at specific positions on a DNA chip could enable point-of-care biosensors with unprecedented multiplexing capabilities. (b) In the current DNA origami design, there are two competing cooperative reactions which could decrease the maximally attainable cooperativity. (c) To introduce further tuning mechanisms, the length of the ssDNAs connecting the two hinge arms (inset) could be adjusted. (d) An alternative sensing mechanism based on chemically induced dimerization could be employed, in order to fully tap the potential of cooperativity. (e) Another DNA origami design that could be tested for cooperativity is the DNA slider mechanism [47].

A drawback of the current design of the scaffolding dynamic DNA origami is that there are two competing mechanisms for cooperativity: on the one hand, the opening of the structure is cooperative because opening of the first closing interaction by a target should increase the force applied to the remaining closing interactions and thus increase the likelihood of opening [176]. At the same time, the reclosing is also cooperative, because once one closing interaction is formed again, the local concentration of the other closing interactions is drastically increased which facilitates the remaining toehold displacement reactions for full reclosing (Figure 6.2b). Furthermore, currently the only mechanism for tuning towards

lower $K_{1/2}$ and higher n_H requires changing the ionic strength of the buffer, which is not easily achievable in real diagnostic settings. Thus, additional mechanisms for exerting a strain onto the binding interactions would be beneficial. Ideally, a redesign of the DNA origami nanostructure would therefore factor in the points: changes to the hinge nanostructure could involve the inclusion of selectable additional ssDNA spacer elements between the two arms of the hinge, which should affect the influence of the coulombic repulsion between the two arms on the binding interactions [47] (Figure 6.2c). Furthermore, the relationship between the positioning of the binding interactions on the hinge axis and the influence of the spacer elements that determine the maximal closed angle of the nanostructure have not been investigated in detail and could offer additional means of tuning. Lastly, the hinge nanostructure could be modified so that the two mechanisms for cooperativity work in the same direction. For this, an assay based on the closing of the hinge nanostructure by chemically induced dimerization [38, 177] could be envisioned (Figure 6.2d). Additionally, computational studies of cooperative mechanisms [178] identified two other fundamental structural classes of such mechanisms next to the hinge-like structure: a sliding box, and a twist design. A DNA origami structure that resembles one of these structural classes (such as the DNA origami slider [47], Figure 6.2e) could be another promising scaffolding element for cooperative multivalent biosensors.

In conclusion, the tools developed in this thesis open up new possibilities for the investigation of biomolecular interactions and provide means to extract more information from single-molecule FRET experiments, potentially leading to new insights in processes as diverse as protein folding, cell-cell recognition or mechanisms of disease.

7 Bibliography

1. Koch, R. *Untersuchungen über die Aetiologie der Wundinfectionskrankheiten* de. <http://archiv.ub.uni-marburg.de/eb/2013/0081> (Philipps-Universität Marburg, 1878).
2. Koch, R. *Die Ätiologie der Tuberkulose* de. <https://edoc.rki.de/handle/176904/5166> (Robert Koch-Institut, 2010).
3. Robert-Koch-Institute. *1901 bis 1910: Erregern auf der Spur – die Rolle der Mikroskopie bei der Erkennung und Erforschung von Krankheitserregern* https://www.rki.de/DE/Content/Institut/Geschichte/Bildband_Salon/1901-1910.html (2023).
4. Chalfie, M., Tu, Y., Euskirchen, G., Ward, W. W. & Prasher, D. C. Green Fluorescent Protein as a Marker for Gene Expression. *Science* **263**, 802–805. <https://doi.org/10.1126/science.8303295> (Feb. 1994).
5. Hoffman, R. M. The multiple uses of fluorescent proteins to visualize cancer in vivo. *Nature Reviews Cancer* **5**, 796–806. <https://doi.org/10.1038/nrc1717> (Oct. 2005).
6. Wilkinson, S. & Marcus, A. *Lung Cancer Metastasis* <https://visualsonline.cancer.gov/details.cfm?imageid=10578>.
7. Kufer, S. K., Puchner, E. M., Gump, H., Liedl, T. & Gaub, H. E. Single-Molecule Cut-and-Paste Surface Assembly. *Science* **319**, 594–596. <https://doi.org/10.1126/science.1151424> (Feb. 2008).
8. Smalley, R. E. Of Chemistry, Love and Nanobots. *Scientific American* **285**, 76–77. <https://doi.org/10.1038/scientificamerican0901-76> (Sept. 2001).
9. Chang, K. Yes, They Can! No, They Can't: Charges Fly in Nanobot Debate. *The New York Times*. <https://www.nytimes.com/2003/12/09/science/yes-they-can-no-they-can-t-charges-fly-in-nanobot-debate.html> (2024) (Dec. 9, 2003).
10. Seeman, N. C. Nucleic acid junctions and lattices. *Journal of Theoretical Biology* **99**, 237–247. [https://doi.org/10.1016/0022-5193\(82\)90002-9](https://doi.org/10.1016/0022-5193(82)90002-9) (Nov. 1982).
11. Rothemund, P. W. K. Folding DNA to create nanoscale shapes and patterns. *Nature* **440**, 297–302. <https://doi.org/10.1038/nature04586> (Mar. 2006).
12. Bell, N. A. W. *et al.* DNA Origami Nanopores. *Nano Letters* **12**, 512–517. <https://doi.org/10.1021/nl204098n> (Dec. 2011).
13. Douglas, S. M., Bachelet, I. & Church, G. M. A Logic-Gated Nanorobot for Targeted Transport of Molecular Payloads. *Science* **335**, 831–834. <https://doi.org/10.1126/science.1214081> (Feb. 2012).

14. Steinhauer, C., Jungmann, R., Sobey, T. L., Simmel, F. C. & Tinnefeld, P. DNA Origami as a Nanoscopic Ruler for Super-Resolution Microscopy. *Angewandte Chemie International Edition* **48**, 8870–8873. <https://doi.org/10.1002/anie.200903308> (Nov. 2009).
15. Gopinath, A., Miyazono, E., Faraon, A. & Rothmund, P. W. K. Engineering and mapping nanocavity emission via precision placement of DNA origami. *Nature* **535**, 401–405. <https://doi.org/10.1038/nature18287> (July 2016).
16. Platnich, C. M., Rizzuto, F. J., Cosa, G. & Sleiman, H. F. Single-molecule methods in structural DNA nanotechnology. *Chemical Society Reviews* **49**, 4220–4233. <https://doi.org/10.1039/c9cs00776h> (2020).
17. Lerner, E. *et al.* Toward dynamic structural biology: Two decades of single-molecule Förster resonance energy transfer. *Science* **359**. <https://doi.org/10.1126/science.aan1133> (Jan. 2018).
18. US National Aeronautics and Space Administration. *Voyager 1 mission homepage* <https://voyager.jpl.nasa.gov/> (2023).
19. Novotny, L. & van Hulst, N. Antennas for light. *Nature Photonics* **5**, 83–90. <https://doi.org/10.1038/nphoton.2010.237> (Feb. 2011).
20. Acuna, G. P. *et al.* Fluorescence Enhancement at Docking Sites of DNA-Directed Self-Assembled Nanoantennas. *Science* **338**, 506–510. <https://doi.org/10.1126/science.1228638> (Oct. 2012).
21. Trofymchuk, K. *et al.* Addressable nanoantennas with cleared hotspots for single-molecule detection on a portable smartphone microscope. *Nature Communications* **12**. <https://doi.org/10.1038/s41467-021-21238-9> (Feb. 2021).
22. Glembockyte, V., Grabenhorst, L., Trofymchuk, K. & Tinnefeld, P. DNA Origami Nanoantennas for Fluorescence Enhancement. *Accounts of Chemical Research* **54**, 3338–3348. <https://doi.org/10.1021/acs.accounts.1c00307> (Aug. 1, 2021).
23. Puchkova, A. *et al.* DNA Origami Nanoantennas with over 5000-fold Fluorescence Enhancement and Single-Molecule Detection at 25 μ M. *Nano Letters* **15**, 8354–8359. <https://doi.org/10.1021/acs.nanolett.5b04045> (Nov. 2015).
24. Vietz, C., Kaminska, I., Paz, M. S., Tinnefeld, P. & Acuna, G. P. Broadband Fluorescence Enhancement with Self-Assembled Silver Nanoparticle Optical Antennas. *ACS Nano* **11**, 4969–4975. <https://doi.org/10.1021/acsnano.7b01621> (Apr. 2017).
25. Holzmeister, P. *et al.* Quantum yield and excitation rate of single molecules close to metallic nanostructures. *Nature Communications* **5**. <https://doi.org/10.1038/ncomms6356> (Nov. 2014).
26. Trofymchuk, K. *et al.* Gold Nanorod DNA Origami Antennas for 3 Orders of Magnitude Fluorescence Enhancement in NIR. *ACS Nano* **17**, 1327–1334. <https://doi.org/10.1021/acsnano.2c09577> (Jan. 2023).

27. Ochmann, S. E. *et al.* Optical Nanoantenna for Single Molecule-Based Detection of Zika Virus Nucleic Acids without Molecular Multiplication. *Analytical Chemistry* **89**, 13000–13007. <https://doi.org/10.1021/acs.analchem.7b04082> (Nov. 2017).
28. Holzmeister, P., Acuna, G. P., Grohmann, D. & Tinnefeld, P. Breaking the concentration limit of optical single-molecule detection. *Chem. Soc. Rev.* **43**, 1014–1028. <https://doi.org/10.1039/c3cs60207a> (2014).
29. Nettels, D., Gopich, I. V., Hoffmann, A. & Schuler, B. Ultrafast dynamics of protein collapse from single-molecule photon statistics. *Proceedings of the National Academy of Sciences* **104**, 2655–2660. <https://doi.org/10.1073/pnas.0611093104> (Feb. 2007).
30. Schuler, B. & Eaton, W. A. Protein folding studied by single-molecule FRET. *Current Opinion in Structural Biology* **18**, 16–26. <https://doi.org/10.1016/j.sbi.2007.12.003> (Feb. 2008).
31. Chung, H. S. & Eaton, W. A. Protein folding transition path times from single molecule FRET. *Current Opinion in Structural Biology* **48**, 30–39. ISSN: 0959-440X. <http://dx.doi.org/10.1016/j.sbi.2017.10.007> (Feb. 2018).
32. Pellegrotti, J. V. *et al.* Controlled Reduction of Photobleaching in DNA Origami–Gold Nanoparticle Hybrids. *Nano Letters* **14**, 2831–2836. <https://doi.org/10.1021/nl500841n> (Apr. 2014).
33. Wientjes, E., Renger, J., Cogdell, R. & van Hulst, N. F. Pushing the Photon Limit: Nanoantennas Increase Maximal Photon Stream and Total Photon Number. *The Journal of Physical Chemistry Letters* **7**, 1604–1609. <https://doi.org/10.1021/acs.jpcllett.6b00491> (Apr. 2016).
34. Wang, Y., Horáček, M. & Zijlstra, P. Strong Plasmon Enhancement of the Saturation Photon Count Rate of Single Molecules. *The Journal of Physical Chemistry Letters* **11**, 1962–1969. <https://doi.org/10.1021/acs.jpcllett.0c00155> (Feb. 2020).
35. Widengren, J. & Schwille, P. Characterization of Photoinduced Isomerization and Back-Isomerization of the Cyanine Dye Cy5 by Fluorescence Correlation Spectroscopy. *The Journal of Physical Chemistry A* **104**, 6416–6428. <https://doi.org/10.1021/jp000059s> (June 2000).
36. Sturzenegger, F. *et al.* Transition path times of coupled folding and binding reveal the formation of an encounter complex. *Nature Communications* **9**. <https://doi.org/10.1038/s41467-018-07043-x> (Nov. 2018).
37. Brun, M. A., Tan, K.-T., Nakata, E., Hinner, M. J. & Johnsson, K. Semisynthetic Fluorescent Sensor Proteins Based on Self-Labeling Protein Tags. *Journal of the American Chemical Society* **131**, 5873–5884. <https://doi.org/10.1021/ja900149e> (Apr. 2009).
38. Glasgow, A. A. *et al.* Computational design of a modular protein sense-response system. *Science* **366**, 1024–1028. <https://doi.org/10.1126/science.aax8780> (Nov. 2019).

39. Ortega, G., Chamorro-Garcia, A., Ricci, F. & Plaxco, K. W. On the Rational Design of Cooperative Receptors. *Annual Review of Biophysics* **52**, 319–337. <https://doi.org/10.1146/annurev-biophys-091222-082247> (May 2023).
40. Tinberg, C. E. *et al.* Computational design of ligand-binding proteins with high affinity and selectivity. *Nature* **501**, 212–216. <https://doi.org/10.1038/nature12443> (Sept. 2013).
41. Eaton, W. A. A retrospective on statistical mechanical models for hemoglobin allostery. *The Journal of Chemical Physics* **157**. <https://doi.org/10.1063/5.0127585> (Nov. 2022).
42. Perutz, M. F. Stereochemistry of Cooperative Effects in Haemoglobin: Haem–Haem Interaction and the Problem of Allostery. *Nature* **228**, 726–734. <https://doi.org/10.1038/228726a0> (Nov. 1970).
43. Habler, O. P. & Messmer, K. F. The physiology of oxygen transport. *Transfusion Science* **18**, 425–435. [https://doi.org/10.1016/s0955-3886\(97\)00041-6](https://doi.org/10.1016/s0955-3886(97)00041-6) (Sept. 1997).
44. Perutz, M. F. Hemoglobin Structure and Respiratory Transport. *Scientific American* **239**, 92–125. ISSN: 00368733, 19467087. <http://www.jstor.org/stable/24955868> (2023) (1978).
45. Reach, G. & Wilson, G. S. Can continuous glucose monitoring be used for the treatment of diabetes? *Analytical Chemistry* **64**, 381A–386A. <https://doi.org/10.1021/ac00030a001> (Mar. 1992).
46. Chamorro-Garcia, A. *et al.* The sequestration mechanism as a generalizable approach to improve the sensitivity of biosensors and bioassays. *Chemical Science* **13**, 12219–12228. <https://doi.org/10.1039/d2sc03901j> (2022).
47. Marras, A. E., Zhou, L., Su, H.-J. & Castro, C. E. Programmable motion of DNA origami mechanisms. *Proceedings of the National Academy of Sciences* **112**, 713–718. <https://doi.org/10.1073/pnas.1408869112> (Jan. 2015).
48. Binnig, G. & Rohrer, H. Scanning tunneling microscopy—from birth to adolescence. *Reviews of Modern Physics* **59**, 615–625. <https://link.aps.org/doi/10.1103/RevModPhys.59.615> (3 July 1987).
49. Binnig, G., Quate, C. F. & Gerber, C. Atomic Force Microscope. *Physical Review Letters* **56**, 930–933. <https://link.aps.org/doi/10.1103/PhysRevLett.56.930> (9 Mar. 1986).
50. Moerner, W. E. & Kador, L. Optical detection and spectroscopy of single molecules in a solid. *Physical Review Letters* **62**, 2535–2538. <https://doi.org/10.1103/physrevlett.62.2535> (May 1989).
51. Funatsu, T., Harada, Y., Tokunaga, M., Saito, K. & Yanagida, T. Imaging of single fluorescent molecules and individual ATP turnovers by single myosin molecules in aqueous solution. *Nature* **374**, 555–559. <https://doi.org/10.1038/374555a0> (Apr. 1995).

52. Noorden, R. V. Nobel for microscopy that reveals inner world of cells. *Nature* **514**, 286–286. <https://doi.org/10.1038/nature.2014.16097> (Oct. 2014).
53. Taylor, R. W. & Sandoghdar, V. Interferometric Scattering Microscopy: Seeing Single Nanoparticles and Molecules via Rayleigh Scattering. *Nano Letters* **19**, 4827–4835. <https://doi.org/10.1021/acs.nanolett.9b01822> (July 2019).
54. Atkins, P., de Paula, J. & Keeler, J. *Atkins' physical chemistry* 12th ed. ISBN: 978-0-19-884781-6 (Oxford University press, Oxford, UK, 2022).
55. Jablonski, A. Efficiency of Anti-Stokes Fluorescence in Dyes. *Nature* **131**, 839–840. ISSN: 1476-4687. <http://dx.doi.org/10.1038/131839b0> (June 1933).
56. Lakowicz, J. R. *Principles of Fluorescence Spectroscopy* 3rd ed. <https://doi.org/10.1007/978-0-387-46312-4> (Springer, New York, USA, 2006).
57. Kolmakov, K. *et al.* Red-Emitting Rhodamine Dyes for Fluorescence Microscopy and Nanoscopy. *Chemistry – A European Journal* **16**, 158–166. ISSN: 1521-3765. <http://dx.doi.org/10.1002/chem.200902309> (Dec. 2009).
58. Ha, T. & Tinnefeld, P. Photophysics of Fluorescent Probes for Single-Molecule Biophysics and Super-Resolution Imaging. *Annual Review of Physical Chemistry* **63**, 595–617. <https://doi.org/10.1146/annurev-physchem-032210-103340> (May 2012).
59. Grimm, J. B. & Lavis, L. D. Caveat fluorophore: an insiders' guide to small-molecule fluorescent labels. *Nature Methods* **19**, 149–158. <https://doi.org/10.1038/s41592-021-01338-6> (Dec. 2021).
60. Vogelsang, J. *et al.* A Reducing and Oxidizing System Minimizes Photobleaching and Blinking of Fluorescent Dyes. *Angewandte Chemie International Edition* **47**, 5465–5469. <https://doi.org/10.1002/anie.200801518> (July 2008).
61. Widengren, J., Chmyrov, A., Eggeling, C., Löfdahl, P.-Å. & Seidel, C. A. M. Strategies to Improve Photostabilities in Ultrasensitive Fluorescence Spectroscopy. *The Journal of Physical Chemistry A* **111**, 429–440. <https://doi.org/10.1021/jp0646325> (Dec. 2006).
62. Glembockyte, V., Lincoln, R. & Cosa, G. Cy3 Photoprotection Mediated by Ni²⁺ for Extended Single-Molecule Imaging: Old Tricks for New Techniques. *Journal of the American Chemical Society* **137**, 1116–1122. <https://doi.org/10.1021/ja509923e> (Jan. 2015).
63. Vogelsang, J. *Advancing single-molecule fluorescence spectroscopy and super-resolution microscopy with organic fluorophores* PhD thesis (Ludwig-Maximilians-Universität München, 2009). <https://edoc.ub.uni-muenchen.de/id/eprint/11480>.
64. Vogelsang, J., Cordes, T., Forthmann, C., Steinhauer, C. & Tinnefeld, P. Controlling the fluorescence of ordinary oxazine dyes for single-molecule switching and superresolution microscopy. *Proceedings of the National Academy of Sciences* **106**, 8107–8112. <https://doi.org/10.1073/pnas.0811875106> (May 2009).

65. Iqbal, A. *et al.* Orientation dependence in fluorescent energy transfer between Cy3 and Cy5 terminally attached to double-stranded nucleic acids. *Proceedings of the National Academy of Sciences* **105**, 11176–11181. <https://doi.org/10.1073/pnas.0801707105> (Aug. 2008).
66. Mazal, H. & Haran, G. Single-molecule FRET methods to study the dynamics of proteins at work. *Current Opinion in Biomedical Engineering* **12**, 8–17. <https://doi.org/10.1016/j.cobme.2019.08.007> (Dec. 2019).
67. Anger, P., Bharadwaj, P. & Novotny, L. Enhancement and Quenching of Single-Molecule Fluorescence. *Physical Review Letters* **96**. <https://doi.org/10.1103/physrevlett.96.113002> (Mar. 2006).
68. Drude, P. Zur Elektronentheorie der Metalle. *Annalen der Physik* **306**, 566–613. <https://doi.org/10.1002/andp.19003060312> (1900).
69. Sommerfeld, A. & Bethe, H. *Elektronentheorie der Metalle* <https://doi.org/10.1007/978-3-642-95002-5> (Springer-Verlag Berlin, Heidelberg, 1967).
70. Maier, S. A. *Plasmonics: Fundamentals and Applications* <https://doi.org/10.1007/0-387-37825-1> (Springer, New York, USA, 2007).
71. Sönnichsen, C., Franzl, T., Wilk, T., von Plessen, G. & Feldmann, J. Plasmon resonances in large noble-metal clusters. *New Journal of Physics* **4**, 93–93. <https://doi.org/10.1088/1367-2630/4/1/393> (Nov. 2002).
72. Kinkhabwala, A. *et al.* Large single-molecule fluorescence enhancements produced by a bowtie nanoantenna. *Nature Photonics* **3**, 654–657. <https://doi.org/10.1038/nphoton.2009.187> (Oct. 2009).
73. Ruppin, R. Decay of an excited molecule near a small metal sphere. *The Journal of Chemical Physics* **76**, 1681–1684. <https://doi.org/10.1063/1.443196> (Feb. 1982).
74. Thomas, M., Greffet, J.-J., Carminati, R. & Arias-Gonzalez, J. R. Single-molecule spontaneous emission close to absorbing nanostructures. *Applied Physics Letters* **85**, 3863–3865. <https://doi.org/10.1063/1.1812592> (Oct. 2004).
75. Purcell, E. M. Spontaneous emission probabilities at radio frequencies. *Physical Review* **69**, 674–674. <https://doi.org/10.1103/physrev.69.674> (June 1946).
76. Xu, H., Bjerneld, E. J., Käll, M. & Börjesson, L. Spectroscopy of Single Hemoglobin Molecules by Surface Enhanced Raman Scattering. *Physical Review Letters* **83**, 4357–4360. <https://doi.org/10.1103/physrevlett.83.4357> (Nov. 1999).
77. Mühlischlegel, P., Eisler, H.-J., Martin, O. J. F., Hecht, B. & Pohl, D. W. Resonant Optical Antennas. *Science* **308**, 1607–1609. ISSN: 1095-9203. <http://dx.doi.org/10.1126/science.1111886> (June 2005).
78. Kuzyk, A., Jungmann, R., Acuna, G. P. & Liu, N. DNA Origami Route for Nanophotonics. *ACS Photonics* **5**, 1151–1163. ISSN: 2330-4022. <http://dx.doi.org/10.1021/acsp Photonics.7b01580> (Feb. 2018).

79. Watson, J. D. & Crick, F. H. C. Molecular Structure of Nucleic Acids: A Structure for Deoxyribose Nucleic Acid. *Nature* **171**, 737–738. <https://doi.org/10.1038/171737a0> (Apr. 1953).
80. Franklin, R. E. & Gosling, R. G. Molecular Configuration in Sodium Thymonucleate. *Nature* **171**, 740–741. <https://doi.org/10.1038/171740a0> (Apr. 1953).
81. Collins, F. *et al.* The NIH-led research response to COVID-19. *Science* **379**, 441–444. <https://doi.org/10.1126/science.adf5167> (Feb. 2023).
82. Drew, H. R. *et al.* Structure of a B-DNA dodecamer: conformation and dynamics. *Proceedings of the National Academy of Sciences* **78**, 2179–2183. <https://doi.org/10.1073/pnas.78.4.2179> (Apr. 1981).
83. Abdel-Monem, M., Durwald, H. & Hofmann-Berling, H. Enzymic Unwinding of DNA. 2. Chain Separation by an ATP-Dependent DNA Unwinding Enzyme. *European Journal of Biochemistry* **65**, 441–449. <https://doi.org/10.1111/j.1432-1033.1976.tb10359.x> (June 1976).
84. Bauer, W. R., Crick, F. H. C. & White, J. H. Supercoiled DNA. *Scientific American* **243**, 118–133. ISSN: 00368733, 19467087. <http://www.jstor.org/stable/24966373> (2023) (1980).
85. Lima, C. D., Wang, J. C. & Mondragón, A. Three-dimensional structure of the 67K N-terminal fragment of E. coli DNA topoisomerase I. *Nature* **367**, 138–146. <https://doi.org/10.1038/367138a0> (Jan. 1994).
86. Holliday, R. A mechanism for gene conversion in fungi. *Genetical Research* **5**, 282–304. <https://doi.org/10.1017/s0016672300001233> (July 1964).
87. Coll, M. *et al.* *Nature Structural Biology* **6**, 913–917. <https://doi.org/10.1038/13277> (Oct. 1999).
88. Chen, J. & Seeman, N. C. Synthesis from DNA of a molecule with the connectivity of a cube. *Nature* **350**, 631–633. <https://doi.org/10.1038/350631a0> (Apr. 1991).
89. Hargittai, I. & Hargittai, B. Nadrian C. Seeman (1945–2021): pioneer of DNA nanotechnology. *Structural Chemistry* **33**, 631–633. ISSN: 1572-9001. <http://dx.doi.org/10.1007/s11224-022-01894-3> (Mar. 2022).
90. Kallenbach, N. R., Ma, R.-I. & Seeman, N. C. An immobile nucleic acid junction constructed from oligonucleotides. *Nature* **305**, 829–831. <https://doi.org/10.1038/305829a0> (Oct. 1983).
91. Ke, Y. *et al.* Multilayer DNA Origami Packed on a Square Lattice. *Journal of the American Chemical Society* **131**, 15903–15908. <https://doi.org/10.1021/ja906381y> (Oct. 2009).
92. Dietz, H., Douglas, S. M. & Shih, W. M. Folding DNA into Twisted and Curved Nanoscale Shapes. *Science* **325**, 725–730 (Aug. 2009).
93. Douglas, S. M. *et al.* Self-assembly of DNA into nanoscale three-dimensional shapes. *Nature* **459**, 414–418. <https://doi.org/10.1038/nature08016> (May 2009).

94. Stein, I. H., Steinhauer, C. & Tinnefeld, P. Single-Molecule Four-Color FRET Visualizes Energy-Transfer Paths on DNA Origami. *Journal of the American Chemical Society* **133**, 4193–4195. <https://doi.org/10.1021/ja1105464> (Jan. 2011).
95. Acuna, G. P. *et al.* Distance Dependence of Single-Fluorophore Quenching by Gold Nanoparticles Studied on DNA Origami. *ACS Nano* **6**, 3189–3195. <https://doi.org/10.1021/nm2050483> (Mar. 2012).
96. Schmied, J. J. *et al.* Fluorescence and super-resolution standards based on DNA origami. *Nature Methods* **9**, 1133–1134. <https://doi.org/10.1038/nmeth.2254> (Dec. 2012).
97. Derr, N. D. *et al.* Tug-of-War in Motor Protein Ensembles Revealed with a Programmable DNA Origami Scaffold. *Science* **338**, 662–665. <https://doi.org/10.1126/science.1226734> (Nov. 2012).
98. Langecker, M. *et al.* Synthetic Lipid Membrane Channels Formed by Designed DNA Nanostructures. *Science* **338**, 932–936. <https://doi.org/10.1126/science.1225624> (Nov. 2012).
99. Yurke, B., Turberfield, A. J., Mills, A. P., Simmel, F. C. & Neumann, J. L. A DNA-fuelled molecular machine made of DNA. *Nature* **406**, 605–608. <https://doi.org/10.1038/35020524> (Aug. 2000).
100. Simmel, F. C., Yurke, B. & Singh, H. R. Principles and Applications of Nucleic Acid Strand Displacement Reactions. *Chemical Reviews* **119**, 6326–6369. <https://doi.org/10.1021/acs.chemrev.8b00580> (Feb. 2019).
101. Roth, E., Azaria, A. G., Girshevitz, O., Bitler, A. & Garini, Y. Measuring the Conformation and Persistence Length of Single-Stranded DNA Using a DNA Origami Structure. *Nano Letters* **18**, 6703–6709. <https://doi.org/10.1021/acs.nanolett.8b02093> (Oct. 2018).
102. Andersen, E. S. *et al.* Self-assembly of a nanoscale DNA box with a controllable lid. *Nature* **459**, 73–76. <https://doi.org/10.1038/nature07971> (May 2009).
103. Pumm, A.-K. *et al.* A DNA origami rotary ratchet motor. *Nature* **607**, 492–498. <https://doi.org/10.1038/s41586-022-04910-y> (July 2022).
104. Shi, X. *et al.* A DNA turbine powered by a transmembrane potential across a nanopore. *Nature Nanotechnology*. <https://doi.org/10.1038/s41565-023-01527-8> (Oct. 2023).
105. Nelson, D. L. & Cox, M. M. *Lehninger principles of biochemistry* 8th ed. en (W. H. Freeman, Jan. 2021).
106. Grabenhorst, E. “Genetic Engineering” von Glycoproteinen: Transfer von Glycosylierungsdomänen humaner Proteine, Charakterisierung der Produkte nach Expression in eukaryontischen Wirtszellen PhD thesis (Technische Universität Braunschweig, 1994). <https://katalog.ub.tu-braunschweig.de/vufind/Record/167953648>.
107. Janda, C. Y. *et al.* Recognition of a signal peptide by the signal recognition particle. *Nature* **465**, 507–510. <https://doi.org/10.1038/nature08870> (Apr. 2010).

108. Zhang, F. *et al.* Molecular mechanism for the umami taste synergism. *Proceedings of the National Academy of Sciences* **105**, 20930–20934. <https://doi.org/10.1073/pnas.0810174106> (Dec. 2008).
109. Du, X. *et al.* Insights into Protein–Ligand Interactions: Mechanisms, Models, and Methods. *International Journal of Molecular Sciences* **17**, 144. <https://doi.org/10.3390/ijms17020144> (Jan. 2016).
110. Jarmoskaite, I., AlSadhan, I., Vaidyanathan, P. P. & Herschlag, D. How to measure and evaluate binding affinities. *eLife* **9** (eds Deindl, S. & Kuriyan, J.) e57264. ISSN: 2050-084X. <https://doi.org/10.7554/eLife.57264> (Aug. 2020).
111. Green, N. M. Avidin. 1. The Use of ¹⁴C-Biotin for kinetic studies and for assay. *Biochemical Journal* **89**, 585–591. <https://doi.org/10.1042/bj0890585> (Dec. 1963).
112. Alberts, B. *et al.* *Molecular Biology of the Cell* 6th ed. en (Garland Science, Taylor & Francis Group, LLC, 2015).
113. Liu, W. *et al.* Structural Basis for Allosteric Regulation of GPCRs by Sodium Ions. *Science* **337**, 232–236. <https://doi.org/10.1126/science.1219218> (July 2012).
114. Reynolds, K. A., McLaughlin, R. N. & Ranganathan, R. Hot Spots for Allosteric Regulation on Protein Surfaces. *Cell* **147**, 1564–1575. <https://doi.org/10.1016/j.cell.2011.10.049> (Dec. 2011).
115. Tzeng, S.-R. & Kalodimos, C. G. Dynamic activation of an allosteric regulatory protein. *Nature* **462**, 368–372. <https://doi.org/10.1038/nature08560> (Nov. 2009).
116. Cui, Q. & Karplus, M. Allostery and cooperativity revisited. *Protein Science* **17**, 1295–1307. <https://doi.org/10.1110/ps.03259908> (Aug. 2008).
117. Hill, A. V. The possible effects of the aggregation of the molecules of hæmoglobin on its dissociation curves. *The Journal of Physiology* **40**, i–vii. <http://jp.physoc.org/content/40/supplement/i.short> (Jan. 1910).
118. Bisswanger, H. *Enzyme Kinetics* 3rd ed. <https://doi.org/10.1002/9783527806461> (Wiley-VCH Verlag, Weinheim, June 2017).
119. Adair, G., Bock, A. & Field, H. The Hemoglobin System. *Journal of Biological Chemistry* **63**, 529–545. [https://doi.org/10.1016/s0021-9258\(18\)85018-9](https://doi.org/10.1016/s0021-9258(18)85018-9) (Mar. 1925).
120. Sen Mojumdar, S. *et al.* Partially native intermediates mediate misfolding of SOD1 in single-molecule folding trajectories. *Nature Communications* **8**. ISSN: 2041-1723. <http://dx.doi.org/10.1038/s41467-017-01996-1> (Dec. 2017).
121. Dutta, R. & Pollak, E. What can we learn from transition path time distributions for protein folding and unfolding? *Physical Chemistry Chemical Physics* **23**, 23787–23795. ISSN: 1463-9084. <http://dx.doi.org/10.1039/d1cp03296h> (2021).
122. Mehlich, A., Fang, J., Pelz, B., Li, H. & Stigler, J. Slow Transition Path Times Reveal a Complex Folding Barrier in a Designed Protein. *Frontiers in Chemistry* **8**. ISSN: 2296-2646. <http://dx.doi.org/10.3389/fchem.2020.587824> (Dec. 2020).

123. Henriksen, N. E. & Hansen, F. Y. *Theories of Molecular Reaction Dynamics* <https://doi.org/10.1093/oso/9780198805014.001.0001> (Oxford University Press, Oxford, UK, Nov. 2018).
124. Kramers, H. Brownian motion in a field of force and the diffusion model of chemical reactions. *Physica* **7**, 284–304. [https://doi.org/10.1016/s0031-8914\(40\)90098-2](https://doi.org/10.1016/s0031-8914(40)90098-2) (Apr. 1940).
125. Chung, H. S. & Eaton, W. A. Single-molecule fluorescence probes dynamics of barrier crossing. *Nature* **502**, 685–688. <https://doi.org/10.1038/nature12649> (Oct. 2013).
126. Hummer, G. From transition paths to transition states and rate coefficients. *The Journal of Chemical Physics* **120**, 516–523. <https://doi.org/10.1063/1.1630572> (Dec. 2003).
127. Chung, H. S., Louis, J. M. & Eaton, W. A. Experimental determination of upper bound for transition path times in protein folding from single-molecule photon-by-photon trajectories. *Proceedings of the National Academy of Sciences* **106**, 11837–11844. <https://doi.org/10.1073/pnas.0901178106> (July 2009).
128. Chung, H. S., McHale, K., Louis, J. M. & Eaton, W. A. Single-Molecule Fluorescence Experiments Determine Protein Folding Transition Path Times. *Science* **335**, 981–984. <https://doi.org/10.1126/science.1215768> (Feb. 2012).
129. Truex, K., Chung, H. S., Louis, J. M. & Eaton, W. A. Testing Landscape Theory for Biomolecular Processes with Single Molecule Fluorescence Spectroscopy. *Physical Review Letters* **115**. ISSN: 1079-7114. <http://dx.doi.org/10.1103/PhysRevLett.115.018101> (July 2015).
130. Neupane, K., Manuel, A. P. & Woodside, M. T. Protein folding trajectories can be described quantitatively by one-dimensional diffusion over measured energy landscapes. *Nature Physics* **12**, 700–703. ISSN: 1745-2481. <http://dx.doi.org/10.1038/nphys3677> (Mar. 2016).
131. Neupane, K. *et al.* Direct observation of transition paths during the folding of proteins and nucleic acids. *Science* **352**, 239–242. ISSN: 1095-9203. <http://dx.doi.org/10.1126/science.aad0637> (Apr. 2016).
132. Hoffer, N. Q., Neupane, K. & Woodside, M. T. Observing the base-by-base search for native structure along transition paths during the folding of single nucleic acid hairpins. *Proceedings of the National Academy of Sciences* **118**. ISSN: 1091-6490. <http://dx.doi.org/10.1073/pnas.2101006118> (Dec. 2021).
133. Kim, J.-Y., Meng, F., Yoo, J. & Chung, H. S. Diffusion-limited association of disordered protein by non-native electrostatic interactions. *Nature Communications* **9**. ISSN: 2041-1723. <http://dx.doi.org/10.1038/s41467-018-06866-y> (Nov. 2018).
134. Kim, J.-Y. & Chung, H. S. Disordered proteins follow diverse transition paths as they fold and bind to a partner. *Science* **368**, 1253–1257. ISSN: 1095-9203. <http://dx.doi.org/10.1126/science.aba3854> (June 2020).

135. Gopich, I. V. & Szabo, A. Decoding the Pattern of Photon Colors in Single-Molecule FRET. *The Journal of Physical Chemistry B* **113**, 10965–10973. ISSN: 1520-5207. <http://dx.doi.org/10.1021/jp903671p> (July 2009).
136. Taumoeofolau, G. H. & Best, R. B. Estimating transition path times and shapes from single-molecule photon trajectories: A simulation analysis. *The Journal of Chemical Physics* **154**. ISSN: 1089-7690. <http://dx.doi.org/10.1063/5.0040949> (Mar. 2021).
137. Douglas, S. M. *et al.* Rapid prototyping of 3D DNA-origami shapes with caDNAo. *Nucleic Acids Research* **37**, 5001–5006. <https://doi.org/10.1093/nar/gkp436> (June 2009).
138. Kim, D.-N., Kilchherr, F., Dietz, H. & Bathe, M. Quantitative prediction of 3D solution shape and flexibility of nucleic acid nanostructures. *Nucleic Acids Research* **40**, 2862–2868. <https://doi.org/10.1093/nar/gkr1173> (Dec. 2011).
139. Castro, C. E. *et al.* A primer to scaffolded DNA origami. *Nature Methods* **8**, 221–229. <https://doi.org/10.1038/nmeth.1570> (Feb. 2011).
140. Poppleton, E., Romero, R., Mallya, A., Rovigatti, L. & Šulc, P. OxDNA.org: a public webserver for coarse-grained simulations of DNA and RNA nanostructures. *Nucleic Acids Research* **49**, W491–W498. <https://doi.org/10.1093/nar/gkab324> (May 2021).
141. Snodin, B. E. K. *et al.* Introducing improved structural properties and salt dependence into a coarse-grained model of DNA. *The Journal of Chemical Physics* **142**. <https://doi.org/10.1063/1.4921957> (June 2015).
142. Šulc, P. *et al.* Sequence-dependent thermodynamics of a coarse-grained DNA model. *The Journal of Chemical Physics* **137**. ISSN: 1089-7690. <http://dx.doi.org/10.1063/1.4754132> (Oct. 2012).
143. Rovigatti, L., Šulc, P., Reguly, I. Z. & Romano, F. A comparison between parallelization approaches in molecular dynamics simulations on GPUs. *Journal of Computational Chemistry* **36**, 1–8. <https://doi.org/10.1002/jcc.23763> (Oct. 2014).
144. Ouldridge, T. E., Louis, A. A. & Doye, J. P. K. Structural, mechanical, and thermodynamic properties of a coarse-grained DNA model. *The Journal of Chemical Physics* **134**. <https://doi.org/10.1063/1.3552946> (Feb. 2011).
145. Wagenbauer, K. F. *et al.* How We Make DNA Origami. *ChemBioChem* **18**, 1873–1885. <https://doi.org/10.1002/cbic.201700377> (Aug. 2017).
146. Ingargiola, A. *phconvert - Library and converter for Photon-HDF5 files* <http://photon-hdf5.github.io/phconvert> (2023).
147. Harris, C. R. *et al.* Array programming with NumPy. *Nature* **585**, 357–362. <https://doi.org/10.1038/s41586-020-2649-2> (Sept. 2020).
148. Hunter, J. D. Matplotlib: A 2D graphics environment. *Computing in Science & Engineering* **9**, 90–95. <https://doi.org/10.1109/MCSE.2007.55> (2007).

149. Virtanen, P. *et al.* SciPy 1.0: Fundamental Algorithms for Scientific Computing in Python. *Nature Methods* **17**, 261–272. <https://doi.org/10.1038/s41592-019-0686-2> (2020).
150. Guennebaud, G., Jacob, B., *et al.* *Eigen v3* <http://eigen.tuxfamily.org>. 2010.
151. Pfeiffer, M. *et al.* Single antibody detection in a DNA origami nanoantenna. *iScience* **24**, 103072. <https://doi.org/10.1016/j.isci.2021.103072> (Sept. 2021).
152. Zhang, Y. *et al.* General Strategy To Improve the Photon Budget of Thiol-Conjugated Cyanine Dyes. *Journal of the American Chemical Society* **145**, 4187–4198. <https://doi.org/10.1021/jacs.2c12635> (Feb. 2023).
153. Nair, D. P. *et al.* The Thiol-Michael Addition Click Reaction: A Powerful and Widely Used Tool in Materials Chemistry. *Chemistry of Materials* **26**, 724–744. ISSN: 1520-5002. <http://dx.doi.org/10.1021/cm402180t> (Sept. 2013).
154. Sletten, E. M. & Bertozzi, C. R. Bioorthogonal Chemistry: Fishing for Selectivity in a Sea of Functionality. *Angewandte Chemie International Edition* **48**, 6974–6998. ISSN: 1521-3773. <http://dx.doi.org/10.1002/anie.200900942> (Sept. 2009).
155. Michie, M. S. *et al.* Cyanine Conformational Restraint in the Far-Red Range. *Journal of the American Chemical Society* **139**, 12406–12409. <https://doi.org/10.1021/jacs.7b07272> (Sept. 2017).
156. Matikonda, S. S. *et al.* Impact of Cyanine Conformational Restraint in the Near-Infrared Range. *The Journal of Organic Chemistry* **85**, 5907–5915. <https://doi.org/10.1021/acs.joc.0c00236> (Apr. 2020).
157. Holzmeister, P., Gietl, A. & Tinnefeld, P. Geminate Recombination as a Photoprotection Mechanism for Fluorescent Dyes. *Angewandte Chemie International Edition* **53**, 5685–5688. <https://doi.org/10.1002/anie.201310300> (Apr. 2014).
158. Close, C. *et al.* Maximizing the Accessibility in DNA Origami Nanoantenna Plasmonic Hotspots. *Advanced Materials Interfaces* **9**. <https://doi.org/10.1002/admi.202200255> (July 2022).
159. Shaw, D. E. *et al.* Atomic-Level Characterization of the Structural Dynamics of Proteins. *Science* **330**, 341–346. ISSN: 1095-9203. <http://dx.doi.org/10.1126/science.1187409> (Oct. 2010).
160. Lindorff-Larsen, K., Piana, S., Dror, R. O. & Shaw, D. E. How Fast-Folding Proteins Fold. *Science* **334**, 517–520. ISSN: 1095-9203. <http://dx.doi.org/10.1126/science.1208351> (Oct. 2011).
161. Bhatt, H. *et al.* Structure of an Unfolding Intermediate of an RRM Domain of ETR-3 Reveals Its Native-like Fold. *Biophysical Journal* **118**, 352–365. ISSN: 0006-3495. <http://dx.doi.org/10.1016/j.bpj.2019.11.3392> (Jan. 2020).
162. Zadeh, J. N. *et al.* NUPACK: Analysis and design of nucleic acid systems. *Journal of Computational Chemistry* **32**, 170–173. ISSN: 1096-987X. <http://dx.doi.org/10.1002/jcc.21596> (Nov. 2010).

163. Eid, J. *et al.* Real-Time DNA Sequencing from Single Polymerase Molecules. *Science* **323**, 133–138. <https://doi.org/10.1126/science.1162986> (Jan. 2009).
164. Nooren, I. M. & Thornton, J. M. Structural Characterisation and Functional Significance of Transient Protein–Protein Interactions. *Journal of Molecular Biology* **325**, 991–1018. [https://doi.org/10.1016/s0022-2836\(02\)01281-0](https://doi.org/10.1016/s0022-2836(02)01281-0) (Jan. 2003).
165. Davis, S. J. *et al.* The nature of molecular recognition by T cells. *Nature Immunology* **4**, 217–224. <https://doi.org/10.1038/ni0303-217> (Mar. 2003).
166. Sanders, C. R. Biomolecular ligand-receptor binding studies: theory, practice, and analysis. *Nashville: Vanderbilt University*, 1–43 (2010).
167. Pillai, A. *et al.* *De novo design of allosterically switchable protein assemblies* 2023. bioRxiv: 11.01.565167 (Biophysics). <https://doi.org/10.1101/2023.11.01.565167>.
168. Quijano-Rubio, A. *et al.* De novo design of modular and tunable protein biosensors. *Nature* **591**, 482–487. ISSN: 1476-4687. <http://dx.doi.org/10.1038/s41586-021-03258-z> (Jan. 2021).
169. Krishna, R. *et al.* *Generalized Biomolecular Modeling and Design with RoseTTAFold All-Atom* Oct. 2023. <http://dx.doi.org/10.1101/2023.10.09.561603>.
170. Shetty, R. M., Brady, S. R., Rothemund, P. W. K., Hariadi, R. F. & Gopinath, A. Bench-Top Fabrication of Single-Molecule Nanoarrays by DNA Origami Placement. *ACS Nano* **15**, 11441–11450. ISSN: 1936-086X. <http://dx.doi.org/10.1021/acsnano.1c01150> (July 2021).
171. Williamson, P., Ijas, H., Shen, B., Corrigan, D. K. & Linko, V. Probing the Conformational States of a pH-Sensitive DNA Origami Zipper via Label-Free Electrochemical Methods. *Langmuir* **37**, 7801–7809. <https://www.ncbi.nlm.nih.gov/pubmed/34128683> (2021).
172. Ghosh, A. *et al.* Graphene-based metal-induced energy transfer for sub-nanometre optical localization. *Nat. Photonics* **13**, 860–865 (2019).
173. Kaminska, I. *et al.* Graphene Energy Transfer for Single-Molecule Biophysics, Biosensing, and Super-Resolution Microscopy. *Adv. Mater.* **33**, e2101099. <https://www.ncbi.nlm.nih.gov/pubmed/33938054> (2021).
174. Oliveira-Silva, R. *et al.* Monitoring Proteolytic Activity in Real Time: A New World of Opportunities for Biosensors. *Trends in Biochemical Sciences* **45**, 604–618. ISSN: 0968-0004. <http://dx.doi.org/10.1016/j.tibs.2020.03.011> (July 2020).
175. Rodriguez-Rios, M., Megia-Fernandez, A., Norman, D. J. & Bradley, M. Peptide probes for proteases – innovations and applications for monitoring proteolytic activity. *Chemical Society Reviews* **51**, 2081–2120. ISSN: 1460-4744. <http://dx.doi.org/10.1039/D1CS00798J> (2022).

176. Hart, D. J., Jeong, J., Gumbart, J. C. & Kim, H. D. Weak tension accelerates hybridization and dehybridization of short oligonucleotides. *Nucleic Acids Research* **51**, 3030–3040. ISSN: 1362-4962. <http://dx.doi.org/10.1093/nar/gkad118> (Mar. 2023).
177. Spencer, D. M., Wandless, T. J., Schreiber, S. L. & Crabtree, G. R. Controlling Signal Transduction with Synthetic Ligands. *Science* **262**, 1019–1024. ISSN: 1095-9203. <http://dx.doi.org/10.1126/science.7694365> (Nov. 1993).
178. Yan, L., Ravasio, R., Brito, C. & Wyart, M. Principles for Optimal Cooperativity in Allosteric Materials. *Biophysical Journal* **114**, 2787–2798. ISSN: 0006-3495. <http://dx.doi.org/10.1016/j.bpj.2018.05.015> (June 2018).

8 List of publications

Peer reviewed publications

1. Viktorija Glembockyte*, Lennart Grabenhorst*, Kateryna Trofymchuk*, and Philip Tinnefeld. DNA Origami Nanoantennas for Fluorescence Enhancement. *Accounts of Chemical Research* **54**, 17, 3338–3348 (2021). doi: 10.1021/acs.accounts.1c00307
2. Lennart Grabenhorst*, Kateryna Trofymchuk*, Florian Steiner, Viktorija Glembockyte, and Philip Tinnefeld. Fluorophore photostability and saturation in the hotspot of DNA origami nanoantennas. *Methods and Applications in Fluorescence* **8**, 024003 (2020). doi: 10.1088/2050-6120/ab6ac8
3. Kateryna Trofymchuk*, Viktorija Glembockyte*, Lennart Grabenhorst, Florian Steiner, Carolin Vietz, Cindy Close, Martina Pfeiffer, Lars Richter, Max L. Schütte, Florian Selbach, Renukka Yaadav, Jonas Zähringer, Qingshan Wei, Aydogan Ozcan, Birka Lalkens, Guillermo P. Acuna, and Philip Tinnefeld. Addressable nanoantennas with cleared hotspots for single-molecule detection on a portable smartphone microscope. *Nature Communications* **12**, 950 (2021). doi: 10.1038/s41467-021-21238-9
4. Jakob Schedlbauer, Philipp Wilhelm, Lennart Grabenhorst, Maria-Elisabeth Federl, Birka Lalkens, Florian Hinderer, Ullrich Scherf, Sigurd Höger, Philip Tinnefeld, Sebastian Bange, Jan Vogelsang, and John M. Lupton. Ultrafast Single-Molecule Fluorescence Measured by Femtosecond Double-Pulse Excitation Photon Antibunching. *Nano Letters* **20**, 2, 1074–1079 (2020). doi: 10.1021/acs.nanolett.9b04354
5. Patrick Eiring*, Ryan McLaughlin*, Siddharth S. Matikonda*, Zhongying Han*, Lennart Grabenhorst*, Dominic A. Helmerich, Mara Meub, Gerti Beliu, Michael Luciano, Venu Bandi, Niels Zijlstra, Zhen-Dan Shi, Sergey G. Tarasov, Rolf Swenson, Philip Tinnefeld, Viktorija Glembockyte, Thorben Cordes, Markus Sauer, and Martin J. Schnermann. Targetable Conformationally Restricted Cyanines Enable Photon-Count-Limited Applications. *Angewandte Chemie International Edition* **60**, 26685 (2021). doi: 10.1002/anie.202109749

6. Cindy Close, Kateryna Trofymchuk, [Lennart Grabenhorst](#), Birka Lalkens, Viktorija Glembockyte, and Philip Tinnefeld. Maximizing the accessibility in DNA origami nanoantenna plasmonic hotspots. *Advanced Materials Interfaces* **9**, 2200255 (2022). doi: 10.1002/admi.202200255
7. Siddharth S. Matikonda*, Gabrielle Hammersley*, Nikita Kumari*, [Lennart Grabenhorst](#), Viktorija Glembockyte, Philip Tinnefeld, Joseph Ivanic, Marcia Levitus, and Martin J. Schnermann. Impact of cyanine conformational restraint in the near-infrared range. *The Journal of Organic Chemistry* **85**, 9, 5907–5915 (2020). doi: 10.1021/acs.joc.0c00236
8. Kevin Kramm, Tim Schröder, Andres Manuel Vera, [Lennart Grabenhorst](#), Philip Tinnefeld, and Dina Grohmann. DNA Origami-Based Single-Molecule Force Spectroscopy and Applications. In: Iddo Heller, David Dulin, and Erwin J.G. Peterman (eds). *Single Molecule Analysis. Methods in molecular biology*, **2694**, 479–507 (2024). doi: 10.1007/978-1-0716-3377-9_23

* equal contribution.

Preprints

1. [Lennart Grabenhorst](#), Flurin Sturzenegger, Moa Hasler, Benjamin Schuler and Philip Tinnefeld. Single-molecule FRET at 10 MHz countrate. *bioRxiv* (2023). doi: 10.1101/2023.12.08.570755
2. [Lennart Grabenhorst*](#), Martina Pfeiffer*, Thea Schinkel, Mirjam Kümmerlin, Jasmin Maglic, Gereon A. Brüggenthies, Florian Selbach, Alexander T. Murr, Philip Tinnefeld, and Viktorija Glembockyte. Engineering Modular and Tunable Single-Molecule Sensors by Decoupling Sensing from Signal Output. *bioRxiv* (2023). doi: 10.1101/2023.11.06.565795

* equal contribution.

Conference contributions

1. [Lennart Grabenhorst](#), Viktorija Glembockyte, and Philip Tinnefeld. Single-molecule FRET experiments at MHz countrates with DNA origami nanoantennas. Poster presented at the 17th Methods and Applications in Fluorescence conference **2022** (Gothenburg, Sweden).

2. Lennart Grabenhorst, Viktorija Glembockyte, and Philip Tinnefeld. Single-molecule FRET experiments at MHz countrates with DNA origami nanoantennas. Talk presented at the FRET satellite meeting **2022** (Gothenburg, Sweden).
3. Lennart Grabenhorst, Martina Pfeiffer, Viktorija Glembockyte, and Philip Tinnefeld. A DNA origami based scaffold as model system for multivalent ligand binding and biosensing. Talk presented at the 26th international workshop on single molecule spectroscopy and super-resolution microscopy **2021** (Berlin, Germany).
4. Lennart Grabenhorst, Viktorija Glembockyte, and Philip Tinnefeld. A DNA origami based modular and tunable biosensor. Poster presented at the FNANO21 conference **2021** (virtual).
5. Lennart Grabenhorst, Birka Lalkens, and Philip Tinnefeld. Single-molecule FRET experiments with microsecond time resolution. Poster presented at the iPOLS conference **2019** (München, Germany).
6. Lennart Grabenhorst, Viktorija Glembockyte, Kateryna Trofymchuk, Cindy Close, Martina Pfeiffer, Renukka Yaadav, Sarah Ochmann, Birka Lalkens, and Philip Tinnefeld. Self-assembled plasmonic DNA origami nanoantennas for diagnostic applications. Poster presented at the Diagnostics-4-Future Conference **2019** (Konstanz, Germany).
7. Lennart Grabenhorst, Viktorija Glembockyte, Kateryna Trofymchuk, Florian Steiner, Birka Lalkens, and Philip Tinnefeld. Plasmonic hotspots for single-molecule biophysics. Poster presented at the 25th international anniversary workshop on single molecule spectroscopy and super-resolution microscopy **2019** (Berlin, Germany).
8. Lennart Grabenhorst, Ija Jusuk, Mario Raab, Florian Selbach, Andrés Manuel Vera, and Philip Tinnefeld. Towards single-molecule sequencing in a plasmonic hotspot. Poster presented at the CeNS Workshop "Celebrating NanoScience" **2018** (Venice, Italy).

9 Acknowledgements

"It is good to have an end to journey toward; but it is the journey that matters, in the end."

— Ursula K. Le Guin

As my journey as a PhD student comes to an end, there are several people I would like to thank for helping me along the way.

Firstly, I want to express my gratitude to Philip, who gave me the opportunity to work on these interesting problems with probably the best equipment and financial support one could wish for. Thanks for giving me the freedom to develop my own ideas. Thank you for many interesting discussions about the projects, for teaching me how to think about projects in terms of "the final figure" and for always being motivated for the football subgroup.

I would like to thank Dr. Jan Vogelsang for being the co-examiner of my thesis and for our short but very memorable collaboration with DNA origami nanoantennas and femtosecond lasers.

Furthermore, I am grateful to Prof. Khmelinskaia, Prof. Liedl, Prof. Hartschuh, and Prof. Stigler for joining my thesis committee.

A huge thank you goes to Viki for all the insightful discussions and feedback. Thank you for introducing me to the world of photophysics and for sparking my interest in all the cool science that is being done around the world. I also would like to thank you for working together on the biosensor project – without your input and hard work, this would never have been realized!

Thank you to Flo Steiner and Alan, who also contributed a lot to the nice working atmosphere in office E1.064. Thanks for all the nice discussions, related or unrelated to our projects.

For showing me the ins and outs of molecular biology, and for always having ideas for the troubleshooting of protein experiments, thank you Andrés.

I would like to thank Tim for his support at the confocal setup, without your help this project would have taken even longer than it already did.

Thank you Alex for always spreading good mood at lunch and for being a reliable source of Expressis.

I am grateful for the excellent social environment in the whole working group, which made it easy to ask people for help when I encountered problems. I am equally grateful for the scientific environment provided by CeNS and the Department of Chemistry, which allowed me to attend many interesting talks.

Thank you to Angelika for keeping the lab running and all the help with my protein expressions, as well as for always being positive and spreading good mood in the lab. Thank you to Moritz Ehrl for providing excellent administrative support and for making sure I am not running out of my contract. Thank you to Silke Steger for further administrative help.

I also would like to thank my collaboration partners, inside or outside of the group, who I enjoyed working with: Cindy Close, Martina Pfeiffer, Flurin Sturzenegger, Moa Hasler, Ben Schuler, Jakob Schedlbauer, Jan Vogelsang, Siddarth Matikonda, Martin Schnermann and many others.

Thanks a lot to Eckart, Sabine, Meret, and Viki for proofreading this thesis and for giving me feedback on how to improve it.

Thank you to my family for supporting me in all sorts of ways and for always giving me the right perspective on how things are.

Finally, I would like to thank everyone who ever reads this thesis in the future – in the end, other people reading it is what makes all of this worth it. I hope you find some things in here that are useful and will continue to stay motivated to expand human knowledge!

10 Appendix

Associated Publication 1

DNA origami nanoantennas for fluorescence enhancement

Viktorija Glembockyte*, [Lennart Grabenhorst*](#), Kateryna Trofymchuk* and Philip Tinnefeld

*equal contribution

Accounts of Chemical Research **54**, 17, 3338–3348 (2021). doi: 10.1021/acs.accounts.1c00307

(open access)

DNA Origami Nanoantennas for Fluorescence Enhancement

Viktorija Glembockyte,[†] Lennart Grabenhorst,[†] Kateryna Trofymchuk,[†] and Philip Tinnefeld*[‡]



Cite This: *Acc. Chem. Res.* 2021, 54, 3338–3348



Read Online

ACCESS |

Metrics & More

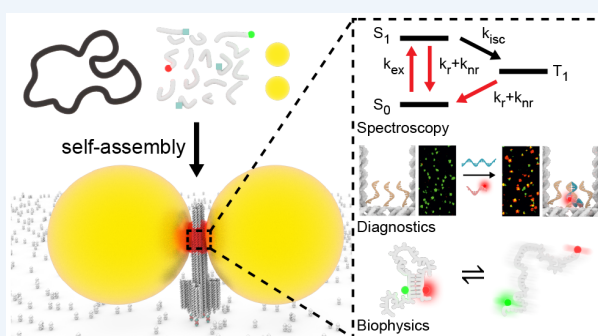
Article Recommendations

CONSPECTUS: The possibility to increase fluorescence by plasmonic effects in the near-field of metal nanostructures was recognized more than half a century ago. A major challenge, however, was to use this effect because placing single quantum emitters in the nanoscale plasmonic hotspot remained unsolved for a long time. This not only presents a chemical problem but also requires the nanostructure itself to be coaligned with the polarization of the excitation light. Additional difficulties arise from the complex distance dependence of fluorescence emission: in contrast to other surface-enhanced spectroscopies (such as Raman spectroscopy), the emitter should not be placed as close as possible to the metallic nanostructure but rather needs to be at an optimal distance on the order of a few nanometers to avoid undesired quenching effects.

Our group addressed these challenges almost a decade ago by exploiting the unique positioning ability of DNA nanotechnology and reported the first self-assembled DNA origami nanoantennas. This Account summarizes our work spanning from this first proof-of-principle study to recent advances in utilizing DNA origami nanoantennas for single DNA molecule detection on a portable smartphone microscope.

We summarize different aspects of DNA origami nanoantennas that are essential for achieving strong fluorescence enhancement and discuss how single-molecule fluorescence studies helped us to gain a better understanding of the interplay between fluorophores and plasmonic hotspots. Practical aspects of preparing the DNA origami nanoantennas and extending their utility are also discussed. Fluorescence enhancement in DNA origami nanoantennas is especially exciting for signal amplification in molecular diagnostic assays or in single-molecule biophysics, which could strongly benefit from higher time resolution. Additionally, biophysics can greatly profit from the ultrasensitive detection volumes provided by DNA nanoantennas that allow single-molecule detection at drastically elevated concentrations as is required, e.g., in single-molecule DNA sequencing approaches.

Finally, we describe our most recent progress in developing DNA NanoAntennas with Cleared HOTspots (NACHOS) that are fully compatible with biomolecular assays. The developed DNA origami nanoantennas have proven robustness and remain functional after months of storage. As an example, we demonstrated for the first time the single-molecule detection of DNA specific to antibiotic-resistant bacteria on a portable and battery-driven smartphone microscope enabled by DNA origami nanoantennas. These recent developments mark a perfect moment to summarize the principles and the synthesis of DNA origami nanoantennas and give an outlook of new exciting directions toward using different nanomaterials for the construction of nanoantennas as well as for their emerging applications.



KEY REFERENCES

- Acuna, G. P.; Möller, F. M.; Holzmeister, P.; Beater, S.; Lalkens, B.; Tinnefeld, P. Fluorescence Enhancement at Docking Sites of DNA-Directed Self-Assembled Nanoantennas. *Science* **2012**, 338, 506–510.¹ *The first study employing the DNA origami technique to build self-assembled optical nanoantennas. The extent of fluorescence enhancement of a single dye precisely positioned in the hotspot of monomeric and dimeric nanoantennas of nanoparticles of various sizes was studied.*
- Vietz, C.; Kaminska, I.; Sanz Paz, M.; Tinnefeld, P.; Acuna, G. P. Broadband Fluorescence Enhancement

with Self-Assembled Silver Nanoparticle Optical Antennas. *ACS Nano* **2017**, 11, 4969–4975.² *Fabricated DNA origami-based nanoantenna comprises large silver nanoparticles and provides fluorescent enhancement over the*

Received: May 20, 2021

Published: August 26, 2021



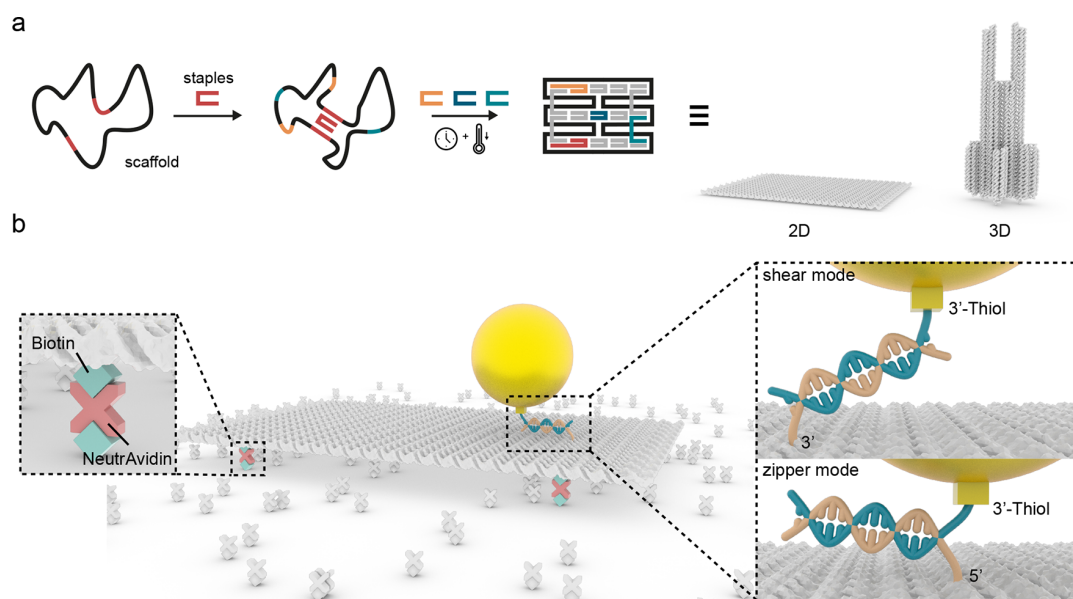


Figure 1. (a) Principle of the DNA origami approach to preparing 2D and 3D DNA nanostructures from the ssDNA scaffold and hundreds of ssDNA staple strands. (b) Immobilization of a DNA nanostructure bearing biotin-modified stands on BSA-biotin-NeutrAvidin-coated glass to perform SM fluorescence measurements (left). Attachment of ssDNA-functionalized NPs via thiol-Au/Ag interactions on DNA origami in zipper and shear binding modes, which provide different separations between DNA origami and NP (right).

visible range. A comparison between the performance of silver- and gold-based antennas is reported.

- Ochmann, S. E.; Vietz, C.; Trofymchuk, K.; Acuna, G. P.; Lalkens, B.; Tinnefeld, P. Optical Nanoantenna for Single Molecule-Based Detection of Zika Virus Nucleic Acids without Molecular Multiplication. *Anal. Chem.* **2017**, *89*, 13000–13007.³ Successful detection of specific DNA and RNA in heat-deactivated blood serum with the help of monomeric DNA origami antennas. Demonstration of multiplexed detection of different targets using fluorescent barcodes.
- Trofymchuk, K.; Glembockyte, V.; Grabenhorst, L.; Steiner, F.; Vietz, C.; Close, C.; Pfeiffer, M.; Richter, L.; Schütte, M. L.; Selbach, F.; Yaadav, R.; Zähringer, J.; Wei, Q.; Ozcan, A.; Lalkens, B.; Acuna, G. P.; Tinnefeld, P. Addressable nanoantennas with cleared hotspots for single-molecule detection on a portable smartphone microscope. *Nat. Commun.* **2021**, *12*, 950.⁴ A novel design of DNA origami providing a place in the hotspot of a dimeric nanoantenna for a tailored bioassay. The first demonstration of single DNA molecule detection on a smartphone camera-based portable microscope.

INTRODUCTION

In line with theoretical considerations by Purcell of the environment-stimulated enhancement of the emission rate of an emitter⁵ and following the first experimental observations by Drexhage,⁶ a whole field of research has emerged around understanding and controlling the interactions between plasmonic nanoparticles (NPs) and fluorophores. Collective oscillations of electrons in the plasmonic NPs illuminated with light at the eigenfrequency of the NPs lead to the subwavelength localization and thus enhancement of the electric field of the incident irradiation close to the surface of the NP. This property allows NPs to act as optical nanoantennas (NAs), analogous to regular radio antennas.^{7,8}

Key findings supported the notion of enormous potential increases in fluorescence emission rates particularly in so-called plasmonic hotspots (regions with the highest electric field enhancement)⁹ while also revealing the importance of precise positioning of the fluorophore relative to the NP surface on the nanometer scale in order to avoid fluorescence quenching effects.¹⁰

Several approaches were employed to address this positioning problem (e.g., attaching a gold (Au) NP to the tip of an AFM cantilever,^{10,11} relying on the rigidity of double-stranded DNA to couple them^{12,13}); however, one method has proven particularly useful: DNA nanotechnology and, in particular, the DNA origami technique. In this approach (Figure 1a), a long (several thousands of nucleotides (nt)) single-stranded DNA (ssDNA) (“scaffold” strand) is folded in a programmable way by hybridizing with hundreds of short (~15–50 nt) single-stranded DNA oligonucleotides (“staple” strands).¹⁴ Specific staple strands can be modified with a molecule of interest (e.g., biotin modification or a fluorophore), and thus this molecule can be positioned on the DNA origami structure with nanometer precision. The nanoscale scaffolding capabilities of the DNA origami technique¹⁴ are of great use when constructing the complex two- and three-dimensional (2D and 3D) geometries¹⁵ (Figure 1a) needed to achieve high fluorescence enhancement (FE) values, and its bottom-up self-assembly reaction scheme enables the parallel production of billions of identical nanostructures. This is in sharp contrast to top-down assembly methods such as electron-beam lithography¹⁶ which intrinsically rely on serial fabrication and only stochastic positioning of fluorescent emitters.

This Account focuses on the progress made in our group from the first DNA origami structures bearing single AuNPs toward DNA origami NanoAntennas with Cleared HOtSpots (NACHOS) that can be tailored for placing complex biomolecular assays and their potential uses in molecular

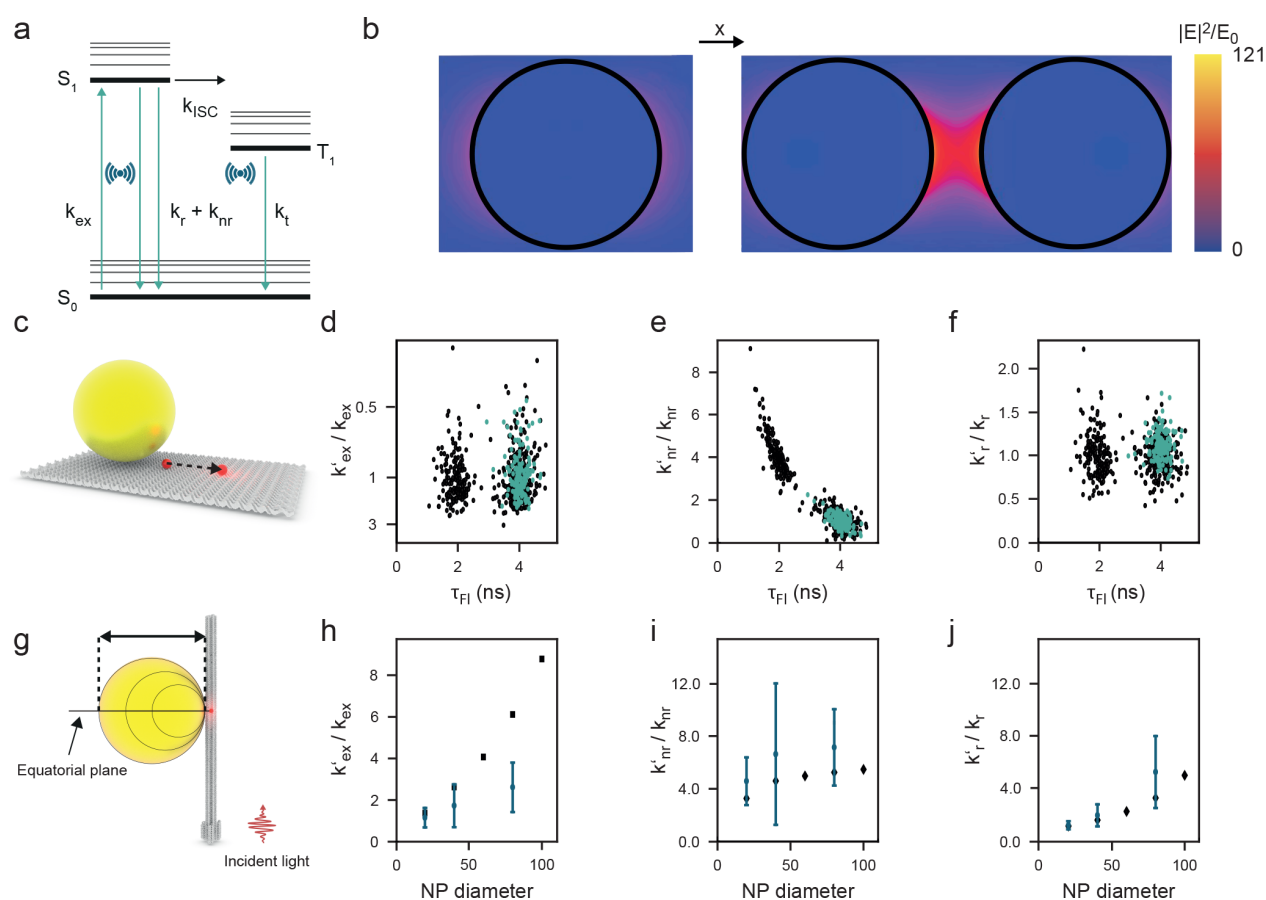


Figure 2. (a) Simplified Jablonski diagram of a fluorophore illustrating the electronic states (S_0 , S_1 , T_1) and the transitions between them by excitation (k_{ex}), radiative (k_r) and nonradiative (k_{nr}) decays, intersystem crossing (k_{ISC}), and the decay from the triplet state (k_t). (b) Numerical simulation of electric field intensity for a monomer (left) and dimer with an interparticle spacing of 23 nm (right) for 80-nm-diameter AuNPs. The excitation light at 640 nm is horizontally polarized.¹ (c) Schematic representation of 20 nm AuNP on 2D rectangular DNA origami. (d–f) Changes in the decay rates (indicated with an apostrophe) for the sample with dye–NP separations of 27.8 nm (cyan circles) and of 8.3 nm (black circles) are normalized to the mean value of the population without NP.²¹ For the 8.3 nm sample, two populations are visible as not all DNA origami carry an NP. τ_{Fl} is the fluorescence lifetime. (g) Schematic representation of 20–100 nm AuNP on 3D pillar DNA origami. (h–j) All relevant photophysical rates are enhanced with increasing particle size (blue, experimental data; black, theoretical simulations).²¹

diagnostics and single-molecule (SM) fluorescence experiments.

FUNDAMENTAL ASPECTS OF INTERACTIONS BETWEEN FLUOROPHORES AND NANOPARTICLES

In the last years, DNA origami has emerged as a modular platform to study the fluorophore–NP interactions at the SM level. To this end, DNA nanostructures containing biotin modifications can be immobilized on glass surfaces, and NPs, functionalized with ssDNA via thiol–Au/Ag interactions,¹⁷ can be annealed to complementary strands protruding from the DNA origami at the designed positions (Figure 1b).

The dye–plasmonic NP interaction depends on the NP size, shape, and material and also on the distance (d) and orientation between the dye and the NP.¹⁰ Whether the emission of a fluorophore is enhanced or quenched in the vicinity of a plasmonic NP is determined by the extent to which the altered local electric field affects its photophysical properties (i.e., the excitation (k_{ex}), radiative (k_r), and nonradiative (k_{nr}) decay rates (Figure 2a)). All of these processes together with the electric field enhancement in the

vicinity of plasmonic NPs can be approximated by numerical simulations (Figure 2b).¹⁸

In 2012, Acuna et al. addressed the distance-dependent interaction between a 10 nm AuNP and a single ATTO647N dye using a rectangular 2D DNA nanostructure (Figure 2c).¹⁹ It was demonstrated that the quenching of fluorophores by AuNPs is strongly dependent on their spatial separation. This dependence deviated from the $1/d^4$ distance dependence that is characteristic of nanosurface energy transfer (NSET)²⁰ and exceeded the typical fluorescence resonance energy transfer (FRET) distances (4–8 nm), showing 50% intensity quenching at 10.4 nm. This phenomenon was further investigated by Holzmeister et al.,²¹ who demonstrated that while k_{ex} and k_r of a dye in the vicinity of a 20 nm AuNP are not strongly affected, k_{nr} is very sensitive to the distance to the NP (Figure 2c–f). In contrast, when an ATTO647N dye is placed in the equatorial plane of larger AuNPs with respect to the direction of the excitation using a pillar-shaped 3D DNA origami, an enhancement of the excitation field and photophysical rates (k_{ex} , k_r , and k_{nr}) was observed (Figure 2b,g–j).^{21,22} This is reflected in a shorter fluorescence lifetime (Figures 2d–f and 3a,c).^{1,4,21,22} The increase in k_{nr} is usually

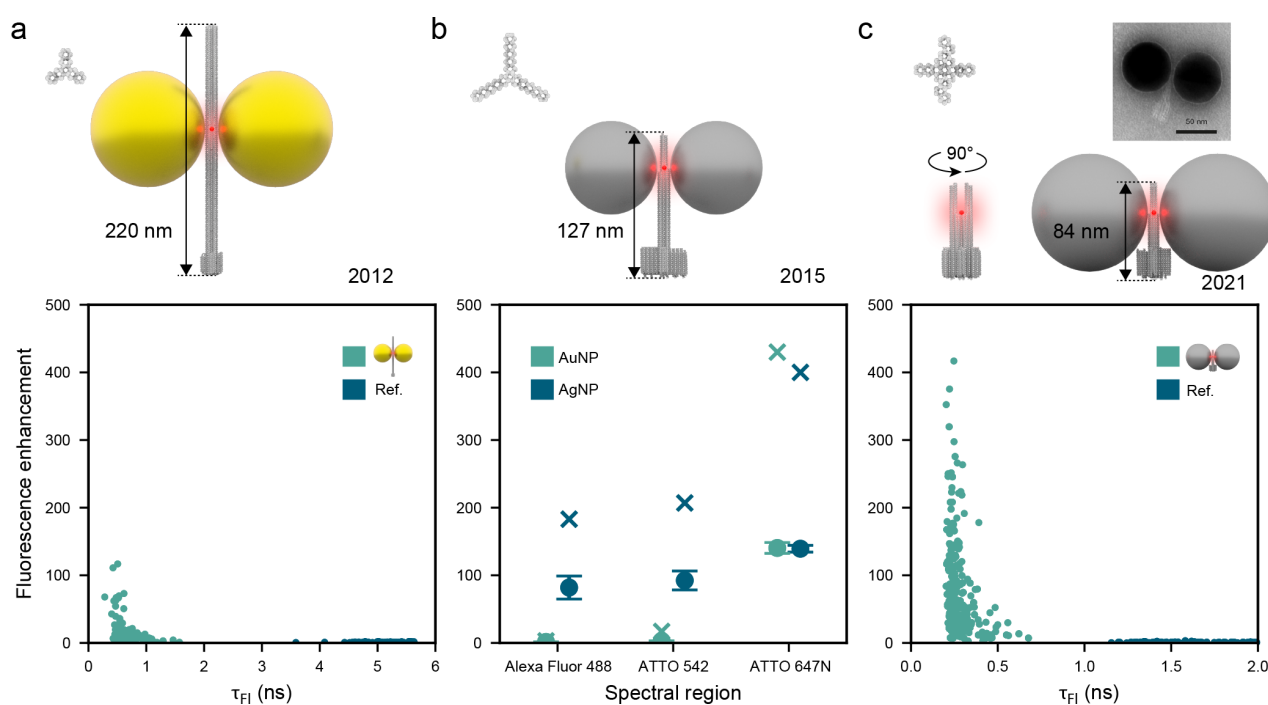


Figure 3. Evolution of DNA origami nanoantennas for fluorescence enhancement. (a) Pillar-shaped DNA origami structure and FE obtained for ATTO647N in the hotspot of dimer 100 nm AuNPs NA (green) in comparison to a reference structure (blue) containing no NPs.¹ (b) Pillar-shaped DNA origami and FE of dyes from different parts of the visible spectrum in the hotspot of dimer 100 nm AuNPs (green) and 80 nm AgNPs (blue) NAs.² Measurements were performed on a wide-field microscope which does not provide fluorescence lifetime (τ_{FI}) information. The monomer subpopulation was excluded from the distribution based on FE values. Dots represent the mean experimental FE with the standard error, and crosses represent the maximal obtained FE values. (c) NACHOS provide a free space in the plasmonic hotspot for placing biomolecular assays.⁴ TEM image of NACHOS with 60 nm AuNP (top). FE obtained on a confocal microscope for Alexa Fluor 647 in the hotspot of dimer 100 nm AgNPs NA (green) in comparison to a reference structure (blue) containing no NPs.

attributed to the energy transfer to dark modes of NPs.¹⁰ Earlier studies have demonstrated that the intrinsic intersystem crossing rate (k_{ISC}) does not change in the presence of plasmonic particles,²³ while the influence on other non-radiative decay pathways (e.g., internal conversion k_{IC}), to the best of our knowledge, has not been reported. The 3D pillar-shaped DNA origami also allowed us to study the angular fluorescence intensity modulation of a single Cy5 dye close to a 40 or 80 nm AuNP, revealing the polarization-dependent enhancement and quenching of fluorescence emission.²² Toward beam-steering nanoantennas, we also demonstrated that the emission of a freely rotating Cy5 dye in the gap of dimer Au NA can be directed by plasmonic effects and follows a dipolar pattern.²⁴

These findings were key in improving our understanding of the interplay between fluorophores and plasmonic NPs. We found that there is an optimal distance and orientation between the dye and the NP surface and that controlling these parameters is pivotal for achieving high FE in DNA NAs. Here we provide a list of the factors that are helpful to consider when designing optical DNA NAs for FE:

1. **Particle Size.** As a first approximation, fluorescence quenching scales with particle volume, while fluorescence enhancement scales with the square of the volume.²⁵ This means that the particles should be chosen to be as large as possible under consideration of other effects, such as retardation, which impose an upper limit on the particle size.²⁶ In our hand, the highest enhancement factors were achieved with 100 nm particles.

2. **Gap Size.** The smaller the gap between NPs, the higher the electric field enhancement.²⁷ However, this also results in more red-shifted plasmon resonance. The dye should not be placed too close to the NP because in this regime the nonradiative decay pathways would outcompete the radiative decay and quenching rather than fluorescence enhancement would be observed.^{19,27}

3. **Excitation and Emission Spectra.** The excitation and emission enhancements are governed by the spectral overlap with the plasmonic near-field, which is typically red-shifted from the far-field (scattering) spectrum.²⁵

4. **Orientation.** The dye has to be in the equatorial plane (as shown in Figure 2g) of the incident light in order to be exposed to the maximum possible electrical field, and the dipole of the molecule should be oriented parallel to the dipole of the NA.^{21,28} Also, excitation polarization has to be aligned with the plasmon longitudinal mode in plasmonic structures with nonspherical symmetry.

FORMING AND CONTROLLING PLASMONIC HOTSPOTS FOR FLUORESCENCE ENHANCEMENT

On the basis of previously formulated principles,^{12,21,28,29} the first FE studies with DNA origamis were performed on a 3D pillar-shaped DNA nanostructure (Figure 2g). Here, FEs of 5- and 8-fold were obtained for a single Cy5 dye at a distance of ~ 12 nm to single 40 and 80 nm AuNPs, respectively.²² However, it was evident from other studies that much higher FE values could be achieved if the dye could be placed in the gap between two or more plasmonic NPs (Figure 2b).³⁰

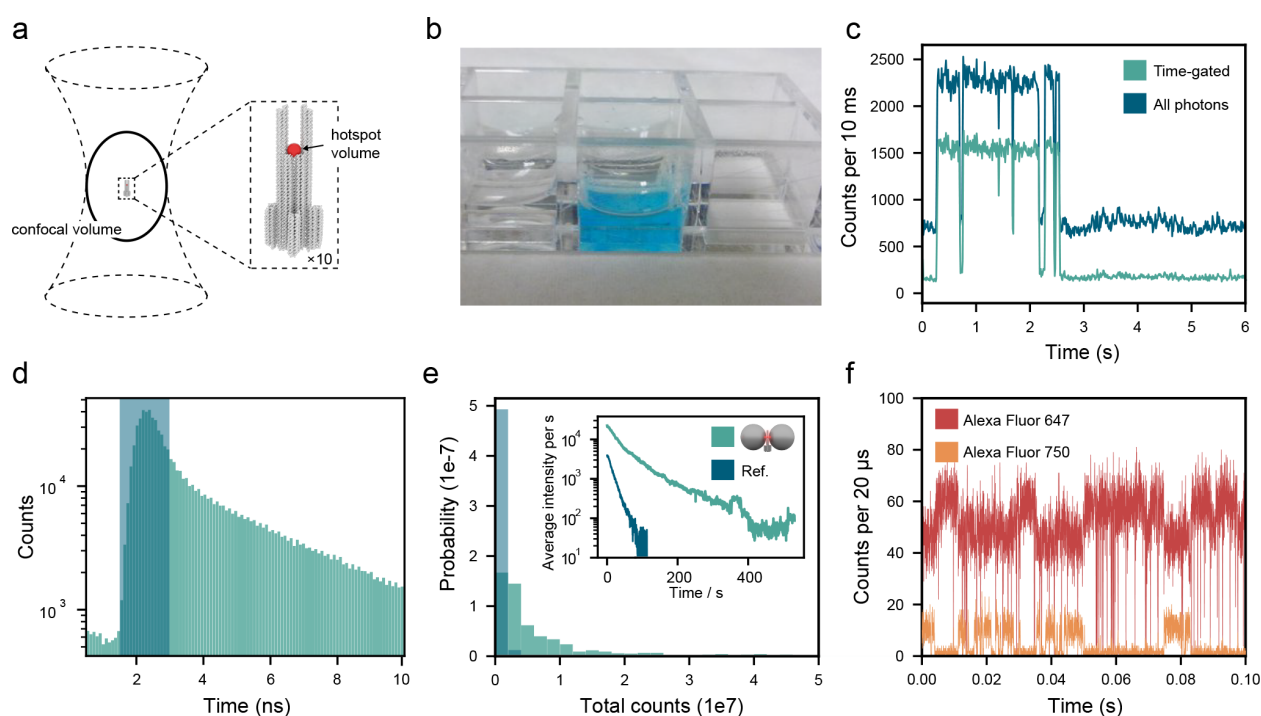


Figure 4. (a) Typical confocal detection volume compared to the plasmonic hotspot (indicated in red) of an NA. (b) Photograph of a sample chamber containing 25 μ M ATTO647N.²⁷ (c, d) Fluorescence transient of ATTO647N in the plasmonic hotspot at 0.5 μ M ATTO647N background.¹ Lifetime gating improves the contrast as molecules in the hotspot have a shorter fluorescence decay (dark blue) while omitting the majority of background photons. (e) Photon budget and average fluorescence intensity over time (inset) of ATTO647N in the reference DNA origami structure (excited at 639 nm, 9 mW) as well as in the hotspot of dimer 100 nm AuNP NA (excited at 639 nm, 1.6 mW).³⁷ (f) High-resolution FRET transient showing fluctuations induced by acceptor blinking enabled by plasmonic-enhanced fluorescence. Photon count rates of 3.5 MHz (donor, red) and 1 MHz (acceptor, orange) are achieved.

The first study utilizing the DNA origami technique to create such self-assembled dimer plasmonic NAs and to place a single dye in the plasmonic hotspot was reported in 2012 by Acuna et al. In this study, the authors designed a pillar-shaped DNA origami¹ and prepared dimer NAs with AuNPs of different sizes (20–100 nm). In line with theoretical predictions, 100 nm dimer NAs with an interparticle gap of \sim 23 nm demonstrated the highest FE factors, reaching 117-fold (Figure 3a).

To improve the FE, the design of the DNA origami evolved over the next few years (Figure 2b,c), aiming to maintain the vertical orientation of the structure for better alignment of the NP's dipole with the polarization of the incident light³¹ and decreasing the interparticle distance by narrowing down the top of the structure to a six-helix bundle (Figure 3b). Further improvements in NA preparation included overcoming the aggregation of larger NPs³² by using longer ssDNA for functionalization and exploiting the zipper-binding geometry (Figure 1d) to decrease the distance between NPs to 12–17 nm and hence obtain a higher electric field enhancement^{26,27} (Figure 1c). These improvements made it possible to obtain FE values of up to 471-fold for a dimer 100 nm AuNP NA.²⁷ A further increase in NP size did not lead to further improvement in FE due to retardation effects and red-shifted plasmon resonance.²⁶

The next step forward in expanding the utility of the plasmonic hotspot was the demonstration of broadband FE with self-assembled AgNP optical antennas.² NAs based on AuNPs provide FE typically in the red and near-infrared

spectral regions. In contrast, AgNPs have a plasmon resonance in the violet-blue spectral region (which can be red-shifted upon their dimerization),³³ allowing their coupling with dyes that span a broad spectral range. Using the improved protocol for large NP functionalization,²⁶ Vietz et al. used AgNPs to assemble optical NAs, demonstrating FE of up to 2 orders of magnitude for dyes spanning almost the whole visible spectrum (Figure 3b).²

On the one hand, the rigid DNA structure between the NPs ensures a well-defined hotspot. The drawback of this NA design, however, is the fact that the majority of the plasmonic hotspot region was blocked by the DNA origami structure itself, which prevents the incorporation of larger biomolecules or biological assays.^{3,34} This problem was recently addressed by a newly designed 3D DNA origami, named NACHOS (Figure 3c), which provides a free space in the plasmonic hotspot region formed by two 100 nm AuNPs or AgNPs. As discussed later, this enabled placing biomolecular assays in the plasmonic hotspot while maintaining high FE reaching >400-fold.⁴

One of the main challenges we faced over the years was the heterogeneity of FE distributions, which reflect the heterogeneity in NP size and shape,³⁵ and the different orientations of NAs with respect to the excitation field. The FE distributions shown also contain a subpopulation of monomer NAs, characterized by a lower FE and higher fluorescence lifetimes (Figure 3a,c; in Figure 3b the monomer contribution to FE values was filtered). Furthermore, one cannot reject the possibility of multimetric binding of NPs to the DNA origami,

which in the future we hope to investigate further by correlative fluorescence/dark field/electron microscopy studies. While this heterogeneity does not pose a limitation for improving SM detection (as long as even low FE values are bright enough to detect them), it represents a challenge to extracting quantitative information when adapting the NAs to boost the fluorescence signals of common ensemble diagnostic assays. Possible strategies to address this heterogeneity problem might include exploiting more homogeneous NPs,³⁶ developing strategies to achieve better coalignment of NA and dye dipoles as well as even more defined and rigid positioning of NPs.

■ DNA ORIGAMI NANOANTENNAS FOR SINGLE-MOLECULE BIOPHYSICS

The ability to position molecules precisely in the plasmonic hotspot paved the way toward exciting new applications in the field of SM biophysics. DNA NAs provide three clear advantages for SM imaging: (1) an enhanced fluorescence signal of a single emitter allows imaging at higher background concentrations of fluorophores; (2) higher count rates by FE enable higher time resolution; and (3) fast depopulation of the excited states in the hotspot improves the photostability of fluorescent labels.

The first advantage is central to a long-lasting problem in the field: the discrepancy between the concentrations needed for SM detection (which are in the pM to nM range) and the concentration range in which most biomolecules are present and active *in vivo* (usually in the μM to mM range).³⁸ Strategies to overcome this problem include the use of elaborate microfluidic setups or highly confined observation volumes (e.g., zero mode wave guides,³⁹ the “antenna in a box” platform,⁴⁰ convex lens-induced confinement (CLIC),⁴¹ or nanopipettes⁴²).

With DNA NAs, an alternative and more straightforward way has emerged. The significantly reduced excitation volume is the key: a plasmonic hotspot typically is on the order of zL, while typical confocal excitation volumes are on the order of fL, a million times larger. Thus, by reducing the effective excitation volume, the background fluorescence can be decreased significantly (Figure 4a). Additionally, the reduced fluorescence lifetime of emitters in the plasmonic hotspot enables a further cleanup step by time-gating the photons (Figure 4c,d).¹ With this, SM detection has been shown to be feasible even in solutions containing micromolar concentrations of fluorophores (Figure 4b–d), extending SM fluorescence experiments to biologically relevant concentration ranges.

Enhancing the photostability of fluorophores is of great importance for all SM fluorescence experiments because the amount of information that can be extracted is fundamentally limited by the survival time of the dye molecule. The increase in photostability strongly correlates with the increase in the radiative rate k_r ²⁹ (an up to 75-fold increase in k_r has been shown in a plasmonic hotspot),⁴³ which results in a vastly reduced time that the fluorophore spends in reactive excited states³⁷ and therefore a decrease of the probability of processes leading to photobleaching. The lifetimes of triplet excited states of fluorophores (common intermediates in the photobleaching pathways as well as precursors of singlet oxygen and other reactive oxygen species) have also been shown to be reduced in the vicinity of plasmonic nanostructures,^{44–46} which could further contribute to improved photostability in

plasmonic hotspots. Pellegrotti et al.,²⁹ for example, demonstrated that a Cy5 dye positioned close the surface of a 80 nm AuNP on average emits more than 4 times more photons before photobleaching. Another study utilizing 80 nm AgNP dimer NAs showed that the photostability of a blue-absorbing fluorophore (Alexa Fluor 488) can also be increased by >30-fold.⁴⁷ More recently, we have also demonstrated an up to 40-fold increase in the total photon budget in DNA NA containing two 100 nm Ag NP for one of the most photostable organic dyes—ATTO647N—which could potentially be further increased by additional photostabilizers in solution (Figure 4e). We have also found that the saturation behavior of dyes is affected when placed in the hotspots of plasmonic NAs, with the maximum photon count rates that can be achieved being limited and specific to the nature of the fluorophore that is used.³⁷

Plasmonic effects can also improve the time resolution of FRET experiments. Many interesting biological processes such as protein folding and aggregation occur on the submillisecond time scale, which is hard to access via conventional methods. Proteins are therefore approximated by two-state systems, but the wealth of information on what happens during the transition from the folded to the unfolded state or vice versa is often hidden. Here, the limiting factor is not the photon budget but the maximum number of detected photons per unit time (the photon count rate). Even with the most elaborate chemical photostabilization procedures, photon count rates achievable with the best fluorophores are usually below 1000 ms^{-1} and the dyes survive only for several milliseconds before photobleaching.^{48,49} As illustrated in Figure 4f, plasmonic effects can also increase the count rates substantially in single-molecule FRET experiments, enabling real-time visualization of transitions on the millisecond to microsecond time scale. The presented transient showing FRET fluctuations induced by acceptor blinking could be followed for 5 s before photobleaching.

In combination with newly developed organic dyes that are spectrally more stable and show reduced blinking behavior on short time scales,^{50,51} this opens up exciting new research directions as fast nonequilibrium dynamics such as barrier crossing events in protein folding⁵² could become accessible with this increased time resolution.

■ DNA ORIGAMI NANOANTENNAS FOR DIAGNOSTICS

Many fluorescence-based molecular diagnostic assays, in particular, those used to detect low-abundance analytes, require molecular amplification of target molecules (e.g., polymerase chain reaction or sandwich ELISA assays).⁵³ Physical amplification of the signal upon detection of single target molecules could provide the means to improve the speed, robustness, and multiplexing capabilities of these assays and overcome the problem of a low signal-to-background ratio originating from the background signal of the large number of other molecules present in the observation volume (e.g., due to scattering, autofluorescence, and nonspecific binding).⁵³ It could also open possibilities to detect single molecules on much cheaper and simpler devices, enabling ultrasensitive detection in point-of-care diagnostic settings.⁵⁴ When aiming at enhancing the signal of a molecular assay with the help of plasmonic NAs, one is faced with an obvious challenge: how to place this assay directly in the plasmonic hotspot. In contrast to other surface-enhanced spectroscopies, the gap between the

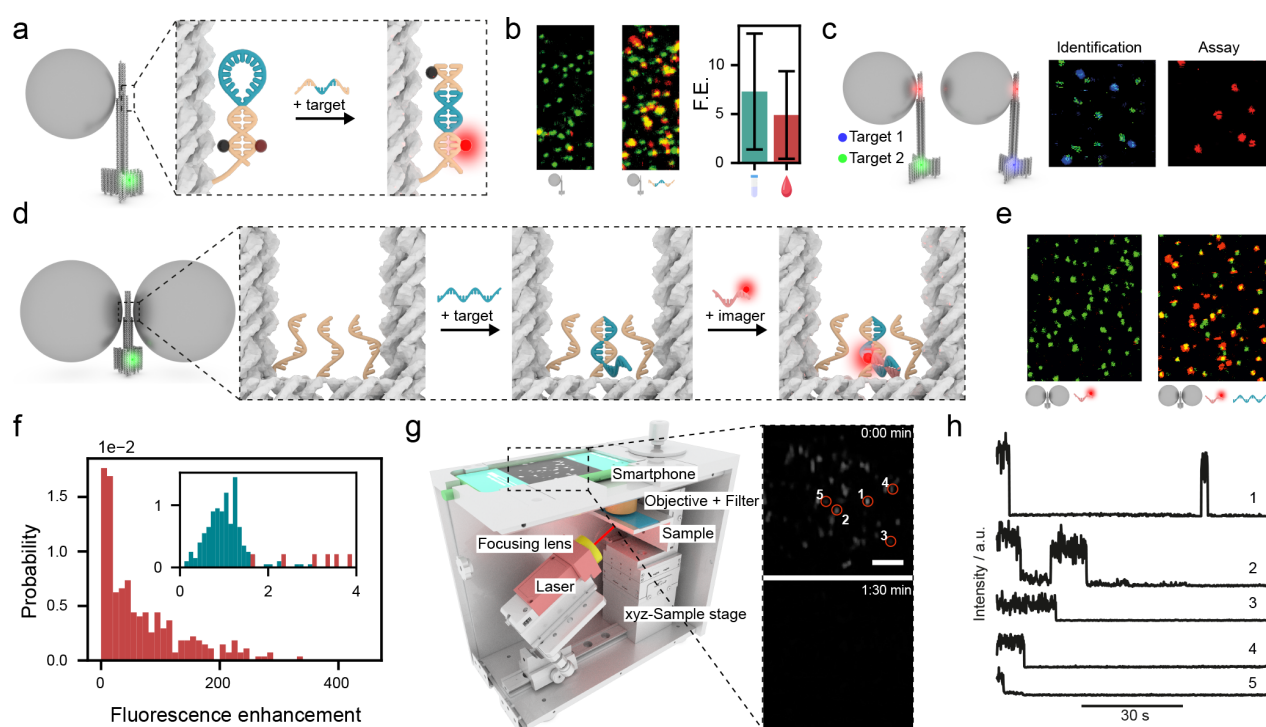


Figure 5. (a) Sketch of the FQH assay designed to detect DNA and RNA specific to the Zika virus.³ (b) Confocal fluorescence scans in heat-deactivated blood serum in the absence and presence of DNA specific to the Zika virus obtained for NA structures (DNA origami containing 80 nm AgNP) and corresponding FE that could be achieved in buffer as well as in blood serum.³ (c) Strategy to achieve multiplexing with NAs by barcoding the DNA origami structures with different dyes (left) and confocal fluorescence scans of the multiplexed detection of two different DNA targets (right).³ (d) Sketch of the sandwich binding assay in the hotspot of NACHOS designed to detect DNA specific to antibiotic-resistant bacteria.⁴ (e) Fluorescence scans of the sandwich binding assay in heat-deactivated blood serum in the absence and presence of the DNA target (left and right panels, respectively).⁴ (f) FE obtained in the sandwich binding assay with NACHOS in heat-deactivated blood serum.⁴ The inset shows the intensity distribution of single fluorophores, illustrating the power of NACHOS to distinguish the target-specific signal from SM impurities. (g) Home-built portable smartphone microscope used to detect single DNA molecules on a smartphone camera with the help of NACHOS (left) and snapshots of the movie obtained on the smartphone camera (right).⁴ (h) Fluorescence intensity vs time transients obtained in the sandwich detection assay (one to three dyes in the hotspot) extracted from the movie shown in g.⁴

nanoparticles in our DNA NAs is usually larger than 10 nm, with the potential to place biomolecular assays in the hotspot. DNA staple strands protruding from the DNA origami directly in the plasmonic hotspot can anchor biomolecular assays.

The first example of a diagnostic DNA NA comprised a pillar-shaped DNA origami (Figure 3b) containing a fluorescence-quenching hairpin (FQH) positioned near the 80 nm AgNP (Figure 5a). In the absence of the target molecule, the hairpin is in its closed state where the fluorescence of reporter dye ATTO647N is quenched by a BlackBerry quencher 650 (BBQ650). Upon binding of the target molecule (DNA or RNA specific to the Zika virus), the hairpin opened, separating the fluorophore and the quencher and generating a fluorescence signal which is amplified by the AgNP (Figure 5b, left). Using this AgNP NA, a specific DNA target could be detected not only in the buffer but also in heat-deactivated human serum with average FE values of 7.3 and 4.9, respectively (Figure 5b, right). Furthermore, by exploiting the modularity of DNA origami and additionally incorporating different fluorophores as barcodes in the base of the NA, two different DNA sequences could be detected simultaneously in one experiment (Figure 5c), demonstrating the multiplexing potential of this DNA NA approach.

One of the main limitations of this NA design (Figure 5a) for diagnostic applications was its moderate FE. Because of the

limited accessibility of the hotspot region (Figure 3a,b) and steric constraints imposed by the DNA origami, only monomer NAs could be obtained, limiting FE values to several fold (Figure 5c).

This motivated us to design NACHOS (Figure 3c), which are the next-generation NAs specifically designed for the incorporation of larger biomolecular assays.⁴ In contrast to previous NA designs, where the hotspot region is almost completely blocked by the DNA nanostructure (Figure 3a,b), the design used for NACHOS has the hotspot region cleared from DNA (Figure 3c). Even upon the binding of 100 nm NPs, different target molecules can access the plasmonic hotspot from above (Figure 3c). To avoid false positive events that we experienced in the hairpin assay due to dark-quencher bleaching,³⁷ we switched to a sandwich binding assay (Figure 5d) that was incorporated into the hotspot to detect a DNA fragment specific to OXA-48 (used for the diagnosis of an infection with antibiotic-resistant *Klebsiella pneumoniae*).^{55,56} Three 17-nucleotide-long capture strands complementary to a part of the target DNA were designed to protrude directly into the plasmonic hotspot of the NACHOS (Figure 5d). Binding of the target DNA sequence then provides an overhang for the 17-nt-long fluorophore-labeled imager strand to be incorporated directly into the plasmonic hotspot where the signal of the reporter dye is amplified by the NA.

In the base of NACHOS, we incorporated green dye ATTO542 to visualize colocalization with imager strands (red) that target detection (Figure 5d). DNA specific to OXA-48 was detected in buffer as well as in heat-deactivated blood serum (Figure 5e, right) with a very low extent (~2.5%) of false positive signal observed in the absence of the target (Figure 5e, left). Because of the successful formation of dimer NAs, FE reaching up to 461-fold (average of 89 ± 7 -fold) could be achieved for this diagnostic assay (Figure 5f), representing more than an order of magnitude improvement compared to the previous design discussed above. One advantage of using NACHOS in combination with the sandwich binding assay is that it allows for a clear differentiation between the amplified signal originating from specific target binding in the zL volume of the NA hotspot and the nonamplified signal from single fluorescent emitters (Figure 5f, inset on the right). This allows us to address one of the major challenges of SM diagnostics, that is, to distinguish positive signals from unavoidable impurities and nonspecific binding.

The high signal amplification provided by NACHOS also enabled us to demonstrate for the first time that single DNA targets can be detected on a portable smartphone microscope.⁴ The custom-built smartphone microscope contained a laser, cheap and nonspecialized low-NA optics, and a Huawei P20 smartphone for detection (Figure 5g). After showing that the FE is sufficient to enable the detection of single fluorophores on the smartphone camera, we also carried out the sandwich detection assay (Figure 5g) using this portable and power-bank-driven device. Fluorescence intensity vs time transients extracted from the smartphone movies demonstrated that the bleaching of one to three dyes incorporated in the hotspot NACHOS was detected on the smartphone camera (Figure 5h), highlighting the ability of the smartphone microscope in combination with NACHOS to provide analytical power comparable to conventional SM microscopy tools.

CONCLUSIONS AND OUTLOOK

Recent years saw the coming of age of DNA nanotechnology, and its impact on several disciplines has undoubtedly been outstanding. Specifically, the field of plasmonics has profited tremendously from the positioning capabilities of the DNA origami technique, with astonishing discoveries made by many groups around the world.^{57–61} In our line of work, we focused on harnessing the power of the approach for FE purposes. We have discovered several intricacies of the interplay between the plasmonic NPs and fluorophores which would have been difficult to address with any other approach. These mechanistic insights enabled us to build plasmonic NAs that can enhance the signals of single emitters by up to several hundred times and for the first time demonstrate that a single fluorophore could be “seen” simply with a smartphone camera. An exciting future direction could involve the use of these DNA NAs for SM detection on even cheaper and more miniaturized devices and their incorporation with high-throughput microfluidic and surface-spotting approaches. Moreover, one could also explore the advantages of other geometries of plasmonic nanostructures (e.g., Au or Ag nanorods which could lead to potentially even higher FEs).

Over the years, our efforts in using DNA NAs for diagnostic purposes have developed from a very basic proof-of-concept level³ toward a viable alternative or augmentation of other diagnostic assays.⁴ Early versions of our DNA NAs suffered from low dimer yields and very heterogeneous enhancement

profiles,¹ and although tremendous progress has been made in this regard, further improvements in this direction are necessary to use our NA assay not only in a qualitative “yes or no”-type manner but also to gain quantitative information about the analyte, as is needed in many diagnostic settings.⁵³ When it comes to the ultrasensitive detection of biomarkers, another consideration is that signal amplification might simply not be sufficient to detect targets at concentrations in the aM–fM range, and efficient approaches to capturing the few target copies present in milliliters of blood are also necessary.^{53,62} To diversify the range of targets that can be detected with DNA NAs, assays will be required to go beyond the detection of DNA and RNA.⁵³ We are currently exploring different approaches to how this could be implemented (e.g., by incorporating nanoswitches⁶³ in the hotspots of NAs for the specific detection of antibodies).

With our understanding of the control of DNA NAs, other ideas moved closer to the scope of reality. It has been anticipated that DNA NAs might have great use in biophysical experiments because of their ability to decrease the effective observation volume,⁶⁴ to increase the time resolution, and to increase the photostability of the fluorescent reporters.^{29,37,47,65} We have already shown that we can observe the switching of a DNA Holliday junction via FRET at extremely low excitation powers.¹ We also studied the effect of the plasmonic effect on the FRET process⁶⁶ and concluded that it should be possible to enhance the overall photon count rate of a FRET assay using DNA NAs. Ongoing work is focusing on exploring these directions with the aim of entering the lower microsecond time scales previously inaccessible to SM fluorescence imaging and providing new mechanistic insights on fast processes such as protein folding and the conformational dynamics of biomolecules.

AUTHOR INFORMATION

Corresponding Author

Philip Tinnefeld – Department of Chemistry and Center for NanoScience, Ludwig-Maximilians-Universität München, 81377 München, Germany; orcid.org/0000-0003-4290-7770; Email: philip.tinnefeld@cup.lmu.de

Authors

Viktorija Glembockyte – Department of Chemistry and Center for NanoScience, Ludwig-Maximilians-Universität München, 81377 München, Germany; orcid.org/0000-0003-2531-6506

Lennart Grabenhorst – Department of Chemistry and Center for NanoScience, Ludwig-Maximilians-Universität München, 81377 München, Germany; orcid.org/0000-0001-9503-1819

Kateryna Trofymchuk – Department of Chemistry and Center for NanoScience, Ludwig-Maximilians-Universität München, 81377 München, Germany; orcid.org/0000-0003-3453-1320

Complete contact information is available at: <https://pubs.acs.org/10.1021/acs.accounts.1c00307>

Author Contributions

†V.G., L.G., and K.T. contributed equally to this work.

Notes

The authors declare no competing financial interest.

Biographies

Viktorija Glembockyte is currently a Marie Skłodowska-Curie Research Fellow at Ludwig-Maximilians-Universität (LMU) München (Germany). She studied chemistry at Jacobs University Bremen (Germany) and obtained a Ph.D. in chemistry from McGill University (Canada) in 2017. In her current research, she combines the advantages of DNA nanotechnology and SM fluorescence imaging for the development of diagnostic tools and tunable biosensors.

Lennart Grabenhorst studied biochemistry in Göttingen (B.Sc.) and Braunschweig (M.Sc.) and is currently a Ph.D. student in Philip Tinnfeld's group at LMU Munich. His research interests include SM fluorescence spectroscopy, biophysics, DNA nanotechnology, and plasmonics.

Kateryna Trofymchuk is currently a postdoctoral researcher at LMU Munich (Germany). She studied physics at Taras Shevchenko National University of Kyiv (Ukraine) and obtained a Ph.D. in physics from University of Strasbourg (France) in 2016. Her current research is focused on combining the advantages of DNA nanotechnology and SM fluorescence imaging for the development of diagnostic tools.

Philip Tinnfeld has been a professor of physical chemistry at LMU since 2017. He studied chemistry at Münster and Heidelberg and received his Ph.D. from the University of Heidelberg in 2002. After postdoctoral work at UCLA (United States) and Leuven (Belgium) and habilitation in physics at Bielefeld University, he became associate professor of biophysics at LMU Munich. In 2010, he was appointed full professor of biophysical chemistry at TU Braunschweig. His research is inspired by our emerging abilities to study and build matter from the bottom up, starting from single molecules. He has contributed to breakthroughs of single-molecule superresolution microscopy, and he combined optical SM detection with DNA nanotechnology for self-assembled, functional devices including energy-transfer switches, calibration nanorulers, nanoadapters, fluorescence signal amplifiers, and molecular force clamps.

ACKNOWLEDGMENTS

P.T. gratefully acknowledges financial support from the DFG (TI 329/9-1, TI 329/9-2, INST 86/1904-1 FUGG, excellence clusters NIM, and e-conversion), Sino-German Center for Research Promotion (grant agreement C-0008), BMBF (grants POCEMON, 13N14336, and SIBOF, 03VP03891). V.G. acknowledges support from the European Union's Horizon 2020 research and innovation program under the Marie Skłodowska-Curie actions (grant agreement no. 840741). V.G. and K.T. acknowledge the support by Humboldt Research Fellowships from the Alexander von Humboldt Foundation.

REFERENCES

- (1) Acuna, G. P.; Möller, F. M.; Holzmeister, P.; Beater, S.; Lalkens, B.; Tinnfeld, P. Fluorescence Enhancement at Docking Sites of DNA-Directed Self-Assembled Nanoantennas. *Science* **2012**, *338*, 506–510.
- (2) Vietz, C.; Kaminska, I.; Sanz Paz, M.; Tinnfeld, P.; Acuna, G. P. Broadband Fluorescence Enhancement with Self-Assembled Silver Nanoparticle Optical Antennas. *ACS Nano* **2017**, *11*, 4969–4975.
- (3) Ochmann, S. E.; Vietz, C.; Trofymchuk, K.; Acuna, G. P.; Lalkens, B.; Tinnfeld, P. Optical Nanoantenna for Single Molecule-Based Detection of Zika Virus Nucleic Acids without Molecular Multiplication. *Anal. Chem.* **2017**, *89*, 13000–13007.
- (4) Trofymchuk, K.; Glembockyte, V.; Grabenhorst, L.; Steiner, F.; Vietz, C.; Close, C.; Pfeiffer, M.; Richter, L.; Schütte, M. L.; Selbach,

F.; Yaadav, R.; Zähringer, J.; Wei, Q.; Ozcan, A.; Lalkens, B.; Acuna, G. P.; Tinnfeld, P. Addressable nanoantennas with cleared hotspots for single-molecule detection on a portable smartphone microscope. *Nat. Commun.* **2021**, *12*, 950.

(5) Purcell, E. M. Spontaneous Emission Probabilities at Radio Frequencies. *Phys. Rev.* **1946**, *69*, 681.

(6) Drexhage, K. H. Influence of a dielectric interface on fluorescence decay time. *J. Lumin.* **1970**, *1–2*, 693–701.

(7) Bharadwaj, P.; Deutsch, B.; Novotny, L. Optical Antennas. *Adv. Opt. Photonics* **2009**, *1*, 438–483.

(8) Novotny, L.; van Hulst, N. Antennas for light. *Nat. Photonics* **2011**, *5*, 83–90.

(9) Kinkhabwala, A.; Yu, Z.; Fan, S.; Avlasevich, Y.; Müllen, K.; Moerner, W. E. Large single-molecule fluorescence enhancements produced by a bowtie nanoantenna. *Nat. Photonics* **2009**, *3*, 654–657.

(10) Anger, P.; Bharadwaj, P.; Novotny, L. Enhancement and Quenching of Single-Molecule Fluorescence. *Phys. Rev. Lett.* **2006**, *96*, 113002.

(11) Kühn, S.; Håkanson, U.; Rogobete, L.; Sandoghdar, V. Enhancement of Single-Molecule Fluorescence Using a Gold Nanoparticle as an Optical Nanoantenna. *Phys. Rev. Lett.* **2006**, *97*, 017402.

(12) Chhabra, R.; Sharma, J.; Wang, H.; Zou, S.; Lin, S.; Yan, H.; Lindsay, S.; Liu, Y. Distance-dependent interactions between gold nanoparticles and fluorescent molecules with DNA as tunable spacers. *Nanotechnology* **2009**, *20*, 485201.

(13) Busson, M. P.; Rolly, B.; Stout, B.; Bonod, N.; Bidault, S. Accelerated single photon emission from dye molecule-driven nanoantennas assembled on DNA. *Nat. Commun.* **2012**, *3*, 962.

(14) Rothemund, P. W. Folding DNA to create nanoscale shapes and patterns. *Nature* **2006**, *440*, 297–302.

(15) Douglas, S. M.; Dietz, H.; Liedl, T.; Högberg, B.; Graf, F.; Shih, W. M. Self-assembly of DNA into nanoscale three-dimensional shapes. *Nature* **2009**, *459*, 414–418.

(16) Fromm, D. P.; Sundaramurthy, A.; Schuck, P. J.; Kino, G.; Moerner, W. E. Gap-Dependent Optical Coupling of Single "Bowtie" Nanoantennas Resonant in the Visible. *Nano Lett.* **2004**, *4*, 957–961.

(17) Mirkin, C. A.; Letsinger, R. L.; Mucic, R. C.; Storhoff, J. J. A DNA-based method for rationally assembling nanoparticles into macroscopic materials. *Nature* **1996**, *382*, 607–609.

(18) Taminiau, T. H.; Stefani, F. D.; van Hulst, N. F. Single emitters coupled to plasmonic nano-antennas: angular emission and collection efficiency. *New J. Phys.* **2008**, *10*, 105005.

(19) Acuna, G. P.; Bucher, M.; Stein, I. H.; Steinhauer, C.; Kuzyk, A.; Holzmeister, P.; Schreiber, R.; Moroz, A.; Stefani, F. D.; Liedl, T.; Simmel, F. C.; Tinnfeld, P. Distance Dependence of Single-Fluorophore Quenching by Gold Nanoparticles Studied on DNA Origami. *ACS Nano* **2012**, *6*, 3189–3195.

(20) Persson, B. N. J.; Lang, N. D. Electron-hole-pair quenching of excited states near a metal. *Phys. Rev. B: Condens. Matter Mater. Phys.* **1982**, *26*, 5409–5415.

(21) Holzmeister, P.; Pibiri, E.; Schmied, J. J.; Sen, T.; Acuna, G. P.; Tinnfeld, P. Quantum yield and excitation rate of single molecules close to metallic nanostructures. *Nat. Commun.* **2014**, *5*, 5356.

(22) Möller, F. M.; Holzmeister, P.; Sen, T.; Acuna, G. P.; Tinnfeld, P. Angular modulation of single-molecule fluorescence by gold nanoparticles on DNA origami templates. *Nanophotonics* **2013**, *2*, 167–172.

(23) Stefani, F. D.; Vasilev, K.; Bocchio, N.; Gaul, F.; Pomozi, A.; Kreiter, M. Photonic mode density effects on single-molecule fluorescence blinking. *New J. Phys.* **2007**, *9*, 21–21.

(24) Hübner, K.; Pilo-Pais, M.; Selbach, F.; Liedl, T.; Tinnfeld, P.; Stefani, F. D.; Acuna, G. P. Directing Single-Molecule Emission with DNA Origami-Assembled Optical Antennas. *Nano Lett.* **2019**, *19*, 6629–6634.

(25) Taylor, A. B.; Zijlstra, P. Single-Molecule Plasmon Sensing: Current Status and Future Prospects. *ACS Sens* **2017**, *2*, 1103–1122.

- (26) Vietz, C.; Lalkens, B.; Acuna, G. P.; Tinnefeld, P. Functionalizing large nanoparticles for small gaps in dimer nanoantennas. *New J. Phys.* **2016**, *18*, 045012.
- (27) Puchkova, A.; Vietz, C.; Pibiri, E.; Wunsch, B.; Sanz Paz, M.; Acuna, G. P.; Tinnefeld, P. DNA Origami Nanoantennas with over 5000-fold Fluorescence Enhancement and Single-Molecule Detection at 25 μM . *Nano Lett.* **2015**, *15*, 8354–8359.
- (28) Lakowicz, J. R.; Fu, Y. Modification of single molecule fluorescence near metallic nanostructures. *Laser Photonics Rev.* **2009**, *3*, 221–232.
- (29) Pellegrotti, J. V.; Acuna, G. P.; Puchkova, A.; Holzmeister, P.; Gietl, A.; Lalkens, B.; Stefani, F. D.; Tinnefeld, P. Controlled reduction of photobleaching in DNA origami-gold nanoparticle hybrids. *Nano Lett.* **2014**, *14*, 2831–2836.
- (30) Li, K.; Stockman, M. I.; Bergman, D. J. Self-Similar Chain of Metal Nanospheres as an Efficient Nanolens. *Phys. Rev. Lett.* **2003**, *91*, 227402.
- (31) Schmied, J. J.; Forthmann, C.; Pibiri, E.; Lalkens, B.; Nickels, P.; Liedl, T.; Tinnefeld, P. DNA Origami Nanopillars as Standards for Three-Dimensional Superresolution Microscopy. *Nano Lett.* **2013**, *13*, 781–785.
- (32) Zhang, X.; Servos, M. R.; Liu, J. Instantaneous and Quantitative Functionalization of Gold Nanoparticles with Thiolated DNA Using a pH-Assisted and Surfactant-Free Route. *J. Am. Chem. Soc.* **2012**, *134*, 7266–7269.
- (33) Coronado, E. A.; Encina, E. R.; Stefani, F. D. Optical properties of metallic nanoparticles: manipulating light, heat and forces at the nanoscale. *Nanoscale* **2011**, *3*, 4042–4059.
- (34) Vietz, C.; Lalkens, B.; Acuna, G. P.; Tinnefeld, P. Synergistic Combination of Unquenching and Plasmonic Fluorescence Enhancement in Fluorogenic Nucleic Acid Hybridization Probes. *Nano Lett.* **2017**, *17*, 6496–6500.
- (35) Tian, L.; Wang, C.; Zhao, H.; Sun, F.; Dong, H.; Feng, K.; Wang, P.; He, G.; Li, G. Rational Approach to Plasmonic Dimers with Controlled Gap Distance, Symmetry, and Capability of Precisely Hosting Guest Molecules in Hotspot Regions. *J. Am. Chem. Soc.* **2021**, *143*, 8631–8638.
- (36) Yoon, J. H.; Selbach, F.; Langolf, L.; Schlücker, S. Ideal Dimers of Gold Nanospheres for Precision Plasmonics: Synthesis and Characterization at the Single-Particle Level for Identification of Higher Order Modes. *Small* **2018**, *14*, 1702754.
- (37) Grabenhorst, L.; Trofymchuk, K.; Steiner, F.; Glembockyte, V.; Tinnefeld, P. Fluorophore photostability and saturation in the hotspot of DNA origami nanoantennas. *Methods Appl. Fluoresc.* **2020**, *8*, 024003.
- (38) Holzmeister, P.; Acuna, G. P.; Grohmann, D.; Tinnefeld, P. Breaking the concentration limit of optical single-molecule detection. *Chem. Soc. Rev.* **2014**, *43*, 1014–1028.
- (39) Levene, M. J.; Korlach, J.; Turner, S. W.; Foquet, M.; Craighead, H. G.; Webb, W. W. Zero-Mode Waveguides for Single-Molecule Analysis at High Concentrations. *Science* **2003**, *299*, 682–686.
- (40) Punj, D.; Mivelle, M.; Moparthi, S. B.; van Zanten, T. S.; Rigneault, H.; van Hulst, N. F.; García-Parajó, M. F.; Wenger, J. A plasmonic ‘antenna-in-box’ platform for enhanced single-molecule analysis at micromolar concentrations. *Nat. Nanotechnol.* **2013**, *8*, 512–516.
- (41) Leslie, S. R.; Fields, A. P.; Cohen, A. E. Convex Lens-Induced Confinement for Imaging Single Molecules. *Anal. Chem.* **2010**, *82*, 6224–6229.
- (42) Vogelsang, J.; Doose, S.; Sauer, M.; Tinnefeld, P. Single-Molecule Fluorescence Resonance Energy Transfer in Nanopipets: Improving Distance Resolution and Concentration Range. *Anal. Chem.* **2007**, *79*, 7367–7375.
- (43) Schedlbauer, J.; Wilhelm, P.; Grabenhorst, L.; Federl, M. E.; Lalkens, B.; Hinderer, F.; Scherf, U.; Höger, S.; Tinnefeld, P.; Bange, S.; Vogelsang, J.; Lupton, J. M. Ultrafast Single-Molecule Fluorescence Measured by Femtosecond Double-Pulse Excitation Photon Antibunching. *Nano Lett.* **2020**, *20*, 1074–1079.
- (44) Wientjes, E.; Renger, J.; Cogdell, R.; van Hulst, N. F. Pushing the Photon Limit: Nanoantennas Increase Maximal Photon Stream and Total Photon Number. *J. Phys. Chem. Lett.* **2016**, *7*, 1604–1609.
- (45) Pacioni, N. L.; González-Béjar, M.; Alarcón, E.; McGilvray, K. L.; Scaiano, J. C. Surface Plasmons Control the Dynamics of Excited Triplet States in the Presence of Gold Nanoparticles. *J. Am. Chem. Soc.* **2010**, *132*, 6298–6299.
- (46) Kéna-Cohen, S.; Wiener, A.; Sivan, Y.; Stavrinou, P. N.; Bradley, D. D. C.; Horsfield, A.; Maier, S. A. Plasmonic Sinks for the Selective Removal of Long-Lived States. *ACS Nano* **2011**, *5*, 9958–9965.
- (47) Kaminska, I.; Vietz, C.; Cuartero-González, Á.; Tinnefeld, P.; Fernández-Domínguez, A. I.; Acuna, G. P. Strong plasmonic enhancement of single molecule photostability in silver dimer optical antennas. *Nanophotonics* **2018**, *7*, 643–649.
- (48) Campos, L. A.; Liu, J.; Wang, X.; Ramanathan, R.; English, D. S.; Munoz, V. A photoprotection strategy for microsecond-resolution single-molecule fluorescence spectroscopy. *Nat. Methods* **2011**, *8*, 143–146.
- (49) van der Velde, J. H. M.; Smit, J. H.; Hebisch, E.; Punter, M.; Cordes, T. Self-healing dyes for super-resolution fluorescence microscopy. *J. Phys. D: Appl. Phys.* **2019**, *52*, 034001.
- (50) Michie, M. S.; Gotz, R.; Franke, C.; Bowler, M.; Kumari, N.; Magidson, V.; Levitus, M.; Loncarek, J.; Sauer, M.; Schnermann, M. J. Cyanine Conformational Restraint in the Far-Red Range. *J. Am. Chem. Soc.* **2017**, *139*, 12406–12409.
- (51) Matikonda, S. S.; Hammersley, G.; Kumari, N.; Grabenhorst, L.; Glembockyte, V.; Tinnefeld, P.; Ivanic, J.; Levitus, M.; Schnermann, M. J. Impact of Cyanine Conformational Restraint in the Near-Infrared Range. *J. Org. Chem.* **2020**, *85*, S907–S915.
- (52) Chung, H. S.; Eaton, W. A. Protein folding transition path times from single molecule FRET. *Curr. Opin. Struct. Biol.* **2018**, *48*, 30–39.
- (53) Wu, Y.; Tilley, R. D.; Gooding, J. J. Challenges and Solutions in Developing Ultrasensitive Biosensors. *J. Am. Chem. Soc.* **2019**, *141*, 1162–1170.
- (54) Zang, F.; Su, Z.; Zhou, L.; Konduru, K.; Kaplan, G.; Chou, S. Y. Ultrasensitive Ebola Virus Antigen Sensing via 3D Nanoantenna Arrays. *Adv. Mater.* **2019**, *31*, 1902331.
- (55) Hrabak, J.; Chudackova, E.; Papagiannitsis, C. C. Detection of carbapenemases in Enterobacteriaceae: a challenge for diagnostic microbiological laboratories. *Clin. Microbiol. Infect.* **2014**, *20*, 839–853.
- (56) Poirel, L.; Héritier, C.; Tolün, V.; Nordmann, P. Emergence of oxacillinase-mediated resistance to imipenem in *Klebsiella pneumoniae*. *Antimicrob. Agents Chemother.* **2004**, *48*, 15–22.
- (57) Thacker, V. V.; Herrmann, L. O.; Sigle, D. O.; Zhang, T.; Liedl, T.; Baumberg, J. J.; Keyser, U. F. DNA origami based assembly of gold nanoparticle dimers for surface-enhanced Raman scattering. *Nat. Commun.* **2014**, *5*, 3448.
- (58) Kuzyk, A.; Schreiber, R.; Fan, Z.; Pardatscher, G.; Roller, E.-M.; Högele, A.; Simmel, F. C.; Govorov, A. O.; Liedl, T. DNA-based self-assembly of chiral plasmonic nanostructures with tailored optical response. *Nature* **2012**, *483*, 311–314.
- (59) Kuzyk, A.; Jungmann, R.; Acuna, G. P.; Liu, N. DNA Origami Route for Nanophotonics. *ACS Photonics* **2018**, *5*, 1151–1163.
- (60) Kuzyk, A.; Schreiber, R.; Zhang, H.; Govorov, A. O.; Liedl, T.; Liu, N. Reconfigurable 3D plasmonic metamolecules. *Nat. Mater.* **2014**, *13*, 862–866.
- (61) Prinz, J.; Schreiber, B.; Olejko, L.; Oertel, J.; Rackwitz, J.; Keller, A.; Bald, I. DNA Origami Substrates for Highly Sensitive Surface-Enhanced Raman Scattering. *J. Phys. Chem. Lett.* **2013**, *4*, 4140–4145.
- (62) Rissin, D. M.; Kan, C. W.; Campbell, T. G.; Howes, S. C.; Fournier, D. R.; Song, L.; Piech, T.; Patel, P. P.; Chang, L.; Rivnak, A. J.; Ferrell, E. P.; Randall, J. D.; Provuncher, G. K.; Walt, D. R.; Duffy, D. C. Single-molecule enzyme-linked immunosorbent assay detects serum proteins at subfemtomolar concentrations. *Nat. Biotechnol.* **2010**, *28*, 595–599.

(63) Ranallo, S.; Rossetti, M.; Plaxco, K. W.; Vallée-Bélisle, A.; Ricci, F. A Modular, DNA-Based Beacon for Single-Step Fluorescence Detection of Antibodies and Other Proteins. *Angew. Chem., Int. Ed.* **2015**, *54*, 13214–13218.

(64) Peng, S.; Wang, W.; Chen, C. Breaking the Concentration Barrier for Single-Molecule Fluorescence Measurements. *Chem. - Eur. J.* **2018**, *24*, 1002–1009.

(65) Chikkaraddy, R.; de Nijs, B.; Benz, F.; Barrow, S. J.; Scherman, O. A.; Rosta, E.; Demetriadou, A.; Fox, P.; Hess, O.; Baumberg, J. J. Single-molecule strong coupling at room temperature in plasmonic nanocavities. *Nature* **2016**, *535*, 127–130.

(66) Bohlen, J.; Cuartero-González, Á.; Pibiri, E.; Ruhlandt, D.; Fernández-Domínguez, A. I.; Tinnefeld, P.; Acuna, G. P. Plasmon-assisted Förster resonance energy transfer at the single-molecule level in the moderate quenching regime. *Nanoscale* **2019**, *11*, 7674–7681.

Recommended by ACS

Gold Nanorod DNA Origami Antennas for 3 Orders of Magnitude Fluorescence Enhancement in NIR

Kateryna Trofymchuk, Philip Tinnefeld, *et al.*

JANUARY 03, 2023
ACS NANO

READ 

Plasmon-Enhanced Fluorescence of Single Quantum Dots Immobilized in Optically Coupled Aluminum Nanoholes

Yupeng Yang, Shi-Li Zhang, *et al.*

FEBRUARY 27, 2023
THE JOURNAL OF PHYSICAL CHEMISTRY LETTERS

READ 

Hybrid Plasmonic Nanostructures for Enhanced Single-Molecule Detection Sensitivity

Ediz Kaan Herkert, Maria F. Garcia-Parajo, *et al.*

APRIL 03, 2023
ACS NANO

READ 

Engineering Plasmon-Enhanced Fluorescent Gold Nanoclusters Using Bovine Serum Albumin as a Novel Separation Layer for Improved Selectivity

Hongyu Chen, Chao Lu, *et al.*

NOVEMBER 16, 2022
ANALYTICAL CHEMISTRY

READ 

Get More Suggestions >

Associated Publication 2

Addressable nanoantennas with cleared hotspots for single-molecule detection on a portable smartphone microscope













Kateryna Trofymchuk*, Viktorija Glembockyte*, [Lennart Grabenhorst](#), Florian Steiner, Carolin Vietz, Cindy Close, Martina Pfeiffer, Lars Richter, Max L. Schütte, Florian Selbach, Renukka Yaadav, Jonas Zähringer, Qingshan Wei, Aydogan Ozcan, Birka Lalkens, Guillermo P. Acuna and Philip Tinnefeld

*equal contribution

Nature Communications **12**, 950 (2021). doi: 10.1038/s41467-021-21238-9

(open access)

Addressable nanoantennas with cleared hotspots for single-molecule detection on a portable smartphone microscope

Kateryna Trofymchuk ^{1,2,7}✉, Viktorija Glembockyte ^{1,7}✉, Lennart Grabenhorst ¹, Florian Steiner ¹, Carolin Vietz ², Cindy Close¹, Martina Pfeiffer¹, Lars Richter ², Max L. Schütte², Florian Selbach ¹, Renukka Yaadav ¹, Jonas Zähringer ¹, Qingshan Wei ³, Aydogan Ozcan⁴, Birka Lalkens⁵, Guillermo P. Acuna ⁶✉ & Philip Tinnefeld ¹✉

The advent of highly sensitive photodetectors and the development of photostabilization strategies made detecting the fluorescence of single molecules a routine task in many labs around the world. However, to this day, this process requires cost-intensive optical instruments due to the truly nanoscopic signal of a single emitter. Simplifying single-molecule detection would enable many exciting applications, e.g., in point-of-care diagnostic settings, where costly equipment would be prohibitive. Here, we introduce addressable NanoAntennas with Cleared HOtSpots (NACHOS) that are scaffolded by DNA origami nanostructures and can be specifically tailored for the incorporation of bioassays. Single emitters placed in NACHOS emit up to 461-fold (average of 89 ± 7 -fold) brighter enabling their detection with a customary smartphone camera and an 8-US-dollar objective lens. To prove the applicability of our system, we built a portable, battery-powered smartphone microscope and successfully carried out an exemplary single-molecule detection assay for DNA specific to antibiotic-resistant *Klebsiella pneumonia* on the road.

¹Department of Chemistry and Center for NanoScience, Ludwig-Maximilians-Universität München, München, Germany. ²Institute for Physical and Theoretical Chemistry - NanoBioScience and Braunschweig Integrated Centre of Systems Biology (BRICS), Technische Universität Braunschweig, Braunschweig, Germany. ³Department of Chemical and Biomolecular Engineering, North Carolina State University, Raleigh, NC, USA. ⁴Electrical & Computer Engineering Department, Bioengineering Department, California NanoSystems Institute (CNSI), and Department of Surgery, University of California, Los Angeles, CA, USA. ⁵Institut für Halbleitertechnik, Laboratory for Emerging Nanometrology LENA, TU Braunschweig, Langer Kamp 6a/b, Braunschweig, Germany. ⁶Département de Physique - Photonic Nanosystems, Université de Fribourg - Faculté des Sciences et Médecine, Fribourg, Switzerland. ⁷These authors contributed equally: Kateryna Trofymchuk and Viktorija Glembockyte. ✉email: kateryna.trofymchuk@cup.lmu.de; viktorija.glembockyte@cup.lmu.de; guillermo.acuna@unifr.ch; philip.tinnefeld@cup.lmu.de

Early detection of disease biomarkers generally requires high sensitivity enabled by molecular amplification mechanisms^{1–5} or physical signal enhancement of commonly used fluorescence signals^{6–9}. Physical fluorescence signal enhancement could enable sensitivity improvement, detection of single molecules on cost-effective and mobile devices and therefore help to distinguish specific signals against an unavoidable background of impurities even in low-resource settings. Fluorescence from emitters such as fluorescent dyes can be enhanced using plasmonic nanoantennas^{10–12}, and the challenge of placing quantum emitters in their hotspots was overcome using DNA origami as constructing material^{13,14}. The immense requirements for small, defined and rigid gaps between the gold or silver nanoparticles forming the gap in the nanoantenna aggravated the usability of the space between the nanoparticles for a biosensing assay. While it was demonstrated that incorporation of a fluorescence quenched hairpin in a nanoantenna hotspot allowed for the specific detection of DNA specific to Zika virus, the limited accessibility of the hotspot and the steric constraints imposed by the DNA origami nanopillar, the capturing strands and the nanoparticles only allowed for the binding of a single nanoparticle (monomer antenna) strongly reducing the achievable enhancement values (average of 7.3)¹⁵. These moderate fluorescence enhancement values were not sufficient for detecting single fluorescence molecules with low numerical aperture (NA) optics. For example, our previous work on benchmarking the sensitivity of smartphone-based detection systems suggested that a signal equivalent to at least 16 single emitters is required for detection on a smartphone-based low-NA microscope¹⁶. Therefore, a diagnostic single-molecule assay fully exploiting the signal amplification potential of DNA origami nanoantennas has not been presented to date and remained highly desirable to enable detection of single molecules with affordable low-NA optics.

In this work, we introduce NanoAntennas with Cleared HOtSpots (NACHOS) that enable high fluorescence signal amplification and are fully addressable, i.e., new analytes can be introduced into the confined regions of dimer nanoantennas. We use these NACHOS for a single-molecule diagnostic assay on a portable and inexpensive smartphone microscope.

Results

Design and fluorescence enhancement of NACHOS. A novel three-dimensional DNA origami structure was designed (Fig. 1a) and folded from an M13mp18-derived scaffold strand and complementary staple strands (Supplementary Tables 1–3). The NACHOS origami design uses two pillars to attach silver nanoparticles and creates the plasmonic hotspot at the bifurcation in the gap between the two pillars and the nanoparticles (see DNA origami sketches in Fig. 1a and full NACHOS structure in Fig. 1b and Fig. 1c). Thus, the space of the hotspot, i.e., between the nanoparticles is left free for placing baits and for binding targets as needed for nucleic acid bioassays. For immobilization, the DNA origami structure is equipped with a rigid cross-like shaped base (approximately 35 nm by 33 nm, Supplementary Figs. 1 and 2) that contains six biotin-modified staple strands (Supplementary Table 3) used for immobilization on BSA-biotin coated coverslips via biotin-NeutrAvidin interactions (Fig. 1b). The two pillars of the DNA origami structure (total height ~83 nm) each contain six protruding staple strands (A_{20} , Supplementary Table 3) which provide anchor points for binding DNA (T_{20})-functionalized 100 nm silver nanoparticles (Fig. 1b). The estimated distance between the nanoparticles is ~12 nm. A transmission electron microscopy (TEM) image of an exemplary nanoantenna produced via solution synthesis is shown in Fig. 1c (see Materials and Methods section for details on magnetic bead-

based solution synthesis). We evaluated the signal amplification that can be achieved in this DNA origami nanoantenna design by incorporating an Alexa Fluor 647-labeled DNA staple strand (Supplementary Table 3) directly into the plasmonic hotspot of the nanoantenna. Single-molecule fluorescence transients of the dye (Fig. 1d, Supplementary Fig. 3) were recorded on a confocal microscope for the DNA origami sample without nanoparticles (orange) as well as for NACHOS containing two 100 nm silver nanoparticles attached to the DNA origami after immobilization on the coverslip (blue, see Materials and Methods section for NACHOS synthesis on the coverslip). Single-step photobleaching in the intensity versus time transients (Fig. 1c) confirms that the detected signal originates from a single fluorescent molecule. Further analysis of single-molecule transients demonstrates that the signal-to-background ratio (SBR) could be significantly improved by the nanoantenna (361 ± 35) when compared to the reference structure (7.4 ± 0.9). The fluorescence enhancement obtained for each nanoantenna was calculated by comparing the intensity of Alexa Fluor 647 in the NACHOS to the mean intensity of Alexa Fluor 647 in the reference structure without nanoparticles. Fluorescence enhancement values of up to 417-fold (average of 74 ± 3 -fold) could be achieved in the new nanoantenna design (Fig. 1e). The broad fluorescence enhancement distribution reflects some heterogeneity with regard to nanoparticle size, shape and orientation, and also includes a subpopulation of monomer nanoantennas. Care was taken that all fluorescent molecules incorporated in the DNA origami nanoantennas were included in the analysis to obtain a representative distribution of fluorescence enhancement values in Fig. 1e. Most importantly, we note that increasing the accessibility of the hotspot region did not compromise the fluorescence enhancement values which are slightly higher than previously reported values for more compact nanoantenna designs^{14,17,18}.

Amplified single-molecule detection of DNA with NACHOS.

To utilize the plasmonic hotspot for single-molecule diagnostics we designed a sandwich binding assay capable of detecting a DNA fragment specific to OXA-48, which is the gene that codes for carbapenemase and is used for the diagnosis of an antibiotic resistant *Klebsiella pneumoniae* infection^{19,20}. Three capture strands specific to the target DNA (Supplementary Table 4) were incorporated, protruding directly into the plasmonic hotspot of the NACHOS. The rationale of using three capturing strands was to optimize the probability of each DNA origami having binding strands accessible to capture the target²¹. The principle of this assay is illustrated in Fig. 2a: a 17-nt long capture strand is complementary to one half of the 34-nt long target DNA strand. Binding of the target DNA sequence then provides an overhang for the 17-nt long dye-labeled imager strand to be incorporated directly in the plasmonic hotspot where the signal of the reporter dye is amplified by the nanoantenna. In addition, the DNA origami structure is labeled with a single ATTO 542 dye close to the base.

Surface scans before incubation with the target and imager strands show green fluorescent spots that represent single NACHOS (Fig. 2b, Supplementary Fig. 4). After incubating (2 h at 37 °C) the NACHOS with the target DNA sequence (2 nM, Supplementary Table 4) as well as with the Alexa Fluor 647-labeled imager strand (6 nM, Supplementary Table 4), the presence of the target DNA could be detected and quantified by counting the number of colocalized green (ATTO 542) and red (Alexa Fluor 647) spots in confocal fluorescence scans (Fig. 2c, Supplementary Fig. 4). Although 2 h were used for the assay, we note that significant binding of target sequence in the hotspot of NACHOS was already achieved after 15 min of incubation at

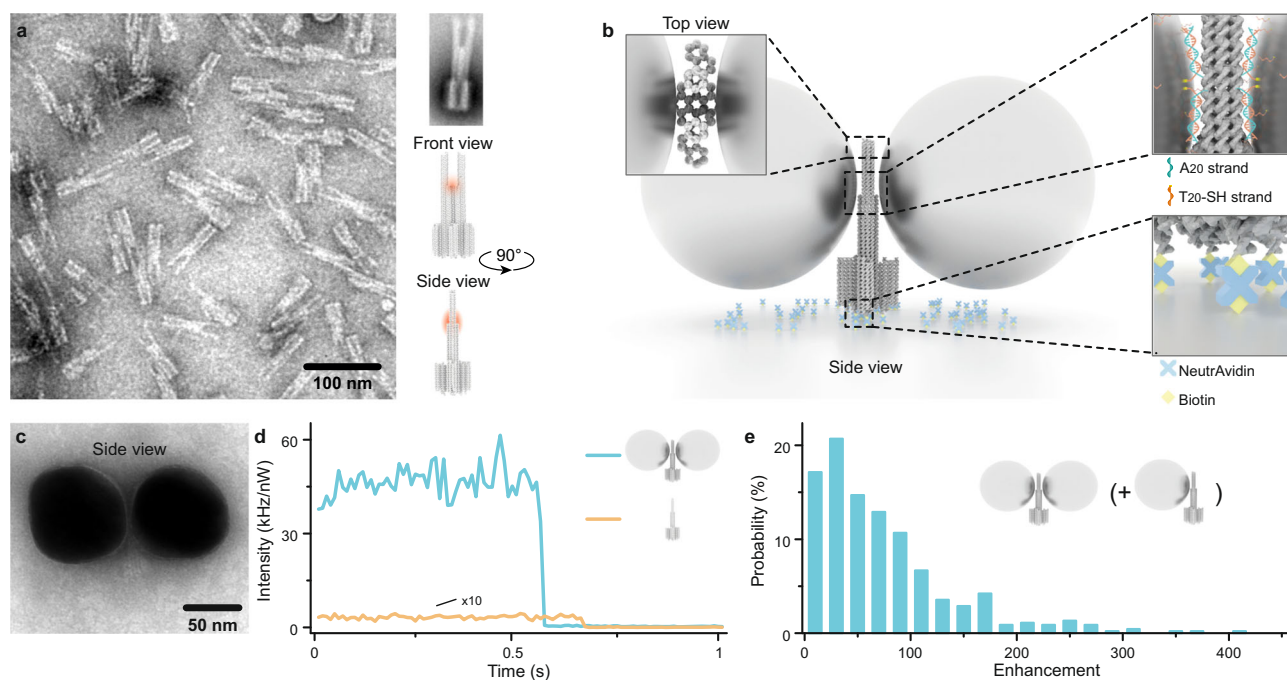


Fig. 1 Concept of the DNA origami nanoantenna with a cleared hotspot. **a** TEM image (left, reproduced at least 3 times) and sketches (right) of the DNA origami structure used for the nanoantenna assembly with the position of the plasmonic hotspot indicated in red. A representative class averaged TEM image of the DNA origami used is shown on the upper right. **b** Schematics of NACHOS assembly: the DNA origami construct is bound to the BSA-biotin coated surface via biotin-NeutrAvidin interactions, thiolated DNA-functionalized 100 nm silver particles are attached to the DNA origami nanoantenna via polyadenine (A₂₀) binding strands in the zipper-like geometry to minimize the distance between the origami and the nanoparticles³⁰. **c** TEM image of a NACHOS with 100 nm silver nanoparticles (reproduced at least 3 times). **d** Single-molecule fluorescence intensity transients, measured by confocal microscopy, normalized to the same excitation power of a single Alexa Fluor 647 dye incorporated in a DNA origami (orange) and in a DNA origami nanoantenna with two 100 nm silver nanoparticles (blue) excited at 639 nm. **e** Fluorescence enhancement distribution of Alexa Fluor 647 measured in NACHOS with 100 nm silver nanoparticles. A total number of 164 and 449 single molecules in the reference (more examples are provided in Supplementary Fig. 3) and NACHOS structures were analyzed, respectively.

37 °C (Supplementary Fig. 5). When the nanoantennas were incubated with the imager strand only (Fig. 2d, f, and Supplementary Fig. 4), very few co-localized spots were observed. This control demonstrated a low fraction (~2.5%) of false positive signals. Incubation of NACHOS with 34-nt long target sequence containing 1-nt, 2-nt and 3-nt mismatches in the target region led to a drop in the number of co-localized spots (Supplementary Fig. 6), indicating a certain degree of selectivity in this assay, which potentially can be further improved by optimizing the sequence and length of the DNA capture strand.

Next, we studied the fluorescence enhancement that could be achieved in this single-molecule DNA diagnostics assay (Fig. 2e). Fluorescence enhancement values were calculated by comparing the intensity of Alexa Fluor 647 in NACHOS that contained only one dye incorporated in the hotspot (i.e., displayed single-step bleaching events in fluorescence transients) to the intensity of single Alexa Fluor 647 dyes incorporated in the reference structure without nanoparticles. As shown in Fig. 2e, fluorescence enhancement values of up to 461-fold (average 89 ± 7 -fold) could be achieved representing more than an order of magnitude improvement compared to previous DNA nanoantennas specific to Zika virus¹⁵. One major advantage of using NACHOS for the sandwich binding assay is that only the signal originating from the specific binding to the target sequence in the zeptoliter volume of the nanoantenna hotspot is amplified. In contrast, any signal originating from non-specific binding of the imager strand to the DNA origami scaffold or the surface of the glass coverslip is not amplified. The clear differentiation between single-molecule emission amplified by the nanoantenna and the one observed from single fluorescent molecules is illustrated in the inset of Fig. 2e.

We quantified the efficiency of the sandwich binding assay in the reference DNA origami structure without nanoparticles as well as in NACHOS containing 100 nm silver nanoparticles by calculating the fraction of DNA origami structures containing the target and imager (% colocalization of green and red spots, Fig. 2f). Binding efficiencies of 66% and 84% were measured in NACHOS (light blue) and in the reference structures (orange), respectively, confirming that the hotspot accessibility for the target DNA sequence is not significantly compromised by attaching two 100 nm silver nanoparticles. We note that ~10 % higher imager binding yield was observed for the reference structure in the presence as well as in the absence of the target strand, which we attribute to higher non-specific sticking of the imager to the reference structure. We hypothesize this non-specific sticking is related to the single-stranded DNA for nanoparticle binding as unspecific binding is reduced after incorporation of two silver nanoparticles in the full nanoantenna construct (Fig. 2f).

To quantify the number of target molecules incorporated in each nanoantenna hotspot, we performed a single-molecule fluorescence photobleaching analysis (Fig. 2g) which allowed us to determine the number of Alexa Fluor 647 imager strands per DNA origami structure by counting the photobleaching steps in single-molecule fluorescence transients (Supplementary Fig. 7). The majority (~60%) of NACHOS contained one imager strand incorporated in the hotspot, one third of nanoantennas contained two imager strands, while three imager strands were observed in ~8–11% of single-molecule transients. The distribution of bleaching steps obtained for NACHOS as well as for the reference structures (Fig. 2g) further supports the observation that the

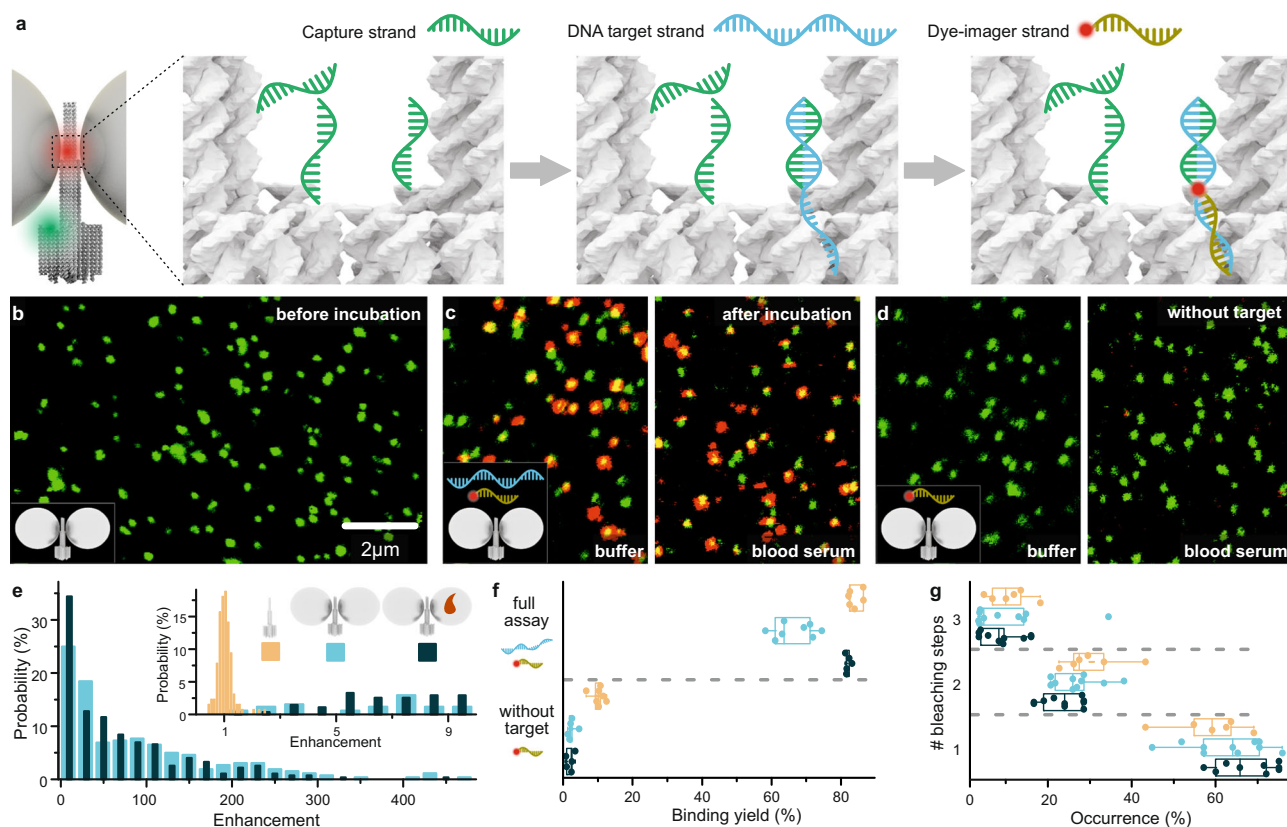


Fig. 2 Single-molecule diagnostic assay with NACHOS. **a** Sketch of NACHOS with three capture strands in the hotspot and a green reference dye (ATTO 542) for labeling of the DNA origami. Capture strands are placed in the NACHOS hotspot region. Upon incubation, they hybridize with DNA target strands specific to *Klebsiella pneumoniae*, exposing a specific, 17-nt long region for the hybridization with the imager strand labeled with Alexa Fluor 647. **b** Confocal fluorescence image of the NACHOS before incubation with DNA target and imager strands. **c** Confocal fluorescence images after incubation with DNA target (2 nM) and imager strands (6 nM) in buffer solution (left) and blood serum (right), scale same as in panel **b**; **d** Confocal fluorescence image of the NACHOS after incubation with only the DNA imager strand (6 nM) in buffer solution (left) and blood serum (right), scale same as in panel **b**. The scans in panels **b**–**d** are representative for at least 20 images. **e** Fluorescence enhancement histogram of the sandwich assay in NACHOS measured in buffer solution (light blue) as well as in blood serum (dark blue). The inset includes a zoom into the enhancement histogram overlaid with an enhancement histogram obtained for non-enhanced single Alexa Fluor 647 dyes (orange). Between 127 and 273 NACHOS and reference structures were analyzed in buffer solution and blood serum, respectively. **f** Binding yield obtained for the full sandwich assay (2 nM target and 6 nM imager strands) and for the control experiment (imager strand only) without nanoparticles (orange) as well as with nanoparticles in buffer solution (light blue) and in blood serum (dark blue). At least 546 spots were analyzed out of at least 5 different areas for each sample. Alexa Fluor 647 was excited at 639 nm and ATTO 542 at 532 nm. **g** Distribution of fluorescence bleaching steps observed in fluorescence transients for NACHOS in buffer solution and in blood serum and reference structures. Over 240 structures from at least 6 different areas per sample were analyzed. The box plots in panels **f** and **g** show the 25/75 percentiles and the whisker represents the 1.5*IQR (inter quartile range) length, the center lines represent the average values.

presence of silver nanoparticles does not obstruct the hotspot accessibility for the DNA target.

Single-molecule detection in human blood serum. To demonstrate that NACHOS can still function in complex biological fluids that compromise many diagnostic assays, we have also performed the sandwich detection assay described above in human blood serum spiked with the target DNA sequence specific to the *OXA-48* gene. The serum was first heat-inactivated and then enriched with 2 nM target DNA sequence as well as 6 nM Alexa Fluor 647 imager strand. The fully assembled NACHOS were then incubated in the serum mixture for 2 h at 37 °C. Fluorescence scans of the NACHOS after incubation with serum and target DNA sequence are included in Fig. 2c, d (as well as Supplementary Fig. 8). Almost identical fluorescence enhancement values (Fig. 2e), target binding efficiencies (Fig. 2f) and number of single-molecule photobleaching steps (Fig. 2g) were obtained for reference and NACHOS samples in highly purified buffer (light blue) and serum (dark blue) conditions

confirming that neither the stability of NACHOS nor the performance of the sandwich assay in NACHOS are compromised. On the contrary, fluorescence enhancement values reaching 457-fold (average of 70 ± 4) could be achieved for the DNA detection assay in target spiked human serum. These findings proof the robustness of NACHOS under realistic assay conditions and provide an important stepping stone towards diagnostic applications.

Single-molecule detection on a portable microscope using NACHOS. Recently, the detection of only 10–16 ATTO 542 molecules was demonstrated using a simple table top setup with a monochrome smartphone camera as detector and a consumer product lens for light collection¹⁶. This inspired us that single-molecule detection might be possible on a portable smartphone microscope with non-specialized low-NA optics^{2,22–24} (see Fig. 3a, b). The microscope uses the monochrome camera of a Huawei P20 smartphone for detection, data processing and interfacing and a battery-driven 638 nm excitation laser with

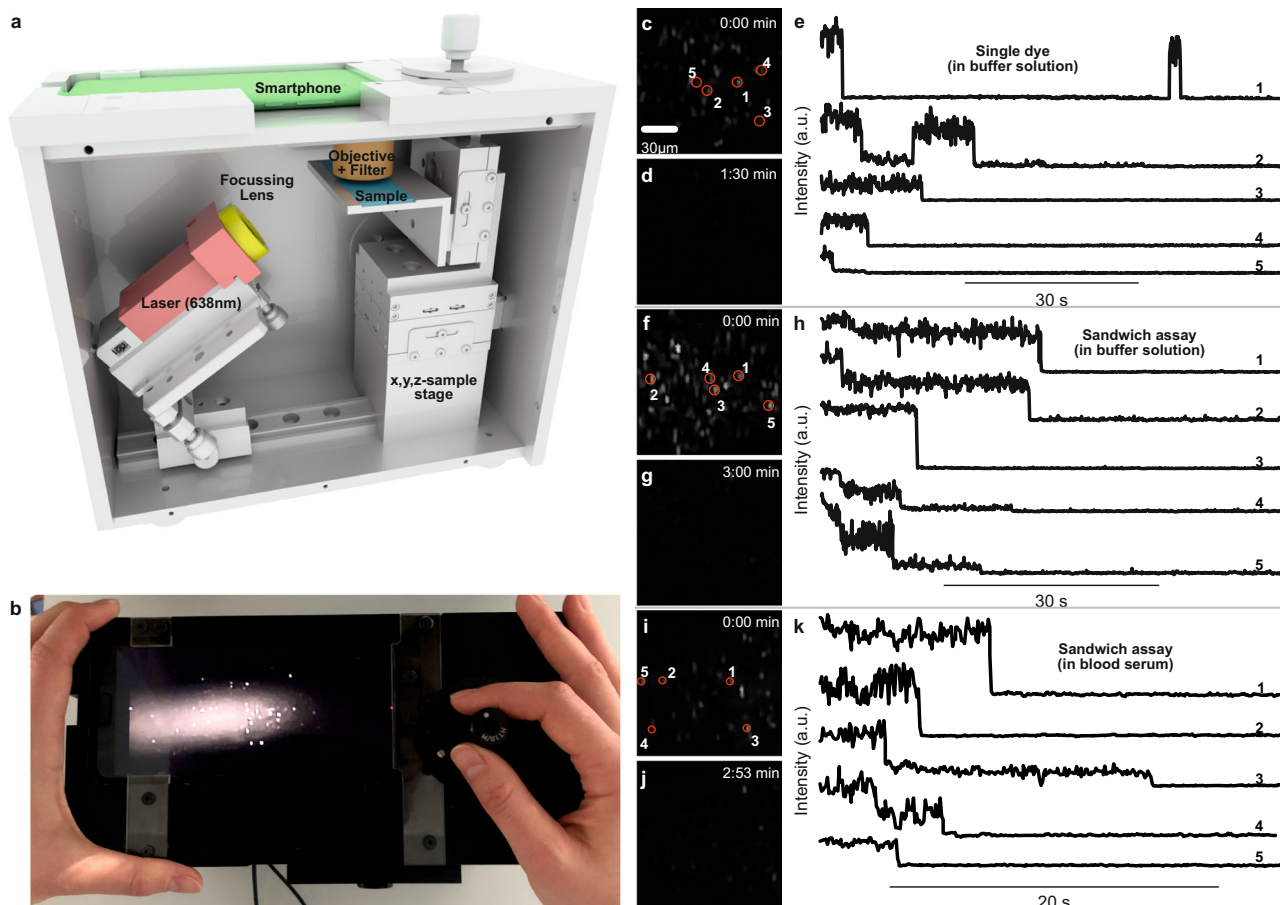


Fig. 3 Single-molecule detection on a portable smartphone microscope. **a** Sketch of the portable smartphone microscope with the battery driven 638 nm laser (red), the focusing lens ($f = 5$ cm) (yellow), the microscope coverslip with the sample (blue), the objective lens and the emission filter (brown), and the smartphone monochrome camera as detector (green). **b** Top view photograph of the portable smartphone microscope. **c** Background corrected fluorescence image of NACHOS with 100 nm silver nanoparticles and a single Alexa Fluor 647 dye. **d** Fluorescence image as in **c** after illumination for 1:30 min. **e** Exemplary fluorescence transients of a single Alexa Fluor 647 in NACHOS measured on the portable microscope setup. Single bleaching steps of dyes and long-time blinking events are visible. **f** Background corrected fluorescence image of NACHOS equipped with a sandwich assay with 100 nm silver nanoparticles and Alexa Fluor 647 imager strands. **g** Fluorescence image as in **f** after illumination of the area for 3:00 min. **h** Exemplary fluorescence transients of Alexa Fluor 647 in a three-capture-strand DNA origami nanoantenna measured on the portable smartphone microscope. **i** Background corrected fluorescence image of NACHOS equipped with the sandwich assay with 100 nm silver nanoparticles and Alexa Fluor 647 imager strands after incubation in blood serum. **j** Fluorescence image as in **i** after illumination of the area for 2:53 min. **k** Exemplary fluorescence transients of Alexa Fluor 647 in a three-capture-strand NACHOS measured on the portable smartphone microscope. Fluorescence transients with one, two, and three bleaching steps (analogous to single-molecule confocal measurements) were observed. The movies represented in the panels **c**, **d**, **f**, **g**, **i** and **j** were reproduced at least 5 times. Three movies for each measurement are provided in the Supplementary Movies. The fluorescence transients shown in panels **e**, **h** and **k** were extracted from a single movie.

180 mW output power. The excitation laser (red in Fig. 3a) is focused on the sample plane at approximately 45° using a lens with a focal length of 5 cm to illuminate an elliptical area of $\sim 150 \times 200 \mu\text{m}^2$. Fluorescence emission is collected and collimated with a consumer product lens ($\text{NA} = 0.25$, 8 US\$, yielding a resolution of $\sim 1.2 \mu\text{m}$ in the red wavelength range), bandpass filtered and focused onto the smartphone detector using the internal lens in the infinite focal distance mode. A discussion of the total price of the components used in the prototype smartphone microscope (sum of ~ 4200 €) can be found in Supplementary Note 1. We envision that the price can be reduced in the case of upscaling production (<1000 €). Importantly, the affordable microscope does not imply expensive sample preparation. The single-molecule nature of measurements requires substantial dilution of the DNA origami samples and DNA functionalized nanoparticles yielding an estimated price per NACHOS coverslip preparation of below 5 € (Supplementary Note 2).

First, we prepared NACHOS with 100 nm silver nanoparticles and a single Alexa Fluor 647 dye in the hotspot. Considering the low resolution of the smartphone microscope, the concentration of NACHOS on the surface was adjusted to a reasonably low density to ensure that only one nanoantenna is present per diffraction limited spot (see Materials and Methods section). To improve the photostability of Alexa Fluor 647 and demonstrate single-molecule bleaching steps, the measurements were carried out in a reducing and oxidizing system (ROXS)^{25,26} with enzymatic oxygen removal. Upon illumination, multiple bright spots were observed on the smartphone screen (Fig. 3c). In the movies recorded with 80 ms per frame, slow single-molecule blinking and bleaching (Supplementary Fig. 9) was observed (see Supplementary Movies 1–3) as indicated by the disappearance of spots over time (compare Fig. 3c, d). Extracted fluorescence transients (spots from one movie) are shown in Fig. 3e, demonstrating typical single-molecule behavior with

blinking and single-step bleaching events. These transients represent the first examples of single-molecule fluorescence detection with a portable smartphone microscope and non-dedicated optics bringing single-molecule detection a step closer to point-of-care settings. The signal-to-background ratio (SBR) and the signal-to-noise ratio (SNR) of the transients on the smartphone microscope are determined to be 25 ± 2 and 3.8 ± 0.2 , respectively. Examples of fast blinking of single ATTO 647N dyes in the hotspot of NACHOS with 100 nm silver nanoparticles can be found in Supplementary Movie 4 and Supplementary Fig. 10.

Next, we tested whether the portable smartphone microscope could also be used for the detection of single DNA molecules in analogy to the sandwich assay discussed in Fig. 2. The sandwich assay with three capture strands for the detection of the resistance gene *OXA-48* imaged with the portable smartphone microscope is shown in Fig. 3f. All fluorescence spots acquired on the smartphone camera were photobleached after 3 min of movie recording (see Supplementary Movies 5–7). The extracted transients (Fig. 3h) exhibit bleaching of the imager strands with 1–3 bleaching steps in accordance with the single-molecule fluorescence transients acquired on the confocal microscope shown in Supplementary Fig. 7. More examples of extracted transients for the sandwich assay with three binding strands in the NACHOS hotspot are included in Supplementary Fig. 12. In control measurements under identical conditions leaving out the nanoparticles, no signal could be detected. As a further control, we incubated the coverslips with silver nanoparticles only. A few dim spots that did not disappear after long illumination are ascribed to scattering from silver nanoparticle aggregates (Supplementary Fig. 11). These results confirm that single-molecule detection of disease-specific DNA can also be performed on our portable smartphone microscope omitting the need for advanced and expensive microscopes. Finally, the DNA detection assay after incubation with human blood serum was also measured on the portable smartphone microscope. Images at the beginning as well as at the end of the movie and exemplary fluorescence transients are shown in Fig. 3i, j, k. The results are almost identical to the measurements in purified buffer solution (Fig. 3f–h) with a decreasing number of isolated fluorescent spots detected on the camera (Fig. 3i, j) due to photobleaching. In a similar way the fluorescent transients (Fig. 3k) show clear single, double and triple bleaching steps with no difference visible between the purified buffer and the blood serum assays. More example movies and transients for the measurements of the sandwich assay inside the NACHOS are shown in Supplementary Movies 8–10 and Supplementary Fig. 13. The photobleaching analysis for the transients from the movie taken on the smartphone microscope is shown in Supplementary Fig. 14 and yields similar distributions for single, double and triple photobleaching steps as compared to the data shown in Fig. 2g, highlighting the ability of the smartphone microscope in combination with NACHOS to provide analytical power comparable to conventional single-molecule microscopy tools.

Self-assembled nanoantennas with a cleared and addressable hotspot represent an inexpensive and versatile platform for fluorescence signal enhancement assays. Single fluorescent molecules immobilized in the hotspot of these newly designed nanoantennas yield higher fluorescence enhancement values than previous approaches with hotspots blocked by the DNA origami nanostructure. NACHOS are robust (see Supplementary Fig. 15 for single-molecule data of a similar sample measured over 13 weeks), stable in complex biological fluids such as human serum, and importantly, the accessibility of the hotspot for target DNA molecules and imagers is not impaired despite the constricted dimensions. A single-molecule sandwich assay with three capturing strands shows equally high fluorescence

enhancement as direct incorporation of a single fluorescent dye in the hotspot and enables single-molecule detection with amplified signal that facilitates discrimination of single-molecule binding events against an unavoidable background of single-molecule impurities (Fig. 2e inset). The demonstration of single-molecule assays on a simple battery-operated smartphone microscope makes DNA origami nanoantennas a stepping-stone for democratizing single-molecule detection with cost-effective and mobile devices relevant for point-of-care applications.

Methods

DNA origami. DNA origami structures were designed in *cadNano*²⁷ and assembled and purified using protocols inspired by Wagenbauer et al.²⁸. Briefly, 25 μ L of p8064 scaffold (produced in-house) at 100 nM were mixed with 18 μ L of unmodified staples pooled from 100 μ M original concentration and 2 μ L of modified staples, pooled from 100 μ M original concentration. All staples were purchased from Eurofins Genomics GmbH (Germany) - for the exact sequences see Supplementary Table 2. 5 μ L of folding buffer (200 mM MgCl₂, 50 mM Tris, 50 mM NaCl, 10 mM EDTA) were added and the mixture was subjected to a thermal annealing ramp (see Supplementary Table 1). Samples were purified using 100 kDa MWCO Amicon Ultra filters (Merck KGaA, Germany) with 4 washing steps with a lower ionic strength buffer (5 mM MgCl₂, 5 mM Tris, 5 mM NaCl, 1 mM EDTA) for 8 mins at 8 krcf, 20 °C.

Functionalization of silver nanoparticles. 100 nm silver nanoparticles (100 nm BioPure Silver Nanospheres (Citrate), nanoComposix, USA) were functionalized with T₂₀ single-stranded DNA oligonucleotides with a thiol modification at the 3'-end (Ella Biotech GmbH, Germany)¹⁵. Briefly, 2 mL of 0.025 mg/mL nanoparticle solution in ultra pure water was heated to 40 °C under permanent stirring. 20 μ L of 10 % Tween 20 and 20 μ L of a potassium phosphate buffer (4:5 mixture of 1 M monobasic and dibasic potassium phosphate, Sigma Aldrich, USA) were added as well as 10 μ L of a 2 nmol thiol-modified single-stranded DNA solution (5'-T₂₀-SH-3') and incubated for 1 h at 40 °C. A salting procedure was then carried out by adding 1 \times PBS buffer containing 3.3 M NaCl stepwise over 45 min to the heated and stirred solution, until a final concentration of 750 mM NaCl was reached. Afterwards, the particles were mixed 1:1 with 1 \times PBS 10 mM NaCl, 2.11 mM P8709 buffer (Sigma Aldrich, USA), 2.89 mM P8584 buffer (Sigma Aldrich, USA), 0.01 % Tween[®] 20 and 1 mM EDTA. To remove the excess thiolated single-stranded DNA, the solution was centrifuged for 15 min at 2.8 krcf and 20 °C. A pellet was formed in which the particles were concentrated. The supernatant was discarded, and the washing step was repeated six more times. After functionalization of the silver nanoparticles were diluted in 1 \times TE buffer (10 mM Tris, 1 mM EDTA) containing 750 mM NaCl to reach the final extinction of 0.05 (0.1 mm path length) at the extinction maxima on a UV-Vis spectrometer (Nanodrop 2000, Thermo Fisher Scientific, USA).

Solution synthesis of DNA origami nanoantennas for TEM imaging. To obtain DNA origami nanoantennas in solution, the structures were initially assembled on streptavidin-coated magnetic beads (Dynabeads[™] MyOne[™] Streptavidin C1, 1 μ m diameter, 10 mg/mL, Thermo Fischer Scientific, USA). **Preparation of magnetic beads:** 3.0 μ L of bead stock solution (~20–30 $\times 10^6$ beads) were washed three times with 50 μ L 1 \times B&W buffer (0.5 mM EDTA, 5 mM Tris-HCl (pH = 8), 1 M NaCl, 0.001 % v/v Tween[®] 20). After removing the supernatant, the beads were diluted in 6.0 μ L 1 \times B&W and incubated with 6.0 μ L of 4 μ M biotinylated ssDNA (mag1, Supplementary Table 5) for 20 min at room temperature. The functionalized beads were purified from excess of ssDNA by placing the tube on a magnet and discarding the supernatant. The beads were redispersed in 50 μ L 1 \times B&W and washed with 1 \times B&W buffer (3 \times 50 μ L). **Immobilization of DNA Origami on Magnetic Beads:** DNA origami (100 μ L, 200 pM in 1 \times B&W buffer) with three ssDNA overhang strands on a bottom partially complementary to the sequence on the magnetic beads (mag2, Supplementary Table 5) were incubated together for 2 h at 37 °C under gentle shaking (450 rpm, Eppendorf ThermoMixer[®] C, Eppendorf AG, Germany). Unbound DNA origami was removed by placing the tube on a magnet and discarding the supernatant. The beads were redispersed in 50 μ L 1 \times B&W and washed with 1 \times B&W buffer (5 \times 50 μ L). **Binding of 100 nm silver nanoparticles:** Nanoantennas were fabricated on magnetic beads by hybridizing with DNA functionalized (5'-T₂₀-SH-3') 100 nm silver nanoparticles to the DNA origamis. For this the supernatant of the with DNA origami coated beads was removed and incubated with 100 μ L of 100 nm silver nanoparticles solution using an excess of five nanoparticles per binding site. During the first three hours of incubation, the solution was mixed every 30 min by gentle pipetting. After overnight incubation at room temperature, the excess of nanoparticles was removed by placing the tube on a magnet and discarding the supernatant. The beads were re-dissolved in 50 μ L 1 \times B&W and washed with 1 \times B&W buffer (5 \times 50 μ L). **Cleavage of the assembled structures:** Nanoantennas were cleaved from the beads surface by performing a toehold-mediated strand displacement reaction. For cleavage, the supernatant of

the bead solution was removed and nanoantennas coated beads were incubated with 20 μ L 10 μ M of the displacement strand (mag3, Supplementary Table 5) for 4 h at room temperature. Unbound DNA origami nanoantennas were recovered for further use by placing the tube on a magnet.

Transmission electron microscopy (TEM) measurements. TEM grids (Formvar/carbon, 400 mesh, Cu, TedPella, Inc., USA) were Ar-plasma cleaned and incubated for 60 s with DNA origami sample (5 μ L, ~ 2–10 nM). Grids were washed with 2 % uranyl formate solution (5 μ L) and incubated again afterwards again 4 s with 2 % uranyl formate solution (5 μ L) for staining. TEM imaging were performed on a JEM-1100 microscope (JEOL GmbH, Japan) with an acceleration voltage of 80 kV.

Sample preparation on the coverslip for single-molecule confocal measurements. Microscope coverslips of 24 mm \times 60 mm size and 170 μ m thickness (Carl Roth GmbH, Germany) were cleaned with UV-Ozone cleaner (PSD-UV4, Novascan Technologies, USA) for 30 min at 100 °C. Adhesive SecureSeal™ Hybridization Chambers (2.6 mm depth, Grace Bio-Labs, USA) were glued on the clean coverslips. The created wells were washed three times with PBS buffer and then incubated with BSA-biotin (0.5 mg/mL, Sigma-Aldrich, USA) and NeutrAvidin (0.2 mg/mL, Thermo Fisher Scientific, USA). The DNA origami (50–100 pM in 1 \times TE buffer containing 750 mM NaCl) was immobilized on the biotin-NeutrAvidin surfaces using covalently attached biotin modifications on the six staple strands on the base. Density of DNA origami nanoantennas on the surface suitable for single-molecule measurements was checked on a microscope. The binding of silver nanoparticles was then performed by incubating the surfaces with 100 μ L of T₂₀-functionalized silver nanoparticles in 1 \times TE buffer containing 2 M NaCl overnight at room temperature. To prevent the evaporation of samples, samples were kept in a sealed humidity chambers during the incubation. The nanoantennas were then imaged in 1 \times TE buffer containing 14 mM MgCl₂.

Diagnostic sandwich assay. To specifically detect the DNA sequence specific to the OXA-48 gene carrying the antibiotic resistance^{19,20}, DNA origami nanoantennas were folded containing three specific capture strands (Supplementary Table 4) extruding from the hotspot region of the nanoantenna. After the assembly of the full nanoantenna in the analogous way to the previous section, the samples were incubated with 2 nM target DNA sequence (34 nt) specific to the OXA-48 gene (Supplementary Table 4) as well as 6 nM Alexa Fluor 647 imager strand (17 nt) labeled with Alexa Fluor 647 (Supplementary Table 4) in 1 \times TE buffer containing 2 M NaCl. The sample was incubated for at 37 °C for 2 h and the excess of the target and imager strands was removed by washing six times with 1 \times TE buffer containing 2 M NaCl. The nanoantennas were then imaged in 1 \times TE buffer containing 14 mM MgCl₂.

For the sandwich assay in serum clotted, whole blood, sterile and filtered human blood serum (Human Serum, (from male AB clotted whole blood), USA origin, sterile-filtered, Sigma-Aldrich, USA) was used. Before adding the serum to the NACHOS and reference samples, the serum was heat inactivated by exposing it for 30 min to 56 °C and spiked with 2 nM target DNA, 6 nM imager strand and 2 M NaCl. The fully assembled NACHOS or reference DNA origami structures were incubated with target-spiked blood serum for 2 h at 37 °C and the excess of target and imager strands was removed by washing six times with 1 \times TE buffer containing 2 M NaCl. NACHOS were then imaged in 1 \times TE buffer containing 14 mM MgCl₂.

Confocal measurements and data analysis. Confocal fluorescence measurements were performed using a home-built confocal setup based on an inverted microscope (IX-83, Olympus Corporation, Japan) and a 78 MHz-pulsed supercontinuum white light laser (SuperK Extreme EXW-12, NKT Photonics A/S, Denmark) with selected wavelengths of 532 nm and 639 nm. The wavelengths are selected via an acousto-optically tunable filter (AOTF, SuperK Dual AOTF, NKT Photonics A/S, Denmark). This is controlled by a digital controller (AODS 20160 8 R, Crystal Technology, USA) via a computer software (AODS 20160 Control Panel, Crystal Technology, Inc., USA). A second AOTF (AA.AOTF.ns: TN, AA Opto-Electronic, France) was used to alternate 532 nm and 639 nm wavelengths if required, as well as to further spectrally clean the laser beam. It is controlled via home-made LabVIEW software (National Instruments, USA). A neutral density filter was used to regulate the laser intensity, followed by a linear polarizer and a $\lambda/4$ plate to achieve circularly polarized excitation. A dichroic beam splitter (ZT532/640rpc, Chroma Technology, USA) and an immersion oil objective (UPlanSApo 100 \times , NA = 1.4, WD = 0.12 mm, Olympus Corporation, Japan) were used to focus the excitation laser onto the sample. Micropositioning was performed using a Piezo-Stage (P-517.3CL, E-501.00, Physik Instrumente GmbH&Co. KG, Germany). The excitation powers at 639 nm were set to 200 nW or for 500 nW for the reference samples and to 50 nW for the NACHOS for the recording of the fluorescence transients. These powers were chosen to ensure that the samples are excited in the linear regime and to avoid saturation in the nanoantenna hotspot²⁹. For the confocal scans, 2 μ W at 532 nm and 2 μ W and 500 nW at 639 nm were used for the reference and NACHOS samples, respectively. Emitted light was then collected using the same objective and filtered from the excitation light by the dichroic beam splitter. The

light was later focused on a 50 μ m pinhole (Linus AG, Germany) and detected using avalanche photodiodes (SPCM, AQR 14, PerkinElmer, Inc., USA) registered by an TCSPC system (HydraHarp 400, PicoQuant GmbH, Germany) after additional spectral filtering (RazorEdge 647, Semrock Inc., USA for the red channel and BrightLine HC 582/75, Semrock Inc., USA for the green channel). A custom-made LabVIEW software (National Instruments, USA) was used to process the acquired raw data. Background correction was made individually for each transient. The extracted data were analyzed in OriginPro2016.

Sample preparation for single-molecule measurements on the smartphone microscope. The geometry of the smartphone-based microscope required samples to be sealed. To this end, microscope cover slides of 22 mm \times 22 mm size and 170 μ m thickness (Carl Roth GmbH, Germany) were cleaned with UV-Ozone cleaner (PSD-UV4, Novascan Technologies, USA) for 30 min at 100 °C. After this a home-made silicon mask with an opening around 15 mm \times 15 mm was glued on a coverslip to create an incubation chamber. Surface functionalization, DNA origami immobilization (5 - 10 pM), nanoantenna formation, and the sandwich sensing assay were performed the same as as described above for the NACHOS assembly on coverslips. To seal the samples, the silicon mask was removed, and a double-sided tape was glued on both sides of the cover slide. Then the cover slides were covered with 76 mm \times 26 mm microscope slides (1 mm thickness, Carl Roth GmbH, Germany) which were priority cleaned with UV-Ozone cleaner for 30 min at 100 °C. Due to limited photostability of Alexa Fluor 647, samples containing the sandwich assay were imaged in the presence of ROXS photostabilization system. A reducing and oxidizing buffer system with enzymatic oxygen removal consisting of 90 % buffer A (14 mM MgCl₂, 50 mM Tris, 2 mM Trolox/Troloxquinone and 1 % w/v Glucose) and 10 % buffer B (glucose oxidase (1 mg/mL), 0.4 % (v/v) catalase (50 μ g/mL), 30 % glycerol, 12.5 mM KCl) was used. After this the chambers were sealed with nail polish and imaged after the drying of the glue.

Single-molecule measurements and analysis on the smartphone. Single-molecule measurements on the smartphone were performed using a home-built portable box. The 638 nm laser diode (0638L-11A, Integrated Optics, UAB, Lithuania) with an output power 180 mW that can be driven by various (portable) voltage sources (Power plug, mobile power bank, (rechargeable) batteries) was focused ($f = 50$ mm) in 45° angle onto the sample. The fluorescence of the molecules was collected using an objective lens (NA = 0.25, LS-40166, UCTRONICS, USA) guiding the light to the monochrome camera of the smartphone (P20, Huawei, China) after spectral filtering (BrightLine HC 731/137, Semrock Inc., USA). Movies were recorded via FreeDCam application and analyzed with ImageJ (FIJI) equipped with FFMPEG plugin using a home written macro to convert MP4 format of the acquired movies to a TIFF format and find the single-molecule signals and extract the fluorescence intensity as a function of illumination time. The extracted data were analyzed in OriginPro2016.

Reporting summary. Further information on research design is available in the Nature Research Reporting Summary linked to this article.

Data availability

The raw data acquired in this study are available in a public Zenodo repository (DOI: 10.5281/zenodo.4384169). This includes TEM images, raw and analyzed confocal data, raw movies acquired on the smartphone device, as well as the caDNAo file for the DNA origami nanostructure reported in this work. Further information is available from the authors upon request.

Code availability

A custom script used to analyze the movies obtained on the smartphone device is available in the Zenodo repository under DOI: 10.5281/zenodo.4384169.

Received: 12 October 2020; Accepted: 13 January 2021;

Published online: 11 February 2021

References

1. Gill, P. & Ghaemi, A. Nucleic acid isothermal amplification technologies: a review. *Nucleosides Nucleotides Nucleic Acids* **27**, 224–243 (2008).
2. Diederich, B., Then, P., Jügler, A., Förster, R. & Heintzmann, R. cellSTORM-Cost-effective super-resolution on a cellphone using dSTORM. *PLoS ONE* **14**, e0209827–e0209827 (2019).
3. Gu, L. et al. Research progress on rolling circle amplification (RCA)-based biomedical sensing. *Pharmaceuticals* **11**, 35 (2018).
4. Fakrudin, M. et al. Nucleic acid amplification: alternative methods of polymerase chain reaction. *J. Pharm. Bioallied. Sci.* **5**, 245–252 (2013).
5. Kühnemund, M. et al. Targeted DNA sequencing and in situ mutation analysis using mobile phone microscopy. *Nat. Commun.* **8**, 13913 (2017).

6. Taylor, A. B. & Zijlstra, P. Single-molecule plasmon sensing: current status and future prospects. *ACS Sens.* **2**, 1103–1122 (2017).
7. Walt, D. R. Optical methods for single molecule detection and analysis. *Anal. Chem.* **85**, 1258–1263 (2013).
8. Li, J.-F., Li, C.-Y. & Aroca, R. F. Plasmon-enhanced fluorescence spectroscopy. *Chem. Soc. Rev.* **46**, 3962–3979 (2017).
9. Bauch, M., Toma, K., Toma, M., Zhang, Q. & Dostalek, J. Plasmon-enhanced fluorescence biosensors: a review. *Plasmonics* **9**, 781–799 (2014).
10. Punj, D. et al. A plasmonic ‘antenna-in-box’ platform for enhanced single-molecule analysis at micromolar concentrations. *Nat. Nanotechnol.* **8**, 512–516 (2013).
11. Anger, P., Bharadwaj, P. & Novotny, L. Enhancement and quenching of single-molecule fluorescence. *Phys. Rev. Lett.* **96**, 113002 (2006).
12. Curto, A. G. et al. Unidirectional emission of a quantum dot coupled to a nanoantenna. *Science* **329**, 930–933 (2010).
13. Rothmund, P. W. K. Folding DNA to create nanoscale shapes and patterns. *Nature* **440**, 297–302 (2006).
14. Acuna, G. P. et al. Fluorescence enhancement at docking sites of DNA-directed self-assembled nanoantennas. *Science* **338**, 506–510 (2012).
15. Ochmann, S. E. et al. Optical nanoantenna for single molecule-based detection of zika virus nucleic acids without molecular multiplication. *Anal. Chem.* **89**, 13000–13007 (2017).
16. Vietz, C. et al. Benchmarking smartphone fluorescence-based microscopy with DNA origami nanobeads: reducing the gap toward single-molecule sensitivity. *ACS Omega* **4**, 637–642 (2019).
17. Puchkova, A. et al. DNA origami nanoantennas with over 5000-fold fluorescence enhancement and single-molecule detection at 25 nm. *Nano Lett.* **15**, 8354 (2015).
18. Vietz, C., Lalkens, B., Acuna, G. P. & Tinnefeld, P. Synergistic combination of unquenching and plasmonic fluorescence enhancement in fluorogenic nucleic acid hybridization probes. *Nano Lett.* **17**, 6496 (2017).
19. Hrabak, J., Chudackova, E. & Papagiannitsis, C. C. Detection of carbapenemases in Enterobacteriaceae: a challenge for diagnostic microbiological laboratories. *Clin. Microbiol. Infect.* **20**, 839–853 (2014).
20. Poirel, L., Héritier, C., Toliun, V. & Nordmann, P. Emergence of oxacillinase-mediated resistance to imipenem in *Klebsiella pneumoniae*. *Antimicrob. Agents Chemother.* **48**, 15–22 (2004).
21. Strauss, M. T., Schueder, F., Haas, D., Nickels, P. C. & Jungmann, R. Quantifying absolute addressability in DNA origami with molecular resolution. *Nat. Commun.* **9**, 1600 (2018).
22. Wei, Q. et al. Fluorescent imaging of single nanoparticles and viruses on a smart phone. *ACS Nano* **7**, 9147–9155 (2013).
23. Wei, Q. et al. Imaging and sizing of single DNA molecules on a mobile phone. *ACS Nano* **8**, 12725–12733 (2014).
24. Ozcan, A. Mobile phones democratize and cultivate next-generation imaging, diagnostics and measurement tools. *Lab Chip* **14**, 3187–3194 (2014).
25. Vogelsang, J. et al. A reducing and oxidizing system minimizes photobleaching and blinking of fluorescent dyes. *Angew. Chem. Int. Ed.* **47**, 5465–5469 (2008).
26. Ha, T. & Tinnefeld, P. Photophysics of fluorescent probes for single-molecule biophysics and super-resolution imaging. *Annu. Rev. Phys. Chem.* **63**, 595–617 (2012).
27. Douglas, S. M. et al. Rapid prototyping of 3D DNA-origami shapes with caDNAo. *Nucleic Acids Res.* **37**, 5001–5006 (2009).
28. Wagenbauer, K. F. et al. How we make DNA origami. *ChemBioChem* **18**, 1873–1885 (2017).
29. Grabenhorst, L., Trofymchuk, K., Steiner, F., Glembockyte, V. & Tinnefeld, P. Fluorophore photostability and saturation in the hotspot of DNA origami nanoantennas. *Methods Appl. Fluoresc.* **8**, 024003 (2020).
30. Vietz, C., Lalkens, B., Acuna, G. P. & Tinnefeld, P. Functionalizing large nanoparticles for small gaps in dimer nanoantennas. *N. J. Phys.* **18**, 045012 (2016).

Acknowledgements

The authors thank Vivien Behrendt and Benedikt Hauer (Fraunhofer-Institut für Physikalische Messtechnik IPM, Freiburg, Germany) for cooperation on the assay development and Prof. Tim Liedl/Prof. Joachim Rädler (Ludwig-Maximilians-Universität,

Department für Physik, Munich, Germany) for providing access to their facilities especially to the transmission electron microscope. The authors thank Tomas Giscius for manufacturing the portable smartphone microscope. P.T. gratefully acknowledges financial support from the DFG (INST 86/1904-1 FUGG, excellence clusters NIM and e-conversion), BMBF (Grants POCEMON, 13N14336, and SIBOF, 03VP03891), and the European Union’s Horizon 2020 research and innovation program under grant agreement No. 737089 (Chipscope). G.P.A. gratefully acknowledges support by the Swiss National Science Foundation through the National Center of Competence in Research Bio-Inspired Materials and through grant number 200021_184687. V.G. and K.T. acknowledge the support by Humboldt Research Fellowships from the Alexander von Humboldt Foundation. A.O. acknowledges the support of NSF PATHS-UP and HHMI. BL acknowledges funding by the Deutsche Forschungsgemeinschaft (DFG, German Research Foundation) under Germany’s Excellence Strategy – EXC-2123 QuantumFrontiers – 390837967 and “Niedersächsisches Vorab” through “Quantum- and Nano-Metrology (QUANOMET)” initiative within the project NL-1.

Author contributions

P.T., A.O. and G.P.A. conceived the project, L.G. and B.L. developed the DNA origami structure, K.T., V.G. and M.P. optimized the solution synthesis procedure, F.Se. performed the TEM measurements, K.T., V.G., C.C., M.P. and R.Y. developed the sandwich assay and prepared samples, performed and analyzed the measurements on the confocal microscope, C.V., L.R., M.L.S., Q.W., A.O. and G.P.A. worked on an earlier version of the smartphone microscope, K.T., V.G., F.St. and J.Z. constructed the portable smartphone microscope, K.T., V.G. and F.St. performed and analyzed the measurements on the smartphone microscope, K.T., V.G., L.G., F.St. and P.T. wrote the manuscript. All authors have read and approved the final manuscript.

Funding

Open Access funding enabled and organized by Projekt DEAL.

Competing interests

P.T. and G.P.A. are inventors on an awarded patent of the described bottom-up method for fluorescence enhancement in molecular assays, EP1260316.1, 2012, US20130252825 A1. The remaining authors declare no competing interests.

Additional information

Supplementary information The online version contains supplementary material available at <https://doi.org/10.1038/s41467-021-21238-9>.

Correspondence and requests for materials should be addressed to K.T., V.G., G.P.A. or P.T.

Peer review information *Nature Communications* thanks the anonymous reviewer(s) for their contribution to the peer review of this work. Peer reviewer reports are available.

Reprints and permission information is available at <http://www.nature.com/reprints>

Publisher’s note Springer Nature remains neutral with regard to jurisdictional claims in published maps and institutional affiliations.



Open Access This article is licensed under a Creative Commons Attribution 4.0 International License, which permits use, sharing, adaptation, distribution and reproduction in any medium or format, as long as you give appropriate credit to the original author(s) and the source, provide a link to the Creative Commons license, and indicate if changes were made. The images or other third party material in this article are included in the article’s Creative Commons license, unless indicated otherwise in a credit line to the material. If material is not included in the article’s Creative Commons license and your intended use is not permitted by statutory regulation or exceeds the permitted use, you will need to obtain permission directly from the copyright holder. To view a copy of this license, visit <http://creativecommons.org/licenses/by/4.0/>.

© The Author(s) 2021

Supporting Information for

Addressable Nanoantennas with Cleared Hotspots for Single-Molecule Detection on a Portable Smartphone Microscope

Kateryna Trofymchuk^{1,2†*}, Viktorija Glembockyte^{1†*}, Lennart Grabenhorst¹, Florian Steiner¹, Carolin Vietz², Cindy Close¹, Martina Pfeiffer¹, Lars Richter², Max L. Schütte², Florian Selbach¹, Renukka Yaadav¹, Jonas Zähringer¹, Qingshan Wei³, Aydogan Ozcan⁴, Birka Lalkens⁵, Guillermo P. Acuna^{6*}, and Philip Tinnefeld^{1*}

¹ Department of Chemistry and Center for NanoScience, Ludwig-Maximilians-Universität München, Butenandtstr. 5-13, 81377 München, Germany

² Institute for Physical and Theoretical Chemistry - NanoBioScience and Braunschweig Integrated Centre of Systems Biology (BRICS), Technische Universität Braunschweig, Braunschweig, Germany

³ Department of Chemical and Biomolecular Engineering, North Carolina State University, Raleigh, NC, 27695, United States

⁴ Electrical & Computer Engineering Department, Bioengineering Department, California NanoSystems Institute (CNSI), and Department of Surgery, University of California, Los Angeles, California 90095, United States

⁵ Institut für Halbleitertechnik, Laboratory for Emerging Nanometrology LENA, TU Braunschweig, Langer Kamp 6a/b, 38106 Braunschweig, Germany

⁶ Département de Physique - Photonic Nanosystems, Université de Fribourg - Faculté des Sciences et Médecine Chemin de Musée 3, CH-1700 Fribourg, Switzerland

† These authors contributed equally: Kateryna Trofymchuk, Viktorija Glembockyte

* email: kateryna.trofymchuk@cup.lmu.de; viktorija.glembockyte@cup.lmu.de; guillermo.acuna@unifr.ch; philip.tinnefeld@cup.uni-muenchen.de

Table of contents

Supplementary Table 1. Temperature ramp used for folding DNA origami nanostructures	3
Supplementary Table 2. Unmodified staple strands used to fold the DNA origami nanostructures	4
Supplementary Table 3. Modified staple strands used for the immobilization of the DNA origami structure, nanoparticle binding and fluorescence labelling	9
Supplementary Table 4. Modified staple strands used for the sandwich detection assay	10
Supplementary Table 5. Modified staple strands used for solution synthesis of NACHOS	11
Supplementary Figure 1. Base layout of the DNA origami nanostructure used to build NACHOS	12
Supplementary Figure 2. Staple layout of the DNA origami nanostructure used to build NACHOS	13
Supplementary Figure 3. Exemplary single-molecule fluorescence transients of Alexa Fluor 647 dye	14
Supplementary Figure 4. Fluorescence scans of the DNA origami reference structure acquired in buffer solution	15
Supplementary Figure 5. Incubation time series for the reference DNA origami structure and the NACHOS	16
Supplementary Figure 6. Testing specificity of binding for variations of the Oxa-48 DNA sequence	17
Supplementary Figure 7. Exemplary fluorescence transients of the sandwich assay in DNA origami reference structures without nanoparticles and in NACHOS	18
Supplementary Figure 8. Fluorescence scans of the DNA origami reference structure acquired in blood serum	19
Supplementary Figure 9. Additional fluorescence transients of single Alexa Fluor 647	20
Supplementary Figure 10. Fluorescence transients of single ATTO647N dyes in NACHOS recorded on the smartphone microscope	21
Supplementary Figure 11. Negative controls on the smartphone	22
Supplementary Figure 12. Additional fluorescence transients of the sandwich assay in NACHOS measured in buffer solution	23
Supplementary Figure 13. Additional fluorescence transients of the sandwich assay inside NACHOS measured in blood serum	24
Supplementary Figure 14. Bleaching step analysis	25
Supplementary Figure 15. Fluorescence enhancement histograms of a single ATTO 647N dye in NACHOS of a previous design	26
Supplementary Note 1. Discussion pertaining the costs of the smartphone microscope	27
Supplementary Note 2. Discussion pertaining the costs per sample for the diagnostic assay on a smartphone microscope	28
Supplementary References	28

Supplementary Table 1. Temperature ramp used for folding DNA origami nanostructures

Temperature [°C]	Time [s]
65	300
65	50
64	95
63	95
62	95
61	95
60	540
59	540
58	1140
57	1740
56	2340
55	2940
54	3540
53	3540
52	3540
51	3540
50	3540
49	3540
48	3540
47	3540
46	3540
45	3540
44	2940
43	2340
42	1740
41	1140
40	1140
39	1140
38	540
37	540
36	290
35	290
34	290
33	290
32	290
31	290
30	290
29	50
28	50
27	50
26	50
25	50

Supplementary Table 2. Unmodified staple strands used to fold the DNA origami nanostructures

Name	Sequence (5'→3')
1	TTTAAATGTTTGCTGAGATTTAGGACCCACGCGAA
2	TTAGAACGCAATTAAGACAAATACATACATAAA
3	TTTAAGCAAATTCACAAAGTATTAAGAGGCTCGGA
4	TAAATACCCGGATATCATCAACGGTCAATCATAAGACCATCGATAC
5	GAAGGGATAGCGAGATAGTTCGGCCAGGAAGAAGAATGAGGT
6	GCAACTGGCGAAAGGGGAGTAAAGTTGCCGGAGTGAGACCGGTCCAAAC
7	ACGAGGAGAGGGCGGTTTGATGGTGGGGCCCACCCT
8	CGGTGTACAGACCAACAAAGCTAACGGAAAAAATCTACG
9	AATATCGGCACGCGCGGGCCGGAAGCATAAAAGCT
10	CAGAACAATATATCGGCCATCAAACACAGTTGAAAGGAA
11	TGAGGAAAACAGCCTGATTGCTTTGTTGC
12	GAACGCCTCCATATTATTTTA
13	AGTTCTGTCCCCCGAGGCGCTGGCAAGTGTTTG
14	CTTAAATCCCGGCGGTTGTG
15	AGCAATACTTCATCACGCAAATATCGCCAGTA
16	TTCATTTACCATATTGCGGAACAAAGAA
17	CTACAATTTTTTTGAAGAAAAAGCTTTAAAACAGAAATAAAGAAAAAT
18	CCTACATATCTAAAGCATCACCTCAAATTTGC
19	GGTGGCTCCAACGGCATTTCGCACTCAATCCACGCCATCCA
20	CGGAATTACCGTGTGCGAAGACAAAGAAAACAGTAAACAAAC
21	TTCAATGATAAATTAATGC
22	GTCGAGGACCCGCCGCACCTTTTACATCCGCTGAGCAT
23	GTAATCAGAAACGAGCCTTTAGTGCTTCTCAGAACGA
24	GCGACCCACCAAGTAGAATCATTAAAGGTGAAAATA
25	GTCTGAGCAAAGAAGATAATGGGAAGGAG
26	TCACGCGTGGGAACAAATGTCACTGCGCGCCGCGG
27	ATTAGAGCATTTTTGCGAGCTGAAAAGGTCTA
28	TGTGATAAATTTAGCCGGAACGAGATATATTCTCA
29	TCCCGGGCGAAAGCCACCGTCTTTCCAGAGCCGAA
30	AATAAACCGAATCTTTTCATAATCAGGA
31	CAGACCAGTTACAAAATAAAGGCTTCAGTAGGAGTATTATTAATGC
32	CGTAGGCGCATAACTGACCAACTTTGTTGCGCGATACATTGCAAAAAG
33	AATAATAACCGGCGCAGAGAGTAATCTCGCCT
34	CATTATATTTTATCTTCTGACCTAAAGATGATCAATATA
35	AGGACGTTAAGAACGGTTTAATTTCAACGAGAAACCAA
36	AGGAGGCTTTAACGCCAAACGAACTGCTCAT
37	ACCACCCTTAGATGAGTGACCTGTCGTGCCAGAAT
38	GGTGATAAGAAGTGGCATGATAATAACAGCCCTTTAATATC
39	CCCCTTTTCTTGTGTGAAATTGTAAAGCACTTGT
40	CATTTAAACTCCATATAGATTCATCAGTGAACAAGAACTCATC
41	AACAGACAATAGTTTATCCGCTGGTAAATGTGCAG
42	CGGATCGGATGTGCTGCAAGGCGATCAGTGCCAGGTGGAGCC
43	CCGAGCTCGAACTTGACGAAAGGTAAGAGGCATTTATTT
44	TGGGCACTAAAAAAGAGTCTGTCCTTTGATTTCAAACCTTAC

45	GAGTCAACTAATTTAGGCAAGTAATCCTGAACAGA
46	AGAGTTCGTAAAGCTGATCTCATAAGGATTGACTGCCAGTTTGAGGCAG
47	TACGCGGGATACGAGGGCAACGGAATTATACCAAG
48	ATCCTTTGCAACAGGAAAAACGCT
49	GAAGGTATTATCACCCAGCAAATCACCTTACCATTAGC
50	TTGCAAAGACAAAAGGGAATGAAATAGCAAGCAGCACC
51	GCAAGACTGGATAGCGTGAATCCCCTGTATGCGC
52	AGCACCTCAAATCCTCCAGGAAGGGTCATTCTTTAATTGTACAGGTG
53	TTTGCGTATTGACAATTCCACACAAAATTGGG
54	AAACGGACGACGTCGGTGACGCAACAGCGAGTATAGTTATTTTGATGGGG
55	ATATAATACACGTACTACACCAGCTAACACCATTACCAGTCACA
56	TATTTTAACTCAAAGCTGCATTGCCTGGGGTGCCTAAATCCTTAGAC
57	AAAGGAAGCTTGATGTTGAAACCTG
58	GTCAGACCTCAAGAGAAGGAT
59	TTATCAGCTTGCTTACACTAT
60	AAAAATTAAGCCTATTATTCTGAAGTTGATAGATTGCAAACCTC
61	TTTGCGGGCCTCTGTGGTGCT
62	CACCGGAATCATTTCAAAATTATTT
63	TAAAGGAAGCTCTGGAAGTGCAGACGAGTAGGCATAAACTGTAATGTCA
64	GAGCGTCCACTACCTCCGTAATTTTAGTTACAAAATCGCCGT
65	TACCAGAATCAAGTTTGCCTTATTTAAAACTAATAAGACCCGCATGC
66	GCAGCAGAGGTCGTCGCAATTGCG
67	TGAGATCGGCTATAATATACCGACAGGGAAAGAGCGAAAGGAGCGGCAGT
68	CTTGGTAAACGCCAGGGTACGACGTGGAT
69	CGCGCAGTATATTTCGACAATGAATATACAGTA
70	AAGAGGTAGTACCTTGAGAAAGGCCGACAATGCCATAGTAG
71	TGCACGACAATTGCGAATGCCCCCTCGGCTGGCCA
72	GCTTTGAGGACTAATACGAAGAAAACGAAAGAGGCCCCAGCGGATT
73	ATATAAAATTCATATGGTTTATTACCGAGGAA
74	GCAGTTGGTAAAAGGCGGCCGCGTGGTGGGTGGTAGCAGGCTGCA
75	GTCCTTTCATGCATGTCCCAGTAAAGTGCCCGTATAAAAGGAGGTAATC
76	ACATTACAAAGGATTAAGGTGCCGTCGAGAGGACATGAAACAA
77	TAGTACTAAAGTACGGTGCCGAAAGATTTTTGATTGTAATTTTGTTGGGT
78	AGTGAATTTTCTCAAACCTCAGAGCCACCGAACCCACAC
79	TTATTCGGTCGGGTATTAGCCGTTTTTTTCGATTTA
80	TCATCGTAACATTCCAAGAACATAGCCCCCT
81	GCCGCTACCACCACTGCCGTATCCGCTCGGCGCCAGCTGGTC
82	ACAGTGCTTTACCGAACGAACTGGTTGCTAGCGGTAAC
83	TGCCCCGCTTCCAGGTGTTGTTT
84	ATAGAGCCGCACTCCAAGTC
85	GCGGTCAGTATAGAAGATTAGCCCTTAAAGGGATTTTAG
86	GGGGTTTATATCGCATATGCATTGACCATTAGATA
87	ATTCTAGCGATGTGTAAAAATGAATCGGCCAAAAA
88	AAGTTTTGACGCTCAAATCCGGTATTCTAATAA
89	TACTGTGTCGAAATCCGCAAAGTATAGCAAC
90	TATTAAATCATACAAAATCATAGCGTCAAATTAT
91	CACGGGGGTAATAGTAAAACAGTTAGACGTTAGCCCTCAACAACCCAG

92	GACACGTAGATCCTTATTACG
93	ACCAACATGGCGCGTAACGATCTTACAACATTTTG
94	TTAAAGAGATCTATGACCGCTAAATCGGTTGTCCC
95	AAAAGAATTTCTTAAACATTACGAGACCAAAA
96	CCTAGTTTCCTTTCACCACTTGTAGCAGCACCGACAGTATCGGCCTACCG
97	CTGTCATACCGGCCCTGGCCCTGAGAAGA
98	AACTGTAAAACGACGGCTAAGTTGCGC
99	AAAGTCTTTCCTTATAAGAGTGTACACAGACAGTAAATGAG
100	GCAAACCACGGTTTTGTGACAATCAAAAGTAACCG
101	CATTGAAGACAGTTCATGAGGAAGTTGGGTAAATAC
102	AATTGTTTCATTCCATATTCAAAAAGCTATCAATTG
103	AGAGAGAAATAACAAGCGTTTGGCATAAGTA
104	TCAATGCTCAGTACCAGGGAGACTCGATTGGCCCA
105	ACCTTATGCGATTTTGGGAAGACAACATTAA
106	TAGTATCAAATTCCTTACAGGCGTTTTAGCGAAACG
107	AGCGGGAGCTAAACAGGAGTTTTTACAATAGATTT
108	ACGGAGCCGTTAATCAGTGAGGCCTTG
109	TTTGACCGCCAGGAAAGCTAATCAGAGCAAACAAA
110	AGGAAGCGCAGCGATCCCGTGCCGCGGAACGTAAACGATGCTGATACG
111	AGGACGTCAGACTGTAGC
112	ACTGTATCACCGTACTCCAGTTAACTGAATTCCGCCACTACGTGAAAATC
113	GAAAATTCGCAGGCGCTCAGATGCCGGGTTAATCTCCAAGAGAACCTG
114	TCGCCGGCTGGAGGTTTCTTTGCTCACTTTTGGGTAGCTACT
115	CGACACGCCAAATTACCGCGCCCAAAATCCAAGCC
116	CAGAGCGGGGTCATTGCGTCTGGCCGGTTGAGCAGTCTTGCCCCC
117	TCCCATGCGTTCTTTGCCGATTTTCAGGTTTACGG
118	TAAAAGGAATGGCTATTAGTCGAACTGAAAAA
119	TCAGTGAGAATCAAATCAGATATAGAACAGCCCTCAGAGTACCGTTAATC
120	CTATGAGTAATGTGTAGAAAAGGGTTAA
121	AGACCGGCAAACGCGGTCCGTTTT
122	GGACAAATCACCTCAATATGAAAATTTGACGCTCA
123	TTTGACCAAAAAGAAATACGTAATGCCACAGACTTTTCATC
124	AAAAATAGGAGCCGGGCTCAGCAAATCGTTAAAAGGAGGCC
125	AATCAAGAATTGAGTTAAATAGCATTTTTTTGTATCCCTAGCAAGCGCC
126	GAATTGCCAGAATTCAACTATTACACCAAATACCAGAACGAGTAG
127	GTTGCGTCGGATTCTCGTAGCATTTCCTCGTAA
128	AGCCAACGTGGCACCAGAATCTTACCAACGCTACC
129	GCCACGAAACGTTTCGCCACGTGCATCCGTAATGGGATAGGGCC
130	ATCCTGAAAACAAACCTTTTTTAATGGACGCGAGAGGTTTGA
131	TGCCTATAATAGGTATTATAGGATAAAAGCATAGTAAGAGCATCGA
132	ATCAAGATTGTTTGTATTTCCTGATTATCATTTAATAAACTTT
133	CAAGGGGCAACTCATGGTCATAGCTAAGGGAGAGA
134	ACCGAGGCTGGCTGACCTTTCATTAGGTAGAAACCAGTC
135	GAGAACAAGCAAACCAAATCAATATTTTCGTCACTACAAGGATTTT
136	TTTGGACATTCTGGCCAATTGGCAGGCCTGCA
137	TGTACGGAGGGAAGTGAGCGCTTTAAGAATAGAAAAGAAACGCAA
138	TACGTATCATGACTTGCGGGAGGTATCCTGAACCACCACTTGATATAT

139	ACGGAACGTCATTTAGTGATGAAGGCATAAAACTGGTGCCCCGGAA
140	GCAGCAACAATATCGAAGAACAGTAATAACATCACACC
141	GAGGGAATCCTGAGAAGTGGCCGATAAAACATATT
142	AAAACCGCCACCCTCAGATTTTAAACGATACAGTCACCGGGATA
143	GTTTACCAGACGACTCAGAAGAGTCTGGAAAAGCCCAA
144	AGACAATCGCCATTAATAAAGAATCAGCAGA
145	TAGCGAGTCTTTACTCGATGATGTACCCCTTCCTGCTG
146	ATAACGGTAATTTTCACACCGATAGAAAGAG
147	TTCAAATTGAATTAATTAATT
148	GTACGAACGTTATTAATCTGTTTACTTTTTAATTAAAGCGA
149	TGTGCGGTTGCGGTATGCTCA
150	AGGCTTGCCCTGACTTTAATC
151	TGCTTCTGTAAACGAATTA
152	ATCTAGCCAGCAGCATCCAGCGGTGCCGGTAATAATTCGTAAA
153	AAGTTTGACCATAACAAAGTTTTGTCTGAAGGAATGACAACAGGA
154	GGACGTCACCCGGTTCGAGTTTCATGTGCACGTTT
155	AATCAAATTAGTACCGCCACCGAGTAACGCGTCATCCGGAACCGCGCCTAAC
156	CGGAGAGCGGGAGAAATAAAGCCTCAGAATT
157	ACAGTGCGACTTTACAAACAAAAGCCAAGTCAATACTATCATTTCC
158	TACATCAAACCTGAAAAAGAGACGCATACCAGTCGG
159	CGTGTGAATTATTAAGAGGGAGAAACAATAAACGTCAGACTCG
160	ACTAAATGGGCTTGAGATTGGCT
161	TGAGCAAAGCGTAAGTATAGCCCGGTTCCGGAACCAGAATCCCTCAGAAAC
162	TCACAGAGAGTAACCCAAGCTATCCAGCGCACGGAAATTGCAAC
163	ATACAGAACCCTTCTGACGTCTGAAAGAGCCA
164	GATAAAATCAGAGCCGGGACATCCCTTACACTAAA
165	CGCCAGCCAGAAAGCGTACTGAGTATGGTGCT
166	ATCCATGTAATAGATTAAGCACGTATAACGTGCGCTAGTTT
167	CATAACAGTTGATTACTCGGT
168	AACAAAATCGGCACGCTGCGCGTAACAGGGCGTTT
169	TGAAAGCCCAAAGAAACCGACATTAGGGAGG
170	CCAGAGCGCCATACAGCGCCATGTTGATTGAGAAGCTAACAG
171	TTCTCGCACGCTGATGGATTATTTACACAGAGATGTGGCAC
172	CTTAGCATCAGACGATCCACAACCTATCTTTCCAG
173	TACGCCAATTTAGAGCTTAATCTCACCCACCATAAGAAA
174	TATTTGCCGTTGCACATCTGCCCTTACCGGTGTA
175	ACCATCGATAGGCCGGAAATTAGAGCGTCACCGACT
176	TTTAGAACCCTCATATATTTTAAATGGACAGTCGGTCAGG
177	TAGCATTTTGGGGCGCGGATGGCTTAGATCCAACA
178	AGCAAACGCTTAATAGCTATATTTTCATAACATCCAATA
179	TAATTACTAGCCTTAAATCAAGATTTTGCACAGCATTGGAGGCAG
180	TGATCGGGAAAGCTAACTCACATTTATTAATGCTTAGGTTG
181	GAAAGGAAGGGAAGAACCGGCGATCCCCGGCCGTGAGAGCCTCCGTACAGT
182	GAAGGTTATCTAAAAT
183	AAGGCCGCTTTTGGCG
184	CACCCTGAACAAGCCG
185	CTCGTCGCTGGCCCTCCTCCGTGCCTTAATTTAGAAACCAGTAC

186

TTGGAACAAGACGCCGCCAG

Supplementary Table 3. Modified staple strands used for the immobilization of the DNA origami structure (biotinX), nanoparticle binding (npbindX) and fluorescence labelling.

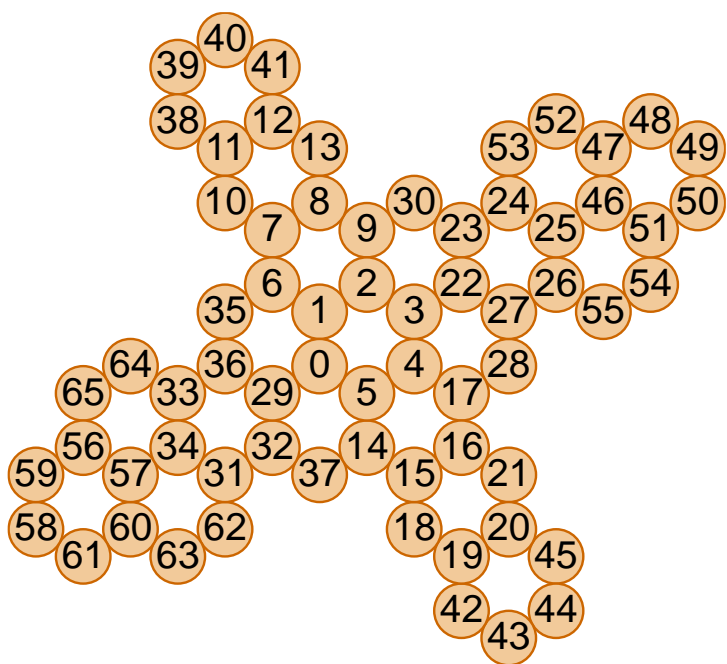
Name	Sequence (5'→3')
biotin1	biotin - AGAATATAAAGTCCCATCCGTTCTTCGGGG
biotin2	biotin - AGTTACCAGAAGGAAAGCAGATAAGTCAGAGGGTAATCGCA
biotin3	biotin - ACAACTTTCAACTGAGGCTATGT
biotin4	biotin - AGGGCGATCGGTGCGGTGCGCAACCGGAAACAATCGGCCGGG
biotin5	biotin - TTCATCGGCATTGACGGGACCAATAGACCCTCAATTCATTCCAA
biotin6	biotin - TAGATGGGCGCATCGTAACTTCAGGCGCCT
npbind1	CATTTTCGTCAACATGTTTTAAGTTTTAATTCGAGAAAAAAAAAAAAAAAAAAAAAAAAA
npbind2	GGTTATATAACTATATGTGAATAAAAAAAAAAAAAAAAAAAAAAAAAAAAAAAAAA
npbind3	ACCATCAACCGTTCTAGCCGCAAAAAAAAAAAAAAAAAAAAAAAAAAAAAAAAAA
npbind4	ATAAAAATGCTGATGCAATGTGAAAAAAAAAAAAAAAAAAAAAAAAAAAAAAAAA
npbind5	AAAGAATTAGCAAAATTAAGCAGCCTTTAAAAAAAAAAAAAAAAAAAAAAAAAAAAA
npbind6	ACCACCAAAGGGTTAGAACCTCAATTACGAATAACCTAAAAAAAAAAAAAAAAAAAAA AAA
npbind7	AATCATACAGCCTGTTTTGCTGAATATAATGCGAAAAAAAAAAAAAAAAAAAAAAA
npbind8	AATATAATCCAATGATAAATAAGGCGTTAAAAAAAAAAAAAAAAAAAAAAAAAAAAA
npbind9	AAATCACCATCAATATGATATGACCGGAAAAAAAAAAAAAAAAAAAAAAAAAAAAA
npbind10	CTTCAAAGCTGTAGCCAAATGGTCAATAAGCAAGGCATAAAAATTAAAAAAAAAAAA AAAAAAAAAAAA
npbind11	AAAAGTTTGAGTAACATTATCAAAAAAAAAAAAAAAAAAAAAAAAAAAAAA
npbind12	AATACCGATCATCAGATTATACTTCTGAATGATGACATAAATCAAAAAAAAAAAAAA AAAAAAAAAA
base_dye ATTO542	TTTGTGATCTCACGTAAATTTCTGCTCA-ATTO542
hotspot_dye ATTO647N	TAATCACTGTTGCCCTGATTAATACGTTAATA-ATTO647N
hotspot_dye AlexaFluor 647	TAATCACTGTTGCCCTGATTAATACGTTAATA-AlexaFluor647

Supplementary Table 4. Modified staple strands used for the sandwich detection assay: 3 capture staples (captureX), synthetic 34 nt target strand (target34) and Alexa Fluor 647 imager strand (Alexa647 imager). Complementary regions are depicted in the same colour. The unmodified staple strands from Supplementary Table 2 and modified staple strands from Supplementary Table 3 which are replaced by the capture strands and therefore should be left in order to fabricate the NACHOS out are indicated in the second column.

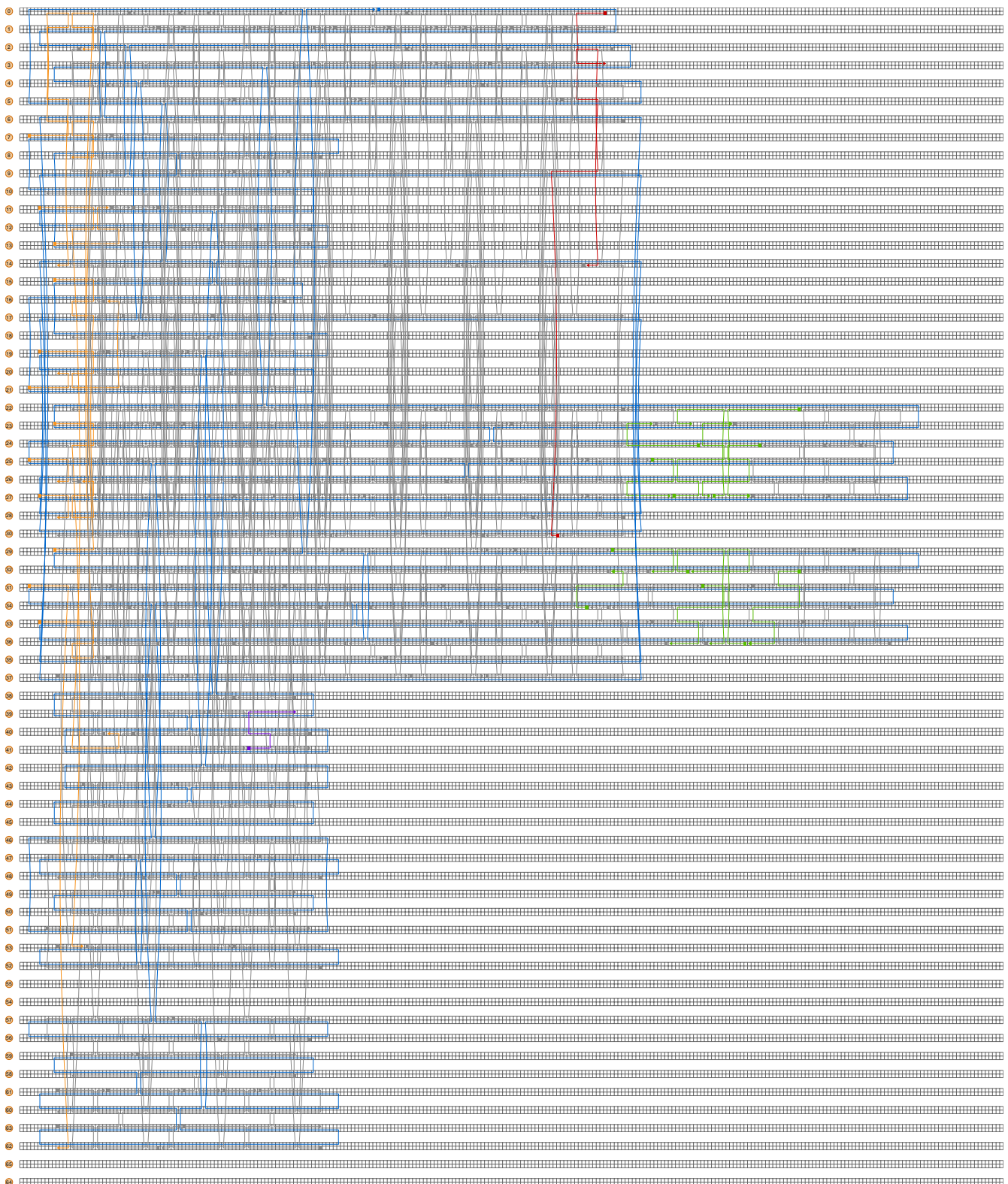
Name	Strands to leave out	Sequence (5'→3')
capture1	hotspot_dye strand from Table3	TAATCACTGTTGCCCTGATTAAATACGTTAATATTTTTCGG GCAATGTAGACA
capture2	186 from Table 2	TTCGGGCAATGTAGACATTTGGAACAAGACGCCGCCCCAG
capture3	156 from Table 2	TTCGGGCAATGTAGACACGGAGAGCGGGAGAAATAAAGCC TCAGAATT
target34		TGTCTACATTGCCCGAAATGTCCTCATTACCATA
Alexa647 imager		TATGGTAATGAGGACAT-AlexaFluor647

Supplementary Table 5. Modified staple strands used for solution synthesis of NACHOS. Overhang modifications (modificationX) exchange biotinX staples from the Supplementary Table 3 of the DNA origami structure. Complementary regions are depicted in the same colour. Corresponding unmodified strands from Supplementary Table 2 and modified strands from Supplementary Table 3 should be left out.

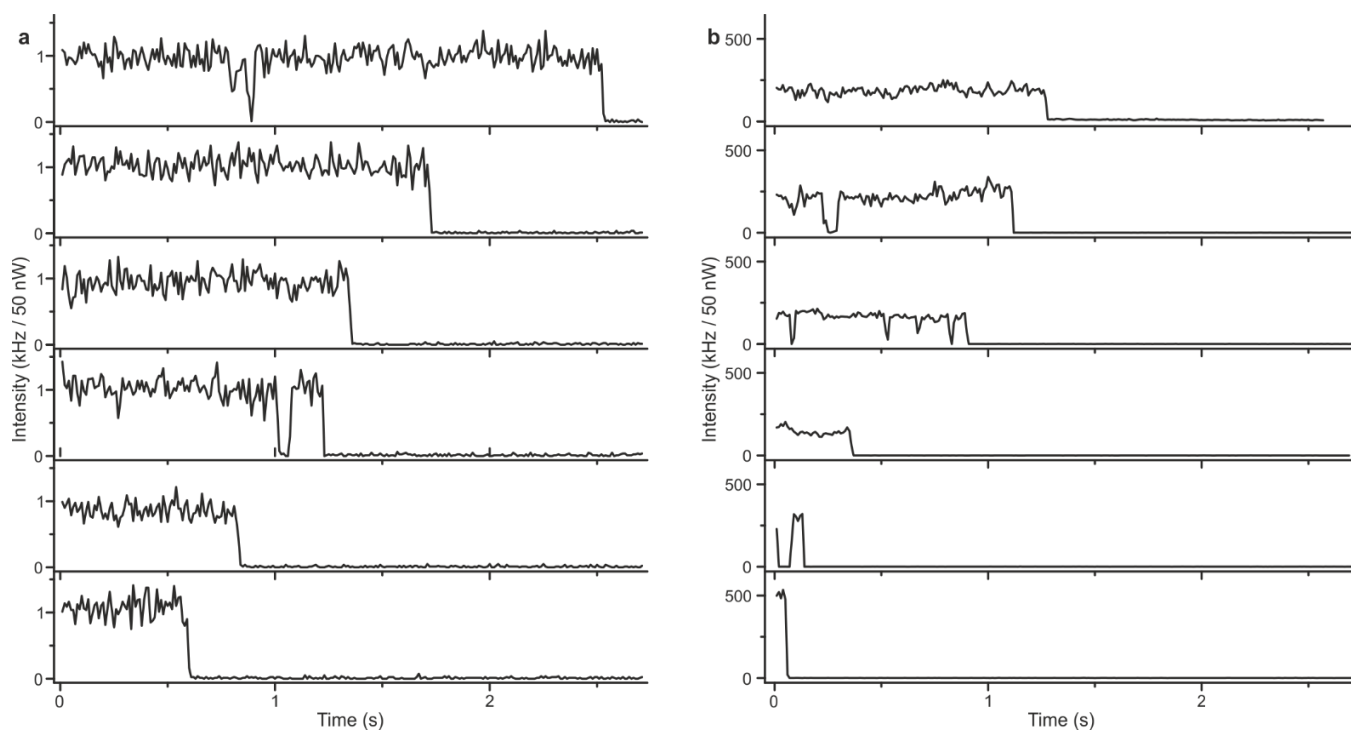
Name	Replacing strand	Sequence (5'→3')
modification1	biotin1 Table 3	GTGATGTAGGTGGTAGAGGAAAGAATATAAAGTCCCAT CCGTTCTTCGGGG
modification2	biotin2 Table 3	AGTTACCAGAAGGAAAGCAGATAAGTCAGAGGGTAATC GCA
modification3	biotin3 Table 3	GTGATGTAGGTGGTAGAGGAAACAAC TTTCAACTGAGG CTATGT
modification4	biotin4 Table 3	AGGGCGATCGGTGCGGTGCGCAACCGGAAACAATCGGC GGG
modification5	biotin5 Table 3	TTCATCGGCATTGACGGGACCAATAGACCCTCAATTCAT TCCAA
modification6	biotin6 Table 3	GTGATGTAGGTGGTAGAGGAA TAGATGGGCGCATCGTA ACTTCAGGCGCCT
mag1		TCTCCATGTCAC T TCTCTACCACCTACATCACCTTC TTCTTCTTCTT - biotin
mag2		GTGATGTAGGTGGTAGAGGAA
mag3		AAGAAGAAGAAGGTGATGTAGGTGGTAGAGGAA GAAGT GACATGGAGA



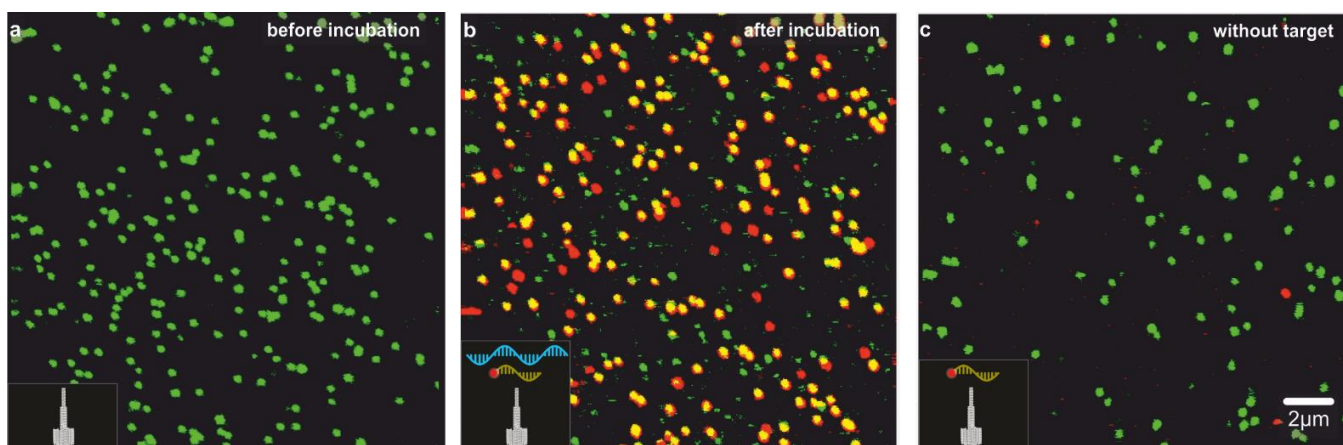
Supplementary Figure 1. Base layout of the DNA origami nanostructure used to build NACHOS



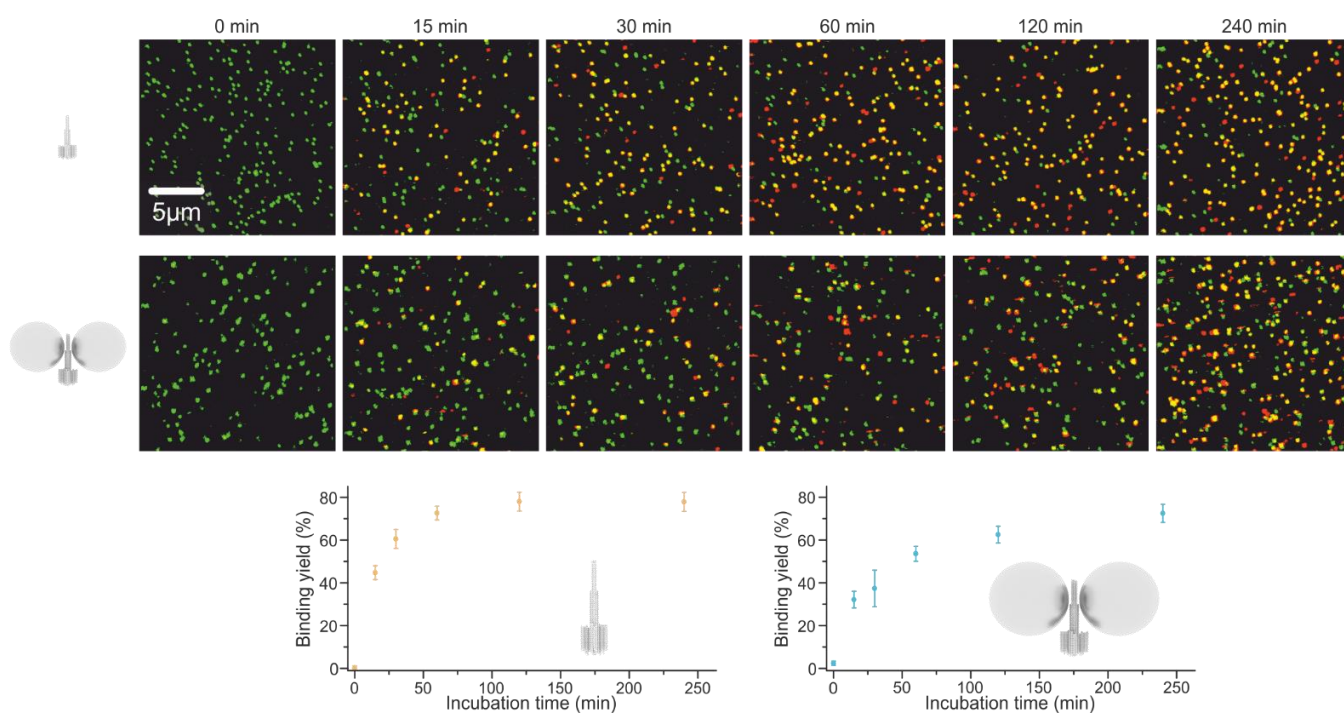
Supplementary Figure 2. Staple layout of the DNA origami nanostructure used to build NACHOS (yellow = biotin staples, red = hotspot staple, green= nanoparticle binding staples, purple = base dye staple)



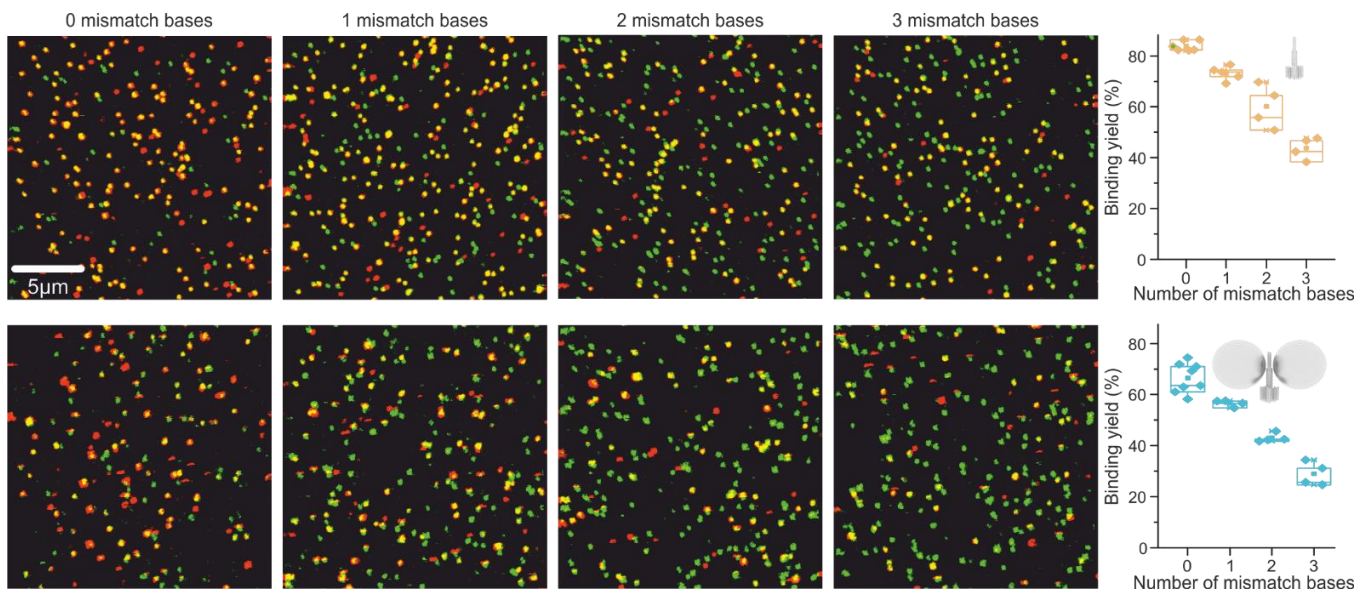
Supplementary Figure 3. Exemplary single-molecule fluorescence transients of Alexa Fluor 647 dye in DNA origami reference structures without nanoparticles (a) and in NACHOS (b). The samples are measured at 639 nm with 200 nW and 50 nW excitation power for panel (a) and (b), respectively, and the transients are normalized to the same excitation power.



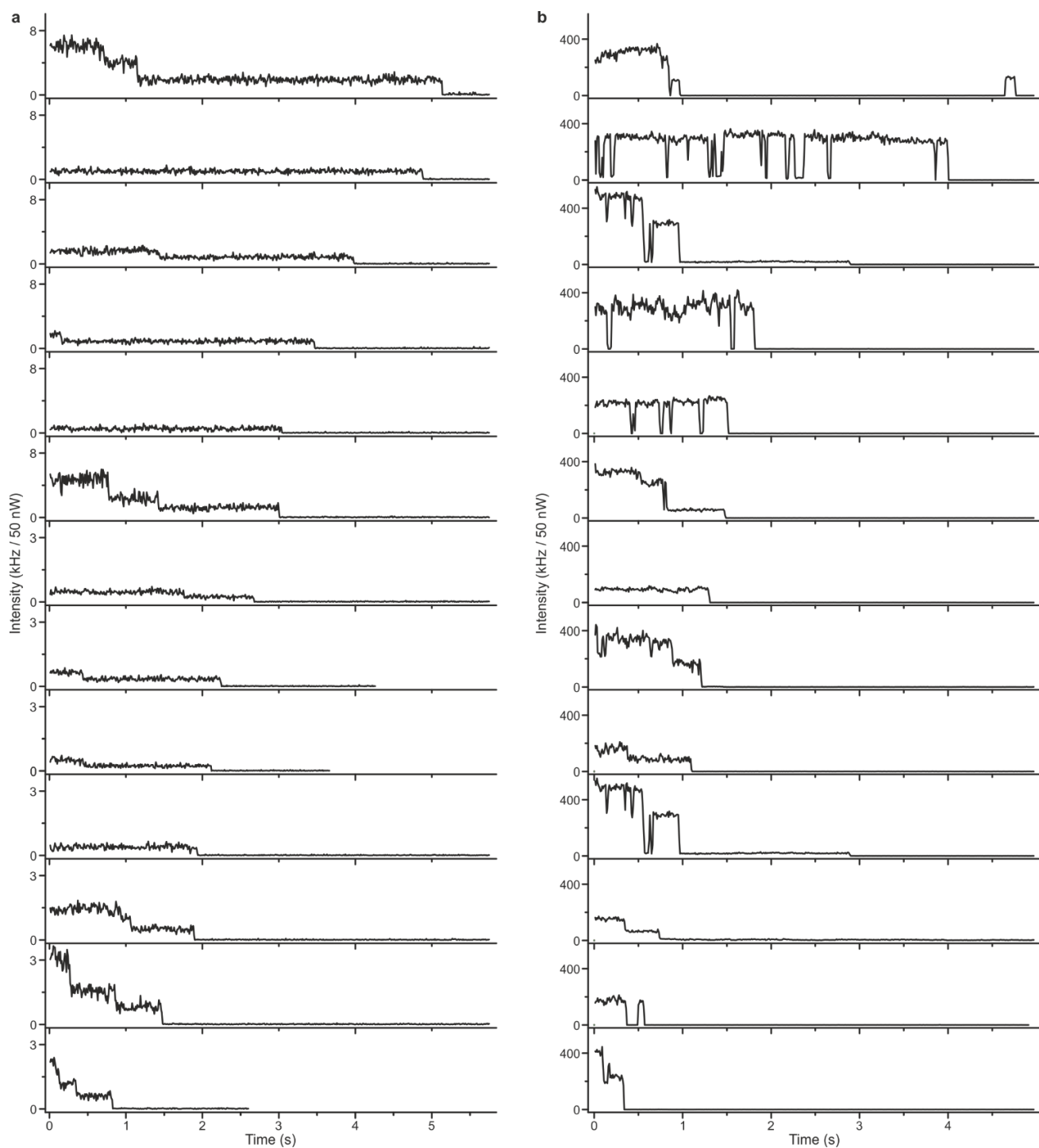
Supplementary Figure 4. Fluorescence scans of the DNA origami reference structure (without nanoparticles) measured in buffer solution acquired before incubation (a), after incubation with the full sandwich assay (b), and after incubation with the imager strand only (c). Excitation was carried out at 532 nm and 639 nm with 2 μ W excitation power. At least 20 different areas were measured for each sample.



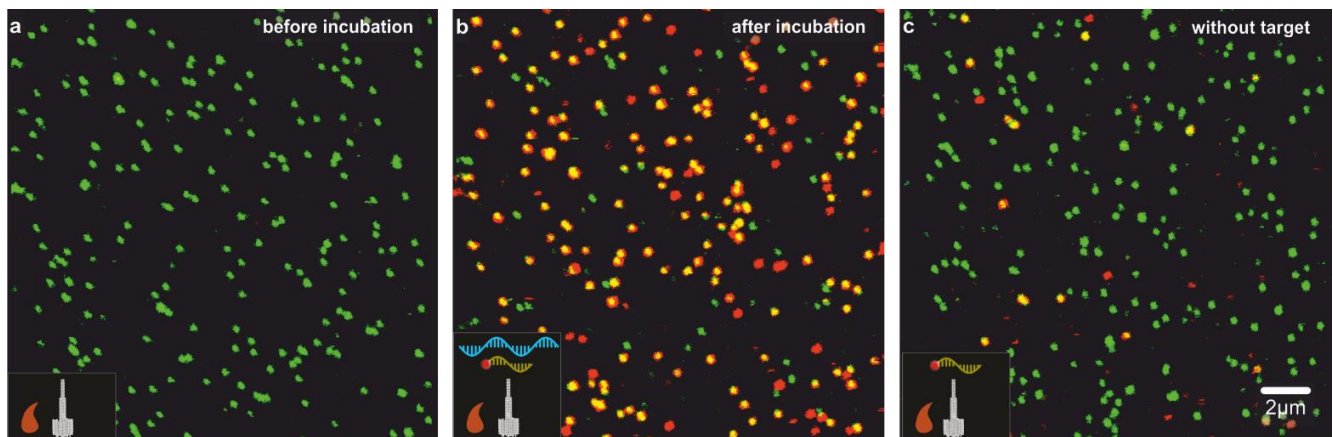
Supplementary Figure 5. Incubation time series for the reference DNA origami structure (first row) and the NACHOS (second row). The binding yield efficiency for every incubation time is calculated from at least 4 different areas of the sample and represented at the bottom. The error bars represent the standard deviation from the mean. Measured at 532 nm and 639 nm with 2 μ W excitation power for the reference structure and at 532 nm with 2 μ W and 639 nm with 500 nW for the NACHOS structure.



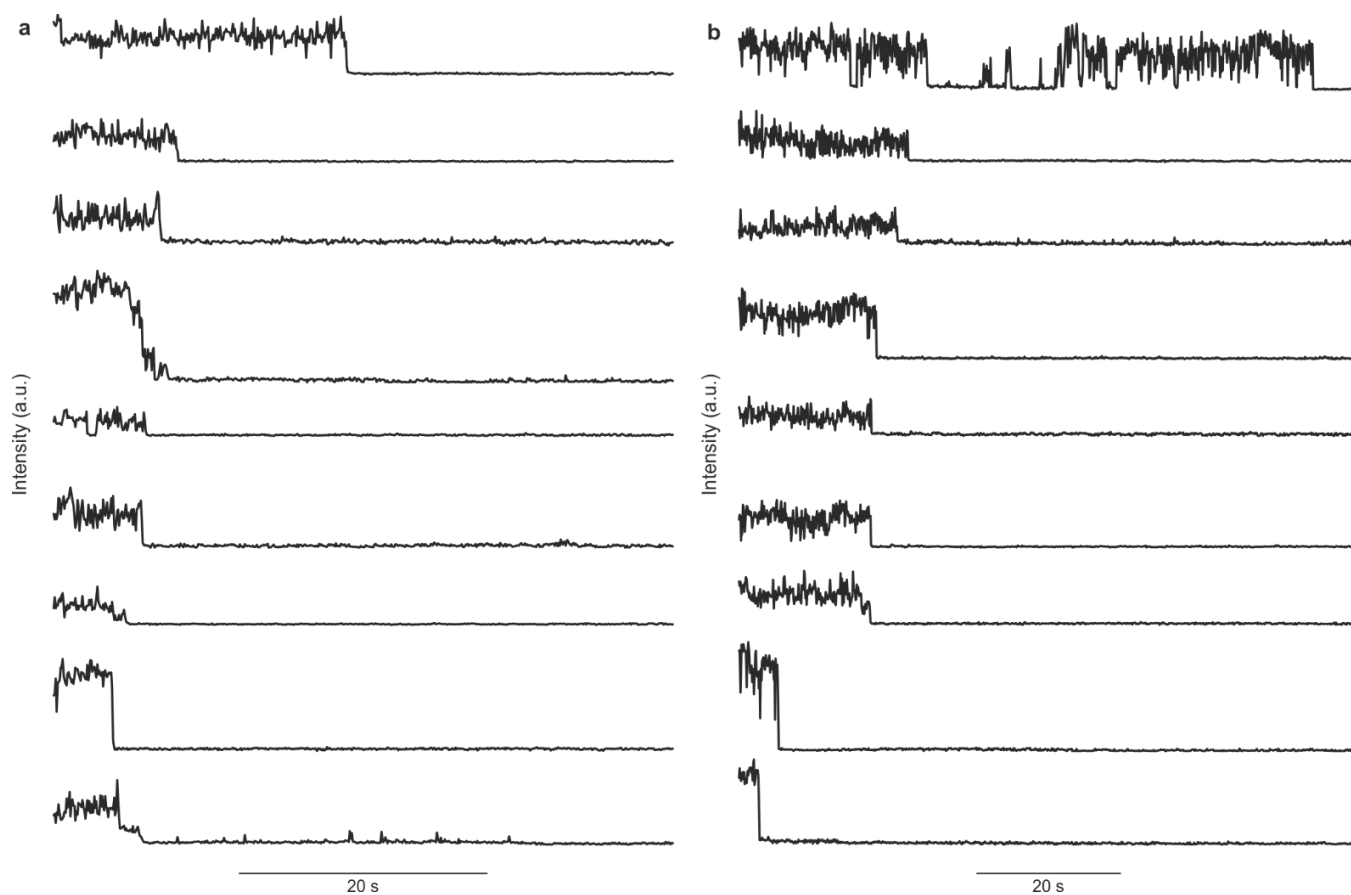
Supplementary Figure 6. Testing specificity of binding for variations of the Oxa-48 DNA sequence: scans and binding yield for perfectly matching DNA target and targets with 1, 2, and 3 mismatches in the reference DNA nanostructure (top row) and in NACHOS (bottom row). The calculated binding yield efficiency is represented in the right panels from at least 4 different areas of each sample. The box plots show the 25/75 percentiles and the whiskers represent the $1.5 \times \text{IQR}$ (inter quartile range) values, the center lines represent the average values. Measured at 532 nm and 639 nm with 2 μW excitation power for the reference structure and at 532 nm with 2 μW and 639 nm with 500 nW for the NACHOS structure.



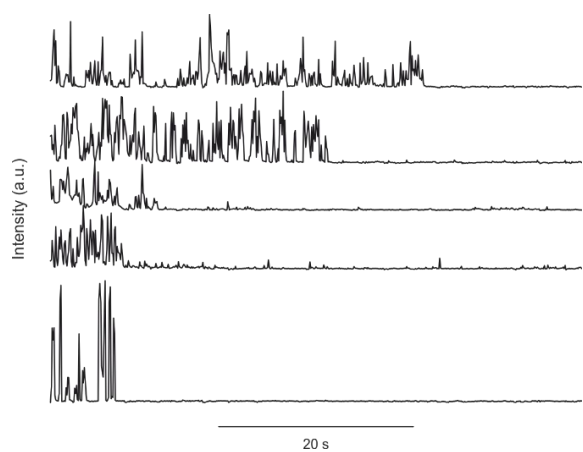
Supplementary Figure 7. Exemplary fluorescence transients of the sandwich assay in DNA origami reference structures without nanoparticles (a) and in NACHOS (b) The samples are measured at 639 nm with 500 nW and 50 nW excitation power for panel (a) and (b), respectively, and the transients are normalized to the same excitation power.



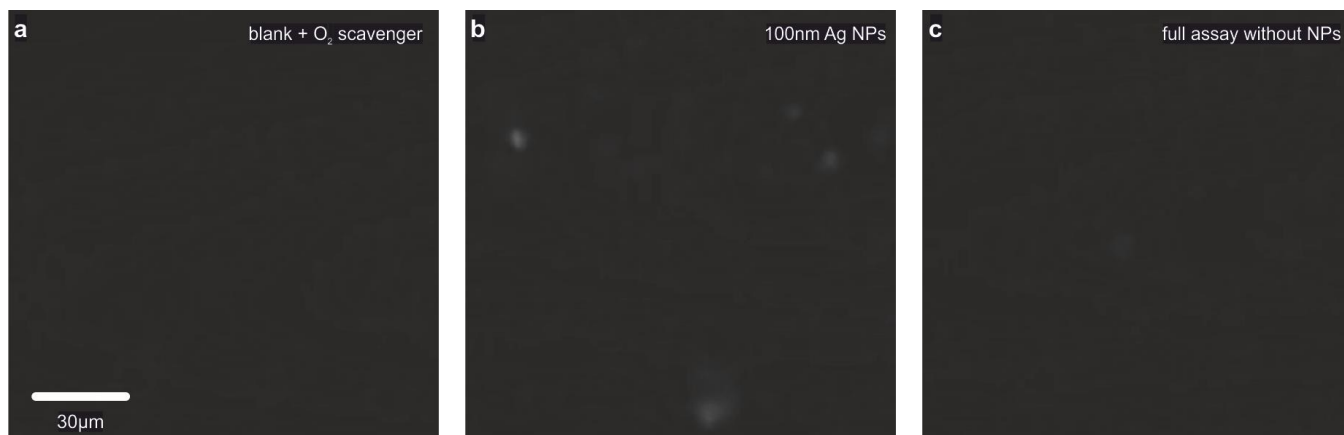
Supplementary Figure 8. Fluorescence scans of the DNA origami reference structure (without nanoparticles) acquired in blood serum before incubation (a), after incubation with the full sandwich assay (b), and after incubation with the imager strand only (c). Measured at 532 nm and 639 nm with 2 μ W excitation power. At least 20 different areas were measured for each sample.



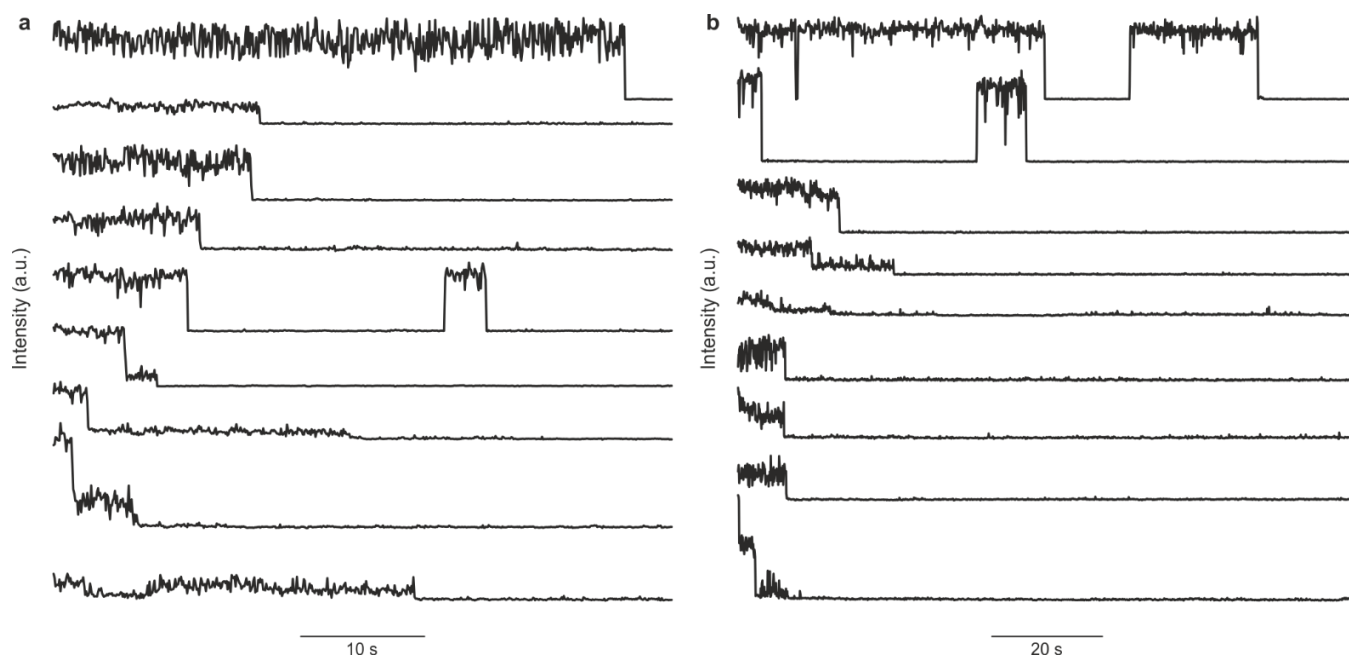
Supplementary Figure 9. Additional fluorescence transients of single Alexa Fluor 647 dyes in NACHOS obtained from two more movies (a, b) recorded on the smartphone microscope.



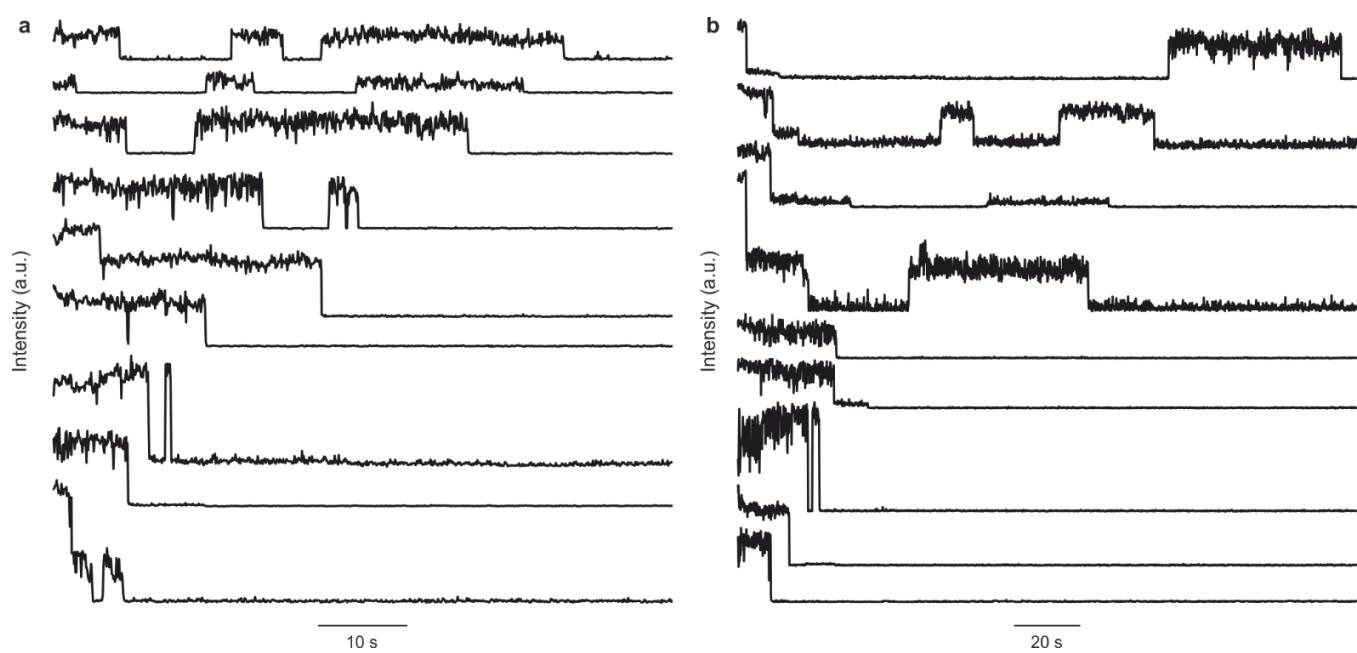
Supplementary Figure 10. Fluorescence transients of single ATTO647N dyes in NACHOS recorded on the smartphone microscope (80 ms integration time).



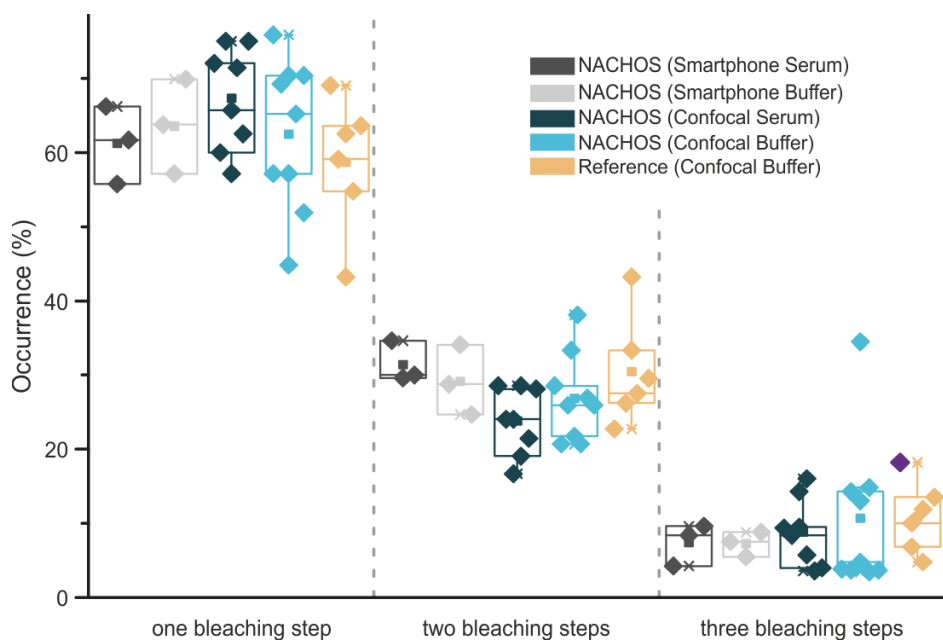
Supplementary Figure 11. Negative controls on the smartphone (a) cleaned surface with buffer solution, (b) incubated only with 100 nm silver nanoparticles, and (c) full sandwich assay on NACHOS without silver nanoparticles in ROXS¹. For each control measurement at least 4 movies were recorded.



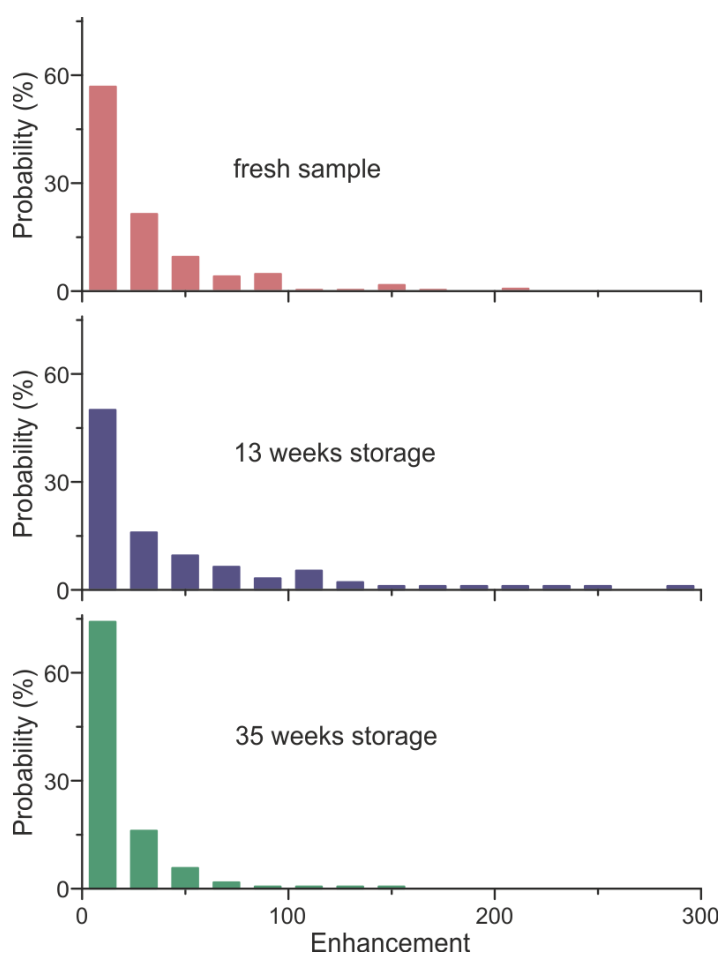
Supplementary Figure 12. Additional fluorescence transients of the sandwich assay in NACHOS measured in buffer solution from two more movies (a, b) recorded on the smartphone microscope.



Supplementary Figure 13. Additional fluorescence transients of the sandwich assay inside NACHOS measured in blood serum from two more movies (a, b) recorded on the smartphone microscope.



Supplementary Figure 14. Bleaching step analysis obtained for the reference structure (orange) and for NACHOS measured on the confocal setup in buffer solution (light blue) as well as in blood serum (dark blue) (same data as shown in Fig. 2g) and for 244 traces extracted from the smartphone microscope in buffer solution (light grey) as well as in blood serum (dark grey). The box plots represent the statistics of at least 4 different areas for each sample with the 25/75 percentiles and the whiskers represent the 1.5*IQR values, the canter lines represent the average values.



Supplementary Figure 15. Fluorescence enhancement histograms of a single ATTO 647N dye in NACHOS of a previous design (only eight binding strands of A₂₅ for nanoparticles, T₂₅-SH used for nanoparticles functionalization). No difference between the fresh sample (red, 294 molecules measured) and the sample measured after 13 weeks (blue, 94 molecules) were observed. Slight changes are visible for the sample measured after ~35 weeks (green, 174 molecules). The sample (Lab-Tek™ II-chambers with TE buffer containing 14 mM MgCl₂ was stored at 4 °C and care was taken to avoid drying of the sample. At least 5 areas were measured for each time point.

Supplementary Note 1. Discussion pertaining the costs of the smartphone microscope

Price list of the current smartphone microscope

Name of the component	Price
Excitation source: Integrated Optics 0638L-11A (Lithuania) Laser incl. power bank and cooling system	1892 €
Smartphone: Huawei P20 (China)	439 €
Objective Lens: UCTRONICS LS-40166 (USA)	~8 €
Filter: Semrock Inc. BrightLine HC 731/137 (USA)	472 €
Focussing lens: Thorlabs Inc. AC254-050-A-ML (USA)	114 €
Sample positioner: 3× Thorlabs Inc. MT1/M (USA)	3× 341 € = 1023 €
Laser positioning: Thorlabs Inc. Optomechanical Components	218 €
Total sum:	~4200 €

Estimated pricelist of future smartphone microscopes

X and Y positioners can be omitted or substituted by cheaper ones since the accuracy is not needed inside the microscope.

Large scale production of the filters with a customize size can reduce the price by at least one order of magnitude, as a currently used standard commercially available filter is big enough to provide material for over 10 filters for smartphone microscopes.

Focussing lens does not have to be an achromatic one, i.e. price reduction to ~30 % of original price possible. Smartphone can be cheaper especially if the smartphone is specialized for camera performance -> price reduction ~50 % possible. We also note that the current smartphone was purchased in early 2019 and the current value of the same smartphone is substantially lower right now. The power density in the current configuration is set to ~ 600 μWcm^{-1} . Due to the high signal-to-background ratio we estimate that a lower power density would also be enough to make NACHOS visible on the smartphone microscope. This can be easily achieved by a high-power LED and an excitation filter to narrow down the excitation spectrum. This kind of LED in combination with a high-end excitation filter in suitable size can reduce the price to ~ 200 €.

Name of the component	Estimated price
Excitation source: e.g. Mouser, 897-LZ110R1020000 incl. power bank and bandpass filter Chroma 620/60 ET (USA)	200 €
Smartphone	220 €
Objective Lens: UCTRONICS LS-40166 (USA)	~8 €
Filter: Semrock Inc. BrightLine HC 731/137 (USA)	45 €
Focussing lens	37 €
Sample positioner (Z axis): Thorlabs Inc. MT1/M (USA)	341 €
Laser positioning: Thorlabs Inc. Optomechanical Components	218 €
Total sum:	~1000 €

Additional discounts of at least 30 % can be expected for large scale purchase of the single components -> final price < 700 € possible.

Supplementary Note 2. Discussion pertaining the costs per sample for the diagnostic assay on a smartphone microscope.

To estimate the price of materials and consumables used for the preparation of one sample, the prices stated in recent bills were used and then divided by the amount of samples that can be prepared from the ordered product.

Name of the product	Price, €	Total volume/ mass/ number of pieces of the product	Volume/ mass/ number of pieces used for one sample	Estimated price for one sample, €
Coverslip 22 mm × 22 mm	21.5	200 pieces	1	0.11
Microscope slide	2.95	50 pieces	1	0.06
BSA-biotin ^a	158	10 mg	0.075 mg	1.19
NeutrAvidin ^a	204	10 mg	0.03 mg	0.67
Unmodified DNA staple strands ^b	1200	200 staples, 100 µl each	1 set per 30,000 samples	0.04
Modified staples ^b	300	6 biotin strands, 100 uL each	1 set per 180,000 samples	0.02
Scaffold* ^b	125	0.5 ml of 100 nM	1 bottle for 12,000 samples	0.01
Amicon filter ^b	407	96	1 filter per 600 samples	0.07
100 nm BioPure Silver Nanospheres (nanoComposix, USA) ^a	215	1 ml	1 bottle for 250 samples	0.86
Thiolated oligos ^a	170	50 bottles of 1 nmol	1 bottle for 5 samples	0.68
Imager strand ^a	150	100 uL of 100 µM	1 bottle for 17000 samples	0.09
Other (buffers, silicon form, electricity, water...) ^c				< 1
Total:				~ 4.8 €

^a Calculation is done based on concentrations given in materials and methods section

^b One preparation of the DNA origami stock (~20 µl of ~ 50 nM) requires 18 uL of pool from unmodified staples, 2 uL of pool from modified staples, 25 uL of the scaffold, and 1 Amicon filter. To prepare one sample for the smartphone measurements 150 µl of 10 pM is required, that is, one DNA origami stock is enough to prepare > 600 samples for the smartphone measurements.

* For the estimation, the price of commercially available scaffold was used. Produced in-house scaffold will yield a lower price.

^c Estimation takes into account costs that are hard to estimate and handling mistakes

The prices can be further reduced by larger scale purchases.

Supplementary References

1. Vogelsang, J. et al. A Reducing and Oxidizing System Minimizes Photobleaching and Blinking of Fluorescent Dyes. *Angewandte Chemie International Edition* **47**, 5465-5469 (2008).

Associated Publication 3

Fluorophore photostability and saturation in the hotspot of DNA origami nanoantennas

Lennart Grabenhorst*, Kateryna Trofymchuk*, Florian Steiner, Viktorija Glembockyte and Philip Tinnefeld

*equal contribution

Methods and Applications in Fluorescence **8**, 024003 (2020). doi: 10.1088/2050-6120/ab6ac8

(open access)

Methods and Applications in Fluorescence



PAPER

Fluorophore photostability and saturation in the hotspot of DNA origami nanoantennas

OPEN ACCESS

RECEIVED

30 August 2019

REVISED

18 December 2019

ACCEPTED FOR PUBLICATION

13 January 2020

PUBLISHED

5 February 2020

Original content from this work may be used under the terms of the [Creative Commons Attribution 4.0 licence](#).

Any further distribution of this work must maintain attribution to the author(s) and the title of the work, journal citation and DOI.



Lennart Grabenhorst^{1,3} , Kateryna Trofymchuk^{1,2,3}, Florian Steiner¹ , Viktorija Glembockyte^{1,4} and Philip Tinnefeld^{1,4}

¹ Department of Chemistry and Center for NanoScience, Ludwig-Maximilians-Universität München, Butenandtstr. 5-13, 81377 München, Germany

² Institute for Physical and Theoretical Chemistry—NanoBioScience and Braunschweig Integrated Centre of Systems Biology (BRICS), Technische Universität Braunschweig, Braunschweig, Germany

³ These authors contributed equally.

⁴ Author to whom any correspondence should be addressed.

E-mail: philip.tinnefeld@cup.lmu.de and viktorija.glembockyte@cup.lmu.de

Keywords: DNA nanotechnology, fluorescence microscopy, photostability, nanophotonics, plasmonics

Supplementary material for this article is available [online](#)

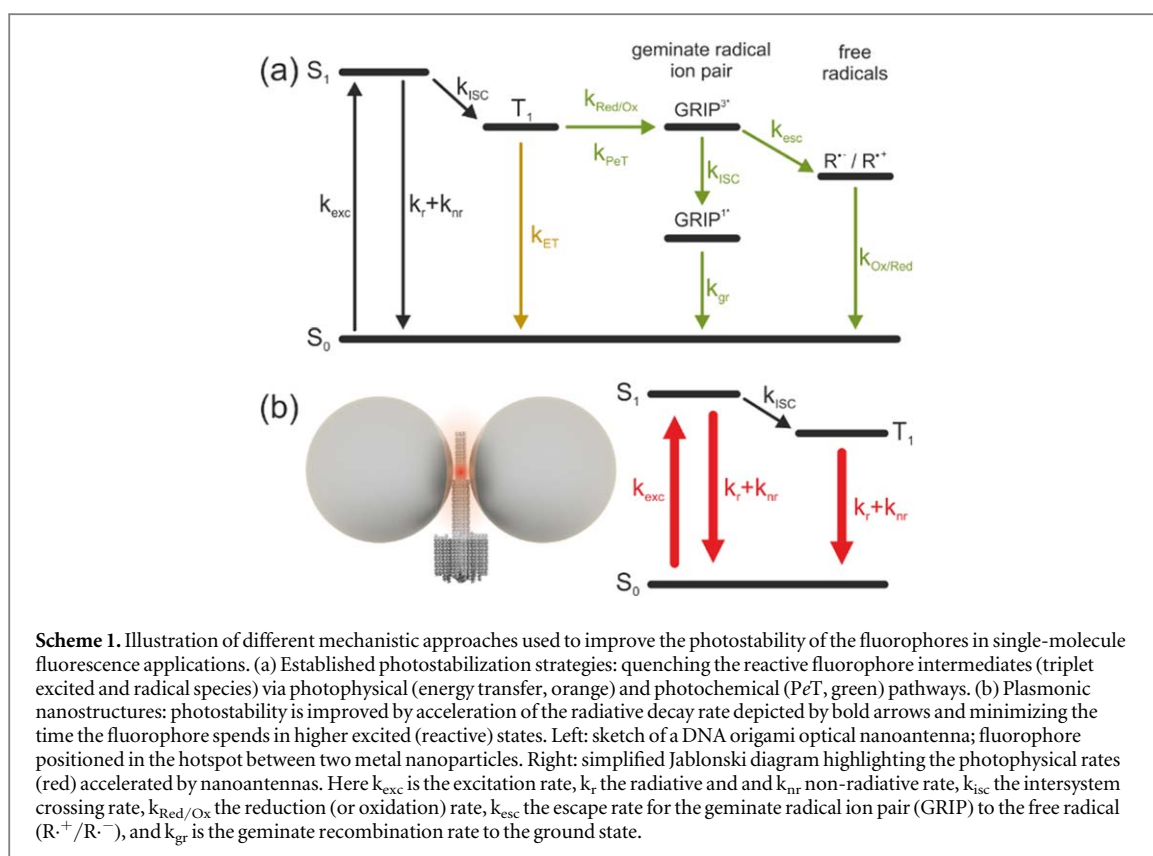
Abstract

Fluorescent dyes used for single-molecule spectroscopy can undergo millions of excitation-emission cycles before photobleaching. Due to the upconcentration of light in a plasmonic hotspot, the conditions for fluorescent dyes are even more demanding in DNA origami nanoantennas. Here, we briefly review the current state of fluorophore stabilization for single-molecule imaging and reveal additional factors relevant in the context of plasmonic fluorescence enhancement. We show that despite the improved photostability of single-molecule fluorophores by DNA origami nanoantennas, their performance in the intense electric fields in plasmonic hotspots is still limited by the underlying photophysical processes, such as formation of dim states and photoisomerization. These photophysical processes limit the photon count rates, increase heterogeneity and aggravate quantification of fluorescence enhancement factors. These factors also reduce the time resolution that can be achieved in biophysical single-molecule experiments. Finally, we show how the photophysics of a DNA hairpin assay with a fluorophore-quencher pair can be influenced by plasmonic DNA origami nanoantennas leading to implications for their use in fluorescence-based diagnostic assays. Especially, we show that such assays can produce false positive results by premature photobleaching of the dark quencher.

Introduction

For many years, researchers have been pushing organic fluorophores to their limits—simply because the fluorophore is the main bottleneck in most experiments involving fluorescence [1]. Photobleaching processes limit both the observation time of the molecule and the achievable time resolution of an experiment. This is especially relevant for observables that cannot be obtained from quasi-ensemble measurements such as nanosecond-fluorescence correlation spectroscopy (ns-FCS) [2] and require true single-molecule data, e.g. the observation of transition paths in conformational dynamics of biomolecules [3]. Furthermore, preliminary bleaching of fluorophores and quenchers can also influence the reliability of

fluorescence-based diagnostic assays. This push for more photons and stable fluorescence signal has led to new mechanistic insights of fluorophore photobleaching pathways as well as to the discovery of a plethora of suitable photostabilization strategies [1, 4–8]. In this paper, we briefly review the processes governing photostability and strategies to increase photostability with a focus on quenching intermediate states on the photobleaching pathway. We then place this discussion into the context of fluorophores next to plasmonic nanostructures. Based on our experimental data of photophysical effects and photostabilization in optical nanoantennas we reason that dim states of fluorophores are strikingly reducing the linear excitation intensity-dependent brightness of fluorophores and increase heterogeneity of fluorescence enhancement



values. In addition, the increased excitation fields and nonlinear bleaching pathways lead to photodestruction of fluorescence quencher molecules potentially leading to false positive results in basic assays of molecular diagnostics.

The total number of photons that can be detected from a given fluorophore is limited by its intrinsic photophysics and photochemistry [1, 9, 10]. An ideal fluorophore would cycle between its ground (S_0) and singlet excited (S_1) states emitting photons and reporting on the position or the state of the fluorescently labelled molecule (scheme 1(a)). At the high excitation rates required for single-molecule detection other photophysical processes come into play [11–13]. Intersystem crossing to the triplet excited state (T_1) can lead to long-lived and reactive triplet species. Furthermore, reduction or (photo)oxidation of the singlet or triplet excited state can lead to the formation of even longer-lived dark radical intermediates. While the triplet excited state is efficiently quenched by molecular oxygen, it leads to the generation of singlet oxygen as well as other reactive oxygen species capable of further accelerating the photobleaching reactions. Hence, established photostabilization approaches used to address these instabilities rely on combining the removal of oxygen (often via the use of enzymatic oxygen scavengers) with the addition of photostabilization additives that act as quenchers of reactive triplet and radical intermediates [8, 14].

With respect to triplet excited state quenchers, two mechanistically distinct approaches have been utilized

(scheme 1(a)). On the one hand, triplet excited states can be quenched via a photophysical pathway (i.e. energy transfer) by photostabilizers like cyclooctatetraene (COT) [8, 14] or Ni^{2+} ions [7, 15, 16]. On the other hand, triplet excited states can also be quenched via photoinduced electron transfer (PeT) with a reducing (e.g. ascorbic acid [5], Trolox [4, 6, 8], β -mercaptoethanol (β -ME) [6]) or an oxidizing agent (e.g. methyl viologen [5], Trolox quinone [4], 4-nitrobenzyl alcohol) which results in the formation of a radical anion or a radical cation, respectively. The resulting radical intermediates are rescued by the simultaneous use of both reducing and oxidizing agents—an approach that is known as reducing and oxidizing system (ROXS) [5]. The formation of long-lived radical intermediates and requirement of the complementary redox partner can be avoided if the PeT is followed by fast back electron transfer [17]. This requires a redox partner capable of assisting an intersystem crossing in the triplet geminate radical ion pair that is formed following the PeT step (scheme 1(a)) [18]. While these solution-based photostabilization approaches have significantly advanced single-molecule fluorescence studies by allowing to extend the experiments from few seconds to tens of minutes and providing photon budgets reaching millions [5, 7], one always has to keep in mind the potential influence of the photostabilizers on the biological system under investigation. One strategy that has been realized over the last decade to address this issue relies on direct coupling of photostabilizers with the fluorophores to

obtain ‘self-healing’ dyes [19]. Several small molecules have been conjugated or proximally linked to different single-molecule dyes that include COT [20–24], Trolox [20–24], 4-nitrobenzyl alcohol (NBA) [20], nitrophenylalanine (NPA) [21, 22, 25, 26], or a *tris*NTA moiety containing three Ni²⁺ ions [16].

The conventional approaches revolve around salvaging the pristine, fluorescent state from its reactive and non-emissive triplet or radical forms by supplying the appropriate reaction partner. Recently, another strategy for photostabilization has evolved which is complementary to these approaches. Plasmonic nanostructures have been shown to have a drastic influence on radiative and non-radiative rate constants [27] (scheme 1(b)), an effect that is generally attributed to changes in the local electric field strength in vicinity of the metal surface [28]. Additionally, the plasmonic nanostructure can also act as an optical antenna on the nanoscale focusing incident excitation light into zeptoliter volumes. When a fluorophore is positioned in such a volume (often referred to as a hotspot) its excitation and emission rates can be enhanced up to several hundred-fold, which allows to enhance its fluorescence signal as well as the photon count rates that can be obtained for single fluorescent molecules. The overall effect of a plasmonic nanostructure on the fluorescence properties of the dye depends on a number of different parameters, such as the distance to the metal surface, the spectral overlap between the excitation and emission spectra of the fluorophore and the plasmon resonance, the size and shape of the plasmonic nanostructure and, in the case of more complex nanoantennas, their spatial arrangement [28–30].

Many studies have focused on the capacity of plasmonic nanoantennas to enhance the fluorescence signal of single emitters, while only a few of them have addressed their unique ability to improve the photostability and the total number of emitted photons [31–34]. Here, the improvement in photostability is typically attributed to an increased radiative rate which, in turn, reduces the time a fluorophore spends in the first excited singlet state and minimizes the probability of photobleaching. In fact, in the simplest approximation where only photobleaching via one photon processes is considered, the total number of photons emitted (N), can be expressed as the ratio of fluorescence quantum yield (Φ_f) and fluorophore bleaching yield (Φ_b) [33, 35]:

$$N = \frac{\Phi_f}{\Phi_b} = \frac{k_r}{k_{all}} \times \frac{k_{all}}{k_b} = \frac{k_r}{k_b} \quad (1)$$

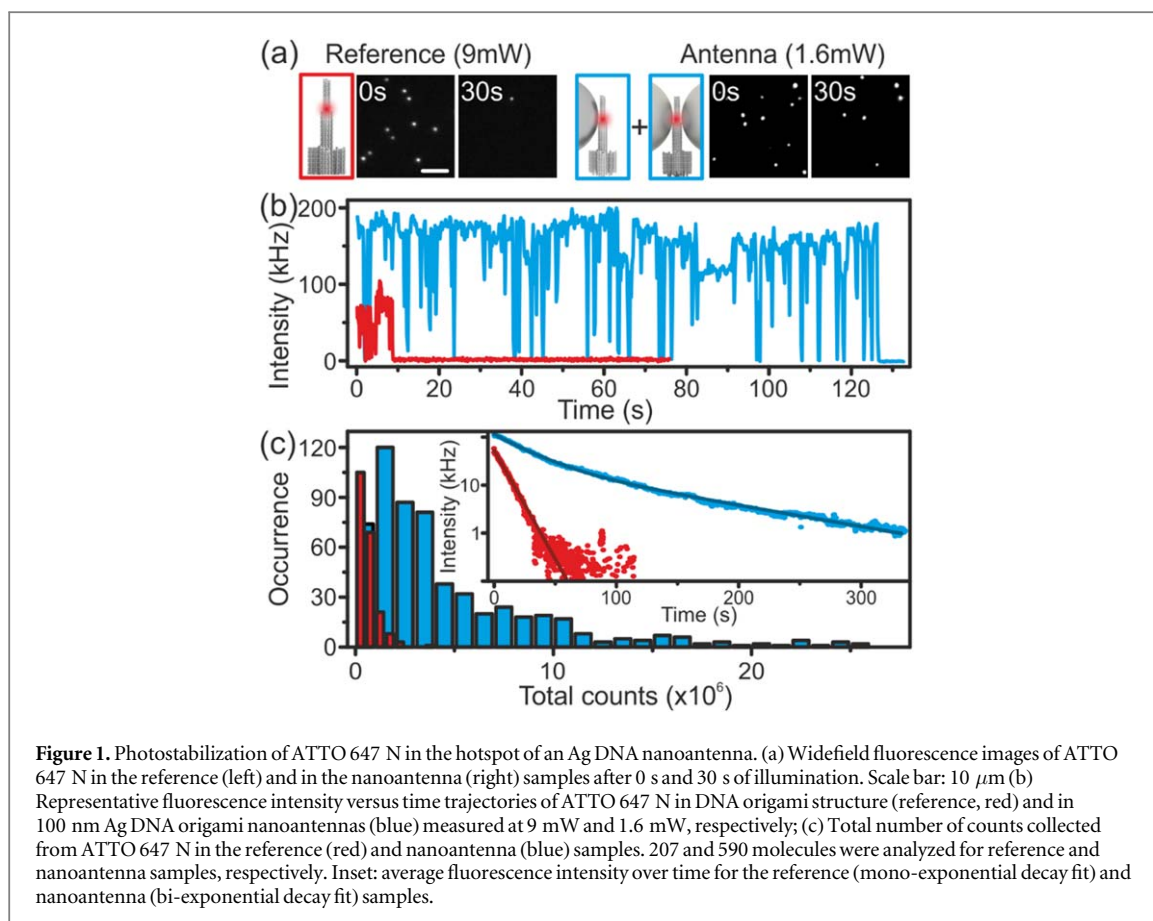
Where, k_r —radiative rate constant, k_b —bleaching rate constant, and k_{all} —sum of all rate constants for photophysical processes occurring from the fluorophore singlet excited state (radiative decay, non-radiative decay, intersystem crossing, and bleaching). Equation (1) illustrates how the photostability of a fluorescent molecule can be improved by either accelerating the radiative rate or decreasing the rate of

photobleaching. While traditional photostabilization approaches discussed earlier (scheme 1(a)) are aimed at slowing down the bleaching processes, photostabilization by plasmonic nanostructures (scheme 1(b)) offers an alternative and, perhaps even complementary approach to improve N by accelerating the radiative rate constant. Additionally, the plasmonic nanoparticles have also been shown to increase the radiative and non-radiative decay rates from the triplet excited states also suppressing the time the fluorophore spends in the excited T_1 state (scheme 1(b)) [32, 36, 37]. Depending on the efficiency of this triplet suppression, this offers an additional possibility to further improve the total photon budget (N) of organic fluorophores when coupled to plasmonic nanoantennas.

Plasmonic hotspots formed by a linear arrangement of two metallic nanoparticles exhibit an even greater electric field enhancement [38, 39], with reported values reaching up to 100-fold acceleration of the radiative decay [38]. For a decade now plasmonic dimer nanoantennas have been successfully fabricated via ion or electron beam lithography [40], but this approach suffers from uncontrolled positioning of a fluorophore in the hotspot: usually dyes are either fixed in an aid polymer coating [38] or they are observed as they diffuse freely through the hotspot region [41]. This not only drastically increases the time and the amount of materials spent for a single experiment but creates a large heterogeneity in the enhancement that is achieved for k_{ex} and k_r , as the enhanced electric field varies a lot within a hotspot [42].

Both problems can be addressed by employing an alternative approach of fabricating nanoantennas—self-assembly using DNA origami. In this technique a long single-stranded DNA (ssDNA) with known sequence is shaped with the help of multiple unique ssDNA to a desired configuration [43]. Labelling of a specific strand with a molecule of interest or a functional group (e.g. fluorophore, biotin, amino group) allows to spatially arrange it on a designed structure [44]. This approach has justified itself for performing detailed studies at the single-molecule level of changes in quantum yield and photophysical rates of fluorophores [27], the distance-dependent quenching of fluorescence [45], Förster resonance energy transfer (FRET) [46, 47] and finally, controlled reduction of photobleaching [31, 33] in proximity of metal nanoparticles. These optical antennas have already been employed for single-molecule detection at 25 μ M concentration [48] and in diagnostic assays [31, 33, 49], in proximity of metal nanoparticles.

Nevertheless, the influence of the nanoantenna on the photophysical properties of fluorophores remains to be fully understood. While it is agreed upon that the increase of the radiative decay rates can effectively lead to enhanced quantum yield of fluorophores, their improved photostability, and higher count rates that can be achieved in single-molecule fluorescence studies [31], we discovered that the achievable photon



output of the dye is not only limited by photobleaching but also by other photoinduced processes. By examining the photophysical properties of three dyes (ATTO 542, ATTO 647 N, and AlexaFluor 647) commonly used for single-molecule spectroscopy when placed in the hotspots of dimer 100 nm Ag DNA origami nanoantennas, we demonstrate that despite their improved photostability by the nanoantenna, the maximum photon count rate that can be achieved is still limited by their intrinsic photophysics, such as formation of dim states or increased rate of photoisomerization. Additionally, we show that the enhanced electric field in the hotspot region also poses challenges to the use of non-fluorescent molecules absorbing light, e.g. dark quenchers which are used in fluorescence-based diagnostic assays.

Results and discussion

Improved photon budgets of fluorophores in plasmonic DNA origami nanoantennas

To demonstrate the ability of nanoantennas to even further push the performance and improve the photon budgets of fluorophores in single-molecule fluorescence applications, we performed the photobleaching experiments with one of the most photostable single-molecule dyes—ATTO 647 N. We evaluated the photostability of this dye when placed in the hotspot of a 100 nm Ag DNA origami nanoantenna and

compared it to the same dye when placed in the reference DNA origami structure containing no nanoparticles (figure 1(a)). The DNA origami structures were immobilized on BSA-biotin coated glass surfaces via biotin/neutralavidin interactions using biotinylated DNA strands on the base of the nanostructure. After this step, the nanoantennas were formed by incorporating DNA functionalized 100 nm Ag nanoparticles. This nanofabrication protocol leads to the mixture of DNA origami structures containing two Ag nanoparticles (dimer) and only one Ag nanoparticle (monomer). The fluorescence intensity of single ATTO 647 N dyes in the nanoantenna and reference structures was monitored over time in a single-molecule wide field microscope in total internal reflection mode. Due to the enhanced local electric field in the nanoantenna hotspot the nanoantenna samples experience higher photon fluxes under the same irradiation intensity. Therefore, in these photobleaching experiments, the nanoantenna samples were excited at 647 nm using a laser power of 1.6 mW, while reference samples were excited at a higher laser power of 9 mW [50].

Our single-molecule photobleaching studies demonstrate that even if the photostability of ATTO 647 N is remarkable it can be further improved with the help of a 100 nm Ag nanoantenna without any additional photostabilizers or the need for oxygen removal. Figure 1(a) shows fluorescence images of

ATTO 647 N in the reference and Ag nanoantenna samples acquired at the beginning of the photobleaching experiment (0 s) and after 30 s of illumination. While most of the dyes in the reference sample are photobleached, the fluorescence of ATTO 647 N in the nanoantenna sample is preserved despite the higher fluorescence signal under these excitation powers (see also figure 1(c), inset). Single-molecule fluorescence intensity versus time trajectories were extracted from these photobleaching experiments (see figure 1(b) for exemplary single-molecule trajectories) and the total number of counts until photobleaching was calculated for several hundreds of molecules from the reference and nanoantenna samples. The histograms of total counts detected until photobleaching (figure 1(c)) reveal on average ~10-fold, up to 40-fold for the most efficient nanoantennas improvement in ATTO 647 N photostability when in the hotspot of 100 nm Ag nanoantennas. Here, it is also worth noting that the heterogeneous distribution of total photon counts arises from the heterogeneous fluorescence enhancement and photostabilization efficiencies [39, 51]. The heterogeneous sample composition (monomer and dimer nanoantennas) also results in a bi-exponential photobleaching behavior when compared to the mono-exponential bleaching behavior of the reference sample (figure 1(c), inset).

Based on equation (1) and the radiative rate enhancement estimated by comparing fluorescence intensities normalized by power in nanoantenna samples to reference samples, one would expect a larger improvement in total number of detected photons for ATTO 647 N in the dimer Ag nanoantennas. Previous studies by Pellegrotti *et al* [33], have shown that at least for monomer Au nanoantennas, the total number of emitted photons by the fluorophore Cy5 was directly proportional to the changes in radiative rate of the fluorophore. However, one also has to consider that due to the electric field enhancement in dimer nanoantennas, fluorophores can experience an order of magnitude higher excitation rates when compared to monomer nanoantennas. Under these excitation conditions higher order photobleaching pathways, such as absorption of a second photon in the S_1 or T_1 states, might become relevant and the approximation made to derive equation (1) might not hold anymore. An indication for this is that no correlation can be seen between fluorescence intensity and total number of emitted photons (See figure S1 is available online at stacks.iop.org/MAF/8/024003/mmedia).

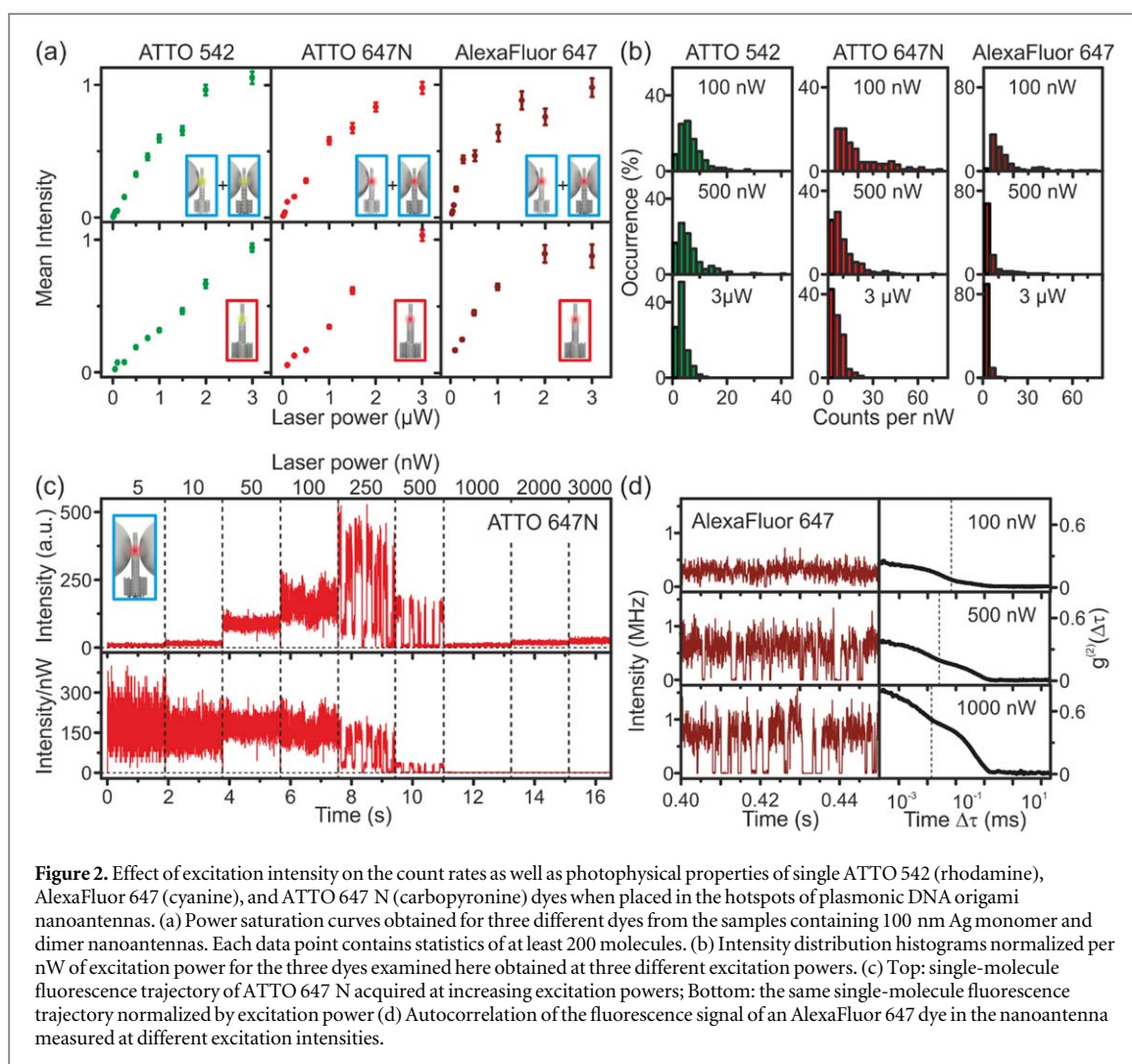
Power saturation and its implications in achieving high count rates required for studying fast dynamics

By providing means to enhance the fluorescence signal and fluorophore photostability, self-assembled DNA nanoantennas hold tremendous promise for advancing single-molecule experiments that require high photon count rates, e.g. studies of single-molecule

dynamics that occur on ms to μ s time scales. Naively, one would expect that the fluorescence enhancement values provided by nanoantennas directly translate into increased photon count rates. However, by studying the photophysical properties of three common dyes used in single-molecule spectroscopy, e.g. ATTO 542 (rhodamine), ATTO 647 N (carbopyronine), and AlexaFluor 647 (cyanine) when placed in the nanoantenna hotspot, we learned that the picture is more complex. As the dye molecules in the plasmonic hotspot experience a different photophysical environment and much higher photon fluxes, their saturation behavior changes. Figure 2(a) shows the global saturation behavior: in all cases, the onset of saturation is clearly visible for the nanoantenna samples. In the reference samples, however, ATTO 542 and ATTO 647 N show no visible saturation at the same excitation powers, only for AlexaFluor 647 we observe saturation in the reference sample which can be attributed to an accelerated cis-trans isomerization [52] as it will be shown later. Figure 2(b) contains the normalized intensity distribution histograms (per nW of excitation power, calculated by integration of the intensity of a confocal spot) obtained for the three dyes in nanoantenna hotspots. At low excitation powers (100 nW) a wide distribution of intensities is observed assigned to heterogeneous fluorescence enhancement in monomer and dimer nanoantennas. However, as the excitation power is increased (500 nW and 3 μ W in figure 2(b)) the distributions become narrower and shift to lower intensities suggesting that the most enhanced and thus the brightest fluorophores are the most sensitive to this saturation behavior.

In contrast to earlier studies on plasmonic enhanced light harvesting complexes [34], we found that this saturation is not originating from any fundamental emission limit of the fluorophore but rather from populating a second emissive state that is less bright in nature. While at low excitation intensities, the formation of this dim state is observed upon longer irradiation times, under increased excitation intensities and, in particular, in the hotspot of nanoantenna where the photon flux is highly increased, these dim states form rather readily. This is illustrated by the single-molecule fluorescence trajectory obtained for ATTO 647 N in the hotspot of a dimer Ag nanoantenna acquired at increasing excitation intensity. Reversible switching between dim and bright states can already be observed at 250 nW, while at 500 nW only the dim state of the dye is visible. A similar photo-induced formation of dim states was observed when analyzing single-molecule trajectories of ATTO 542 and AlexaFluor 647 (see figure S2).

Further mechanistic studies are required to confirm the exact nature of these dim states, however, we propose that it might be related to the formation of spectrally-shifted emissive forms of the fluorophores. Such spectral shifts leading to the formation of blue- and red-shifted emissive forms of fluorophores have



previously been observed in single-molecule fluorescence studies of rhodamine [53, 54], oxazine [53], cyanine [53], carbopyronine [5], terrylene diimide [55], and amino-triangulenium [56] dyes. The most extensive mechanistic studies of such spectral instabilities have been carried out for rhodamine class of dyes, where the spectral shift and formation of photo bleaching products have been associated with N-dealkylation of tertiary amine groups which proceeds via formation of a radical cation [57, 58]. In this respect, elegant strategies have been developed to overcome these spectral instabilities, e.g. by suppressing the formation of twisted intramolecular charge transfer excited states involved in the N-dealkylation [11, 58–62]. Better understanding of the mechanisms leading to these dim states and development of strategies to mitigate them, combined with the ability of plasmonic nanoantennas to enhance fluorescence signal and photostability, could provide exciting opportunities to push organic fluorophores beyond their current limits.

For the cyanine dye AlexaFluor 647 an additional saturation process is present, which was attributed to photoisomerization from fluorescent *trans* state to a non-fluorescent *cis* state [52, 63]. figure 2(d), shows single-molecule fluorescence trajectories and

corresponding autocorrelation curves obtained for AlexaFluor 647 at increasing excitation intensities. The enhanced photoisomerization at increasing excitation intensities is evident from the increase in the amplitude and the rate of the μs -time component. This additional non-radiative relaxation pathway in cyanines together with photoinduced formation of dim states results in a pronounced saturation behavior observed for both reference and nanoantenna samples of AlexaFluor 647 (figure 2(a)). These results suggest that when it comes to achieving high photon count rates, non-rigidified cyanine dyes are not the best fluorophores of choice.

The formation of dim states is the limiting factor in all experiments requiring very high photon count rates, such as single-molecule FRET experiments on fast timescales. Additionally, the power dependence shown in figure 2(a), also implies that one should be cautious when quantifying the fluorescence enhancement values provided by the nanoantenna. As illustrated in figure 2(b), the fluorescence intensity of the dye in the nanoantenna, hence, the calculated fluorescence enhancement, is very sensitive to the excitation intensity chosen for a given experiment. This photo-induced transition to the dark states might also impact

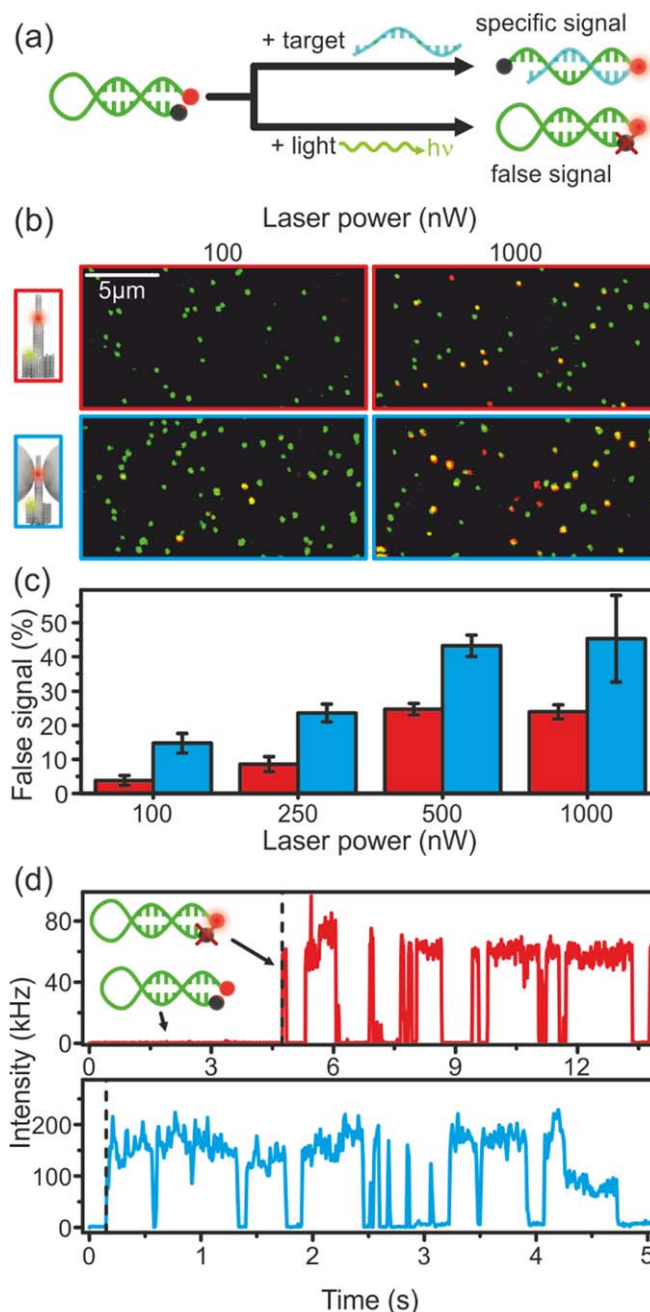


Figure 3. Fluorescence-quenching hairpin (FQH) and accelerated photobleaching of dark quenchers in the hotspot. (a) Schematic representation of FQH construct (for sequence, see SI) bearing ATTO 647 N on the 5'-end and Black Berry Quencher (BBQ650) on the 3'-end. Fluorescence signal from ATTO 647 N ('opened' FQH) is observed either after detection of the target DNA and opening (specific signal) or due to bleaching of BBQ650 (false signal); (b) Confocal fluorescence scans of the DNA origami reference (red) and 100 nm Ag nanoantenna samples bearing an FQH in the hotspot (blue) before addition of the target DNA. Scans are acquired at different powers while exciting with a 639 nm pulsed laser. The DNA origami is labeled with an ATTO 542 dye to allow co-localization of DNA origami and opened FQH. (c) Quantification of the false signal from the confocal fluorescence scans of the DNA origami and DNA origami nanoantennas containing an FQH at different excitation powers, calculated by division of the yellow spots (DNA origami with 'opened' FQH) by the sum of the yellow and green spots (DNA origami with 'closed' FQH). 260 to 440 spots were analyzed for each excitation power. Error bars represent the standard deviation from the mean of the three different scans analyzed. (d) Representative single-molecule trajectories of an FQH illuminated with a 639 nm laser (2 μW for reference (red), 1 μW for nanoantenna (blue)) demonstrating a bleaching event of BBQ650 indicated by the onset of ATTO 647 N fluorescence.

the results of novel biosensing assays in the hotspots of DNA nanoantennas, which rely on a sufficiently high contrast between enhanced and non-enhanced signal. It is therefore of utmost importance to ensure that the dye is emitting from its bright state in order to realize the full potential of plasmonic fluorescence enhancement.

Bleaching of dark quenchers in nanoantenna hotspot and its implications in diagnostics

The modular nature of DNA origami allows the introduction of biorecognition units into the hotspot region of nanoantennas, which offers means to improve the signal-to-noise ratio and overall performance of bioassays. For the successful application of

this concept, it is important to fully understand the photophysical behavior of the reporting unit, which usually consists of one or multiple fluorophores, in the plasmonic hotspot. In our efforts to utilize DNA nanoantennas for diagnostics, we discovered that the performance of diagnostic assays can be significantly influenced by photoinstabilities of dark quenchers when subjected to strong electric fields in the plasmonic hotspot.

Previously, we demonstrated the successful incorporation of a fluorescence-quenching hairpin (FQH) in DNA origami monomer nanoantennas and its application for single-molecule based detection of Zika virus nucleic acids [49]. An FQH, or a molecular beacon, is a self-hybridized nucleic acid sequence containing a fluorescent dye on the one end and a dark quencher on the other end (figure 3(a)). In its closed state, energy transfer from the fluorophore to the quencher occurs due to their close proximity. Upon the detection of the nucleic acid target, which is complementary to a part of the FQH, the hairpin opens increasing the distance between the fluorophore and the quencher and leading to onset of the fluorescence signal (specific signal) [64]. However, we report that photobleaching of the quencher can lead to false positive signal in single-molecule DNA hairpin assays. Due to non-quantitative labelling efficiency and possible photobleaching during handling or measurement steps not every FQH contains a dark quencher. This leads to emission of ATTO 647 N signal (false signal) (figure 3(a)) and therefore decreases the effectiveness of the assay. Although dark quenchers are less likely to take part in different photochemical reactions due to the very short excited state lifetime [65], their photophysics have not been studied under the conditions created in a plasmonic hotspot. Moreover, the effect of these photophysical processes to the bioassay performance has not been assessed.

To perform studies of FQH at the single-molecule level in a hotspot, DNA origami structures were labeled with a green dye (ATTO 542) for initial localization of the construct. The detection efficiency (opening of FQH) in the nanoantenna can be calculated by dividing the number of yellow spots in a fluorescence scan (co-localized signal from ATTO 542 and ATTO 647 N) by the total amount of spots in a fluorescence scan. Even before addition of the target, a small percentage of co-localized spots can be observed due to the reasons mentioned above. Fluorescence scans performed with different excitation powers at 639 nm excitation laser (100 nW—1000 nW) demonstrate an increase in the amount of ‘opened’ FQH both for the reference sample (4%–24%) as well as for the 100 nm Ag nanoparticles nanoantenna (15%–45%) (figures 3(b) and (c)). The higher level of false positive signal in the nanoantenna sample can be related to the photobleaching of the dark quencher. From this result it is possible to estimate the quencher survival time knowing the time of exposure for each spot as it is

explained in the SI and shown in figure S3. To investigate the photostability of the dark quencher, we illuminated green spots detected in the fluorescence scan with a 639 nm laser at an intensity of 2 μ W (reference, red) and 1 μ W (nanoantenna, blue). After some time, we observed the occurrence of a signal in the red channel for both, the reference and the nanoantenna sample, which corresponds to the donor fluorescence (figure 3(d)). The reduced quencher survival time is visible in the nanoantenna even at lower excitation power due to the tight focusing of the light. A similar photobleaching behavior has been reported earlier for an ATTO 532/BBQ650 FRET pair [65].

Although the photostability of conventional fluorophores in a plasmonic hotspot is increased [31, 33], the behavior we observed for a fluorophore/quencher reporting unit was very different. In the present study we demonstrated that the dark quencher serving as an energy acceptor in a hotspot can be selectively photobleached in dimer nanoantennas leading to the strong false positive signal and decrease of the overall contrast of the assay.

Conclusion

By using plasmonic nanoantennas, we drastically reduced conventional photobleaching pathways and revealed additional photoinduced processes that limit the maximum photon output of three classes of fluorophores tested here. During our study, we encountered two problems related to the intrinsic photophysics of these dyes: population of weakly fluorescent, dim states - which seems to be a general feature of all tested fluorophores - as well as acceleration of photoisomerization rates at higher excitation powers for cyanine derivatives. Both problems pose a limit on the photon count rates that can be achieved in the plasmonic hotspot. The formation of the dim states could be potentially overcome by utilizing spectrally stable fluorophores [11, 59, 60] The second problem can be circumvented relatively easy by employing fluorophores that do not undergo photo-induced isomerization (e.g. carbopyronines or rhodamines) or by altering the molecular structure of the cyanine dye in order to sterically hinder the isomerization [66].

Here, we also demonstrated that the enhanced excitation rate in the nanoantenna hotspot can affect non-fluorescent chromophores, e.g. dark quenchers. Once placed in a hotspot, the dark quencher experiences not only an efficient energy transfer from the donor dye but also an enhanced electric field and thus an increased excitation rate, which together leads to accelerated photobleaching. This premature photobleaching can be an issue when using fluorogenic probes in a hotspot for different biosensing assays. As illustrated in this work, fast quencher photobleaching can also lead to high false positive signal and decrease

of the overall contrast of the assay. In our case, the photobleaching could be substantially reduced when using lower excitation powers. Alternatively, one could also consider utilizing more stable and robust fluorescence quenchers, such as small gold nanoparticles.

To conclude, we showed that plasmonic hotspots can be employed to substantially enhance the photostability of conventional fluorophores. This enables exciting new applications for fluorescent molecules in which photostability and photon count rate are of crucial importance, such as low-cost single-molecule detectors for point-of-care diagnostics [49], where even the cheapest cameras could potentially be used to detect an infectious disease, or single-molecule biophysics, where the time resolution for FRET experiments could be increased substantially [67]. Here, we show that despite this improved photostability, the performance of conventional dyes used in single-molecule spectroscopy when combined with plasmonic nanoantennas is still limited by their underlying photophysical processes, such as formation of dim states or photoinduced isomerization. We envision that better mechanistic understanding of these limitations and mitigation of the unwanted photophysical pathways, such as the ones described in this work, will contribute to further advancing single-molecule fluorescence applications.

Materials and methods

Fabrication of DNA origami nanoantennas

DNA origami structures were designed in caDNA2 [68] and assembled and purified using protocols based on Wagenbauer *et al* [69]. In brief, 25 μl of p8064 scaffold (produced in-house) at 100 nM were mixed with 18 μl of unmodified staples pooled from 100 μM original concentration and 2 μl of modified staples, pooled from 100 μM original concentration. All staples were purchased from Eurofins Genomics GmbH (Germany). 5 μl of folding buffer (200 mM MgCl_2 , 50 mM Tris, 50 mM NaCl, 10 mM EDTA) were added and the mixture was subjected to a thermal annealing ramp (table S1). Samples were purified using 100 kDa MWCO Amicon Ultra filters (Merck, Germany) with 4 washing steps with a lower ionic strength buffer (5 mM MgCl_2 , 5 mM Tris, 5 mM NaCl, 1 mM EDTA) for 5 min at 10000 rpm, 20 °C.

LabTek-II chambers (Thermo Fisher Scientific, USA) were cleaned with 1 M KOH for at least 20 min, washed three times with PBS buffer and then incubated with BSA-Biotin (0.5 mg mL^{-1} , Sigma-Aldrich, USA) and streptavidin (0.2 mg mL^{-1} , Thermo Fisher Scientific, USA). The origami was immobilized on the biotin-streptavidin surfaces using covalently attached biotin modifications on the six staple strands on the base. Density of DNA origami nanoantennas on the

surface suitable for single-molecule measurements was checked on a microscope.

100 nm silver nanoparticles were functionalized with ssDNA based on previously described procedures [49]. 100 nm Silver Nanospheres (Citarate, Biopure) were purchased from nanoComposix (USA). 2 ml nanoparticles (330-fold diluted in MiliQ water) were mixed with 20 μl Tween20 (10%) and 20 μl of a 4:5 (v:v) mixture of 1 M monobasic and dibasic potassium phosphate buffers (Sigma Aldrich, USA) and 20 μl of a 100 μM solution of 3'-thiolated T25 oligonucleotides (Ella Biotech, Germany) and stirred for 1 h at 40 °C. Then, the sodium chloride concentration was subsequently raised to 750 mM using PBS buffer containing 3.3 M NaCl. The solution was centrifuged at 2.8 krcf for 8 min at 20 °C. The supernatant was discarded, and the pellet was re-suspended in PBS containing 10 mM NaCl, 2.11 mM P8709 buffer (Sigma Aldrich, USA), 2.89 mM P8584 buffer (Sigma Aldrich, USA), 0.01% Tween20 and 1 mM EDTA. This washing step was repeated five times. Then, the pellet was re-suspended in TE buffer containing 750 mM NaCl and the concentration was adjusted to reach 0.1 absorption at 485 nm (maximum of absorbance) on a UV-vis spectrometer (Nanodrop 2000, Thermo Fisher Scientific, USA). To bind the nanoparticles to the origami, the chambers were incubated with 100 μl of this solution overnight.

Confocal microscopy

Confocal fluorescence measurements were performed using a home-built confocal setup based on an Olympus IX-83 inverted microscope (Japan) and a 78 MHz-pulsed supercontinuum white light laser (SuperK Extreme, NKT Photonics, Denmark) with selected wavelengths of 532 nm and 639 nm. The wavelengths are selected via an acousto-optically tunable filter (AOTF, SuperK Dual AOTF, NKT Photonics, Denmark). This is controlled by a digital controller (AODS 20160 8 R, Crystal Technology, USA) via a computer software (AODS 20160 Control Panel, Crystal Technology, USA). A second AOTF (AA.AOTF.ns: TN, AA Opto-Electronic, France) was used to alternate 532 nm and 639 nm wavelengths if required, as well as to further spectrally clean the laser beam. It is controlled via home-made LabVIEW software (National Instruments, USA). A neutral density filter was used to regulate the laser intensity, followed by a linear polarizer and a $\lambda/4$ plate to achieve circularly polarized excitation. A dichroic beam splitter (ZT532/640rpc, Chroma, USA) and an immersion oil objective (UPlanSApo 100 \times , NA = 1.4, WD = 0.12 mm, Olympus, Japan) were used to focus the excitation laser onto the sample. Micropositioning was performed using a Piezo-Stage (P-517.3CL, E-501.00, Physik Instrumente GmbH&Co. KG, Germany). Emitted light was then collected using the same

objective and filtered from the excitation light by the dichroic beam splitter. The light was later focused on a 50 μm pinhole (Linos) and detected using Single-Photon Avalanche Diodes (SPCM, AQR 14, PerkinElmer, USA) registered by an TCSPC system (Hydra-Harp 400, PicoQuant, Germany) after additional spectral filtering (RazorEdge 647, Semrock, USA for a red channel and HC582/75, AHF Analysentechnik, Germany for a green channel). A custom-made LabVIEW software (National Instruments, USA) was used to process the acquired raw data. The autocorrelation of the Alexa Fluor 647 signal was calculated using SymphoTime 64 (PicoQuant, Germany). For the fluorescence autocorrelation, measurements were carried out in a reducing and oxidizing buffer system with enzymatic oxygen removal consisting of 90% buffer a (100 mM MgCl_2 , 40 mM Tris, 2 mM Trolox/Trolox-quinone and 1% w/v Glucose) and 10% buffer b (glucose oxidase (1 mg ml^{-1}), 0.4% (v/v) catalase (50 $\mu\text{g ml}^{-1}$), 30% glycerol, 12.5 mM KCl in 50 mM TRIS).

Photostability studies on the wide-field microscope

Single-molecule photostability studies of nanoantenna and the reference samples were performed on the commercial Nanoimager S (ONI, UK). Samples were illuminated with a 640-nm laser at 53.5° angle to achieve evanescent excitation due to total internal reflection at the glass-water interface. Reference samples were excited with laser power of 9 mW, while nanoantenna samples were imaged at 1.6 mW. The laser beam was focused onto the back-focal plane of an oil-immersion objective (100 \times , NA = 1.4) and the emission light was detected with an sCMOS camera. Simultaneous photobleaching of few hundreds of fluorescent molecules was recorded in the field of view of 50 \times 80 μm . For further analysis, only the central region with even illumination was used. Single-molecule fluorescence intensity versus time trajectories were extracted using a home-built analysis routine in ImageJ. The intensity of a circular regions of 8 pixels in diameter around the molecules were integrated as a function of time. For the background correction from these transients the average intensity of at least 15 regions of the 8-pixel areas containing no molecules was subtracted. To get the total counts from molecules the sum of intensity after the background subtraction was calculated.

Acknowledgments

We gratefully acknowledge financial support from the DFG (INST 86/1904-1 FUGG, excellence clusters NIM and e-conversion), BMBF (Grants POCEMON, 13N14336, and SIBOF, 03VP03891), and the European Union's Horizon 2020 research and innovation

program under grant agreement No. 737089 (Chip-scope). V G and K T acknowledge the support by Humboldt Research Fellowship from the Alexander von Humboldt Foundation. The authors have declared that no conflicting interests exist.

ORCID iDs

Lennart Grabenhorst  <https://orcid.org/0000-0001-9503-1819>

Florian Steiner  <https://orcid.org/0000-0002-9148-5837>

Viktorija Glembockyte  <https://orcid.org/0000-0003-2531-6506>

Philip Tinnefeld  <https://orcid.org/0000-0003-4290-7770>

References

- [1] Ha T and Tinnefeld P 2012 Photophysics of fluorescent probes for single-molecule biophysics and super-resolution imaging *Annu. Rev. Phys. Chem.* **63** 595–617
- [2] Nettels D, Gopich I V, Hoffmann A and Schuler B 2007 Ultrafast dynamics of protein collapse from single-molecule photon statistics *Proc. Natl Acad. Sci. USA* **104** 2655–60
- [3] Chung H S, McHale K, Louis J M and Eaton W A 2012 Single-molecule fluorescence experiments determine protein folding transition path times *Science* **335** 981–4
- [4] Cordes T, Vogelsang J and Tinnefeld P 2009 On the mechanism of trolox as antiblinking and antibleaching reagent *J. Am. Chem. Soc.* **131** 5018–9
- [5] Vogelsang J, Kasper R, Steinhauer C, Person B, Heilemann M, Sauer M and Tinnefeld P 2008 A reducing and oxidizing system minimizes photobleaching and blinking of fluorescent dyes *Ang. Chem. Int. Ed.* **47** 5465–9
- [6] Rasnik I, McKinney S A and Ha T 2006 Nonblinking and long-lasting single-molecule fluorescence imaging *Nat. Meth.* **3** 891–3
- [7] Glembockyte V, Lin J and Cosa G 2016 Improving the photostability of red- and green-emissive single-molecule fluorophores via Ni^{2+} mediated excited triplet-state quenching *J. Phys. Chem. B* **120** 11923–9
- [8] Dave R, Terry D S, Munro J B and Blanchard S C 2009 Mitigating unwanted photophysical processes for improved single-molecule fluorescence imaging *Biophys. J.* **96** 2371–81
- [9] Gust A, Zander A, Gietl A, Holzmeister P, Schulz S, Lalkens B, Tinnefeld P and Grohmann D 2014 A starting point for fluorescence-based single-molecule measurements in biomolecular research *Molecules* **19** 15824
- [10] Cordes T, Maiser A, Steinhauer C, Schermelleh L and Tinnefeld P 2011 Mechanisms and advancement of antifading agents for fluorescence microscopy and single-molecule spectroscopy *Phys. Chem. Chem. Phys.* **13** 6699–709
- [11] Grimm J B et al 2016 Bright photoactivatable fluorophores for single-molecule imaging *Nat. Methods* **13** 985–8
- [12] Zheng Q and Lavis L D 2017 Development of photostable fluorophores for molecular imaging *Curr. Opin. Struct. Biol.* **39** 32–8
- [13] Stennett E M S, Ciuba M A and Levitus M 2014 Photophysical processes in single molecule organic fluorescent probes *Chem. Soc. Rev.* **43** 1057–75
- [14] Widengren J, Chmyrov A, Eggeling C, Löfdahl P-Å and Seidel C A M 2006 Strategies to improve photostabilities in ultrasensitive fluorescence spectroscopy *J. Phys. Chem. A* **111** 429–40
- [15] Glembockyte V, Lincoln R and Cosa G 2015 Cy3 photoprotection mediated by Ni^{2+} for extended single-

- molecule imaging: old tricks for new techniques *J. Am. Chem. Soc.* **137** 1116–22
- [16] Glembockyte V, Wieneke R, Gatterdam K, Gidi Y, Tampé R and Cosa G 2018 Tris-N-nitrotriacetic acid fluorophore as a self-healing dye for single-molecule fluorescence imaging *J. Am. Chem. Soc.* **140** 11006–12
- [17] Holzmeister P, Gietl A and Tinnefeld P 2014 Geminate recombination as a photoprotection mechanism for fluorescent dyes *Ang. Chem. Int. Ed.* **53** 5685–8
- [18] Glembockyte V and Cosa G 2017 Redox-based photostabilizing agents in fluorescence imaging: the hidden role of intersystem crossing in geminate radical ion pairs *J. Am. Chem. Soc.* **139** 13227–33
- [19] Tinnefeld P and Cordes T 2012 ‘Self-healing’ dyes: intramolecular stabilization of organic fluorophores *Nat. Meth.* **9** 426–7
- [20] Altman R B, Terry D S, Zhou Z, Zheng Q, Geggieger P, Kolster R A, Zhao Y, Javitch J A, Warren J D and Blanchard S C 2012 Cyanine fluorophore derivatives with enhanced photostability *Nat. Meth.* **9** 68–71
- [21] van der Velde J H M *et al* 2016 A simple and versatile design concept for fluorophore derivatives with intramolecular photostabilization *Nat. Commun.* **7** 10144
- [22] van der Velde J H M, Oelerich J, Huang J, Smit J H, Hiermaier M, Ploetz E, Herrmann A, Roelfes G and Cordes T 2014 The power of two: covalent coupling of photostabilizers for fluorescence applications *J. Phys. Chem. Lett.* **5** 3792–8
- [23] van der Velde J H M, Ploetz E, Hiermaier M, Oelerich J, de Vries J W, Roelfes G and Cordes T 2013 Mechanism of intramolecular photostabilization in self-healing cyanine fluorophores *Chem. Phys. Chem.* **14** 4084–93
- [24] Zheng Q, Jockusch S, Zhou Z, Altman R B, Warren J D, Turro N J and Blanchard S C 2012 On the mechanisms of cyanine fluorophore photostabilization *J. Phys. Chem. Lett.* **3** 2200–3
- [25] van der Velde J H M, Uusitalo J J, Ugen L-J, Warszawik E M, Herrmann A, Marrink S J and Cordes T 2015 Intramolecular photostabilization via triplet-state quenching: design principles to make organic fluorophores ‘self-healing’ *Farad. Discuss.* **184** 221–35
- [26] Smit J H, van der Velde J H M, Huang J, Trauschke V, Henrikus S S, Chen S, Eleftheriadis N, Warszawik E M, Herrmann A and Cordes T 2019 On the impact of competing intra- and intermolecular triplet-state quenching on photobleaching and photoswitching kinetics of organic fluorophores *Phys. Chem. Phys.* **21** 3721–33
- [27] Holzmeister P, Pibiri E, Schmied J J, Sen T, Acuna G P and Tinnefeld P 2014 Quantum yield and excitation rate of single molecules close to metallic nanostructures *Nat. Commun.* **5** 5356
- [28] Anger P, Bharadwaj P and Novotny L 2006 Enhancement and quenching of single-molecule fluorescence *Phys. Rev. Lett.* **96** 113002
- [29] Heck C, Prinz J, Dathe A, Merk V, Stranik O, Fritzsche W, Kneipp J and Bald I 2017 Gold nanolenses self-assembled by DNA origami *ACS Photonics* **4** 1123–30
- [30] Maier S A 2007 *Plasmonics: Fundamentals and Applications*. (United States of America: Springer Science & Business Media)
- [31] Kaminska I, Vietz C, Cuartero-González Á, Tinnefeld P, Fernández-Domínguez A I and Acuna G P 2018 Strong plasmonic enhancement of single molecule photostability in silver dimer optical antennas *Nanophotonics* **7** 643–9
- [32] Kéna-Cohen S, Wiener A, Sivan Y, Stavrinou P N, Bradley D D C, Horsfield A and Maier S A 2011 Plasmonic sinks for the selective removal of long-lived states *ACS Nano* **5** 9958–65
- [33] Pellegrotti J V, Acuna G P, Puchkova A, Holzmeister P, Gietl A, Lalkens B, Stefani F D and Tinnefeld P 2014 Controlled reduction of photobleaching in DNA origami–gold nanoparticle hybrids *Nano Lett.* **14** 2831–6
- [34] Wientjes E, Renger J, Cogdell R and van Hulst N F 2016 Pushing the photon limit: nanoantennas increase maximal photon stream and total photon number *J. Phys. Chem. Lett.* **7** 1604–9
- [35] Hirschfeld T 1976 Quantum efficiency independence of the time integrated emission from a fluorescent molecule *Appl. Opt.* **15** 3135–9
- [36] Zhang Y, Aslan K, Previte M J R, Malyn S N and Geddes C D 2006 Metal-enhanced phosphorescence: interpretation in terms of triplet-coupled radiating plasmons *J. Phys. Chem. B* **110** 25108–14
- [37] Pacioni N L, González-Béjar M, Alarcón E, McGilvray K L and Scaiano J C 2010 Surface plasmons control the dynamics of excited triplet states in the presence of gold nanoparticles *J. Am. Chem. Soc.* **132** 6298–9
- [38] Kinkhabwala A, Yu Z, Fan S, Avlasevich Y, Müllen K and Moerner W E 2009 Large single-molecule fluorescence enhancements produced by a bowtie nanoantenna *Nat. Photonics* **3** 654–7
- [39] Acuna G P, Moller F M, Holzmeister P, Beater S, Lalkens B and Tinnefeld P 2012 Fluorescence enhancement at docking sites of DNA-directed self-assembled nanoantennas *Science* **338** 506–10
- [40] Sundaramurthy A, Schuck P J, Conley N R, Fromm D P, Kino G S and Moerner W E 2006 Toward nanometer-scale optical photolithography: utilizing the near-field of bowtie optical nanoantennas *Nano Lett.* **6** 355–60
- [41] Punj D, Mivelle M, Moparthy S B, van Zanten T S, Rigneault H, van Hulst N F, Garcia-Parajo M F and Wenger J 2013 A plasmonic ‘antenna-in-box’ platform for enhanced single-molecule analysis at micromolar concentrations *Nat. Nanotechnol.* **8** 512–6
- [42] Chikkaraddy R *et al* 2018 Mapping nanoscale hotspots with single-molecule emitters assembled into plasmonic nanocavities using DNA origami *Nano Lett.* **18** 405–11
- [43] Rothmund P W K 2006 Folding DNA to create nanoscale shapes and patterns *Nature* **440** 297–302
- [44] Schreiber R, Do J, Roller E-M, Zhang T, Schüller V J, Nickels P C, Feldmann J and Liedl T 2013 Hierarchical assembly of metal nanoparticles, quantum dots and organic dyes using DNA origami scaffolds *Nat. Nanotechnol.* **9** 74
- [45] Acuna G P *et al* 2012 Distance dependence of single-fluorophore quenching by gold nanoparticles studied on DNA origami *ACS Nano* **6** 3189–95
- [46] Aissaoui N, Moth-Poulsen K, Käll M, Johansson P, Wilhelmsson L M and Albinsson B 2017 FRET enhancement close to gold nanoparticles positioned in DNA origami constructs *Nanoscale* **9** 673–83
- [47] Bohlen J, Cuartero-González Á, Pibiri E, Ruhlandt D, Fernández-Domínguez A I, Tinnefeld P and Acuna G P 2019 Plasmon-assisted Förster resonance energy transfer at the single-molecule level in the moderate quenching regime *Nanoscale* **11** 7674–81
- [48] Puchkova A, Vietz C, Pibiri E, Wunsch B, Sanz Paz M, Acuna G P and Tinnefeld P 2015 DNA origami nanoantennas with over 5000-fold fluorescence enhancement and single-molecule detection at 25 μ M *Nano Lett.* **15** 8354–9
- [49] Ochmann S E, Vietz C, Trofymchuk K, Acuna G P, Lalkens B and Tinnefeld P 2017 Optical nanoantenna for single molecule-based detection of zika virus nucleic acids without molecular multiplication *Anal. Chem.* **89** 13000–7
- [50] We note that decreasing the power at which we excite the reference would have prevented us from detecting every molecule, while increasing the power at which we excite the nanoantenna sample would have led to saturation effects
- [51] Vietz C, Kaminska I, Sanz Paz M, Tinnefeld P and Acuna G P 2017 Broadband fluorescence enhancement with self-assembled silver nanoparticle optical antennas *ACS Nano* **11** 4969–75
- [52] Widengren J and Schwille P 2000 Characterization of photoinduced isomerization and back-isomerization of the cyanine dye Cy5 by fluorescence correlation spectroscopy *J. Phys. Chem. A* **104** 6416–28
- [53] Tinnefeld P, Herten D-P and Sauer M 2001 Photophysical dynamics of single molecules studied by spectrally-resolved

- fluorescence lifetime imaging microscopy (SFLIM) *J. Phys. Chem. A* **105** 7989–8003
- [54] Heilemann M, Tinnefeld P, Sanchez Mosteiro G, Garcia Parajo M, Van Hulst N F and Sauer M 2004 Multistep energy transfer in single molecular photonic wires *JACS* **126** 6514–5
- [55] Liao Z, Hooley E N, Chen L, Stappert S, Müllen K and Vosch T 2013 Green emitting photoproducts from terrylene diimide after red illumination *JACS* **135** 19180–5
- [56] Liao Z, Bogh S A, Santella M, Rein C, Sørensen T J, Laursen B W and Vosch T 2016 Emissive photoconversion products of an amino-triangulenium dye *J. Phys. Chem. A* **120** 3554–61
- [57] Evans N A 1973 Photofading of rhodamine dyes: II. Photodealkylation of rhodamine B *J. Soc. Dyers Colour.* **89** 332
- [58] Butkevich A N, Bossi M L, Lukinavicius G and Hell S W 2019 Triarylmethane fluorophores resistant to oxidative photobleaching *J. Am. Chem. Soc.* **141** 981–9
- [59] Song X, Johnson A and Foley J 2008 7-Azabicyclo[2.2.1]heptane as a unique and effective dialkylamino auxochrome moiety: demonstration in a fluorescent rhodamine dye *JACS* **130** 17652–3
- [60] Liu X, Qiao Q, Tian W, Liu W, Chen J, Lang M J and Xu Z 2016 Aziridinyl fluorophores demonstrate bright fluorescence and superior photostability by effectively inhibiting twisted intramolecular charge transfer *JACS* **138** 6960–3
- [61] Grimm J B et al 2015 A general method to improve fluorophores for live-cell and single-molecule microscopy *Nat. Methods* **12** 244–50
- [62] Grimm J B et al 2017 A general method to fine-tune fluorophores for live-cell and *in vivo* imaging *Nat. Methods* **14** 987–94
- [63] Levitus M and Ranjit S 2011 Cyanine dyes in biophysical research: the photophysics of polymethine fluorescent dyes in biomolecular environments *Q. Rev. Biophys.* **44** 123–51
- [64] Tyagi S and Kramer F R 1996 Molecular beacons: probes that fluoresce upon hybridization *Nat. Biotechnol.* **14** 303–8
- [65] Holzmeister P, Wunsch B, Gietl A and Tinnefeld P 2014 Single-molecule photophysics of dark quenchers as non-fluorescent FRET acceptors *Photochem. Photobiol. Sci.* **13** 853–8
- [66] Michie M S, Gotz R, Franke C, Bowler M, Kumari N, Magidson V, Levitus M, Loncarek J, Sauer M and Schnermann M J 2017 Cyanine conformational restraint in the far-red range *J. Am. Chem. Soc.* **139** 12406–9
- [67] Chung H S and Eaton W A 2018 Protein folding transition path times from single molecule FRET *Curr. Opin. Struct. Biol.* **48** 30–9
- [68] Douglas S M, Marblestone A H, Teerapittayanon S, Vazquez A, Church G M and Shih W M 2009 Rapid prototyping of 3D DNA-origami shapes with caDNAno *Nucleic Acids Res.* **37** 5001–6
- [69] Wagenbauer K F, Engelhardt F A S, Stahl E, Hecht V K, Stommer P, Seebacher F, Meregalli L, Ketterer P, Gerling T and Dietz H 2017 How we make DNA origami *Chem. Bio. Chem.* **18** 1873–85

Supporting Information for

Fluophore Photostability and Saturation in the Hotspot of DNA Origami Nanoantennas

Lennart Grabenhorst,^{1†} Kateryna Trofymchuk,^{1,2†} Florian Steiner,¹ Viktorija Glembockyte,^{*,1} and Philip Tinnefeld^{*,1}

¹ Department of Chemistry and Center for NanoScience, Ludwig-Maximilians-Universität München, Butenandtstr. 5-13, 81377 München, Germany

² Institute for Physical and Theoretical Chemistry – NanoBioScience and Braunschweig Integrated Centre of Systems Biology (BRICS), Technische Universität Braunschweig, Braunschweig, Germany

Tab. S1 Unmodified staple strands

Name	Sequence (5'→3')
P1A1	CTTAAATCCCGGCGGTTGTG
P1A2	CAAGGGGCAACTCATGGTCATAGCTAAGGGAGAGA
P1A3	TGGGCACTAAAAAAGAGTCTGTCCTTTGATTTCAAACCTTAC
P1A4	TCAATGCTCAGTACCAGGGAGACTCGATTGGCCCA
P1A5	ATACAGAACCCTTCTGACGTCTGAAAGAGCCA
P1A6	TTTAAATGTTTGTCTGAGATTTAGGACCCACGCGAA
P1A7	GAAGGTATTATCACCCAGCAAAATCACCTTACCATTAGC
P1A8	AGAGTTCGTAAAGCTGATCTCATAAGGATTGACTGCCAGTTTGAGGCAG
P1A9	TGTGATAAATTTAGCCGGAACGAGATATATTCTCA
P1A10	TACGCCAATTTAGAGCTTAATCTCACCCACCATAAGAAA
P1A11	GTTGCGTCGGATTCTCGTAGCATTCTCGTAA
P1A12	AGGCTTGCCCTGACTTTAATC
P1B1	TTTGACCAAAAAGAAATACGTAATGCCACAGACTTTCATC
P1B2	AATTGTTTCATTCCATATTCAAAAAGCTATCAATTG
P1B3	AGGTTACTAGCCTTAAATCAAGATTTTGCACAGCATTGGAGGCAG
P1B4	TAGTACTAAAGTACGGTGCCGAAAGATTTTGTATTGTAATTTGTTGGGT
P1B5	CTTCAAAGCTGTAGCCAAATGGTCAATAAGCAAGGCATAAAAA
P1B6	ATCCATGTAATAGATTAAGCACGTATAACGTGCGCTAGTTT
P1B7	AAAAATAGGAGCCGGGCTCAGCAAATCGTTAAAAGGAGGCC
P1B8	ATCCTTTGCAACAGGAAAAACGCT
P1B9	GTCGAGGACCCGCCGCACCTTTTACATCCGCTGAGCAT
P1B10	GAAAATTCGCAGGCGCTCAGATGCCGGGTAAATCTCAAAGAGAACCTG
P1B11	TAGCGAGTCTTTACTCGATGATGTACCCCTTCCTGCTG
P1B12	TAGTATCAAATTCTTACAGGCGTTTTAGCGAAACG
P1C1	ATCTAGCCAGCAGCATCCAGCGGTGCCGTAATAATTTTCGTAAA
P1C2	AGCCAACGTGGCACCAGAATCTTACCAACGCTACC
P1C3	TGCTTCTGTAAACGAATTA
P1C4	TTCCTCGCACGCTGATGGATTATTTACACAGAGATGTGGCAC
P1C5	AGGAGGCTTTAACGCCAAACGAACTGCTCAT
P1C6	AAGTTTGACCATAACAAAGTTTTGTGCAAGGAATGACAACAGGA
P1C7	CGTAGGCGCATAACTGACCAACTTTGTTGCGGATACATTGCAAAAAG
P1C8	AGACAATCGCCATTAAAAAGAATCAGCAGA
P1C9	TAAATACCCGGATATCATCAACGGTCAATCATAAGACCATCGATAC
P1C10	CGCCAGCCAGAAAGCGTACTGAGTATGGTGCT
P1C11	AAAAGTTTGAGTAACATTATCATAATTG
P1C12	AAGAGGTAGTACCTTGAGAAAGGCCGACAATGCCATAGTAG
P1D1	AGGACGTCAGACTGTAGC
P1D2	TCGCCGGCTGGAGGTTTCTTTGCTCACTTTTGGGTAGCTACT
P1D3	AGTGAATTTTCTCAAACCCTCAGAGCCACCGAACCCACAC
P1D4	GCCACGAAACGTTTCGCCACGTGCATCCGTAATGGGATAGGGCC
P1D5	TACTGTGTGCAAATCCGCAAAGTATAGCAAC

P1D6	TCATCGTAACATTCCAAGAACATAGCCCCCT
P1D7	ACCACCTTAGATGAGTGACCTGTCGTGCCAGAAT
P1D8	ACGGAACGTCATTTAGTGATGAAGGCATAAACTGGTGCCCCGGAA
P1D9	AGAGAGAAATAACAAGCGTTTGCCATAAGTA
P1D10	CACGGGGTAATAGTAAAACAGTTAGACGTTAGCCCTCAACAACCCAG
P1D11	TGAGATCGGCTATAATATACCGACAGGGAAAGAGCGAAAGGAGCGGCAGT
P1D12	TACGCGGGATACGAGGGCAACGGAATTATACCAAG
P1E1	ATAGAGCCGCACTCCAAGTC
P1E2	AACAAAATCACCATCAATAACCCTCAATAAAT
P1E3	ACTAAATGGGCTTGAGATTGGCT
P1E4	CAGAACAATATATCGGCCATCAAACACAGTTGAAAGGAA
P1E5	CCGAGCTCGAACTTGACGAAAGGTAAGAGGCATTTATTT
P1E6	AAAAATTAAAGCCTATTATTCTGAAGTTGATAGATTGCAAACCCCTC
P1E7	GAGAACAAGCAAAACCAAATCAATATTTTCGTCACTACAAGGATTTT
P1E8	TGCACGACAATTGCGAATGCCCCCTCGGCTGGCCA
P1E9	TACGTATCATGACTTGCGGGAGGTATCCTGAACCACCACTTGATATAT
P1E10	CATTATATTTTATCTTCTGACCTAAAGATGATCAATATA
P1E11	TGATCGGGAAAGCTAACTCACATTTATTAATGCTT
P1E12	GAGTCAACTAATTTAGGCAAGTAATCCTGAACAGA
P1F1	CATAACAGTTGATTACTCGGT
P1F2	GCAGCAACAATATCGAAGAACAGTAATAACATCACACC
P1F3	TAGCATTTTGGGGCGCGGATGGCTTAGATCC
P1F4	AATATCGGCACGCGCGGGCCGGAAGCATAAAAAGCT
P1F5	GCTTTGAGGACTAATACGAAGAAAACGAAAGAGGCCCCAGCGGATT
P1F6	ATCAAGATTGTTTGTATTCTGATTATCATTTAATAAACTTT
P1F7	AAAGTCTTTCCCTATAAGAGTGTACACAGACAGTAAATGAG
P1F8	ATTCTAGCGATGTGTAAAAATGAATCGGCCAAAAA
P1F9	ACGAGGAGAGGCGGTTTTGATGGTGGGGCCACCCT
P1F10	CATTGAAGACAGTTCATGAGGAAGTTGGGTAAATAC
P1F11	CGGAGAGCGGGAGAAATAAAGCCTCAGAATT
P1F12	AGCAATACTTCATCACGCAATATCGCCAGTA
P1G1	AGGACGTTAAGAACGGTTTAATTTCAACGAGAAACCAA
P1G2	TACCAGAATCAAGTTTGCCTTATTTAAAACTAATAAGACCGCCATGC
P1G3	ATAACGGTAATTTTCACACCGATAGAAAGAG
P1G4	CTTGGTAACGCCAGGGTACGACGTGGAT
P1G5	AAAACCGCCACCCTCAGATTTTAAACGATACAGTCACCGGGATA
P1G6	CATTTAACTCCATATAGATTCATCAGTGAACAAGAACTCATC
P1G7	CCTACATATCTAAAGCATCACCTCAAATTTGC
P1G8	AACTGTAAAACGACGGCTAAGTTGCGC
P1G9	AAGTTTTGACGCTCAAATCCGGTATTCTAATAA
P1G10	TTAGAACGCAATTAAGACAAATACATACATAAA
P1G11	CTATGAGTAATGTGTAGAAAAGGGTTAA
P1G12	GTCCTTTCATGCATGTCCAGTAAAGTGCCCGTATAAAAGGAGGTAATC
P1H1	GACACGTAGATCCTTATTACG

P1H2	TCCCGGGCGAAAGCCACCGTCTTTCCAGAGCCGAA
P1H3	AATACCGATCATCAGATTATACTTCTGAATGATGACATAAAT
P1H4	AACAAAATCGGCACGCTGCGCGTAACAGGGCGTTT
P1H5	CAGAGCGGGGTCATTGCGTCTGGCCGTTGAGCAGTCTTGCCCCC
P1H6	CTACAATTTTTTTGAAGAAAAAGCTTTAAAACAGAAATAAAGAAAAAT
P1H7	AGTTCTGTCCCCCGAGGCGCTGGCAAGTGTTTG
P1H8	GCAGCAGAGGTGCTCGCAATTGCG
P1H9	GAGCGTCCACTACCTCCGTAATTTTAGTTACAAAATCGCCGT
P1H10	CTCCTGCAGGG
P1H11	GAATTGCCAGAATTCAACTATTACACCCAAATACCAGAACGAGTAG
P1H12	AATCAAGAATTGAGTTAAATAGCATTTTTTGTATCCCTAGCAAGCGCC
P2A1	GGTGGCTCCAACGGCATTTCGCACTCAATCCACGCCATCCA
P2A2	TTCATTTACCATATTGCGGAACAAAGAA
P2A3	ATTAGAGCATTTTTTGCAGCTGAAAAGGTCTA
P2A4	ACCTTATGCGATTTTGGGAAGACAACATTA
P2A5	TGTGCGGTTGCGGTATGCTCA
P2A6	TCACAGAGAGTAACCCAAGCTATCCCAGCGCACGGAAATTGCAAC
P2A7	ATATAAAATTCATATGGTTTATTACCGAGGAA
P2A8	CGTGTGAATTATTAAGAGGGAGAAACAATAAACGTCAGACTCG
P2A9	ACCGAGGCTGGCTGACCTTTCATTAGGTAGAAACCAGTC
P2A10	GGGGTTTATATCGCATATGCATTGACCATTAGATA
P2A11	AGGAAGCGCAGCGATCCCGTGCCGCCGGAACGTAAACGATGCTGATACG
P2A12	TTATCAGCTTGCTTACACTAT
P2B1	CAACCGCATCG
P2B2	TTATTCGGTCGGGTATTAGCCGTTTTTTTCGATTTA
P2B3	ATCCTGAAAACAAACCTTTTTTAATGGACGCGAGAGGTTTGA
P2B4	AATCAAATTAGTACCGCCACCGAGTAACGCGTCATCCGGAACCGCGCCTAAC
P2B5	CGCGCAGTATATTTCGACAATGAATATACAGTA
P2B6	TATTAAATCATAAAAATCATAGCGTCAAATTAT
P2B7	AAAGGAAGCTTGATGTTGAAACCTG
P2B8	TTGCAAAGACAAAAGGGAATGAAATAGCAAGCAGCACC
P2B9	TGTACGGAGGGAAGTGAGCGCTTTAAGAATAGAAAAGAAAACGCAA
P2B10	CCAGAGCGCCATACAGCGCCATGTTGATTCAGAAGCTAACAG
P2B11	TTTGCGGGCCTCTGTGGTGCT
P2B12	TATTTGCCGTTGCACATCTGCCCTTACCGGTGTA
P2C1	GTAATCAGAAACGAGCCTTTAGTGCCTTCTCAGAACGA
P2C2	TTTTCATAACATCCATATATTTTAAATGGACAGTCGGTCAGG
P2C3	GTTTACCAGACGACTCAGAAGAGTCTGGAAAAGCCCAA
P2C4	CAGACCAGTTACAAAATAAAGGCTTCAGTAGGAGTATTATTAATGC
P2C5	GCAACTGGCGAAAGGGGAGTAAAGTTGCCGGAGTGAGACCGGTCCAAAC
P2C6	GCAAGACTGGATAGCGTGAATCCCCTGTATGCGC
P2C7	AGCTACTT
P2C8	GGTGATAAGAACTGGCATGATAATAACAGCCCTTTAATATC
P2C9	TCCCATGCGTTCTTTGCCGATTTTCAGGTTTACGG

P2C10	CCCCTTTTCTTGTGTGAAATTGTTAAAGCACTTGT
P2C11	TAAAAGGAATGGCTATTAGTCGAACTGAAAAA
P2C12	TTTTTAGATGATATGACCGGAAGCAAACGCTTAATAGCTATA
P2D1	CACCGGAATCATTTCAAAATTATTT
P2D2	CGGTGTACAGACCAACAAAGCTAACGGAAAAAATCTACG
P2D3	ACTGTATCACCGTACTCCAGTTAACTGAATTCGCCACTACGTGAAAATC
P2D4	AACAGACAATAGTTTATCCGCTGGTAAATGTGCAG
P2D5	ACGGAGCCGTTAATCAGTGAGGCCTTG
P2D6	GATAAAATCAGAGCCGGGACATCCCTTACACTAAA
P2D7	GCAAACCACGGTTTTGTCACAATCAAAGTAACCG
P2D8	AAAAGAATTTCTTAAACATTACGAGACCAAAA
P2D9	GAACGCCTCCATATTATTTTA
P2D10	AATAATAACCGGCGCAGAGAGTAATCTCGCCT
P2D11	ACCATCGATAGGCCGGAAATTAGAGCGTCACCGACT
P2D12	AATAAACCAGAATCTTTTCATAATCAGGA
P2E1	ACCAACATGGCGCGTAACGATCTTACAACATTTTG
P2E2	TGAGCAAAGCGTAAGTATAGCCCGGTTTCGGAACCAGAATCCCTCAGAAAC
P2E3	TACATCAAACCTGAAAAAGAGACGCATACCAGTCGG
P2E4	GCGACCCACCAAGTAGAATCATTAAAGGTGAAAATA
P2E5	TTTGGACATTCTGGCCAATTGGCAGGCCTGCA
P2E6	AAACGGACGACGTCGGTGACGCAACAGCGAGTATAGTTATTTTGATGGGG
P2E7	CTGTCATACCGGCCCTGGCCCTGAGAAGA
P2E8	ACAGTGCGACTTTACAAACAAAAGCCAAGTCAATACTATCATTTCC
P2E9	CCTAGTTTTCCTTTCACCACTTGTAGCAGCACCGACAGTATCGGCCTACCG
P2E10	AGCGGGAGCTAAACAGGAGTTTTTACAATAGATTT
P2E11	TAAAGGAAGCTCTGGAACCTGCGAACGAGTAGGCATAAACTGTAATGTCA
P2E12	GAGGGAATCCTGAGAAGTGGCCGATAAAACATATT
P2F1	GAAGGGATAGCGAGATAGTTCGGCCAGGAAGAAGAATGAGGT
P2F2	AGCACCTCAAATCCTCCAGGAAGGGTCATTCCTTTAATTGTACAGGTG
P2F3	TATTTTAACCTCAAAGCTGCATTGCCTGGGGTGCCTAAATCCTTAGAC
P2F4	TGCCCGCTTTCAGGTGTTGTTTC
P2F5	AGACCGGCAAACGCGGTCCGTTTT
P2F6	TGAGGAAAACAGCCTGATTGCTTTGTTGC
P2F7	ACATTACAAAGGATTAAGGTGCCGTCGAGAGGACATGAAACAA
P2F8	TTTGACCGCCAGGAAAGCTAATCAGAGCAAACAAA
P2F9	GCGGTCAGTATAGAAGATTAGCCCTTAAAGGGATTTTAG
P2F10	TGAAAGCCCAAAGAAACCGACATTAGGGAGG
P2F11	TTAAAGAGATCTATGACCGCTAAATCGGTTGTCCC
P2F12	CGGAATTACCGTGTGCAAGACAAAGAAAACAGTAAACAAAC
P2G1	ACAGTGCTTTACCGAACGAACCTGGTTGCTAGCGGTAAC
P2G2	TTTGCGTATTGACAATTCCACACAAAATTGGG
P2G3	CGGATCGGATGTGCTGCAAGGCGATCAGTGCCAGGTGGAGCC
P2G4	CGACACGCCAAATTACCGCGCCCAAATCCAAGCC
P2G5	GCCGCTACCACCACTGCCGTATCCGCTCGGCGCCAGCTGGTC

P2G6	CTTAGCATCAGACGATCCACAACCTATCTTTCCAG
P2G7	TGCCTATAATAGGTATTATAGGATAAAAGCATAGTAAGAGCATCGA
P2G8	GCAGTTGGTAAAAAGGCGGCCGCGTGGTGGGTGGTAGCAGGCTGCA
P2G9	GTCAGACCTCAAGAGAAGGAT
P2G10	GTCTGAGCAAAAAGAAGATAATGGGAAGGAG
P2G11	GGACAAATCACCTCAATATGAAAATTTGACGCTCA
P2G12	GTACGAACGTTATTAATCTGTTTACTTTTTAATTAAGCGA
P2H1	TTTCAATGATAAATTAATGC
P2H2	TCAGTGAGAATCAAATCAGATATAGAACAGCCCTCAGAGTACCGTTAATC
P2H3	TTCAAATTGAATTAATTAATT
P2H4	TTTAAGCAAATTCACAAAGTATTAAGAGGCTCGGA
P2H5	ATATAATACACGTACTACACCAGCTAACACCATTACCCAGTCACA
P2H6	TCACGCGTGGGAACAAATGTCACTGCGCGCCGCGG
P2H7	GGACGTCACCCGGTCGCAGTTTCATGTGCACGTTT
P2H8	GGAACAAGACGCCGCCCCAG

Tab. S2 Modified staple strands

Name	Sequence (5'→3')
biotin1	biotin-AAGGCCGCTTTTTGCG
biotin2	biotin-TTCATCGGCATTGACGGGACCAATAGACCCTCAATTCATTCCAA
biotin3	biotin-GTCATAAATTTTT
biotin4	biotin-ACAACCTTCAACTGAGGCTATGT
biotin5	biotin-AGTTACCAGAAGGAAAGCAGATAAGTCAGAGGGTAATCGCA
biotin6	biotin-CACCCTGAACAAGCCG
biotin7	biotin-GAAGGTTATCTAAAAT
biotin8	biotin-CTCGTCGCTGGCCCTCCTCCGTGCCTTAATTTAGAAACCAGTAC
biotin9	biotin-GAAAGGAAGGGAAGAACC GGCGATCCCCGGCCGTGAGAGCCTCCGTACGCT
biotin10	biotin-TAGATGGGCGCATCGTAACTTCAGGCGCCT
biotin11	biotin-AGAATATAAAGTCCCATCCGTTCTTCGGGG
biotin12	biotin-AGGGCGATCGGTGCGGTGCGCAACCGGAAACAATCGGCGGG
npbind1	AAAGAATTAGCAAAATTAAGCAGCCTTTAAAAAAAAAAAAAAAAAAAAAAAAAA AA
npbind2	CAATATAATCCAATGATAAATAAGGCGTTAAAAAAAAAAAAAAAAAAAAAAAAAA AAAA
npbind3	ATAAAAATGCTGATGCAATGTGAAAAAAAAAAAAAAAAAAAAAAAAAAAAA
npbind4	CATACAGCCTGTTTTGCTGAATATAATGCGAAAAAAAAAAAAAAAAAAAAAAAAAA AAA
npbind5	ACCACCAAAGGGTTAGAACCTCAATTACGAATAACCTAAAAAAAAAAAAAAAAAA AAAAAAAAAA
npbind6	ACCATCAACCGTTCTAGCCGAAAAAAAAAAAAAAAAAAAAAAAAAAAAA
npbind7	GGTTATATAACTATATGTGAATAAAAAAAAAAAAAAAAAAAAAAAAAAAAAA
npbind8	CATTCGTCAACATGTTTTAAGTTTTAATTCGAGAAAAAAAAAAAAAAAAAAAAA AAAAAA
base_ATTO54 2	TTTGTGATCTCACGTAATTTCTGCTCA-ATTO542
base_ATTO64 7N	TTTGTGATCTCACGTAATTTCTGCTCA-ATTO647N

hotspot_ATT O647N	TAATCACTGTTGCCCTGATTAAATACGTTAATA-ATTO647N
hotspot_ATT O542	TAATCACTGTTGCCCTGATTAAATACGTTAATA-ATTO542
hotspot_Alexa 647	TAATCACTGTTGCCCTGATTAAATACGTTAATA-Alexa647
hotspot_FQH	TAATCACTGTTGCCCTGATTAAATACGTTAATA(dTATTO647N)AATGAGGACAT TTCGGGCAATGTGCCTCATT-BBQ650

Tab. S3 Folding temperature ramp

temp [°C]	time [s]
65	300
65	50
64	95
63	95
62	95
61	95
60	540
59	540
58	1140
57	1740
56	2340
55	2940
54	3540
53	3540
52	3540
51	3540
50	3540
49	3540
48	3540
47	3540
46	3540
45	3540
44	2940
43	2340
42	1740
41	1140
40	1140
39	1140
38	540
37	540
36	290
35	290
34	290
33	290
32	290
31	290
30	290
29	50
28	50
27	50
26	50
25	50

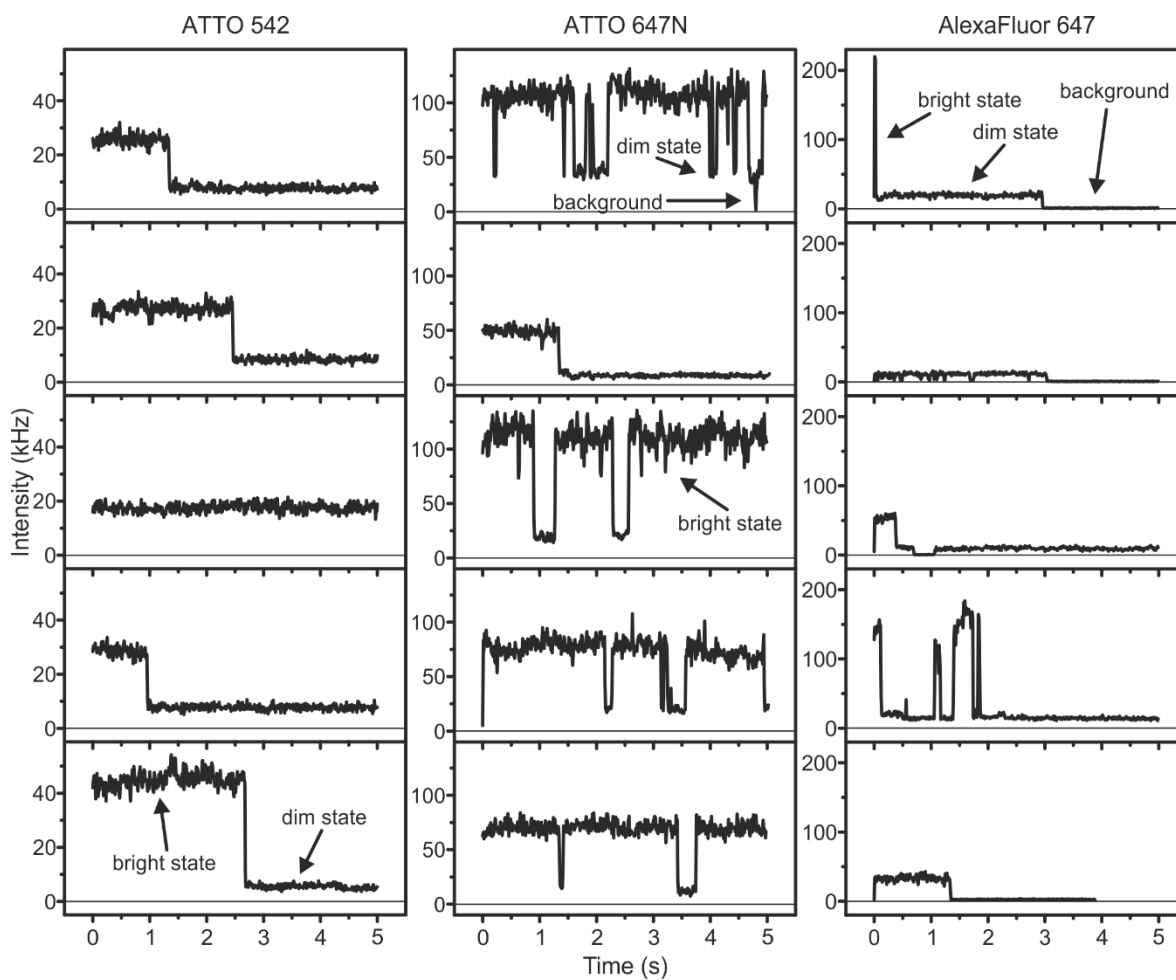


Fig. S1: Example fluorescence intensity as a function of time for single fluorophores of ATTO 542, ATTO 647N, AlexaFluor 647 placed in the hotspot of 100 nm Ag nanoantennas.

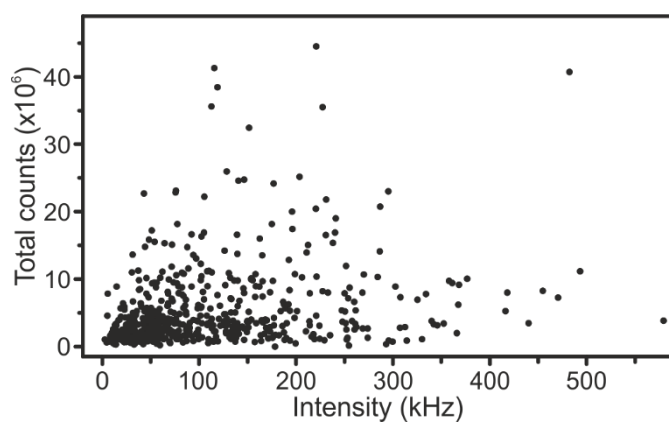


Fig. S2: Total number of counts vs. photon count rate for the dataset described in Fig. 1.

Associated Publication 4

Single-molecule FRET at 10 MHz count rates

Lennart Grabenhorst, Flurin Sturzenegger, Moa Hasler, Benjamin Schuler and Philip Tinnefeld

bioRxiv (2023), doi: 10.1101/2023.12.08.570755

(open access)

Single-Molecule FRET at 10 MHz Count Rates

Lennart Grabenhorst ¹, Flurin Sturzenegger², Moa Hasler², Benjamin Schuler ^{2,3}, and Philip Tinnefeld ^{1*}

¹Department of Chemistry and Center for NanoScience, Ludwig-Maximilians-Universität München, München, Germany

²Department of Biochemistry, University of Zurich, Zurich, Switzerland

³Department of Physics, University of Zurich, Zurich, Switzerland

*Correspondence should be addressed to P.T. (philip.tinnefeld@cup.uni-muenchen.de)

Abstract: A bottleneck in many studies utilizing single-molecule Förster Resonance Energy Transfer (smFRET) is the attainable photon count rate as it determines the temporal resolution of the experiment. As many biologically relevant processes occur on timescales that are hardly accessible with currently achievable photon count rates, there has been considerable effort to find strategies to increase the stability and brightness of fluorescent dyes. Here, we use DNA nanoantennas to drastically increase the achievable photon count rates and to observe fast biomolecular dynamics in the small volume between two plasmonic nanoparticles. As a proof of concept, we observe the coupled folding and binding of two intrinsically disordered proteins which form transient encounter complexes with lifetimes on the order of 100 μ s. To test the limits of our approach, we also investigated the hybridization of a short single-stranded DNA to its complementary counterpart, revealing a transition path time of 17 μ s at photon count rates of around 10 MHz, which is an order-of-magnitude improvement when compared to the state of the art. Concomitantly, the photostability was increased, enabling many seconds long megahertz fluorescence time traces. Due to the modular nature of the DNA origami method, this platform can be adapted to a broad range of biomolecules, providing a promising approach to study previously unobservable ultrafast biophysical processes.

Introduction

Single-molecule Förster Resonance Energy Transfer (smFRET) experiments are a cornerstone in the investigation of biomolecular dynamics [1] as they enable the observation of the molecule of interest 'in action', specifically within its natural environment, and give a real-time movie that can span timescales from milliseconds to minutes or in some cases even hours [2]. Crucially, although methods enabling access to faster timescales through correlation techniques exist [3, 4] time-resolving individual rare events, such as the rapid jumps across the barriers between two conformational states (e.g. protein or nucleic acid folding), requires very high count rates from single molecules [5, 6]. These transition paths have gained increasing interest and smFRET experiments have been playing a major role for revealing the nature and timescales of these paths [7, 8]. However, the photon count rates (PCR) required for accessing the relevant microsecond timescale mandate the use of high excitation intensities leading to saturation and increased photobleaching, which makes the task of measuring these transition paths very challenging. Plasmonic hotspots have been shown to increase the photostability and brightness of fluorescent labels [9, 10], and offer a potentially complementary strategy to the more commonly used chemical photostabilization [11–13]. Coupling the emitters to plasmonic hotspots not only increases the electric field between the two plasmonic nanoparticles, but also increases the emission rates of the fluorophore, leading to a shorter time that the molecule spends in the reactive excited states as well as reducing the time until the fluorophore is available for re-excitation [14, 15]. This, in turn, results in improved photostability of fluorescent labels and also enables higher fluorescence intensities without saturation [9, 16, 17]. First examples employing similar strategies for diffusing molecules have appeared and showed promising results [18, 19], but they are limited to the submillisecond timescales of molecular diffusion through the excitation volume, which makes the complete observation of complex biomolecular pathways unlikely. DNA origami nanoantennas [20, 21] have overcome the challenge of selective immobilization of biomolecules in plasmonic hotspots. Recent iterations have optimized the usability of the plasmonic hotspots in NACHOS (NAntennas with Cleared HOtSpots) improving binding kinetics and the immobilization of larger functional entities such as diagnostic assays [22] and even antibodies [23] in these zeptoliter volumes. In this work, we explore the use of NACHOS for biophysical single-molecule FRET experiments. Recent studies have shown that the electromagnetic environment of plasmonic hotspots has an influence on the FRET rate coefficient as well as the FRET efficiency [24–26], but their use in biophysics is largely unexplored.

Here, we optimize DNA origami nanoantennas for biophysical experiments with a careful selection of parameters, including the choice of donor and acceptor fluorophores. With optimized hotspots, we demonstrate strongly enhanced countrates and long-lasting single-molecule FRET time traces. Unaltered biomolecular function is demonstrated by reproducing the lifetime of a short-lived intermediate in the coupled folding and binding of two intrinsically disordered proteins. Transition path times of down to a few microseconds are then reported for a DNA hybridization reaction.

Results and Discussion

An important first step of this endeavor is the choice of a suitable FRET pair. Photophysical characteristics such as the formation of short-lived dark or dim states [9] can complicate the analysis of the data and need to be avoided or accounted for in the analysis. Furthermore, both fluorophores should be spectrally red-shifted with respect to the plasmon resonance of the gold dimer nanoantenna [27]. In consideration of these aspects, we examined FRET pairs covering the red and near IR spectral region (a deeper discussion on dye selection and DNA origami nanoantenna production is found in Supplementary Note 1).

First, we investigated the binding of the nuclear-coactivator binding domain of the CBP/p300 transcription factor (NCBD) to the activation domain of SRC-3 (ACTR). Previous studies with smFRET [28] revealed that these intrinsically disordered proteins (IDPs) form a transient encounter complex before they form a fully folded heterodimer. The lifetime of this encounter complex has been determined experimentally to approximately 80 μ s – 100 μ s, depending on the ionic strength of the buffer [28], which offers a way to test whether our system is compatible with measuring protein dynamics. Using a single-stranded DNA (ssDNA) handle attached to a cysteine residue close to the N-terminus, we immobilized ACTR labelled with AlexaFluor 647 in the plasmonic hotspot (Fig. 1a, b). Free NCBD labelled with LD750 was then added to the imaging buffer which led to the appearance of short segments of high FRET efficiency in the fluorescence recordings, indicating the binding of NCBD to ACTR. To identify nanoantennas showing reversible binding events without prematurely photobleaching the FRET pair, we started the acquisition of single-molecule fluorescence trajectories at lower excitation intensities (10 – 20 nW). Then, we increased the excitation intensity (1 – 4 μ W) to acquire high intensity time traces. With the fluorescence enhancement and increased photostability provided by the DNA origami nanoantenna, we were able to increase the average photon count rate by almost 3-fold to 588 kHz compared to earlier studies with a different FRET pair [28] (see Supplementary Note 2) and achieved a maximum photon count rate of over 2 MHz, with a mean observation time of 0.66 s, which also represents a significant improvement. While intermediates with longer lifetimes can sometimes be directly observed in the time traces (Fig. 1c, left), quantifying intermediates with shorter lifetimes remains challenging (Fig. 1c, right, see Fig. S1 for more examples). Consistent with previous mechanistic studies of FRET in plasmonic nanostructures [24–26], the FRET efficiency of the bound state is decreased in the plasmonic hotspot — we obtained a mean value of $\langle E_B \rangle = 0.49$ (uncorrected, compare Fig. S7)

In order to fully quantify the most likely lifetime of the intermediate state, we used the photon-by-photon maximum likelihood approach [7, 28, 31]. Here, the likelihood of a transition between two states via an intermediate with FRET efficiency E_I and lifetime τ_I is compared to the likelihood of an instantaneous transition (Fig. 1d). To account for acceptor blinking, we included an additional dark state in the analysis [32]. We also normalized each E_I value to the respective transition-wise bound state (E_B) and unbound state (E_U) FRET efficiency values: $E_{i, \text{norm}} = (E_I - E_U) / (E_B - E_U)$, to account for the slightly broadened FRET distributions resulting from the heterogenous fluorescence enhancement by the nanoantenna (see SI for details on the analysis). This means that for an $E_{i, \text{norm}}$ value of 0.5, the intermediate state lies exactly halfway between E_U and E_B . As we noticed a decrease of the total photon count rate of the system upon binding of NCBD (Fig. S1), we additionally carried out simulations of binding events with non-constant total photon count rates and found no significant influence on the robustness of the analysis (see Supplementary Note 3 and Figs. S3 and S4). From a total of 141 transitions, we obtained a value of 96 ± 13 μ s for the most likely lifetime of the intermediate state and an $E_{i, \text{norm}}$ value of 0.58 ± 0.04 (Fig. 1e–f). These values are in excellent agreement with

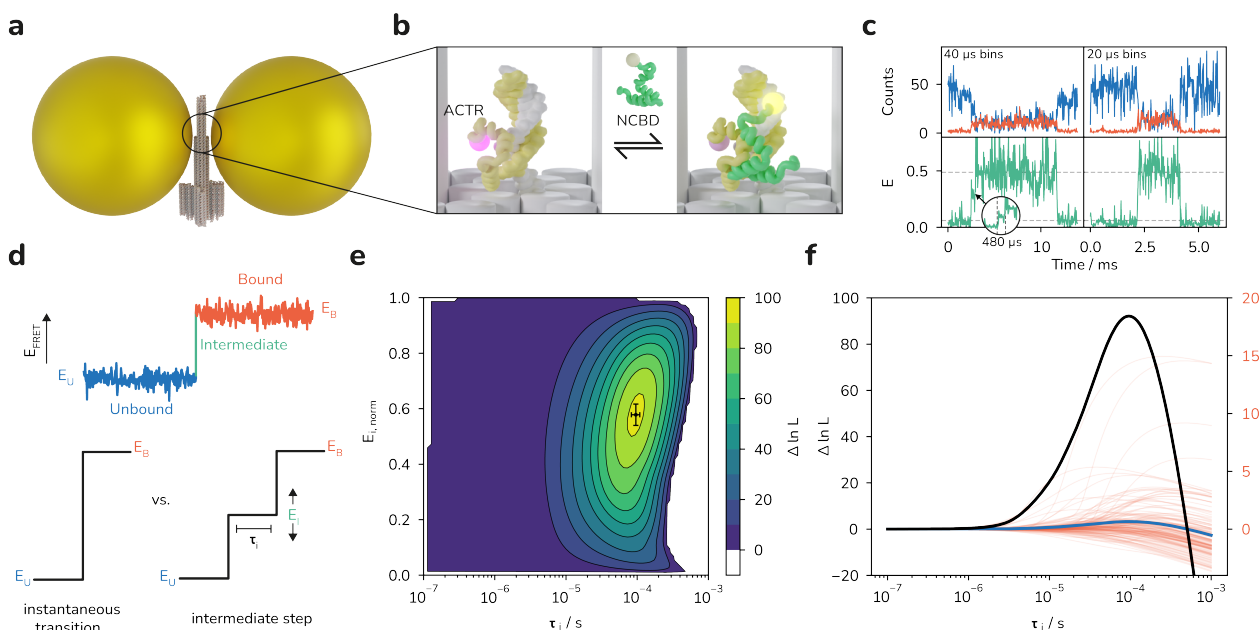


Figure 1: Investigation of the coupled folding and binding of ACTR to NCBD using DNA origami nanoantennas. (a) Illustration of the DNA origami nanoantenna with 100 nm gold nanoparticles. (b) Depiction of the binding reaction of ACTR to NCBD. We used ssDNA handles to immobilize ACTR (yellow) labelled with AlexaFluor 647 in the plasmonic hotspot region. NCBD (green) labelled with LD750 is freely diffusing in solution and transiently binds to ACTR. Cartoon representations were obtained from the PDB [29, 30]. (c) Exemplary fluorescence time traces (orange: acceptor, blue: donor) and corresponding uncorrected FRET efficiencies (E , green) of binding events represented with 40 μ s (left) and 20 μ s (right) binning. The inset on the left highlights a potential intermediate state. The dashed lines indicate the mean values for bound (E_B) and unbound (E_U). (d) Schematic depiction of the two models that are compared in the maximum likelihood analysis [7]: an instantaneous transition from the unbound to the bound state is compared to a transition that includes an intermediate step with FRET efficiency E_I and of lifetime τ_i . (e) 2D contour plot of the log-likelihood difference $\Delta \ln L$ between the two models summed up over 141 transitions. The most likely values are $\tau_i = 96 \pm 13 \mu$ s and $E_{i,norm} = 0.58 \pm 0.04$. The errors were calculated from the diagonal elements of the covariance matrix. (f) Plot of $\Delta \ln L$ values versus τ_i / s for single transitions (red, right scale) and the sum of all transitions (black) as well as their average (blue, right scale) calculated at the most likely value for $E_{i,norm}$.

previously reported values at similar ionic strength ($90 \pm 10 \mu$ s [28]), which illustrates the potential of our approach to be applied to other biomolecular processes.

To test our approach on even faster reactions and simultaneously avoid potential negative effects on the photostability of our labels by the neighboring amino acids and labelling chemistries (e.g. cysteine or maleimide [33]), we next set out to investigate the transient binding of a short ssDNA to a ssDNA docking site placed in the plasmonic hotspot. DNA-DNA hybridization is believed to occur via a 2–3 nucleotide (nt) nucleation site which then transforms into the stably bound state via zippering of the remaining bases [34]. In our experiments, we used a 6-nt long ssDNA labelled with Dy-751 at the 3'-end, which hybridizes to a docking site labelled at the 3'-end with a Cy5B [35, 36] fluorophore (Fig. 2a). We achieved a mean PCR of 2.42 MHz and a maximum count rate of 8.93 MHz, which is approximately an order of magnitude higher than previously reported PCRs in smFRET experiments [7, 37, 38] and also substantially higher than what we observed in the experiments described earlier. It is worth emphasizing that because of the increased photostability, we were sometimes able to observe the same molecule for up to 30 seconds at photon count rates of 2 MHz and record up to 57 million photons from one FRET pair (Fig. 2b). This allowed us to occasionally observe more than 20 transitions on one molecule, which illustrates how the nanoantenna approach facilitates data acquisition. Figure 2c shows two exemplary snapshots from fluorescence time traces of a binding event (see Fig. S2 for more examples). At the chosen 2–4 μ s bin sizes, acceptor blinking becomes visible (indicated by arrows), substantiating the need to account for it in the analysis. We observed a total of 405 transitions and analyzed these according to the photon-by-photon maximum likelihood approach described above. We found a mean value of the uncorrected FRET efficiency of the bound state of 0.48, a most likely transition path time of $17 \pm 1 \mu$ s and an $E_{i,norm}$ value of 0.30 ± 0.02 (Fig

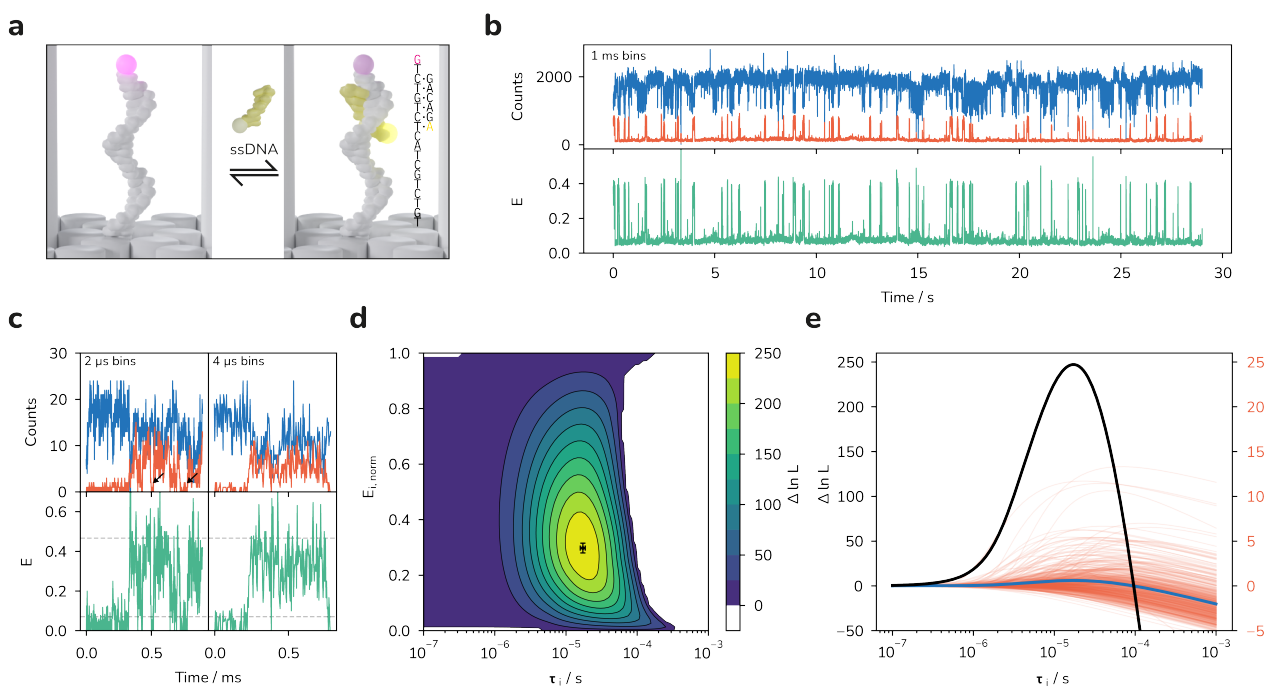


Figure 2: Investigation of DNA-DNA hybridization reactions in the plasmonic hotspot. (a) Illustration of the experiment: a 6 nt ssDNA labelled with Dy-751 hybridizes to a ssDNA docking site labelled at the 3'-end with a Cy5B fluorophore. The DNA sequences are shown in the inset. (b) The increased photostability allows for the observation of several binding events at high count rates. Top: acceptor (orange) and donor (blue) fluorescence time trace at 1 ms binning. Bottom: corresponding uncorrected FRET time trace. (c) Exemplary fluorescence time traces (top) showing donor (blue) and acceptor (orange) fluorescence during a hybridization event at 2 and 4 μ s binning. The corresponding uncorrected FRET time trace is shown below. The arrows indicate possible acceptor blinking events. (d) 2D contour plot of the log likelihood difference $\Delta \ln L$ of a transition of duration τ_i with FRET efficiency $E_{i, \text{norm}}$ to an instantaneous transition summed over 405 transitions. The most likely values are $\tau_i = 17 \pm 1 \mu\text{s}$ and $E_{i, \text{norm}} = 0.30 \pm 0.02$. The errors are calculated from the diagonal elements of the covariance matrix. (e) Plot of $\Delta \ln L$ values versus τ_i for single transitions (red, right scale) and the sum of all transitions (black) as well as their average (blue, right scale) calculated at the most likely value for $E_{i, \text{norm}}$.

2b). To test the influence of the FRET pair on the results, we repeated the experiment with AlexaFluor 647 as donor and ATTO740 as acceptor fluorophores. Although we were able to achieve slightly higher count rates (mean count rate: 5.34 MHz, with maximum count rates of up to 16.4 MHz, see Fig. S3), the FRET efficiency of the bound state was notably lower ($\langle E_B \rangle = 0.30$), potentially making it more difficult to distinguish between the bound and the unbound states. This can at least partially be explained by the lower Förster radius of this dye pair (see Table S3). Nevertheless, we still obtained a transition path time that agrees with the one measured with the Cy5B/Dy-751 FRET pair ($\tau_i = 20 \pm 3 \mu\text{s}$) with a most likely value for $E_{i, \text{norm}}$ of 0.21 ± 0.02 .

Previous FRET studies on DNA hairpin formation were able to determine an upper bound of $2.5 \mu\text{s}$ for the hybridization of a 4 nt long hairpin stem [39] and optical tweezer experiments reported values around $30 \mu\text{s}$ for much longer hairpins [40]. Our results thus lie in a plausible range of transition path times for 6-nt DNA-DNA hybridization event, although further experiments will be needed to fully understand the process of hybridization. For example, in preliminary experiments, the inclusion of an AT-mismatch in the short strand labelled with ATTO740 led to an increase of τ_i to $41 \pm 3 \mu\text{s}$ with a similar value for $E_{i, \text{norm}}$ of 0.229 ± 0.012 (see Fig. S4).

Conclusion

In summary, we showed that DNA origami nanoantennas can be used to accelerate data acquisition and increase the attainable photon count rates in smFRET experiments on biomolecular dynamics. As a proof of concept, we investigated the coupled folding and binding of two IDPs as well as the hybridization of two ssDNAs and showed that we could resolve processes on the microsecond timescale. With the resulting higher time resolution [41, 42], previously inaccessible biological processes could

be investigated. To this end, the modular nature of the DNA origami technique allows the swift incorporation of new biomolecules of interest, making this platform broadly applicable as a tool for the improvement of temporal resolution in smFRET experiments. Another benefit which we did not focus on in this work is the possibility to work at much higher concentrations of labelled species due to the ultra-small volume of fluorescence enhancement in the nanoantennas, which also allows the observation of biomolecular interactions with micromolar dissociation constants [43] – we estimated the dissociation constant of the mismatched DNA-DNA interaction (Fig. S4) to 200 μM and still were able to clearly resolve the binding events at 3.6 μM concentration of the short strand in solution (Fig. S8). Recent iterations of the DNA origami nanoantenna could accommodate even larger biomolecules and should further reduce the potential impact of the constricted environment on the experiments [44]. The development of new near-infrared fluorophores showing less blinking on the low microsecond timescale [45] which potentially interferes with the maximum-likelihood analysis should make it possible to further push the time resolution and possibly, in combination with more efficient sampling methods, bridge the gap towards the timescales of molecular dynamics simulations [46–48].

Acknowledgements

L.G. thanks Viktorija Glembockyte for many insightful discussions. The authors thank Martin J. Schnermann and Ryan McLaughlin for providing the Cy5B dye. F.S., M.H., and B.S. thank Daniel Nettels for discussion and providing data analysis tools. This work was supported by the German research foundation (DFG, grant number TI 329/9-2, project number 267681426, INST 86/1904-1 FUGG, excellence cluster e-conversion EXC 2089/390776260), the Free State of Bavaria under the Excellence Strategy of the Federal Government and the Länder through the ONE MUNICH Project Munich Multiscale Biofabrication, and the Swiss National Science Foundation (B.S.).

References

1. Lerner, E. et al. Toward dynamic structural biology: Two decades of single-molecule Förster resonance energy transfer. *Science* **359**. doi:10.1126/science.aan1133 (2018).
2. Kümmerlin, M., Mazumder, A. & Kapanidis, A. N. Bleaching-resistant, Near-continuous Single-molecule Fluorescence and FRET Based on Fluorogenic and Transient DNA Binding. *Chemphyschem* **24**, e202300175. doi:10.1002/cphc.202300175 (2023).
3. Nettels, D., Gopich, I. V., Hoffmann, A. & Schuler, B. Ultrafast dynamics of protein collapse from single-molecule photon statistics. *Proc. Natl. Acad. U.S.A.* **104**, 2655–60. doi:10.1073/pnas.0611093104 (2007).
4. Dimura, M. et al. Quantitative FRET studies and integrative modeling unravel the structure and dynamics of biomolecular systems. *Current Opinion in Structural Biology* **40**, 163–185. doi:10.1016/j.sbi.2016.11.012 (2016).
5. Schuler, B. & Eaton, W. A. Protein folding studied by single-molecule FRET. *Curr Opin Struct Biol* **18**, 16–26. doi:10.1016/j.sbi.2007.12.003 (2008).
6. Hoffer, N. Q. & Woodside, M. T. Probing microscopic conformational dynamics in folding reactions by measuring transition paths. *Curr Opin Chem Biol* **53**, 68–74. doi:10.1016/j.cbpa.2019.07.006 (2019).
7. Chung, H. S., McHale, K., Louis, J. M. & Eaton, W. A. Single-molecule fluorescence experiments determine protein folding transition path times. *Science* **335**, 981–4. doi:10.1126/science.1215768 (2012).
8. Chung, H. S. & Eaton, W. A. Protein folding transition path times from single molecule FRET. *Curr Opin Struct Biol* **48**, 30–39. doi:10.1016/j.sbi.2017.10.007 (2018).
9. Grabenhorst, L., Trofymchuk, K., Steiner, F., Glembockyte, V. & Tinnefeld, P. Fluorophore photostability and saturation in the hotspot of DNA origami nanoantennas. *Methods Appl Fluoresc* **8**, 024003. doi:10.1088/2050-6120/ab6ac8 (2020).
10. Pellegrotti, J. V. et al. Controlled Reduction of Photobleaching in DNA Origami–Gold Nanoparticle Hybrids. *Nano Lett.* **14**, 2831–2836. doi:10.1021/nl500841n (2014).
11. Vogelsang, J. et al. A reducing and oxidizing system minimizes photobleaching and blinking of fluorescent dyes. *Angew Chem Int Ed Engl* **47**, 5465–9. doi:10.1002/anie.200801518 (2008).
12. Glembockyte, V., Lin, J. & Cosa, G. Improving the Photostability of Red- and Green-Emissive Single-Molecule Fluorophores via Ni^{2+} Mediated Excited Triplet-State Quenching. *J Phys Chem B* **120**, 11923–11929. doi:10.1021/acs.jpcc.6b10725 (2016).
13. Ha, T. & Tinnefeld, P. Photophysics of fluorescent probes for single-molecule biophysics and super-resolution imaging. *Annu Rev Phys Chem* **63**, 595–617. doi:10.1146/annurev-physchem-032210-103340 (2012).

14. Holzmeister, P. et al. Quantum yield and excitation rate of single molecules close to metallic nanostructures. *Nat Commun* **5**, 5356. doi:10.1038/ncomms6356 (2014).
15. Schedlbauer, J. et al. Ultrafast Single-Molecule Fluorescence Measured by Femtosecond Double-Pulse Excitation Photon Antibunching. *Nano Lett* **20**, 1074–1079. doi:10.1021/acs.nanolett.9b04354 (2020).
16. Wientjes, E., Renger, J., Cogdell, R. & van Hulst, N. F. Pushing the Photon Limit: Nanoantennas Increase Maximal Photon Stream and Total Photon Number. *J Phys Chem Lett* **7**, 1604–9. doi:10.1021/acs.jpcllett.6b00491 (2016).
17. Wang, Y., Horacek, M. & Zijlstra, P. Strong Plasmon Enhancement of the Saturation Photon Count Rate of Single Molecules. *J Phys Chem Lett* **11**, 1962–1969. doi:10.1021/acs.jpcllett.0c00155 (2020).
18. Nuesch, M. F. et al. Single-molecule Detection of Ultrafast Biomolecular Dynamics with Nanophotonics. *J Am Chem Soc* **144**, 52–56. doi:10.1021/jacs.1c09387 (2022).
19. Tiwari, S., Roy, P., Claude, J.-B. & Wenger, J. Achieving High Temporal Resolution in Single Molecule Fluorescence Techniques Using Plasmonic Nanoantennas. *Advanced Optical Materials*. doi:10.1002/adom.202300168 (2023).
20. Acuna, G. P. et al. Fluorescence enhancement at docking sites of DNA-directed self-assembled nanoantennas. *Science* **338**, 506–10. doi:10.1126/science.1228638 (2012).
21. Glembockyte, V., Grabenhorst, L., Trofymchuk, K. & Tinnefeld, P. DNA Origami Nanoantennas for Fluorescence Enhancement. *Acc Chem Res* **54**, 3338–3348. doi:10.1021/acs.accounts.1c00307 (2021).
22. Trofymchuk, K. et al. Addressable nanoantennas with cleared hotspots for single molecule detection on a portable smartphone microscope. *Nat Commun* **12**, 950. doi:10.1038/s41467-021-21238-9 (2021).
23. Pfeiffer, M. et al. Single antibody detection in a DNA origami nanoantenna. *iScience* **24**, 103072. doi:10.1016/j.isci.2021.103072 (2021).
24. Ghenuche, P. et al. Matching Nanoantenna Field Confinement to FRET Distances Enhances Förster Energy Transfer Rates. *Nano Lett* **15**, 6193–201. doi:10.1021/acs.nanolett.5b02535 (2015).
25. Bohlen, J. et al. Plasmon-assisted Förster resonance energy transfer at the single-molecule level in the moderate quenching regime. *Nanoscale* **11**, 7674–7681. doi:10.1039/C9NR01204D (2019).
26. Bidault, S. et al. Competition between Förster Resonance Energy Transfer and Donor Photodynamics in Plasmonic Dimer Nanoantennas. *ACS Photonics* **3**, 895–903. doi:10.1021/acsphotonics.6b00148 (2016).
27. Vietz, C., Kaminska, I., Sanz Paz, M., Tinnefeld, P. & Acuna, G. P. Broadband Fluorescence Enhancement with Self-Assembled Silver Nanoparticle Optical Antennas. *ACS Nano* **11**, 4969–4975. doi:10.1021/acsnano.7b01621 (2017).
28. Sturzenegger, F. et al. Transition path times of coupled folding and binding reveal the formation of an encounter complex. *Nat Commun* **9**, 4708. doi:10.1038/s41467-018-07043-x (2018).
29. Kjaergaard, M., Teilum, K. & Poulsen, F. M. Conformational selection in the molten globule state of the nuclear coactivator binding domain of CBP. *Proc Natl Acad Sci U S A* **107**, 12535–40. doi:10.1073/pnas.1001693107 (2010).
30. Demarest, S. J. et al. Mutual synergistic folding in recruitment of CBP/p300 by p160 nuclear receptor coactivators. *Nature* **415**, 549–53. doi:10.1038/415549a (2002).
31. Gopich, I. V. & Szabo, A. Decoding the pattern of photon colors in single-molecule FRET. *J Phys Chem B* **113**, 10965–73. doi:10.1021/jp903671p (2009).
32. Chung, H. S., Cellmer, T., Louis, J. M. & Eaton, W. A. Measuring ultrafast protein folding rates from photon-by-photon analysis of single molecule fluorescence trajectories. *Chem Phys* **422**, 229–237. doi:10.1016/j.chemphys.2012.08.005 (2013).
33. Zhang, Y. et al. General Strategy To Improve the Photon Budget of Thiol-Conjugated Cyanine Dyes. *J Am Chem Soc*. doi:10.1021/jacs.2c12635 (2023).
34. Ouldrige, T. E., Sulc, P., Romano, F., Doye, J. P. & Louis, A. A. DNA hybridization kinetics: zippering, internal displacement and sequence dependence. *Nucleic Acids Res* **41**, 8886–95. doi:10.1093/nar/gkt687 (2013).
35. Michie, M. S. et al. Cyanine Conformational Restraint in the Far-Red Range. *J Am Chem Soc* **139**, 12406–12409. doi:10.1021/jacs.7b07272 (2017).
36. Eiring, P. et al. Targetable Conformationally Restricted Cyanines Enable Photon-Count-Limited Applications. *Angew Chem Int Ed Engl* **60**, 26685–26693. doi:10.1002/anie.202109749 (2021).
37. Campos, L. A. et al. A photoprotection strategy for microsecond-resolution single-molecule fluorescence spectroscopy. *Nat Methods* **8**, 143–6. doi:10.1038/nmeth.1553 (2011).
38. Chung, H. S. & Eaton, W. A. Single-molecule fluorescence probes dynamics of barrier crossing. *Nature* **502**, 685–8. doi:10.1038/nature12649 (2013).
39. Truex, K., Chung, H. S., Louis, J. M. & Eaton, W. A. Testing Landscape Theory for Biomolecular Processes with Single Molecule Fluorescence Spectroscopy. *Phys Rev Lett* **115**, 018101. doi:10.1103/PhysRevLett.115.018101 (2015).
40. Neupane, K. et al. Direct observation of transition paths during the folding of proteins and nucleic acids. *Science* **352**, 239–42. doi:10.1126/science.aad0637 (2016).

41. Taumoeolau, G. H. & Best, R. B. Estimating transition path times and shapes from single-molecule photon trajectories: A simulation analysis. *J Chem Phys* **154**, 115101. doi:10.1063/5.0040949 (2021).
42. Makarov, D. E., Berezhkovskii, A., Haran, G. & Pollak, E. The Effect of Time Resolution on Apparent Transition Path Times Observed in Single-Molecule Studies of Biomolecules. *J Phys Chem B* **126**, 7966–7974. doi:10.1021/acs.jpcc.2c05550 (2022).
43. Holzmeister, P., Acuna, G. P., Grohmann, D. & Tinnefeld, P. Breaking the concentration limit of optical single-molecule detection. *Chem Soc Rev* **43**, 1014–28. doi:10.1039/c3cs60207a (2014).
44. Close, C. et al. Maximizing the Accessibility in DNA Origami Nanoantenna Plasmonic Hotspots. *Advanced Materials Interfaces* **9**. doi:10.1002/admi.202200255 (2022).
45. Matikonda, S. S. et al. Impact of Cyanine Conformational Restraint in the Near-Infrared Range. *J Org Chem* **85**, 5907–5915. doi:10.1021/acs.joc.0c00236 (2020).
46. Noe, F., Olsson, S., Kohler, J. & Wu, H. Boltzmann generators: Sampling equilibrium states of many-body systems with deep learning. *Science* **365**. doi:10.1126/science.aaw1147 (2019).
47. Bottaro, S. & Lindorff-Larsen, K. Biophysical experiments and biomolecular simulations: A perfect match? *Science* **361**, 355–360. doi:10.1126/science.aat4010 (2018).
48. Shaw, D. E. et al. Atomic-level characterization of the structural dynamics of proteins. *Science* **330**, 341–6. doi:10.1126/science.1187409 (2010).

Single-Molecule FRET at 10 MHz Count Rates

Supporting information

Lennart Grabenhorst¹, Flurin Sturzenegger², Moa Hasler², Benjamin Schuler^{2,3}, and Philip Tinnefeld^{1,*}

¹Department of Chemistry and Center for NanoScience,
Ludwig-Maximilians-Universität München, München, Germany
²Department of Biochemistry, University of Zurich, Zurich, Switzerland
³Department of Physics, University of Zurich, Zurich, Switzerland
*Correspondence: philip.tinnefeld@cup.uni-muenchen.de

Contents

1	Materials and methods	2
1.1	DNA origami synthesis	2
1.2	Nanoantenna preparation	2
1.3	Protein expression and labelling	3
1.4	Single-molecule surface preparation	4
1.5	Confocal microscopy	4
1.6	Data analysis	5
2	Supplementary notes	7
2.1	Considerations on the choice of the FRET pair	7
2.2	Note on the comparison of nanoantenna and reference measurements	7
2.3	Simulations of photon time traces	8
3	Supplementary tables	9
4	Supplementary figures	11
	References	17

1 Materials and methods

1.1 DNA origami synthesis

DNA origami nanostructures were produced and purified as described previously. [1] Purification of the DNA origami was achieved using 100 kDa MWCO filters (Merck). The filters were filled with 450 μ L FoB5 buffer (10 mM TRIS, 5 mM $MgCl_2$, 5 mM NaCl, 1 mM EDTA) and centrifuged at 10 krcf for 7 minutes to wet the membrane. Then, the filtrate was discarded and the filter was filled with 450 μ L of FoB5 buffer and 50 μ L of the folded origami sample. The mixture was centrifuged at 7 krcf for 12 minutes. This process was repeated 3 more times. The ACTR-DNA-origami construct was prepared as follows: 25 μ L of filter purified DNA origamis bearing the protein docking sequence were mixed with 1 μ L of the AF647-labeled ACTR protein at 10 μ M. The mixture was heated to 37°C and slowly cooled to 20 °C over the course of 1 hr using a thermocycler. Samples were subjected to another 3 rounds of filter purification as described previously.

DNA sequences

All sequences needed to synthesize the DNA origami were described previously. [1] Here we summarize the additional oligonucleotides needed for the experiment.

- 5'-TAATCACTGTTGCCCTGATTAAATACGTTAATAAGTGATGTAGGTGGTAGAGGAA-3' staple for **binding ACTR** in the hotspot
- 5'-TTCCTCTACCACCTACATCAC-3' ssDNA labelled with **maleimide** used to tag ACTR
- 5'-TAATCACTGTTGCCCTGATTAAATACGTTAATAATGCTCTGCTACTCTGTCTG-3' staple with **docking site labelled** with either Cy5B or AlexaFluor 647 at the 3'-end
- 5'-GACAGA-3' short ssDNA **labelled** with either Dy 751 or ATTO 740 at the 3'-end

The dye labelled oligonucleotides were obtained from biomers.net GmbH, Germany, except for the ATTO 740-labelled strand, which was obtained from Eurofins Genomics GmbH, Germany and the Cy5B labelled strand, which was produced in-house using Cy5B maleimide and C6-Amino-labelled DNA obtained from Eurofins Genomics GmbH, Germany as previously described. [2]

1.2 Nanoantenna preparation

DNA functionalized spherical gold nanoparticles (100 nm diameter) were produced as described previously [1], with slight modifications: 2 mL of a 0.025 mg/mL solution of 100 nm gold nanoparticles were mixed with 20 μ L of 10% Tween 20 and 20 μ L of potassium phosphate buffer (4:5 mixture of 1 M monobasic and 1 M dibasic potassium phosphate, Sigma Aldrich, USA) as well as 4 nmol of thiol-modified ssDNA (5'-T20-SH-3', Ella Biotech GmbH, Germany) dissolved in 20 μ L ultrapure H_2O and 30 μ L of TCEP in ultrapure H_2O at 60 mM. The solution was then stirred on a magnetic stirrer at 40 °C for 1 hr. Then, PBS with additional

3.3 M of NaCl was added stepwise to a final concentration of 750 mM NaCl. Then, the particle solution was mixed 1:1 with PBS supplemented with 10 mM NaCl, 2.11 mM P8709 buffer (Sigma Aldrich, USA), 2.89 mM P8584 buffer (Sigma Aldrich, USA), 0.01% Tween 20 and 1 mM EDTA. The solution was centrifuged for 8 min at 2.8 krcf and the supernatant was discarded. This procedure was repeated 5 more times. Then, the supernatant was discarded and the particles were resuspended in 10 mM TRIS, 1 mM EDTA, 750 mM NaCl buffer to an extinction at 550 nm of approximately 0.1 as measured on a UV-VIS spectrometer (NanoDrop2000, Thermo Fisher Scientific, USA). The immobilized DNA origamis were then incubated at RT overnight with this solution to form the nanoantennas.

1.3 Protein expression and labelling

Protein expression

For NCBD, a construct with a single cysteine residue and proline residues 20 and 23 replaced by alanine (to suppress kinetic heterogeneity due to peptidyl-prolyl cis/trans isomerization [3]) was generated by site-directed mutagenesis. Furthermore, the expression construct contained an N-terminal His₆-tag cleavable with HRV 3C protease (sequence of the cleaved construct: GPNRSISPSA LQDLLRTLKS ASSAQQQQV LNILKSNPQL MAAFIKQRTA KYVANQPGMQ C). NCBD was co-expressed [4] with wild-type ACTR from a pET-47b(+) vector. Expression was carried out in *Escherichia coli* C41(DE3) (Merck). Cells were grown at 37 °C in TYH medium (for 1 L: 20 g tryptone, 10 g yeast extract, 11 g HEPES, 5 g NaCl, 1 g MgSO₄, pH 7.3), supplied with 0.5% (w/v) glucose, until they reached an OD₆₀₀ of 0.8. Then, 1 mM IPTG was added to the culture. Expression continued for 1 h at 37 °C, after which cells were harvested by centrifugation. The harvested cells were lysed by sonication, and the His₆-tagged protein was enriched via immobilized metal ion affinity chromatography on Ni-IDA resin (Agarose Bead Technologies). The His₆-tag was then cleaved with HRV 3C protease and separated from the protein by another round of IMAC. Finally, NCBD was separated from ACTR and other impurities via reversed-phase HPLC (RP-HPLC) on a C18 column (Reprosil Gold 200, Dr. Maisch, Germany) with a water/0.1% trifluoroacetic acid-acetonitrile gradient. The purified protein was lyophilized, resuspended in buffer, and stored at -80 °C until use. For ACTR, a double-cysteine construct, with one cysteine close to the N-terminus for attachment to the DNA origami, and one close to the C-terminus for the dye, was generated by site-directed mutagenesis. Furthermore, the expression construct contained an N-terminal His₆-tag cleavable with HRV 3C protease (sequence of the cleaved construct: GPCGTQNRPL LRNSLDDLVG PPSNLEGQSD ERALLDQLHT LLSNTDATGL EEIDRALGIP ELVNQGQALE PKQDC). ACTR was co-expressed with wild-type NCBD from a pET-47b(+) vector and purified as described above.

Protein labelling

For NCBD, lyophilized protein was dissolved under nitrogen atmosphere at a concentration of 340 µM in 10 mM potassium phosphate buffer, pH 7.0, and was labeled for 3 h with a 1.6-fold molar excess of LD750-maleimide (Lumidyne Technologies) to protein. Labeled

protein was separated from unlabeled protein with RP-HPLC on a C18 column (Reprosil Gold 200, Dr. Maisch, Germany) with a water/0.1% trifluoroacetic acid-acetonitrile gradient. For ACTR, in a first step, the more reactive cysteine at position 3 was labeled with a 3'-maleimide-functionalized oligodeoxynucleotides (biomers.net GmbH) with the sequence 5'-TTC CTC TAC CAC CTA CAT CAC-3'-maleimide. Lyophilized protein was dissolved under nitrogen atmosphere to 280 μ M in 100 mM potassium phosphate buffer, pH 7.0, and was labeled for 3 h at a 0.5-fold molar ratio of oligodeoxynucleotide to protein. Singly labeled protein was separated from unlabeled and doubly labeled protein with RP-HPLC on a Reprosil-Pur 200 C18-AQ column (Dr. Maisch, Germany), with a water/0.1 M triethylammonium acetate-acetonitrile gradient. In a second step, the cysteine at position 75 was labeled with AlexaFluor647 maleimide. The lyophilized protein/oligodeoxynucleotide construct was dissolved under nitrogen atmosphere to a final concentration of 44 μ M in 100 mM potassium phosphate buffer, pH 7.0, and was labeled for 3 h at a 1.5-fold molar ratio of dye to protein. Labeled protein was again separated from unlabeled protein with RP-HPLC on a Reprosil-Pur 200 C18-AQ column, with a water/0.1 M triethylammonium acetate-acetonitrile gradient. The purified constructs were lyophilized, resuspended in buffer, and stored at -80 °C until use.

1.4 Single-molecule surface preparation

Microscopy slides (24 mm \times 60 mm size and 170 μ m thickness (Carl Roth GmbH, Germany) were cleaned in an ozonator (PSD-UV4, Novascan Technologies, USA) at 100 °C for 30 mins. Then, 2 CoverWell™ Perfusion Chamber gaskets (9 mm diameter, 0.5 mm deep, Grace Biolabs) were glued on the slides and the glue was strengthened by placing the slide on a 100 °C heating plate for 30 seconds. Surfaces then were cleaned by incubating with 1 M KOH for 10 mins. The chambers then were washed 4 times with PBS. The surfaces then were passivated by incubation with BSA-Biotin (1 mg/mL in 10 mM TRIS, 1 mM EDTA, 50 mM NaCl, Sigma Aldrich, USA) for 10 mins. The chambers were then washed with PBS (3 times). Then, the chambers were incubated with NeutrAvidin™ (0.25 mg/mL in PBS, freshly diluted from a 1 mg/mL stock in ultrapure H₂O, Thermo Fisher Scientific, USA) for 10 minutes. After washing with PBS (3 times), chambers were ready for use.

1.5 Confocal microscopy

Data was acquired on a home-built setup based on an Olympus IX-71 microscope body. A LDH-D-C-640 laser (636 nm) in continuous wave mode was focussed to a diffraction-limited spot and sent through a linear polarizer (LPVISE100-A, Thorlabs GmbH) and a quarter-wave plate (AQWP05M-600, Thorlabs GmbH) to obtain circularly polarized light. An oil-immersion objective (UPLSAPO100XO, NA1.40, Olympus Deutschland GmbH) was used to focus the light onto the sample. We used a piezo stage (P-517.3CD, Physik Instrumente GmbH & Co. KG) and a piezo controller (E-727.3CDA, Physik Instrumente GmbH & Co. KG) to scan the sample. The fluorescence was separated from the excitation laser with a dichroic beam splitter (zt488/543/635/730rpc, Chroma Technologies) and focussed on a 50 μ m diameter pinhole (Thorlabs GmbH). The fluorescence was then split between the red and infrared channel using a beam splitter (HC BS 749 SP, Chroma). The red fluorescence was distributed to 2

APDs (SPCM-AQRH-14-TR and SPCM-AQR-15, Excelitas Technologies GmbH & Co. KG, Germany) using a nonpolarizing 50:50 beam splitter (CCM1-BS013/M, Thorlabs GmbH). The infrared channel was distributed to 2 APDs (SPCM-AQRH-14-TR and SPCM-AQR-15, Excelitas Technologies GmbH & Co. KG, Germany) using a nonpolarizing 50:50 beam splitter (CCM1-BS014/M, Thorlabs GmbH). Events were registered by a multichannel picosecond event timer (HydraHarp 400, PicoQuant GmbH) in T2 mode and the hardware was controlled using a commercial software (SymPhoTime 64, PicoQuant GmbH) We used a photostabilizing system consisting of enzymatic oxygen removal by glucose oxidase/catalase as well as a reducing/oxidizing system with Trolox/Troloxquinone for all of the experiments. Specifically, the buffer consisted of 50 mM TRIS, 500 mM NaCl, 2 mM Trolox/Troloxquinone, 2% (w/v) Glucose, 165 U/mL Glucose oxidase, 2170 U/mL Catalase dissolved in D₂O for all experiments. [5, 6] For the experiments with ATTO 740, the pH value of the buffer was adjusted to 7 before use. We used lower excitation powers (10 nW – 20 nW) to scan the surfaces and find the coordinates of the single molecules. Then we placed the laser focus on these coordinates, checked if the fluorescence transient exhibited binding events and then increased the laser power to 1 μ W – 4 μ W by removing a neutral density filter in the excitation path.

1.6 Data analysis

Data were analysed using home-written python code with a backend written in C++ using Eigen [7] which is available on Gitlab. [8] For the maximum likelihood analysis of photon-by-photon trajectories we used the method developed by Gopich and Szabo [9] and applied to transition paths by Chung and Eaton. [10–12] Here, the likelihood of detecting a sequence of photons j with colors c_i is given by

$$L_j = \nu_{\text{fin}}^T \prod_{i=2}^N [\mathbf{F}(c_i) \exp(\mathbf{K}\tau_i)] \mathbf{F}(c_1) \nu_{\text{ini}} \quad (1)$$

with τ_i being the interphoton time and \mathbf{K} being the rate matrix either for the two state model with acceptor blinking:

$$\mathbf{K} = \begin{bmatrix} -k_D - k_d & k_{A,\text{app}} & k_b & 0 \\ k_D & -k_{A,\text{app}} - k_d & 0 & k_b \\ k_d & 0 & -k_D - k_b & k_{A,\text{app}} \\ 0 & k_d & k_D & k_{A,\text{app}} - k_b \end{bmatrix} \quad (2)$$

or the model with an intermediate state

$$\mathbf{K} = \begin{bmatrix} -k'_D - k_d & k_i & 0 & k_b & 0 & 0 \\ k'_D & -2k_i - k_d & k'_{A,\text{app}} & 0 & k_b & 0 \\ 0 & k_i & -k'_{A,\text{app}} - k_d & 0 & 0 & k_b \\ k_d & 0 & 0 & -k'_D - k_b & k_i & 0 \\ 0 & k_d & 0 & k'_D & -2k_i - k_b & k'_{A,\text{app}} \\ 0 & 0 & k_d & 0 & k_i & -k'_{A,\text{app}} - k_b \end{bmatrix} \quad (3)$$

Here, k_D is the dissociation rate constant, k_d and k_b are the rate constants for the conversion between bright and dark states, $k_{A,app}$ is the apparent association rate and k_i is the rate with which the intermediate state is depopulated. \mathbf{F} is the photon color matrix and is given by

$$\mathbf{F}_{\text{acceptor}} = \begin{bmatrix} E_B & 0 & 0 & 0 \\ 0 & E_U & 0 & 0 \\ 0 & 0 & E_d & 0 \\ 0 & 0 & 0 & E_d \end{bmatrix} \quad \text{and} \quad \mathbf{F}_{\text{donor}} = \mathbf{I} - \mathbf{F}_{\text{acceptor}} \quad (4)$$

for the two state model and

$$\mathbf{F}_{\text{acceptor}} = \begin{bmatrix} E_B & 0 & 0 & 0 & 0 & 0 \\ 0 & E_I & 0 & 0 & 0 & 0 \\ 0 & 0 & E_U & 0 & 0 & 0 \\ 0 & 0 & 0 & E_d & 0 & 0 \\ 0 & 0 & 0 & 0 & E_d & 0 \\ 0 & 0 & 0 & 0 & 0 & E_d \end{bmatrix} \quad \text{and} \quad \mathbf{F}_{\text{donor}} = \mathbf{I} - \mathbf{F}_{\text{acceptor}} \quad (5)$$

for the model with an intermediate state. Here, \mathbf{I} is the identity matrix, E_B is the FRET efficiency in the bound state, E_U is the FRET efficiency in the unbound state and E_I is the FRET efficiency of the intermediate state. E_d is the FRET efficiency of the dark state, which we set equal to E_U . Because we are analyzing single transitions from the unbound to the bound state, we set $k_{A,app} = k_D = 0.01s^{-1}$, $k'_{A,app} = k'_D = 0.02s^{-1}$ and

$$\nu_{\text{ini}}^{\mathbf{T}} = (0 \quad p_b \quad 0 \quad 1 - p_b) \quad \text{and} \quad \nu_{\text{fin}} = (p_b \quad 0 \quad 1 - p_b \quad 0) \quad (6)$$

for the two state model and

$$\nu_{\text{ini}}^{\mathbf{T}} = (0 \quad 0 \quad p_B \quad 0 \quad 0 \quad 1 - p_B) \quad \text{and} \quad \nu_{\text{fin}} = (p_B \quad 0 \quad 0 \quad 1 - p_B \quad 0 \quad 0) \quad (7)$$

for the model with an intermediate state with $p_b = k_b/(k_b + k_d)$. For the fitting procedure, it is beneficial to define $k = k_b + k_d$. We manually picked single transitions and fit them with the two state model to obtain E_B , E_U , k and p_b . We discarded transitions where the fit did not converge (41 and 33 discarded transitions for the experiment with the IDPs and the experiments with the DNA hybridization, respectively) and where E_B was more than 2 σ away from the mean value (7 and 19 discarded transitions). Then we used the obtained fit parameters to calculate $\Delta \ln L$ with $\tau_i = 1/(2k_i)$ and E_I as the only free parameters. To summarize the results, we normalized the obtained E_I values to the respective E_U and E_B values via $E_{i, \text{norm}} = (E_I - E_U)/(E_B - E_U)$ for each transition.

2 Supplementary notes

2.1 Considerations on the choice of the FRET pair

The most important parameters for the choice of a suitable FRET pair are the absorption spectra of the dyes with respect to the plasmon resonance of the nanoantenna, because the fluorescence enhancement is the region slightly red shifted to the plasmon resonance. The plasmon resonance peak can be approximated by the scattering cross-section of the nanoantenna. As shown previously [13], for dimers of 80 nm silver nanoparticles (AgNPs), the plasmon resonance lies at 500–650 nm while for 100 nm gold nanoparticles (AuNPs) it lies in the region of 600–750 nm. Because of increased scattering of AgNPs, we opted to utilize nanoantennas based on AuNPs, which meant that we had to work with dyes absorbing in the red to near-IR spectral range. We also noticed a negative influence of pulsed excitation on the photostability of the fluorophores which is why we used CW excitation at 640 nm.

The next considerations were possible dim or dark states of the fluorophores. We showed that carbopyronine dyes such as ATTO 647N show pronounced dim state formation in nanoantenna environments. [14] On the other hand, cyanine dyes did not show such behavior: dark state formation, e.g. by trans-cis isomerization was accelerated, but no second intensity state was observed, which makes these class of dyes superior for this application. For this reason, we chose cyanine dyes as donor dyes – either AlexaFluor 647 or Cy5B. [2]

For the acceptor fluorophores, the same considerations apply, but the available options of near-IR absorbing dyes are more limited. They comprise mainly cyanine based dyes such as AlexaFluor 750, Lumidyne (LD) 750 or Dyomics (Dy-)751 and as an alternative ATTO740 (structure unpublished, to the best of our knowledge). We tried most of them with similar success so that the more deciding factor in this regard was the attainable proximity ratio in the bound state, which is likely influenced by Dye-DNA or Dye-Protein interactions and the compatibility with our labelling reaction (ATTO740 is pH sensitive, LD-750 and AlexaFluor 750 were not commercially available on very short oligonucleotides). We note that in all cases, the use of ROXS and oxygen removal leads to sub-microsecond acceptor blinking [15] which we attribute to trans-cis isomerization as well as ROXS-induced radical blinking. This could potentially be overcome by alternative photostabilization methods which rely on efficient direct depopulation of the triplet excited states (e.g. energy transfer mechanisms). [16]

2.2 Note on the comparison of nanoantenna and reference measurements

To assess the increase in maximum photon count rates and total observation times, the fairest comparison would be to use the same FRET pair (AlexaFluor 647 and LD750) measured without the DNA nanoantenna. However, since the photostability of this red/IR dye pair outside of the plasmonic hotspot was very poor (see exemplary time traces in Figure S7), we could only compare our results in the DNA nanoantenna to the previous state of the art, which in this case was the more photostable green/red FRET pair consisting of Cy3B and CF660R. [17]

2.3 Simulations of photon time traces

To test the robustness of the analysis based on transfer efficiencies for the case of varying total photon count rates, we simulated photon time traces with varying total photon count rates and subjected them to the analysis. For the sake of simplifying the procedure, we did not include the possibility of photoblinking in these simulations. Time traces were simulated by drawing random interphoton times from an exponential distribution with the respective count rate and assigning them to the donor or acceptor channel with the relative probability given by the FRET efficiency of the given state. The datasets were then analysed with the same procedure, with the rate matrices K for the two state and the three state model, respectively, given by

$$\mathbf{K} = \begin{bmatrix} -k_{\text{off}} & k_{\text{on}} \\ k_{\text{off}} & -k_{\text{on}} \end{bmatrix} \quad \text{and} \quad \mathbf{K} = \begin{bmatrix} -k_{\text{off}} & k_i & 0 \\ k_{\text{off}} & -2k_i & k_{\text{on}} \\ 0 & k_i & -k_{\text{on}} \end{bmatrix} \quad (8)$$

The results are shown in Supplementary Figures 3 and 4. In conclusion, while the total photon count rate during the transition seems to affect the accuracy of the result and especially the total log likelihood difference, the varying photon count rates themselves seem to have only a minor effect on the extracted values.

3 Supplementary tables

Table S1: Mean fit results for the two state model. Errors indicate standard errors obtained from each dataset.

Sample	Parameter	Fit result
ACTR-NCBD AlexaFluor 647/LD 750 (141 transitions)	E_B	0.489 ± 0.012
	E_U	0.060 ± 0.002
	k	$1240 \pm 137 \text{ ms}^{-1}$
	p_b	0.849 ± 0.012
DNA hybridization Cy5B/Dy751 (405 transitions)	E_B	0.467 ± 0.004
	E_U	0.070 ± 0.001
	k	$412 \pm 49 \text{ ms}^{-1}$
	p_b	0.880 ± 0.005
DNA hybridization AlexaFluor 647/ATTO740 (96 transitions)	E_B	0.302 ± 0.007
	E_U	0.047 ± 0.001
	k	$705 \pm 107 \text{ ms}^{-1}$
	p_b	0.954 ± 0.004
DNA hybridization (mismatch) AlexaFluor 647/ATTO740 (204 transitions)	E_B	0.272 ± 0.003
	E_U	0.042 ± 0.001
	k	$674 \pm 57 \text{ ms}^{-1}$
	p_b	0.945 ± 0.005

Table S2: Fit results for the three state model. Errors are calculated from the diagonal elements of the covariance matrix.

Sample	Parameter	Fit result
ACTR-NCBD AlexaFluor 647/LD 750	τ_i	$96 \pm 13 \mu\text{s}$
	$E_{i, \text{norm}}$	0.58 ± 0.04
	$\Delta \ln L (\tau_i, E_{i, \text{norm}})$	92.146
DNA hybridization Cy5B/Dy751	τ_i	$17 \pm 1 \mu\text{s}$
	$E_{i, \text{norm}}$	0.30 ± 0.02
	$\Delta \ln L (\tau_i, E_{i, \text{norm}})$	247.261
DNA hybridization AlexaFluor 647/ATTO740	τ_i	$20 \pm 3 \mu\text{s}$
	$E_{i, \text{norm}}$	0.21 ± 0.02
	$\Delta \ln L (\tau_i, E_{i, \text{norm}})$	67.301
DNA hybridization (mismatch) AlexaFluor 647/ATTO740	τ_i	$41 \pm 3 \mu\text{s}$
	$E_{i, \text{norm}}$	0.23 ± 0.01
	$\Delta \ln L (\tau_i, E_{i, \text{norm}})$	278.717

Table S3: Estimated Förster radii for all FRET pairs used in this study.

FRET pair	Estimated R_0
AlexaFluor 647 – LD750	75.7 Å
Cy5B – Dy751	70.9 Å
AlexaFluor 647 – ATTO740	65.4 Å

4 Supplementary figures

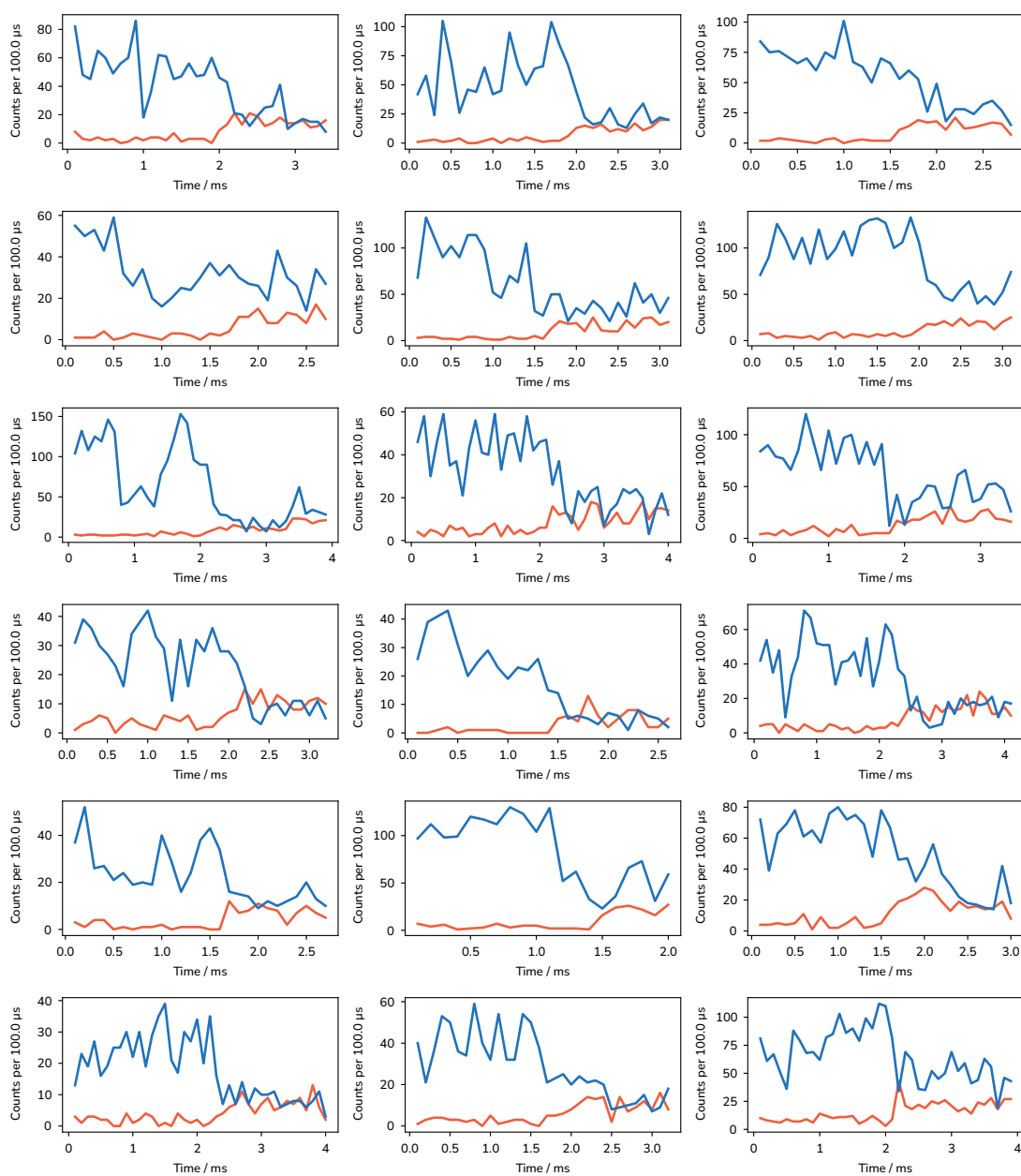


Figure S1: Exemplary fluorescence time traces containing transitions for the ACTR-NCBD experiment. Blue: donor fluorescence, red: acceptor fluorescence.

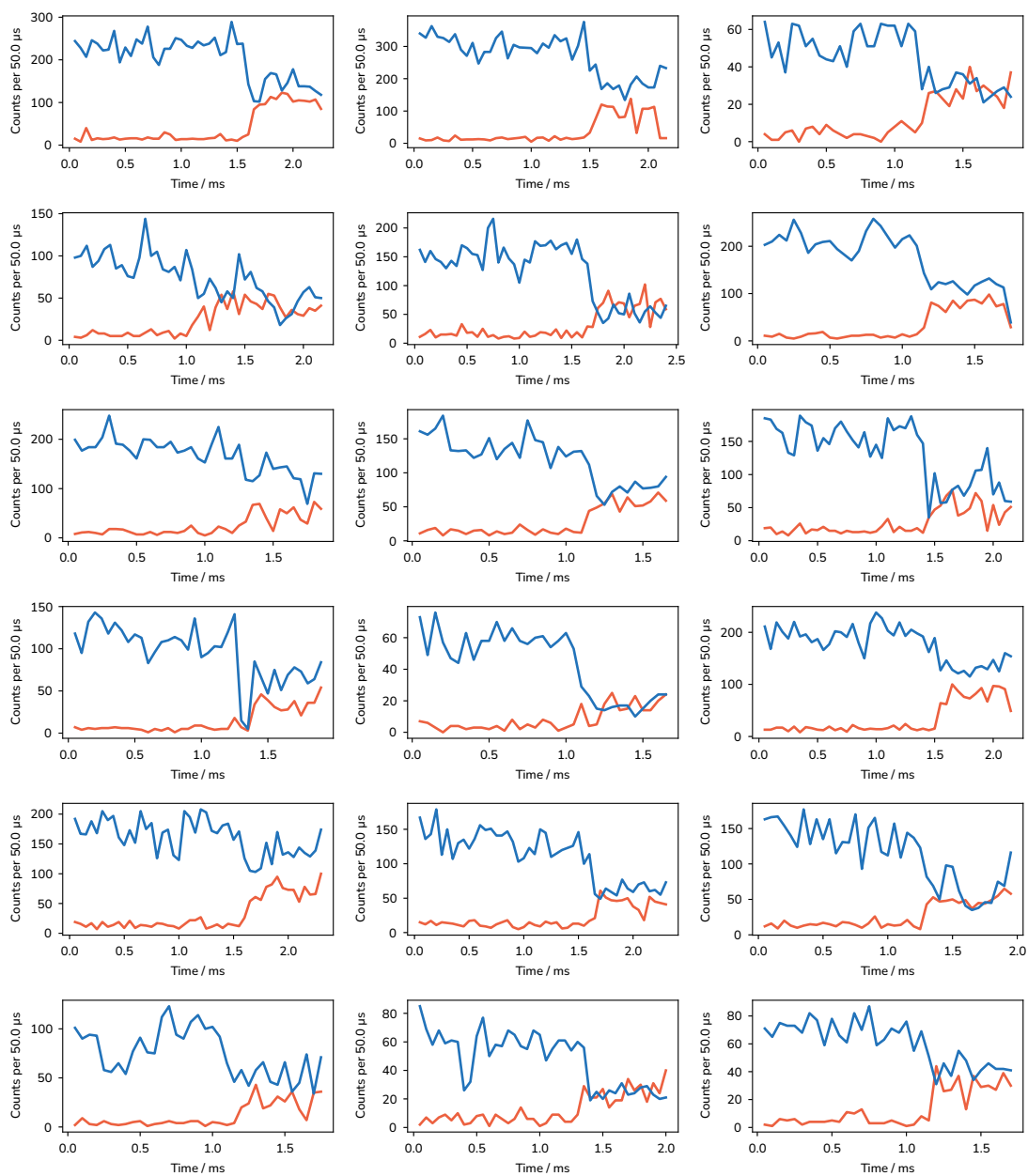


Figure S2: Exemplary fluorescence time traces containing transitions for the DNA hybridization experiment. Blue: donor fluorescence, red: acceptor fluorescence.

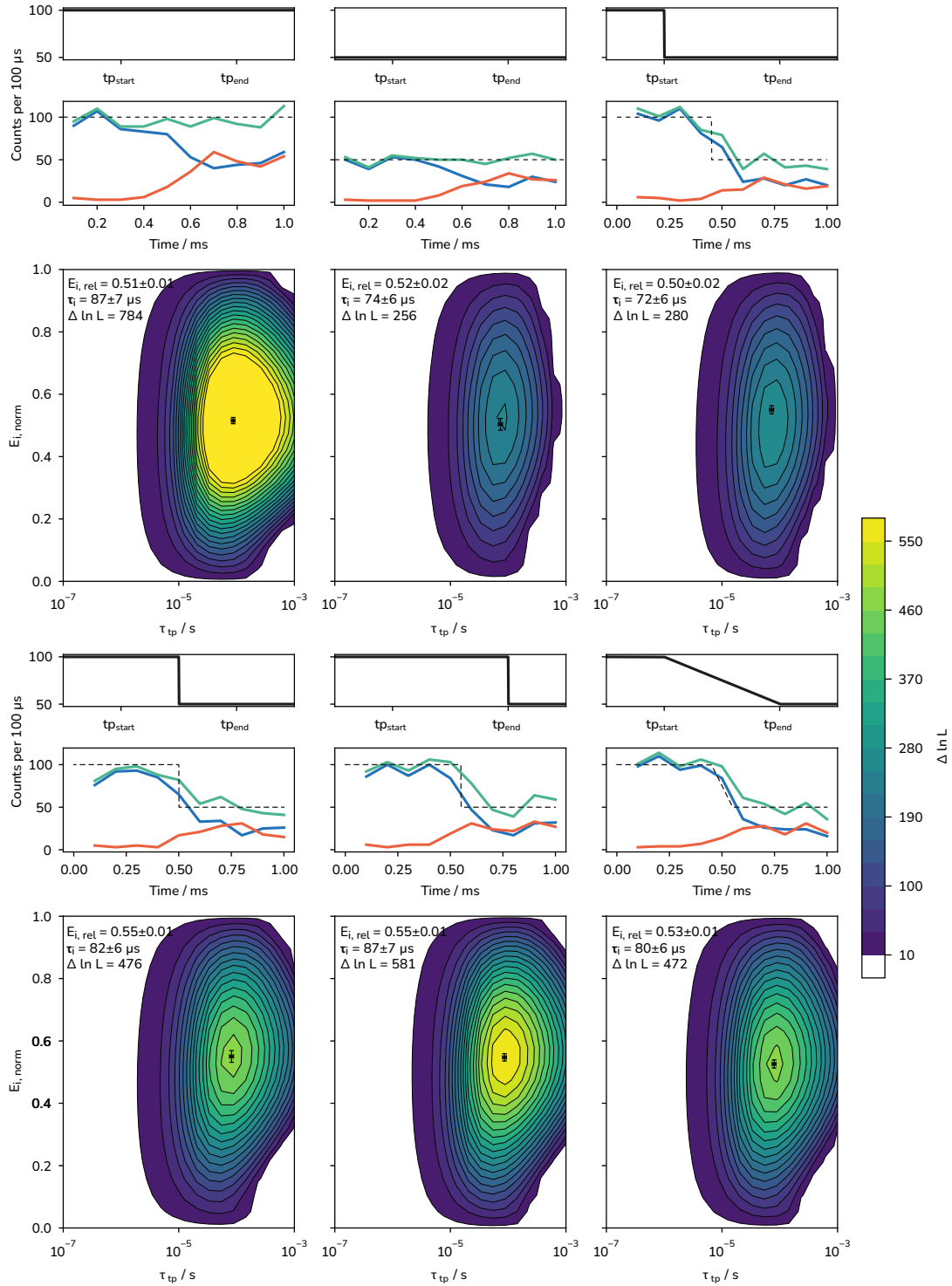


Figure S3: Analysis of the influence of varying photon count rates on the robustness of the analysis. For each set, 200 transitions (1 ms windows) were simulated. Input parameters were chosen to resemble the experiments with the IDPs ($E_B = 0.5$, $E_{i, \text{norm}} = 0.5$, $E_U = 0.05$, $\tau_i = 100 \mu\text{s}$, PCR = 1–0.5 MHz) Blue: donor fluorescence, Red: acceptor fluorescence, Green: sum of both channels, Black: input count rate for the simulation. The most likely values are indicated in the plots. The errors were calculated from the diagonal elements of the covariance matrix. See Supplementary Note 2 for details on the analysis.

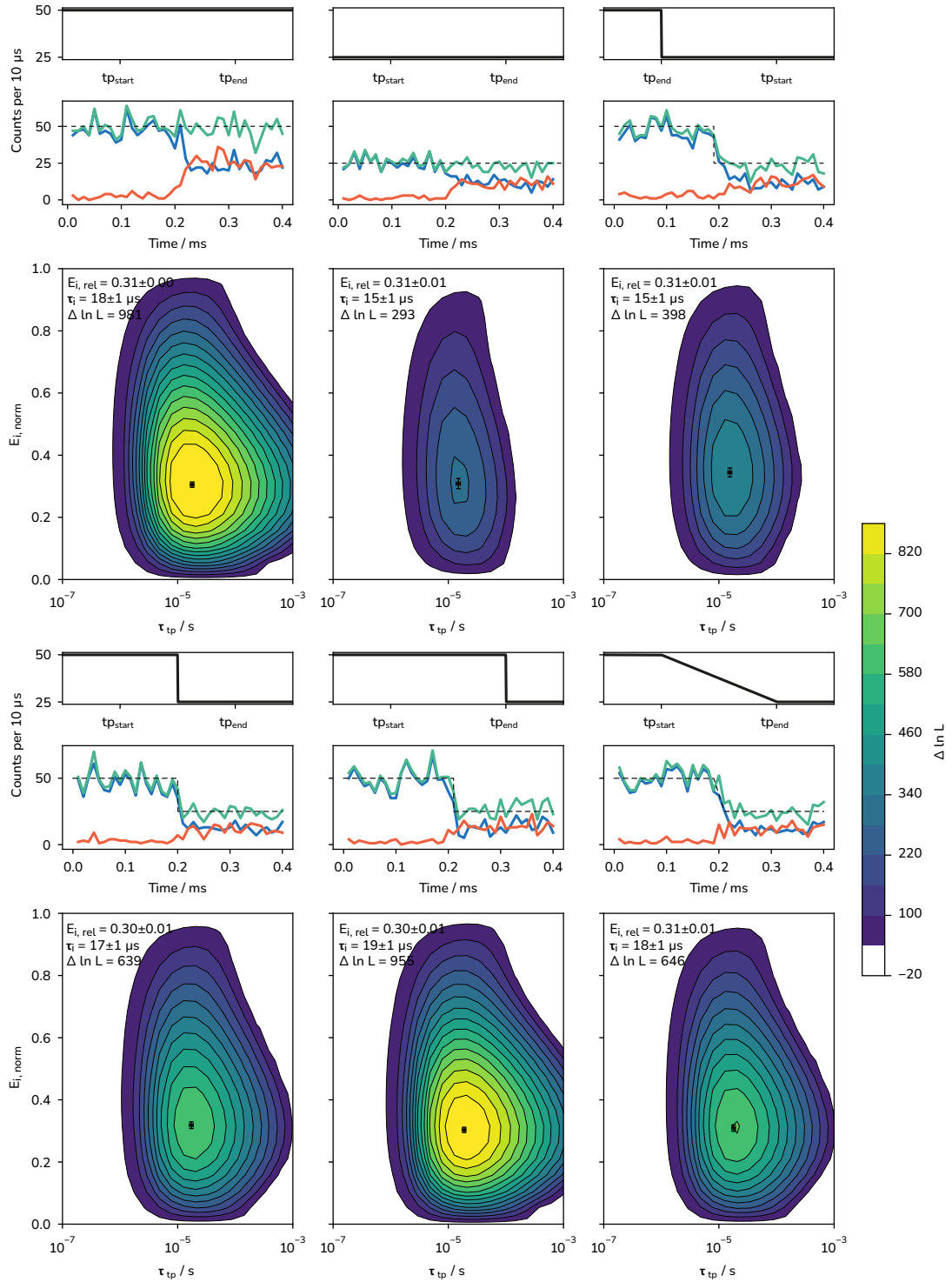


Figure S4: Analysis of the influence of varying photon count rates on the robustness of the analysis. For each set, 200 transitions (1 ms windows) were simulated. Input parameters were chosen to resemble the experiments with the DNA hybridization reaction ($E_B = 0.5$, $E_{i, \text{norm}} = 0.3$, $E_U = 0.05$, $\tau_i = 20 \mu\text{s}$, $\text{PCR} = 5\text{--}2.5 \text{ MHz}$) Blue: donor fluorescence, Red: acceptor fluorescence, Green: sum of both channels, Black: input count rate for the simulation. The most likely values are indicated in the plots. The errors were calculated from the diagonal elements of the covariance matrix. See Supplementary Note 2 for details on the analysis.

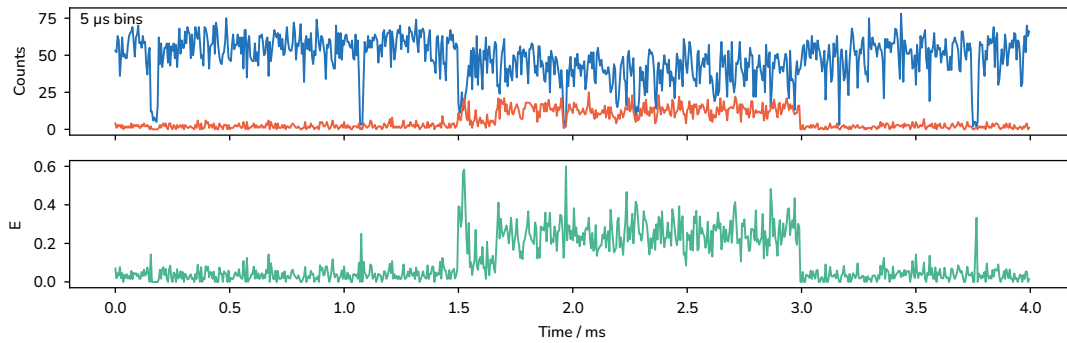


Figure S5: Exemplary binding event of the 6 nt long ssDNA to the docking site at 5 μ s binning. Blue: donor (AlexaFluor 647) fluorescence, red: acceptor (ATTO740) fluorescence (top). The bottom panel shows the uncorrected FRET efficiency. This snippet contains photon count rates of up to 16.4 MHz (average: 10.8 MHz).

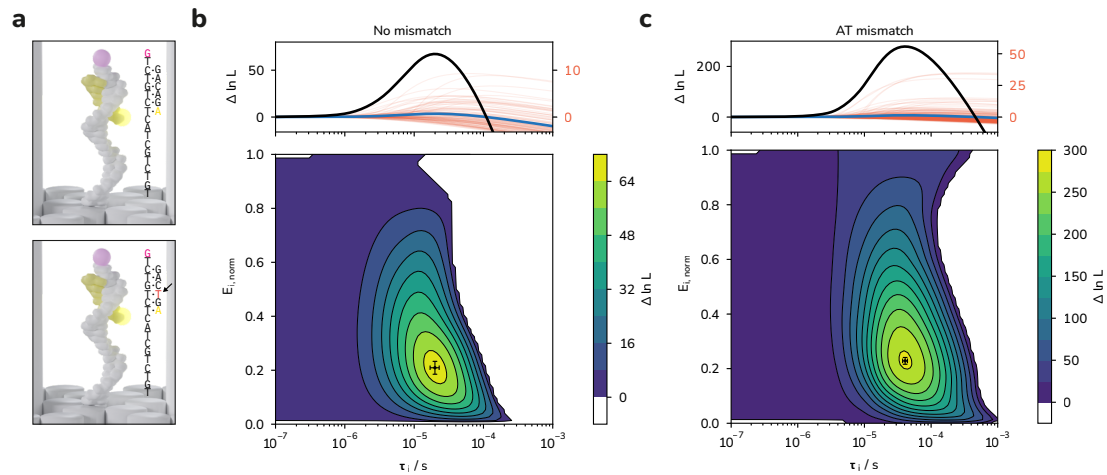


Figure S6: (a) Depiction of the position of the AT mismatch in the short ssDNA strand (bottom) as well as the sequence of the perfectly matched staple (top). (b) 2D contour plot of the log-likelihood difference $\Delta \ln L$ for the perfectly matched sample with AlexaFluor 647 and ATTO740 summed up over 96 transitions (bottom) as well as a plot showing $\Delta \ln L$ values versus τ_i for single transitions (red, right scale) and the sum of all transitions (black) as well as their average (blue, right scale) calculated at the most likely value for $E_{i, \text{norm}}$. The most likely values are $\tau_i = 20 \pm 3 \mu\text{s}$ and $E_{i, \text{norm}} = 0.21 \pm 0.02$. (c) Same plots as (b) but for the sample with an AT mismatch in the short ssDNA stand. The most likely values are $\tau_i = 41 \pm 3 \mu\text{s}$ and $E_{i, \text{norm}} = 0.23 \pm 0.01$. The errors were calculated from the diagonal elements of the covariance matrix.

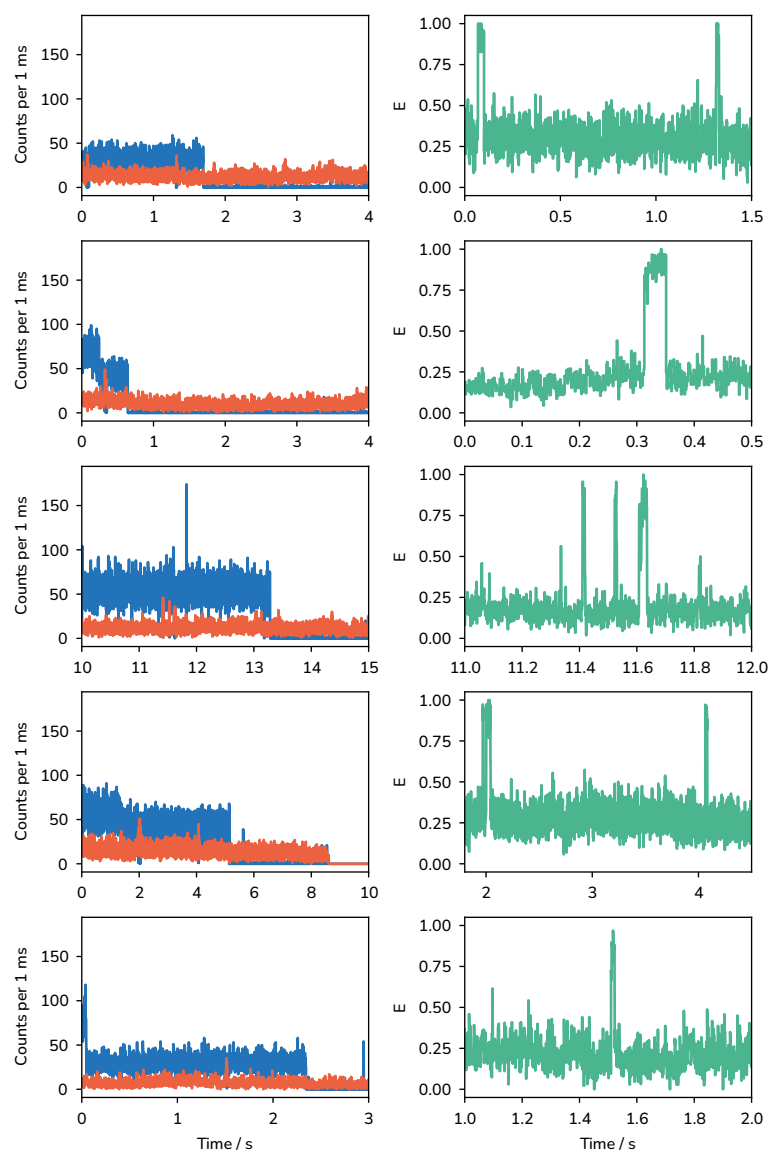


Figure S7: Exemplary time traces for the ACTR/NCBD system labelled with AlexaFluor 647 and LD750 immobilized on the DNA origami without attached nanoparticles. Left: donor (blue) and acceptor (red) fluorescence time traces. Right: corresponding zoom-ins on binding events in the uncorrected FRET time traces. Time traces were acquired at 1–2 μ W excitation intensity.

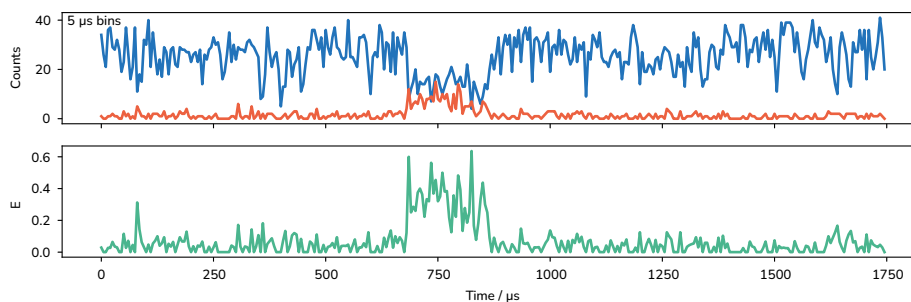


Figure S8: Exemplary time trace showing a DNA-DNA hybridization reaction for the sample with an AT-mismatch (estimated $K_d \approx 200 \mu\text{M}$) at $5 \mu\text{s}$ binning. The concentration of the short DNA strand used for this experiment was $3.6 \mu\text{M}$. Blue: donor (AlexaFluor 647) fluorescence, red: acceptor (ATTO740) fluorescence (top). The bottom panel shows the uncorrected FRET efficiency.

References

1. Trofymchuk, K. *et al.* Addressable nanoantennas with cleared hotspots for single-molecule detection on a portable smartphone microscope. *Nature Communications* **12**. <https://doi.org/10.1038/s41467-021-21238-9> (Feb. 2021).
2. Eiring, P. *et al.* Targetable Conformationally Restricted Cyanines Enable Photon-Count-Limited Applications. *Angewandte Chemie International Edition* **60**, 26685–26693. eprint: <https://onlinelibrary.wiley.com/doi/pdf/10.1002/anie.202109749>. <https://onlinelibrary.wiley.com/doi/abs/10.1002/anie.202109749> (2021).
3. Zosel, F., Mercadante, D., Nettels, D. & Schuler, B. A proline switch explains kinetic heterogeneity in a coupled folding and binding reaction. *Nature Communications* **9**. ISSN: 2041-1723. <http://dx.doi.org/10.1038/s41467-018-05725-0> (Aug. 2018).
4. Soranno, A. *et al.* Single-molecule spectroscopy reveals polymer effects of disordered proteins in crowded environments. *Proceedings of the National Academy of Sciences* **111**, 4874–4879. ISSN: 1091-6490. <http://dx.doi.org/10.1073/pnas.1322611111> (Mar. 2014).
5. Roy, R., Hohng, S. & Ha, T. A practical guide to single-molecule FRET. *Nature Methods* **5**, 507–516. <https://doi.org/10.1038/nmeth.1208> (May 2008).
6. Cordes, T., Vogelsang, J. & Tinnefeld, P. On the Mechanism of Trolox as Antiflicking and Antibleaching Reagent. *Journal of the American Chemical Society* **131**, 5018–5019. <https://doi.org/10.1021/ja809117z> (Mar. 2009).
7. Guennebaud, G., Jacob, B., *et al.* *Eigen v3* <http://eigen.tuxfamily.org>. 2010.
8. Grabenhorst, L. *AnnaLLH* <https://gitlab.lrz.de/>. 2023.
9. Gopich, I. V. & Szabo, A. Decoding the Pattern of Photon Colors in Single-Molecule FRET. *The Journal of Physical Chemistry B* **113**, 10965–10973. <https://doi.org/10.1021/jp903671p> (July 2009).

10. Chung, H. S., McHale, K., Louis, J. M. & Eaton, W. A. Single-Molecule Fluorescence Experiments Determine Protein Folding Transition Path Times. *Science* **335**, 981–984. <https://doi.org/10.1126/science.1215768> (Feb. 2012).
11. Chung, H. S., Cellmer, T., Louis, J. M. & Eaton, W. A. Measuring ultrafast protein folding rates from photon-by-photon analysis of single molecule fluorescence trajectories. *Chemical Physics* **422**, 229–237. <https://doi.org/10.1016/j.chemphys.2012.08.005> (Aug. 2013).
12. Kim, J.-Y., Meng, F., Yoo, J. & Chung, H. S. Diffusion-limited association of disordered protein by non-native electrostatic interactions. *Nature Communications* **9**. <https://doi.org/10.1038/s41467-018-06866-y> (Nov. 2018).
13. Vietz, C., Kaminska, I., Paz, M. S., Tinnefeld, P. & Acuna, G. P. Broadband Fluorescence Enhancement with Self-Assembled Silver Nanoparticle Optical Antennas. *ACS Nano* **11**, 4969–4975. <https://doi.org/10.1021/acsnano.7b01621> (Apr. 2017).
14. Grabenhorst, L., Trofymchuk, K., Steiner, F., Glembockyte, V. & Tinnefeld, P. Fluorophore photostability and saturation in the hotspot of DNA origami nanoantennas. *Methods and Applications in Fluorescence* **8**, 024003. <https://doi.org/10.1088/2050-6120/ab6ac8> (Feb. 2020).
15. Vogelsang, J. *et al.* A Reducing and Oxidizing System Minimizes Photobleaching and Blinking of Fluorescent Dyes. *Angewandte Chemie International Edition* **47**, 5465–5469. <https://doi.org/10.1002/anie.200801518> (July 2008).
16. Glembockyte, V. & Cosa, G. Redox-Based Photostabilizing Agents in Fluorescence Imaging: The Hidden Role of Intersystem Crossing in Geminate Radical Ion Pairs. *Journal of the American Chemical Society* **139**, 13227–13233. <https://doi.org/10.1021/jacs.7b08134> (Sept. 2017).
17. Sturzenegger, F. *et al.* Transition path times of coupled folding and binding reveal the formation of an encounter complex. *Nature Communications* **9**. ISSN: 2041-1723. <http://dx.doi.org/10.1038/s41467-018-07043-x> (Nov. 2018).

Associated Publication 5

Engineering Modular and Tunable Single Molecule Sensors by Decoupling Sensing from Signal Output

Lennart Grabenhorst*, Martina Pfeiffer*, Thea Schinkel, Mirjam Kümmerlin, Jasmin B. Maglic, Gereon A. Brüggenthies, Florian Selbach, Alexander T. Murr, Philip Tinnefeld and Viktorija Glembockyte

*equal contribution

bioRxiv (2023), doi: 10.1101/2023.11.06.565795

(open access)

Engineering Modular and Tunable Single Molecule Sensors by Decoupling Sensing from Signal Output

Lennart Grabenhorst ^{1†}, Martina Pfeiffer^{1†}, Thea Schinkel ¹, Mirjam Kümmerlin ¹, Jasmin B. Maglic ¹, Gereon A. Brüggenthies ¹, Florian Selbach ¹, Alexander T. Murr¹, Philip Tinnefeld ^{1*}, and Viktorija Glembockyte ^{1*}

¹Department of Chemistry and Center for NanoScience, Ludwig-Maximilians-Universität München, Butenandtstr. 5-13, 81377 München, Germany

[†]These authors contributed equally.

*Correspondence should be addressed to P.T. (philip.tinnefeld@cup.uni-muenchen.de) and V.G. (viktorija.glembockyte@cup.uni-muenchen.de)

Abstract: Biosensors play key roles in medical research and diagnostics, but there currently is a lack of sensing platforms that combine easy adaptation to new targets, strategies to tune the response window to relevant analyte concentration ranges and allow for the incorporation of multiple sensing elements to benefit from multivalency. Utilizing a DNA origami nanostructure as a scaffold for arranging the different sensor components, we here propose an approach for the development of modular and tunable single-molecule sensors capable of detecting a variety of biomolecular targets such as nucleic acids, antibodies and restriction enzymes while offering mechanisms to tune the dynamic window, the specificity, and the cooperativity of the sensor.

Fluorescent sensors are our gateway to a deeper understanding of cellular processes [1–4] and diseases [5–7]. A typical biosensor consists of two functional units: a biorecognition element capable of sensing an analyte or biological activity and a signal transduction element translating it into measurable readout. For virtually every biomolecular target of interest to medical research or diagnostics, it is possible to find a molecule (e.g., antibody, receptor, or aptamer) that binds to it with high specificity and sensitivity. Given that the conformational change upon target binding is often very small, one of the key challenges in transforming these binders into useful fluorescence sensors lies in achieving a measurable fluorescence signal (e.g., change in fluorescence intensity or Fluorescence Resonance Energy Transfer (FRET) between donor and acceptor labels) upon binding. This challenge has been addressed by a number of elegant modular strategies which generalize and simplify the development of new biosensors, for example, by engineering superstructures that elicit large conformational changes upon target binding with the help of semi-synthetic protein chimeras [8–13], chemically induced dimerization [14, 15], de novo protein design [15, 16] or by using conditionally stable ligand-binding domains [17, 18].

A second fundamental challenge in developing new sensors lies in tailoring their response window to the analyte concentration of interest. Binding of a ligand to a single-site recognition element produces a hyperbolic dose-response curve with a fixed response window spanning roughly two orders of magnitude. This limits the utility of the sensor in applications that require either great sensitivity (sharp signal response) or quantification of target molecules in a concentration window that varies or spans several orders of magnitude [19]. Mimicking nature's tricks to overcome this challenge, mechanisms of allosteric control [20–23], sequestration [24], and cooperativity [25–29] have been implemented in synthetic sensor and signaling systems. While these approaches have demonstrated impressive tuning capabilities in aptamer-based sensors enabling measurement of target concentrations across orders of magnitude [22] or narrowing of the response window to as little as 3-fold, they lack the modularity required for straightforward extension to arbitrary analytes. Possible ways to shift the response window of the sensor (e.g., by introducing a mutation in the binding site [11, 14, 15, 17] or changes to the scaffolding structure [8, 9, 16]) have also been outlined in modular sensing platforms, yet, most of these approaches rely on single-site binding and cannot harness additional tuning and design advantages available to multivalent sensors (e.g., cooperativity or multiplexing).

Strategies to simultaneously decouple sensing from signal transduction, tune the response window of the sensor and combine multiple sensing elements are of great interest, as they would allow independent tuning of sensor

properties and thus greatly increase the speed at which new sensors can be developed. However, a global sensor approach that addresses all these challenges in one platform has yet to be realized. To lay out fundamental strategies that could combine all these requirements, in this work we harnessed the nanoscale arranging capabilities and modularity of DNA origami nanostructures. Using a dynamic nanostructure to assemble different sensor elements, we obtained almost digital FRET signal readout with single-molecule sensitivity, outlined strategies to tune the response and specificity of a sensor as well as developed multiplexed sensors capable of more complex sensing operations.

Engineering of a spatially decoupled signal transduction element

To decouple sensing from signal output and build a sensor platform with a high optical contrast, we utilized a dynamic DNA origami nanostructure [30–32] capable of undergoing large conformational changes. It consists of two ca. 65-nm long arms connected by a single-stranded (ss) scaffold DNA region (Fig. 1a). In absence of additional interactions, the two arms fluctuate around an equilibrium angle of ca. 90° (Fig. 1b, upper panel). However, by introducing DNA-DNA closing interactions on the two arms it can be folded and purified in a closed conformation, with both arms almost parallel to each other (Fig. 1b, lower panel). In the model nanosensor, closing interactions are designed with a ssDNA overhang allowing for toehold-mediated opening of the structure by complementary ssDNA opening strands. At the same time, a short toehold overhang is left upon binding the target, enabling reversible reclosing and mimicking receptor-ligand interactions (Figs. 1a, S1, S2, and S16).

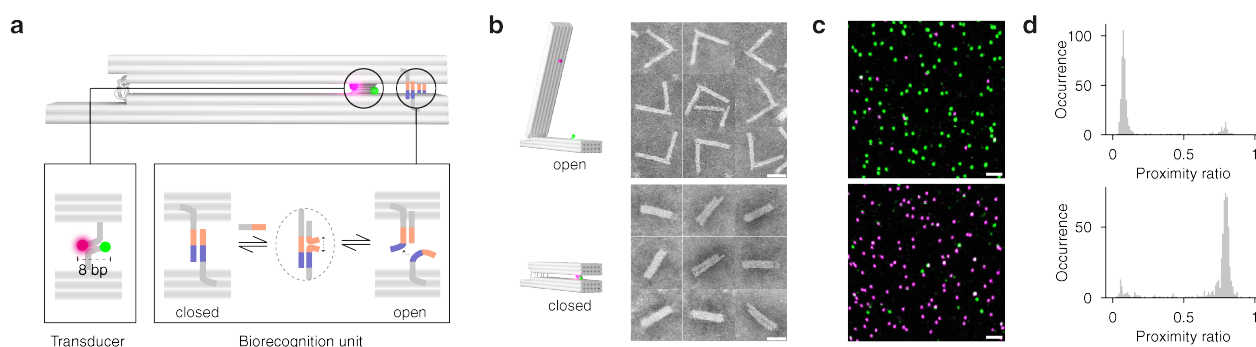


Figure 1: Design of the modular biosensor platform. (a) DNA origami nanostructure used to arrange and decouple sensing from signal output. The signal transduction element consists of a donor (ATTO542) and an acceptor (ATTO647N) dye forming a FRET pair (bottom left) brought together in the orientation required for high FRET in the closed state by weak 8 base pair (bp) DNA hybridization. In the model sensor platform, the biorecognition element is mimicked by a reversible closing interaction based on toehold-mediated DNA strand displacement reaction(s) (bottom right). (b) Snapshots from transmission electron micrographs of the sensors in each of the conformations (scale bar: 40 nm, for full micrographs see Fig. S3). (c) Confocal microscopy scans of surface immobilized biosensors in the open (top) and closed (bottom) conformation (scale bar: 2 μ m). (d) Corresponding spot wise PR histograms illustrating the high FRET contrast between closed and open states of the sensor.

The signal transduction element consists of bright and photostable donor (ATTO542) and acceptor (ATTO647N) fluorophores positioned on the opposing arms forming a FRET pair (Fig. 1a, lower left). We studied different sensor designs at the single-molecule level by incorporating biotinylated ssDNA strands to immobilize the structures on BSA-biotin/Neutravidin-coated coverslips and performing confocal scans. The extent of FRET in different sensor designs was characterized by calculating the proximity ratio (PR, defined as $I_{\text{Red}}/(I_{\text{Red}} + I_{\text{Green}})$) for each nanosensor. The signal output was optimized to minimize the effect of the flexibility of the nanostructure and the impact of changes in ionic strength on the PR distributions (Fig. S4, oxDNA [33] simulations in Videos S1-S2). To this end, two complementary ssDNAs protruding from each of the arms were used to define the positions of the two dyes in the closed state, leading to a narrow distribution of high FRET values ($\langle \text{PR}_{\text{closed}} \rangle$ ca. 0.77, Fig. 1c and 1d, top). The large conformational change upon opening the sensor with ssDNA target separates the dyes in the FRET pair resulting in negligible FRET in the open state ($\langle \text{PR}_{\text{open}} \rangle$ ca. 0.08, Fig. 1d, bottom). This high optical contrast allowed for the unambiguous assignment of the two conformational states and enabled the detailed characterization of the sensor response.

Tuning the response window of the biosensor

A universal sensor platform would allow to readily assemble new sensors from a large pool of already existing receptor-ligand interactions. This calls for strategies to tune both, onset, and sharpness, of the sensor response to enable monitoring relevant concentration changes of target molecules without the need to re-engineer these interactions. In natural receptor-ligand systems, this is commonly achieved by hierarchical assembly of multiple binding units or allosteric modulation of the binding interaction [34]. We laid out and tested several strategies inspired by these mechanisms to tune the signal response of the nanosensor without altering the sensing interaction itself. The high signal contrast between open and closed conformations enabled us to read out the equilibrium distributions with high precision and thus conduct single-molecule titration experiments with the ssDNA target as a model ligand (Fig. 2a). By quantifying the fraction of open sensors ($PR < 0.3$, Fig. 2b) at each target concentration and fitting the resulting binding curve with the Hill equation, we characterized the response window of each sensor design in terms of overall affinity $K_{1/2}$ which represents the target concentration where half of the sensors are open, and the Hill coefficient n_H , which is a measure of the cooperativity in a system (Fig. 2b).

Inspired by naturally occurring multivalent systems, we rationalized that increasing the number of sensing interactions would provide means to engineer cooperativity in our nanosensors. As expected, multivalency induced cooperative behavior to our system: going from two to four interactions, n_H increased from 0.98 ± 0.08 to 1.55 ± 0.15 , respectively, while in the sensor with six interactions, we achieved a cooperativity of 1.73 ± 0.13 . Additionally, going from two to four sensing elements led to an almost 10-fold increase in $K_{1/2}$ (from 100 ± 10 nM to 1.09 ± 0.09 μ M, respectively) and adding two more closing interactions further doubled $K_{1/2}$ to 2.03 ± 0.10 μ M (Fig. 2d). We propose that this cooperativity is a result of strain in the closed state of the sensor acting on all interactions induced by coulombic repulsion (i.e., opening of one interaction increases the force acting on the remaining ones). Altogether, increasing the number of sensing elements in these multivalent sensors provided a strategy to sharpen the signal response (narrowing the response window from ≈ 80 -fold to ≈ 12 -fold) due to arising cooperativity while simultaneously shifting $K_{1/2}$ to higher values (Fig. 2d, inset).

To introduce an orthogonal tuning strategy, we set out to alter the force that the backbone structure exerts on the closing interactions. We reasoned that this can be achieved by increasing coulombic repulsion in the closed state [31, 32] and, in turn, characterized the properties of the sensor containing two closing interactions at varying ionic strengths (Fig. 2e). As expected, decreasing the NaCl concentration from 400 mM NaCl to 50 mM led to an earlier response, shifting $K_{1/2}$ by 6-fold from 601 ± 20 nM to 100 ± 10 nM, which we attributed to destabilization of the closed state of the sensor. Interestingly, the cooperativity was also sensitive to the ionic strength: we obtained n_H values of 0.81 ± 0.02 , 0.87 ± 0.04 , 0.98 ± 0.08 in the presence of 400 mM, 200 mM, and 50 mM NaCl, respectively (Fig. 2d). This result is in line with our earlier assumption that cooperativity increases with coulombic repulsion. The negative cooperativity obtained at higher ionic strengths, however, highlights the existence of a competing cooperative process. Here, multiple closing interactions facilitate the reclosing, in turn, providing means to extend the response window of the nanosensors. Overall, the destabilization of the closed state provided a mechanism to increase the cooperativity and shift the response window to lower concentrations providing an orthogonal direction in the n_H vs. $K_{1/2}$ space (insets in Fig. 2d and 2e).

Finally, by including additional ssDNA strands that hybridize to each other in the closed conformation we investigated the possibility to implement allosteric control. Introduction of two transient DNA-DNA interactions on the inside of the two arms of the structure led to a 7-fold increase of $K_{1/2}$ from 100 ± 10 nM to 705 ± 65 nM (Fig. 2f) illustrating the sensitivity of this platform to small alterations. Varying the strength of these stabilizing interactions provides a mechanism to fine-tune the overall affinity of the nanosensor. Analogous to what was observed at increasing ionic strengths (Fig. 2e), the stabilization of the closed state via this strategy has led to a decrease in n_H from 0.98 ± 0.08 to 0.8 ± 0.05 consistent with facilitated reclosing. Altogether, the three illustrated approaches present strategies to tune the onset ($K_{1/2}$) and sharpness (n_H) of the sensor without altering the sensing interaction itself with strategies that are orthogonal to each other (insets in Figs. 2d-f) and can be combined to cover an extended $K_{1/2}$ and n_H parameter space, something that so far has been challenging to implement in synthetic sensor systems [27, 28].

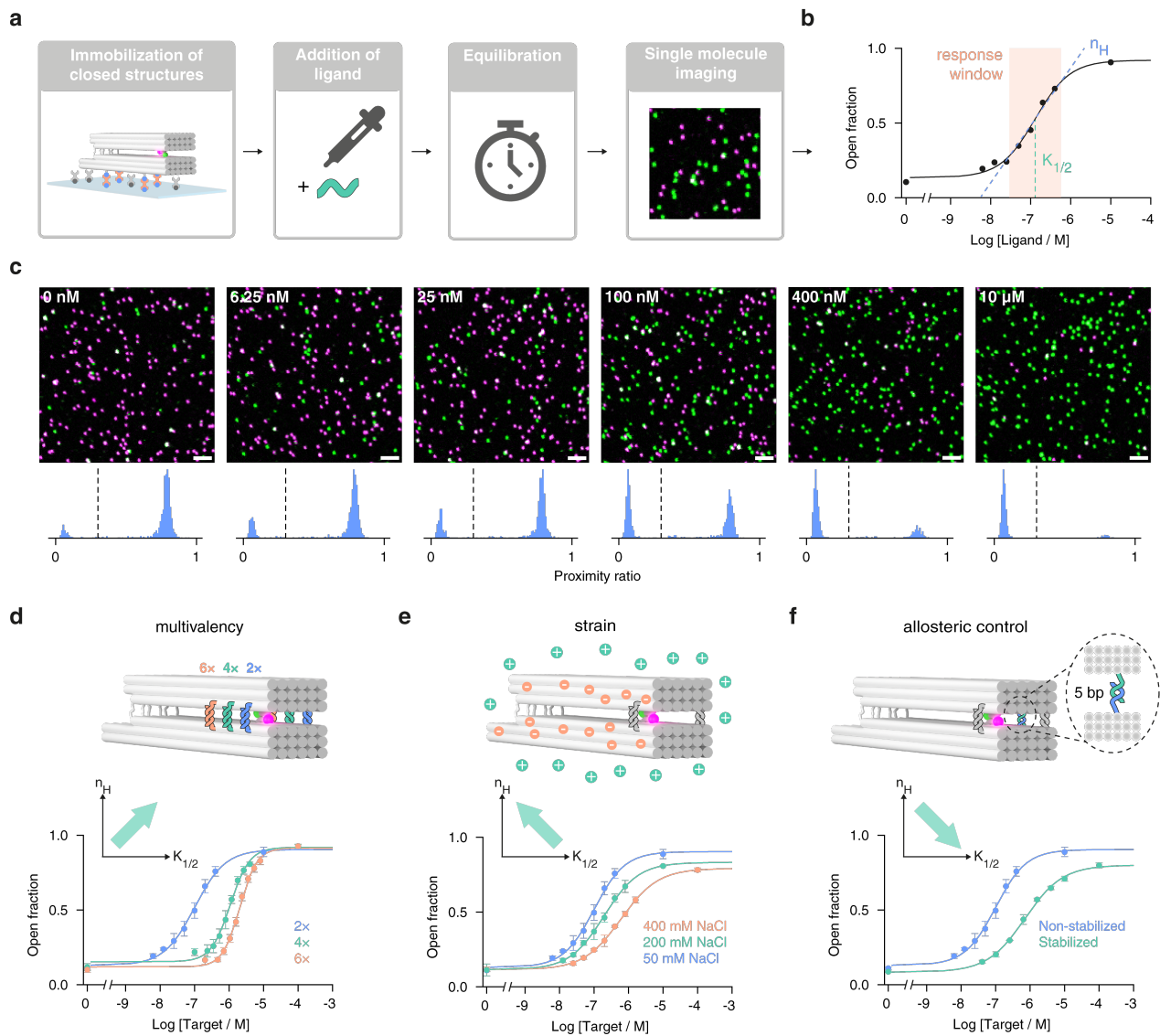


Figure 2: Studying and tuning the response window of the sensors on the single molecule level. (a) Workflow to investigate the response window of different sensor designs: sensors are immobilized via Biotin-NeutrAvidin interactions. For each target concentration, one surface is prepared, and a defined concentration of target is added. After equilibration, confocal scans are acquired, and the fraction of closed structures is determined by analyzing on average 681 single nanosensors for each concentration. (b) The response window, i.e., the overall affinity of the sensor ($K_{1/2}$) and the extent of cooperativity (n_H) are determined by fitting the titration curve with the Hill equation. (c) Example confocal fluorescence scans for different target concentrations with respective PR histograms shown below (scale bar: 2 μ m, dashed line represents the PR threshold used to assign sensors as open). (d) Increasing the number of sensing elements shifts the $K_{1/2}$ of the sensor to higher values and increases the cooperativity. (e) Decreasing the ionic strength increases the coulombic repulsion and destabilizes the closed state of the sensor, leading to lower $K_{1/2}$ and higher n_H . (f) Introducing additional DNA-DNA stabilization interactions stabilizes the closed state of the sensor and leads to an increase of $K_{1/2}$ and a decrease of n_H . Titration curves show mean values of three independent measurements with the error bars corresponding to the standard deviation.

Harnessing multivalency for increased target specificity

One of the key properties sought after in biosensors is the ability to detect target analytes specifically in a large pool of other similar biomolecules. As such, we investigated whether multivalency could be utilized to improve the specificity of the nanosensor. We rationalized that increasing the number of sensing elements would amplify the overall binding energy difference of two energetically similar targets. To confirm this, we first studied the opening of a nanosensor containing four sensing interactions in the presence of 17-nt perfectly matching target as well as targets containing one (C-C mismatch, $\Delta\Delta G$ from the perfectly matched target of 5.4 kcal/mol as estimated by NUPACK [35], Fig. S5) and two (C-C + T-T mismatch, $\Delta\Delta G$ 6.2 kcal/mol) nucleotide mismatches (Fig. 3a). For the perfectly matched target the nanosensor opened at nanomolar concentrations, whereas in the presence of targets containing one or two nucleotide mismatches no opening was observed even at 10 μM (Fig. 3b) illustrating the ability of the nanosensor to specifically detect perfectly matched targets even in ≈ 1000 -fold excess of similar off-targets.

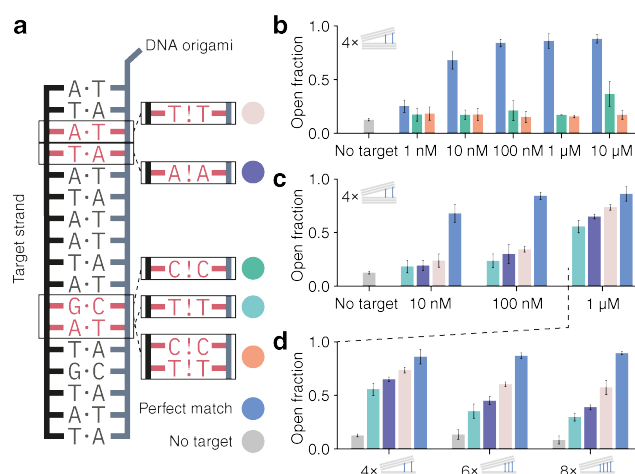


Figure 3: Harnessing sensor multivalency for increased target specificity. (a) Schematic of the model receptor-ligand opening interaction (left). For testing specificity of different sensor designs, we included mismatches into the opening interaction (right), mimicking a ligand (off-target) with similar binding strength. (b) Comparing the perfectly matched opening interaction (blue) to an interaction with one (green) and two (orange) single nucleotide mismatches shows drastic differences in sensor response: while perfectly matched target (blue) opens the sensor at nanomolar concentrations, both mismatched targets exhibit almost no response up to 10 μM concentration. (c) Testing targets with even smaller free energy differences from the perfect match. (d) Increasing the number of closing interactions from 4 to 8 increases the capabilities of the sensor to differentiate these targets from the perfect match as illustrated with the sensor opening measured in the presence of 1 μM target concentrations. Plots show the mean values of three independent measurements with the error bars corresponding to the standard deviation. Examples for all confocal fluorescence scans are found in Fig. S6.

Exploring this potential further, we investigated whether we could differentiate off-targets with even smaller $\Delta\Delta G$ s (2.3 — 3.6 kcal/mol, A-A and T-T mismatches, Fig. 3c and Fig. S5). By incubating the nanosensor containing four sensing interactions with different targets, we could show that at up to 100 nM target concentration it is possible to clearly differentiate the energetically similar off-targets by both comparing the equilibrium fraction of open nanosensors or by monitoring the nanosensor opening kinetics (Fig. S7). Nonetheless, as the concentration of the target strands is further increased to 1 μM (Fig. 3c) this differentiation becomes more difficult. While the specificity of the nanosensor at micromolar concentrations of targets may be less relevant for detection of nucleic acids, we deemed that it is still crucial for the utility of the modular sensing platform, where the desired response of the sensor lies at higher concentrations (e.g., sensing of metabolites). We conducted additional studies with nanosensors containing 6 and 8 closing interactions to demonstrate that multivalency can further improve the specificity when desired. As shown in Fig. 3d, increasing the number of sensing interactions increased the differences in opening fraction when compared to the perfect match. With the nanosensor containing 8 closing interactions, we were able to differentiate between two off-targets with single T-T and A-A mismatches that have an estimated difference in binding energy as little as 0.51 kcal/mol (less than 1 $k_B T$, Fig. S5).

Extension to other biomolecular targets and incorporation of logic sensing operations

We next demonstrated that the large optical signal contrast developed in our model nanosensor can indeed be swiftly and modularly adapted to other biomolecular targets without the need to tediously re-optimize the signal output. A single molecule sensor for anti-Digoxigenin (anti-Dig) antibodies was engineered by incorporating two specific Dig antigen biorecognition elements on each sensor arm (Fig. 4a). To meet the required geometry for bivalent binding³⁶ the nanosensor was initially kept in the closed state via DNA-DNA interactions. After surface immobilization and antibody incubation, DNA opening staples were added which resulted in $\approx 85\%$ sensors still in the closed state (Fig. 4a, upper panel and Fig. 4b) suggesting that the sensor is held in the closed state by the bivalent binding of the antibody. However, in the absence of the antibody, the nanosensors opened almost quantitatively (Fig. 4a, lower panel and Fig. 4b). As illustrated in Fig. 4a and 4b, the near digital signal contrast optimized for the model sensor is still preserved in the antibody nanosensor. Additionally, we evaluated the specificity (Figs. S8 and S9) as well as the potential of this antibody sensor to be useful in more complex biological fluids by performing the antibody assay described above in 50% blood plasma (Fig. 4c and Fig. S10). The obtained percentages of open sensors measured in blood plasma were within experimental error when compared to those measured in buffer, confirming that neither stability of the DNA origami nanosensor nor the performance of the antibody binding assay were compromised. We also evaluated the sensitive concentration range of the anti-Dig antibody assay under clinically relevant conditions (20 min incubation) to show that the antibody concentration at which the signal change is half the maximum ($C_{\text{half-max}}$) lies at 104 pM, which is in accordance to previously reported values [37] and in a concentration range relevant for diagnostic applications [38] (Fig. S11).

Next, we studied whether the sensor platform can also be utilized for the detection of enzymatic activities. Usually, optical enzyme (e.g., protease or nuclease) activity sensors are designed by placing two labels close to the substrate binding site in a manner that leads to loss of FRET or turn-on of fluorescence signal upon substrate cleavage. In designing such sensors, one is faced with the inherent conflict between placing the labels close enough to the cleavage site to achieve high optical contrast yet far enough not to influence the enzyme-substrate binding which results in many rounds of optimization and often suboptimal signal contrast. This challenge can be globally addressed by the sensor scheme proposed here where target recognition is decoupled and spatially separated from the transduction element. To illustrate this, we designed a single molecule activity sensor for the nuclease XhoI: without the need to re-engineer the transduction element, we simply incorporated the restriction sites for XhoI in the DNA-DNA closing interactions (Fig. 4d). In the presence of XhoI, the closing interactions are cleaved leading to opening of the DNA origami sensor and loss of FRET (Figs. 4e and S12). In contrast, no opening is observed if the nanosensors are closed with DNA-DNA interactions without XhoI cleavage sites, confirming the desired specificity (Figs. 4e, 4f, and S13).

Finally, to illustrate the ability of the proposed nanosensor to modularly exchange and combine different sensing elements on one platform, we designed a sensor capable of detecting two different (anti-Dig and anti-DNP) antibodies (Fig. 4g) acting as a molecular OR gate. Two different antigens (Dig and DNP) were incorporated on the opposing arms of the nanosensor closed via DNA-DNA interactions. Upon addition of DNA opening strands the nanosensor opens when neither of the antibodies are present and stays closed if either or both antibodies are present (Fig. 4i). Fig. 4h and Fig. S14 illustrate that the high FRET contrast is still preserved despite a more complex sensing scheme. In fact, as illustrated in Fig. 4j, the multiplexed sensing is not restricted to the same type of biorecognition elements: by incorporating the XhoI restriction site and another DNA-DNA closing interaction we could build a logic AND gate for two different biomolecular targets: one based on a binding event, and one based on a cleavage reaction. Here we could show that the sensor only opens when both, XhoI and DNA targets, are present (Figs. 4k, l, and Fig. S15). Altogether, the modularity the DNA origami offers to incorporate different biorecognition elements, combined with the preserved robust FRET readout opens many possibilities to engineer new multiplexed sensors as well as logical sensing schemes for answering more complex diagnostic questions.

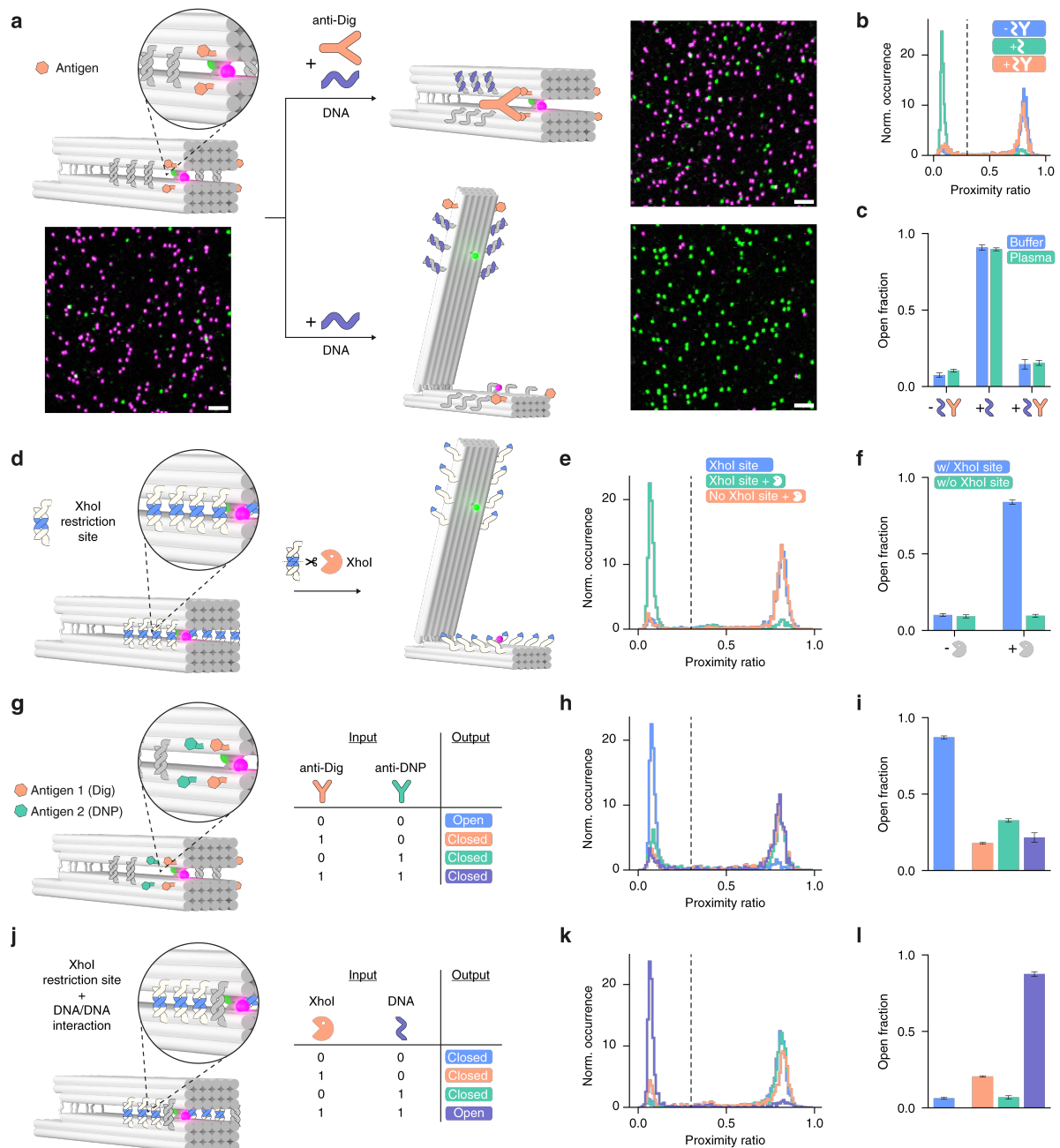


Figure 4: Extension of the sensor platform to different molecular targets and introduction of logic sensing operations. (a) Detection of antibodies by incorporation of antigen recognition elements (Dig) on the opposing arms of nanosensor kept in the closed state via DNA-DNA interactions. Upon addition of DNA opening strands the nanosensor stays closed in the presence and opens in the absence of anti-Dig antibodies. The high signal contrast is illustrated by confocal microscopy scans (scale bar: 2 μm). (b) Spot-wise PR histograms obtained for the antibody sensor in the absence (blue) and in the presence of DNA opening strands (cyan) as well as in the presence of DNA opening strands and 100 nM anti-Dig antibody (orange). (c) Corresponding fraction of open antibody nanosensors obtained in buffer as well as in blood plasma. (d) Detection of enzymatic activity by incorporation of nuclease-specific restriction site in the DNA-DNA closing interaction. (e) Spot wise PR histograms obtained for nanosensors containing the XhoI restriction site in the absence (green) and presence (blue) of XhoI. No opening was observed for nanosensors without the specific restriction site in the presence of XhoI (orange). (f) Corresponding fraction of open nuclease nanosensors with and without restriction site. (g) Multiplexed detection of two different antibodies (anti-Dig and anti-DNP) via a molecular OR gate is achieved via the incorporation of two different antigens (Dig and DNP) on the opposing arms of the closed nanosensor. Upon addition of DNA opening strands the nanosensor stays closed if either or both antibodies are present. (h) Spot wise PR histograms for antibody nanosensor inputs shown in (g). (i) Corresponding fraction of open nanosensors for different antibody nanosensor inputs. (j) Multiplexed detection of two different biomolecular targets (nucleic acid and restriction enzyme) via a logic AND gate can be achieved by incorporation of the restriction site and another DNA-DNA closing interaction. The nanosensor opens only in the presence of both, nucleic acid, and restriction enzyme targets. (k) Corresponding spot wise PR histograms obtained for different molecular inputs of shown in (j). (l) Corresponding fraction of open nanosensors for different nanosensor inputs. Bar plots show the mean values of three independent measurements (each include at least 423 single nanosensors) with the error bars corresponding to the standard deviation.

Conclusions

General and modular strategies to assemble sensors have the potential to vastly speed up the development of new diagnostic tools for health and disease research. Here, we developed a generalizable approach to create DNA origami-based synthetic sensing systems with high signal contrast and single-molecule sensitivity. We harnessed the modularity of DNA origami nanostructures to: 1) modularly assemble all the elements of the sensor, 2) spatially decouple sensing from signal output, 3) provide a large conformational change required for large FRET contrast, 4) implement strategies to tune the response window, 5) engineer multivalent sensors which enabled improved specificity, multiplexing, logic sensing, and additional tuning capabilities via cooperativity.

Optical single molecule sensors allow to detect and monitor target analytes with ultimate sensitivity and unprecedented spatial resolution. However, achieving a large FRET contrast in single-molecule DNA origami sensors so far has been challenging: low FRET contrast and broad FRET distributions often require averaging over hundreds of nanostructures to distinguish the two states of the sensor [39–42]. Here we combined two tricks to solve this: a large conformational change and an additional transient guiding interaction to control the orientation of the dyes in the FRET pair – which led to a high FRET contrast and allowed the clear differentiation of the two sensor states on the single molecule level. The modularity and the ability to immobilize the sensors on the surface in a specific orientation [43] make this approach readily extendable to other readout mechanisms, such as electrochemical readout [44], fluorescence quenching (e.g., by a graphene surface [45, 46]), or bioluminescence energy transfer [9, 11, 17] as well as pave the way towards highly multiplexed sensor chips.

An exciting avenue to explore going forward would be the utilization of de novo designed binders [15, 16] as sensing elements, combining the many possibilities provided by protein design with a high-contrast single molecule readout and multivalent sensing schemes. One of the challenges that would have to be addressed, however, is the stability of DNA origami-based sensors. Here we showed that the sensor is still functional in 50% blood plasma, but further studies will be needed to fully assess the stability of the sensors in complex chemical environments or live cells. Recent progress on stabilization strategies for DNA origami structures [47–49] offers many options that can be tested to achieve maximal performance. Altogether, the modularity, tunability, and sensitivity of the reported approach provide a starting point for the rapid development of tailored and complex sensors for a wide range of analytes.

References

1. Abdelfattah, A. S. *et al.* Bright and photostable chemigenetic indicators for extended in vivo voltage imaging. *Science* **365**, 699–704. doi:10.1126/science.aav6416 (2019).
2. Chen, Y.-N., Cartwright, H. N. & Ho, C.-H. In vivo visualization of nitrate dynamics using a genetically encoded fluorescent biosensor. *Sci. Adv.* **8**, eabq4915. doi:10.1126/sciadv.abq4915 (2022).
3. Cambronne, X. A. *et al.* Biosensor reveals multiple sources for mitochondrial NAD(+). *Science* **352**, 1474–7. doi:10.1126/science.aad5168 (2016).
4. Xue, L. *et al.* Probing coenzyme A homeostasis with semisynthetic biosensors. *Nat. Chem. Biol.* **19**, 346–355. doi:10.1038/s41589-022-01172-7 (2023).
5. Olsen, R. H. J. *et al.* TRUPATH, an open-source biosensor platform for interrogating the GPCR transducerome. *Nat. Chem. Biol.* **16**, 841–849. doi:10.1038/s41589-020-0535-8 (2020).
6. Marvin, J. S. *et al.* A genetically encoded fluorescent sensor for in vivo imaging of GABA. *Nat. Methods* **16**, 763–770. doi:10.1038/s41592-019-0471-2 (2019).
7. Ino, D., Tanaka, Y., Hibino, H. & Nishiyama, M. A fluorescent sensor for real-time measurement of extracellular oxytocin dynamics in the brain. *Nat. Methods* **19**, 1286–1294. doi:10.1038/s41592-022-01597-x (2022).
8. Brun, M. A., Tan, K.-T., Nakata, E., Hinner, M. J. & Johnsson, K. Semisynthetic Fluorescent Sensor Proteins Based on Self-Labeling Protein Tags. *J. Am. Chem. Soc.* **131**, 5873–5884. doi:10.1021/ja900149e (2009).
9. Griss, R. *et al.* Bioluminescent sensor proteins for point-of-care therapeutic drug monitoring. *Nat. Chem. Biol.* **10**, 598–603. doi:10.1038/nchembio.1554 (2014).
10. Xue, L., Prifti, E. & Johnsson, K. A General Strategy for the Semisynthesis of Ratiometric Fluorescent Sensor Proteins with Increased Dynamic Range. *J. Am. Chem. Soc.* **138**, 5258–5261. doi:10.1021/jacs.6b03034 (2016).
11. Yu, Q. *et al.* Semisynthetic sensor proteins enable metabolic assays at the point of care. *Science* **361**, 1122–1126. doi:10.1126/science.aat7992 (2018).

12. Vecchia, M. D. *et al.* Spectrally Tunable Forster Resonance Energy Transfer-Based Biosensors Using Organic Dye Grafting. *ACS Sens.* **7**, 2920–2927. doi:10.1021/acssensors.2c00066 (2022).
13. Hellweg, L. *et al.* A general method for the development of multicolor biosensors with large dynamic ranges. *Nat. Chem. Biol.* **19**, 1147–1157. doi:10.1038/s41589-023-01350-1 (2023).
14. Beltran, J. *et al.* Rapid biosensor development using plant hormone receptors as reprogrammable scaffolds. *Nat. Biotechnol.* **40**, 1855–1861. doi:10.1038/s41587-022-01364-5 (2022).
15. Glasgow, A. A. *et al.* Computational design of a modular protein sense-response system. *Science* **366**, 1024–1028. doi:10.1126/science.aax8780 (2019).
16. Quijano-Rubio, A. *et al.* De novo design of modular and tunable protein biosensors. *Nature* **591**, 482–487. doi:10.1038/s41586-021-03258-z (2021).
17. Feng, J. *et al.* A general strategy to construct small molecule biosensors in eukaryotes. *eLife* **4**, e10606. doi:10.7554/eLife.10606 (2015).
18. Tucker, C. L. & Fields, S. A yeast sensor of ligand binding. *Nat. Biotechnol.* **19**, 1042–1046. doi:10.1038/nbt1101-1042 (2001).
19. Ricci, F., Vallée-Bélisle, A., Simon, A. J., Porchetta, A. & Plaxco, K. W. Using Nature’s ”Tricks” To Rationally Tune the Binding Properties of Biomolecular Receptors. *Acc. Chem. Res.* **49**, 1884–1892. doi:10.1021/acs.accounts.6b00276 (2016).
20. Choi, B. *et al.* Artificial allosteric control of maltose binding protein. *Phys. Rev. Lett.* **94**, 038103. doi:10.1103/PhysRevLett.94.038103 (2005).
21. Vallée-Bélisle, A., Ricci, F. & Plaxco, K. W. Engineering Biosensors with Extended, Narrowed, or Arbitrarily Edited Dynamic Range. *J. Am. Chem. Soc.* **134**, 2876–2879. doi:10.1021/ja209850j (2012).
22. Porchetta, A., Vallée-Bélisle, A., Plaxco, K. W. & Ricci, F. Using distal-site mutations and allosteric inhibition to tune, extend, and narrow the useful dynamic range of aptamer-based sensors. *J. Am. Chem. Soc.* **134**, 20601–4. doi:10.1021/ja310585e (2012).
23. Hariri, A. A. *et al.* Continuous optical detection of small-molecule analytes in complex biomatrices. *bioRxiv*. doi:10.1101/2023.03.03.531030 (2023).
24. Chamorro-Garcia, A. *et al.* The sequestration mechanism as a generalizable approach to improve the sensitivity of biosensors and bioassays. *Chem. Sci.* **13**, 12219–12228. doi:10.1039/D2SC03901J (2022).
25. Dueber, J. E., Mirsky, E. A. & Lim, W. A. Engineering synthetic signaling proteins with ultrasensitive input/output control. *Nat. Biotechnol.* **25**, 660–2. doi:10.1038/nbt1308 (2007).
26. Simon, A. J., Vallée-Bélisle, A., Ricci, F. & Plaxco, K. W. Intrinsic disorder as a generalizable strategy for the rational design of highly responsive, allosterically cooperative receptors. *Proc. Natl. Acad. Sci. U.S.A.* **111**, 15048–53. doi:10.1073/pnas.1410796111 (2014).
27. Ortega, G. *et al.* Rational design to control the trade-off between receptor affinity and cooperativity. *Proc. Natl. Acad. Sci. U.S.A.* **117**, 19136–19140. doi:10.1073/pnas.2006254117 (2020).
28. Ortega, G., Chamorro-Garcia, A., Ricci, F. & Plaxco, K. W. On the Rational Design of Cooperative Receptors. *Annu. Rev. Biophys.* **52**, 319–337. doi:10.1146/annurev-biophys-091222-082247 (2023).
29. Simon, A. J., Vallée-Bélisle, A., Ricci, F., Watkins, H. M. & Plaxco, K. W. Using the Population-Shift Mechanism to Rationally Introduce “Hill-type” Cooperativity into a Normally Non-Cooperative Receptor. *Angew. Chem. Int. Ed.* **53**, 9471–9475. doi:10.1002/anie.201403777 (2014).
30. Marras, A. E., Zhou, L., Su, H. J. & Castro, C. E. Programmable motion of DNA origami mechanisms. *Proc. Natl. Acad. Sci. U.S.A.* **112**, 713–8. doi:10.1073/pnas.1408869112 (2015).
31. Marras, A. E. *et al.* Cation-Activated Avidity for Rapid Reconfiguration of DNA Nanodevices. *ACS Nano* **12**, 9484–9494. doi:10.1021/acsnano.8b04817 (2018).
32. Shi, Z. & Arya, G. Free energy landscape of salt-actuated reconfigurable DNA nanodevices. *Nucleic Acids Res.* **48**, 548–560. doi:10.1093/nar/gkz1137 (2020).
33. Sulc, P. *et al.* Sequence-dependent thermodynamics of a coarse-grained DNA model. *J. Chem. Phys.* **137**, 135101. doi:10.1063/1.4754132 (2012).
34. Smock, R. G. & Gierasch, L. M. Sending signals dynamically. *Science* **324**, 198–203. doi:10.1126/science.1169377 (2009).
35. Zadeh, J. N. *et al.* NUPACK: Analysis and design of nucleic acid systems. *J. Comput. Chem.* **32**, 170–3. doi:10.1002/jcc.21596 (2011).

36. Shaw, A. *et al.* Binding to nanopatterned antigens is dominated by the spatial tolerance of antibodies. *Nat. Nanotechnol.* **14**, 184–190. doi:10.1038/s41565-018-0336-3 (2019).
37. Pfeiffer, M. *et al.* Single antibody detection in a DNA origami nanoantenna. *iScience* **24**, 103072. doi:10.1016/j.isci.2021.103072 (2021).
38. Iyer, A. S. *et al.* Persistence and decay of human antibody responses to the receptor binding domain of SARS-CoV-2 spike protein in COVID-19 patients. *Sci. Immunol.* **5**, eabe0367. doi:10.1126/sciimmunol.abe0367 (2020).
39. Selnihhin, D., Sparvath, S. M., Preus, S., Birkedal, V. & Andersen, E. S. Multifluorophore DNA Origami Beacon as a Biosensing Platform. *ACS Nano* **12**, 5699–5708. doi:10.1021/acsnano.8b01510 (2018).
40. Ochmann, S. E. *et al.* DNA Origami Voltage Sensors for Transmembrane Potentials with Single-Molecule Sensitivity. *Nano Lett.* **21**, 8634–8641. doi:10.1021/acs.nanolett.1c02584 (2021).
41. Büber, E. *et al.* DNA Origami Curvature Sensors for Nanoparticle and Vesicle Size Determination with Single-Molecule FRET Readout. *ACS Nano* **17**, 3088–3097. doi:10.1021/acsnano.2c11981 (2023).
42. Domljanovic, I. *et al.* DNA origami book biosensor for multiplex detection of cancer-associated nucleic acids. *Nanoscale* **14**, 15432–15441. doi:10.1039/d2nr03985k (2022).
43. Gopinath, A. *et al.* Absolute and arbitrary orientation of single-molecule shapes. *Science* **371**, eabd6179. doi:10.1126/science.abd6179 (2021).
44. Williamson, P., Ijas, H., Shen, B., Corrigan, D. K. & Linko, V. Probing the Conformational States of a pH-Sensitive DNA Origami Zipper via Label-Free Electrochemical Methods. *Langmuir* **37**, 7801–7809. doi:10.1021/acs.langmuir.1c01110 (2021).
45. Ghosh, A. *et al.* Graphene-based metal-induced energy transfer for sub-nanometre optical localization. *Nat. Photonics* **13**, 860–865. doi:10.1038/s41566-019-0510-7 (2019).
46. Kaminska, I. *et al.* Graphene Energy Transfer for Single-Molecule Biophysics, Biosensing, and Super-Resolution Microscopy. *Adv. Mater.* **33**, e2101099. doi:10.1002/adma.202101099 (2021).
47. Chandrasekaran, A. R. Nuclease resistance of DNA nanostructures. *Nat. Rev. Chem.* **5**, 225–239. doi:10.1038/s41570-021-00251-y (2021).
48. Scheckenbach, M., Schubert, T., Forthmann, C., Glembockyte, V. & Tinnefeld, P. Self-Regeneration and Self-Healing in DNA Origami Nanostructures. *Angew. Chem. Int. Ed.* **60**, 4931–4938. doi:10.1002/anie.202012986 (2021).
49. Wassermann, L. M., Scheckenbach, M., Baptist, A. V., Glembockyte, V. & Heuer-Jungemann, A. Full Site-Specific Addressability in DNA Origami-Templated Silica Nanostructures. *Adv. Mater.* **35**, e2212024. doi:10.1002/adma.202212024 (2023).

Acknowledgements

We thank Prof. T. Liedl and Prof. J. Rädler for providing access to transmission electron microscopy facilities and the members of the Tinnefeld lab for discussion and feedback, especially Dr. F. Steiner. We also thank Michael Scheckenbach for initial AFM measurements.

Funding

This work was supported by the European Union's Horizon 2020 research and innovation program under the Marie Skłodowska-Curie actions (grant agreement no. 840741, GLUCORIGAMI), the German Research Foundation (DFG, grant number GL 1079/1-1, project number 503042693 to V.G. as well as project number 201269156, SFB 1032 Project A13 and INST 86/1904-1 FUGG to P.T.) as well as the Bavarian Ministry of Science and the Arts through the ONE MUNICH Project "Munich Multiscale Biofabrication". V.G. is also grateful for the support by a Humboldt Research Fellowship from the Alexander von Humboldt Foundation. M.P. acknowledges support by Studienstiftung des deutschen Volkes.

Author contributions

V.G. and P.T. conceived the idea and directed the project. V.G., P.T., L.G. and M.P. further conceptualized the research. L.G. designed the DNA origami sensor and performed oxDNA simulations. L.G., V.G., M.K., and J.M. tested and optimized the design of the sensor and the signal transduction element. F.S. and G.A.B. performed TEM measurements. L.G. and V.G. implemented the sensor tuning strategies and carried out and analyzed single molecule titration experiments with the help of G.A.B. and A.T.M.; T.S. and V.G. designed and carried out the

sensor specificity studies. M.P. carried out and analyzed antibody, nuclease detection, multiplexed detection assays. L.G. wrote the code for single-molecule data analysis. L.G. and V.G. prepared figures. V.G., L.G. and P.T. wrote the manuscript with additional input from M.P.; all authors reviewed and accepted the manuscript.

Competing interests

The authors declare no competing interests.

Data and materials availability

All experimental data supporting the findings of this work as well as DNA origami cadnano files will be made available from a public repository. The custom code for the analysis of single molecule confocal scans is available online (<https://gitlab.lrz.de/tinnefeldlab/cospota>).

Methods

DNA origami design and synthesis

DNA origami nanostructures were designed in caDNAno [1] according to a design published by Marras et al. [2]. All staple strands were ordered at Integrated DNA Technologies, Inc., Belgium except for the fluorescently labeled strands, which were ordered at biomers.net GmbH, Germany. For detailed folding recipes and sequences, see Supplementary Text and Tables S1-S8. The folding was executed in a thermocycler using the temperature ramp as described earlier [3]. After folding, samples were subjected to agarose gel electrophoresis; we employed 1.5% w/v gels in 1×TAE buffer supplemented with 10 mM MgCl₂. Gels were run for at least 3 hours at 70 V. Then, gels were inspected using a gel documentation system (Fusion FX, Vilber Deutschland GmbH, Germany) where we used the red fluorescence channel to identify the bands containing closed DNA origami sensors (an example scan is shown in Fig. S16). These bands were cut using a scalpel and placed on Parafilm. Then, the gel fragments were squeezed with a small glass slide wrapped in Parafilm to extract the DNA origami nanostructures. For storage, we aliquoted the origami solution to 200 μL PCR tubes: we mixed 40 μL of origami solution with 8 μL of 5 M NaCl solution to minimize degradation. Two slightly different versions of the nanosensors were used for different applications - for details on the differences, see Tables S1-S7 and supporting text.

Coarse-grained simulations of DNA origami nanostructures

caDNAno design files were converted to oxDNA [4–6] input files using the tacoxDNA web server [7], the closing interactions were manually added in oxView [8] and the resulting structure was simulated at 20 °C, 400 mM NaCl on the oxDNA.org server [9] with the standard settings as well as the recommended relaxation procedure.

Transmission electron microscopy (TEM) measurements

TEM grids (Formvar/carbon, 400 mesh, Cu, TedPella, Inc., USA) were Ar-plasma cleaned and incubated for 2 min with DNA origami sample (5 μL, 1–5 nM). Grids were washed with 2% uranyl formate solution (5 μL) and incubated for another 4 s with 2% uranyl formate solution (5 μL) for staining. TEM imaging was performed on a JEM-1100 microscope (JEOL GmbH, Japan) with an acceleration voltage of 80 kV.

Preparation of microscopy samples

Microscope slides (24 mm × 60 mm size and 170 μm thickness (Carl Roth GmbH, Germany)) were cleaned in a UV/ozone cleaner (PSD-UV4, Novascan Technologies, USA) for 30 mins at 100 °C. Then, CoverWell perfusion chambers (Grace Bio-Labs, 0.5 mm deep) were glued on top of the slides and the glue was strengthened by heating on a hot plate for ca. 20 s at 100 °C. Then, the chambers were cleaned with 1 M KOH by incubating for 10 mins and then washing with 1× PBS four times. Surfaces were passivated by incubating with BSA-Biotin (1 mg/mL in 1× TE with 50 mM NaCl, Thermo Fisher Scientific, USA) and subsequent washing with 1× PBS buffer three times. Then, chambers were incubated with 0.25 mg/mL NeutrAvidin (Thermo Fisher Scientific, USA) in 1× PBS for 10 mins followed by final washing with 1× PBS three times. DNA origami solutions were diluted in immobilization buffer (10 mM TRIS, 10 mM MgCl₂, 750 mM NaCl) as required to reach the desired surface

density of DNA origami sensors (50–100 pM), which was checked on the confocal microscope. When the desired density was reached, the surfaces were washed in the respective buffer that was used for the experiment.

Single-molecule confocal microscopy measurements

Home-built confocal microscope based on an Olympus IX-83 body (Japan) was used to acquire single molecule fluorescence scans. A supercontinuum white light laser pulsed at 78 MHz (SuperK Extreme, NKT Photonics, Denmark) was used to excite the samples. The excitation wavelength was selected using an acousto-optically tunable filter (SuperK Dual AOTF, NKT Photonics, Denmark) controlled by a digital controller (AODS 20160 8R, Crystal Technology, USA). If needed, a second acousto-optically tunable filter (AA.AOTF.ns:TN, AA Opto-Electronic, France) controlled with a home-written LabVIEW (National Instruments, USA) program was used to alternate between two wavelengths (532- and 639-nm). We used a neutral density filter, a linear polarizer and a $\lambda/4$ plate to achieve circularly polarized excitation light of the desired intensity. For the single-molecule confocal scans 532-nm (2 μ W) excitation was used. The excitation light was sent to the sample through an oil immersion objective (UPlanSApo 100 \times , NA=1.4, WD=0.12 mm, Olympus, Japan) via a dichroic beam splitter (zt532/640rpc, Chroma, USA). A piezo stage (P-517.3CL, E-501.00, Physik Instrumente GmbH&Co. KG, Germany) was used to move the sample in X-Y. The sample was kept in focus over extended periods with the help of a z-drift compensation system (IX3-zdc2-83, Olympus, Japan). The emitted light was collected with the same objective and separated from the excitation light with the same dichroic beam splitter. Then, the emission light was sent through a 50- μ m pinhole, the two emission channels were split using beam splitter (640DCXR, AHF Analysetechnik AG, Germany), additionally filtered with two emission filters (RazorEdge 647, Semrock Inc., USA for the red channel and BrightLine HC 582/75, Semrock Inc., USA for the green channel) and focused onto the single photon detectors (SPCM, AQR 14, PerkinElmer, USA). A custom LabVIEW program was used for data acquisition.

Single-molecule wide-field microscopy measurements

For detection of single-molecule fluorescence transients, a commercial wide-field/TIRF microscope Nanoimager from Oxford Nanoimaging Ltd. was used. Red excitation at 638 nm was realized with a 1100 mW laser, green excitation at 532 nm with a 1000 mW laser, respectively. The relative laser intensities were set to ca. 3.5 mW for green and to ca. 1 mW for red excitation. The microscope was set to TIRF illumination. Data acquisition was initialized by time-lapsed imaging. A frame of 100 ms was recorded every second separately for both excitation lasers. Measurements were carried out at 37 °C.

Single-molecule titrations

For each DNA target concentration a separate chamber with closed nanosensors (Version 2) was prepared. Single-molecule titrations were conducted in the buffer containing 10 mM Tris and 10 mM MgCl₂ with varying amounts of NaCl (see Table S9 for details). Serial dilutions of the 15 bp opening strand (see Table S8) were prepared in the same buffer and each chamber was filled with the opening staple solution and closed using adhesive seal tabs (Grace Bio-Labs, USA). The samples were incubated overnight at room temperature to ensure that the thermal equilibrium has been reached even for very low (nM) target concentrations. The opening of the sensors was quantified by acquiring single-molecule fluorescence scans on the confocal microscope.

Single-molecule pulsed interleaved excitation FRET measurements in solution

For single-molecule FRET measurements of freely diffusing nanostructures (Fig. S7) we used a home-built setup based on an Olympus IX-71 inverted microscope (for a detailed description of the setup, see Ref. [10]). The slides were prepared analogously to single-molecule measurements for surface immobilized samples except the slides were not incubated with NeutrAvidin to measure freely diffusing nanosensors in solution at 500 pM–1 nM concentrations. We used pulsed interleaved excitation with a 532-nm laser at 4 μ W intensity and a 640-nm laser at 5 μ W excitation intensity at 40 MHz repetition rate, respectively. The data was analyzed with the PAM [11] software. All channel burst search was performed to select the single bursts and ALEX 2CDE and |TDX-TAA| filters were used the filter the selected burst data.

Single-molecule studies of target specificity

Nanosensors used for studying target specificity (Version 1) contained a shorter 11 bp closing interactions (for a full list of sequences see Table S8). For each (off) target concentration a separate chamber with closed nanosensors was prepared, filled with the solution containing the target DNA in 10 mM Tris, 1 mM EDTA, 5 mM MgCl₂ and 750 mM NaCl and closed using adhesive seal tabs (Grace Bio-Labs, USA). Samples were incubated overnight to ensure that thermal equilibrium was reached, and the open fraction was determined by performing single-molecule fluorescence scans on the confocal microscope.

Antibody detection assay

Nanosensors used for the detection of IgG antibodies (Version 1) were equipped with two digoxigenin (Dig) functionalities and/or two dinitrophenol (DNP) functionalities per sensor arm (see Table S7 for modified sequences). Additionally, four and six 11 bp DNA-DNA closing interactions, respectively, were incorporated to facilitate bivalent binding of the target antibody in a bridge-like manner to the opposite arms of the nanosensor (Table S3). For each sample a separate chamber with closed nanosensors was prepared. anti-Dig antibodies (Rb monoclonal, Thermo Fisher Scientific, USA, Catalog # 700772, AB_2532342) and/or anti-DNP antibodies (Rat monoclonal, Thermo Fisher Scientific, USA Catalog # 04-8300, AB_2532964) were diluted to 100 nM in the buffer or diluted heparin blood plasma containing 10 mM Tris, 1 mM EDTA, and 750 mM NaCl. Chambers were filled with the antibody solution and incubated for 30 min. Following antibody binding, the DNA-DNA closing interactions were removed by a strand displacement mechanism upon 10 min incubation with 100 μM 17 bp DNA opening DNA strands (Table S8). The closing of the nanosensor by bivalent binding of antibodies was quantified by acquiring single-molecule fluorescence scans on the confocal microscope.

Restriction enzyme activity assay

For monitoring restriction enzyme activity, nanosensors (Version 1) were equipped with six or eight 11 bp DNA-DNA closing interactions containing a 6 bp sequence (Table S6) specific for the binding and cleavage of the restriction enzyme XhoI. For each sample a separate chamber with closed nanosensors was prepared and filled with 1×CutSmart™ buffer (New England BioLabs, USA) containing 50 mM potassium, 20 mM Tris-acetate, 10 mM magnesium acetate, and 100 μg/ml recombinant albumin. 0.5 μL of XhoI (20,000 units/mL, New England BioLabs, USA) were added and incubated for 10 min. The opening of the nanosensor by the cleavage of the DNA-DNA interactions was quantified by acquiring single-molecule fluorescence scans on the confocal microscope. For monitoring the cutting kinetics of the XhoI restriction enzyme cleavage reaction of the closing interactions, single-molecule fluorescence transients were recorded on a wide-field microscope after the addition of 0.5 μL of XhoI (20,000 units/mL, New England BioLabs, USA).

Data analysis

A python script was used to process the acquired single photon counting data which is available on GitLab <https://gitlab.lrz.de/tinnefeldlab/cospota>. Briefly, the software finds single spots using a wavelet decomposition-based approach and then calculates the spotwise PR as $PR = I_{Red}/(I_{Red} + I_{Green})$. We used the spotwise PR to distinguish between open ($PR < 0.3$) and closed ($PR > 0.3$) conformations. Data was plotted and fitted using Matplotlib, Scipy and Numpy. For the estimation of $K_{1/2}$ and n_H , we used the modified Hill equation:

$$\theta([T]) = \theta_{start} + (\theta_{end} - \theta_{start}) \frac{[T]^{n_H}}{K_{1/2}^{n_H} + [T]^{n_H}} \quad (1)$$

which also allowed fitting the start (θ_{start}) and end (θ_{end}) points of the titration curve given by the target concentration $[T]$ and the occupancy at each concentration $\theta([T])$. The reported errors are standard errors of the fit.

Supplemental References

1. Douglas, S. M. *et al.* Rapid prototyping of 3D DNA-origami shapes with caDNAno. *Nucleic Acids Res.* **37**, 5001–6. doi:10.1093/nar/gkp436 (2009).

2. Marras, A. E., Zhou, L., Su, H. J. & Castro, C. E. Programmable motion of DNA origami mechanisms. *Proc. Natl. Acad. Sci. U.S.A.* **112**, 713–8. doi:10.1073/pnas.1408869112 (2015).
3. Trofymchuk, K. *et al.* Addressable nanoantennas with cleared hotspots for single-molecule detection on a portable smartphone microscope. *Nat. Commun.* **12**, 950. doi:10.1038/s41467-021-21238-9 (2021).
4. Ouldridge, T. E., Louis, A. A. & Doye, J. P. Structural, mechanical, and thermodynamic properties of a coarse-grained DNA model. *J. Chem. Phys.* **134**, 085101. doi:10.1063/1.3552946 (2011).
5. Snodin, B. E. *et al.* Introducing improved structural properties and salt dependence into a coarse-grained model of DNA. *J. Chem. Phys.* **142**, 234901. doi:10.1063/1.4921957 (2015).
6. Rovigatti, L., Sulc, P., Reguly, I. Z. & Romano, F. A comparison between parallelization approaches in molecular dynamics simulations on GPUs. *J. Comput. Chem.* **36**, 1–8. doi:10.1002/jcc.23763 (2015).
7. Suma, A. *et al.* TacoxDNA: A user-friendly web server for simulations of complex DNA structures, from single strands to origami. *J. Comput. Chem.* **40**, 2586–2595. doi:10.1002/jcc.26029 (2019).
8. Poppleton, E. *et al.* Design, optimization and analysis of large DNA and RNA nanostructures through interactive visualization, editing and molecular simulation. *Nucleic Acids Research* **48**, e72–e72. doi:10.1093/nar/gkaa417 (May 2020).
9. Poppleton, E., Romero, R., Mallya, A., Rovigatti, L. & Sulc, P. OxDNA.org: a public webserver for coarse-grained simulations of DNA and RNA nanostructures. *Nucleic Acids Res.* **49**, W491–W498. doi:10.1093/nar/gkab324 (2021).
10. Schroder, T. *et al.* Shrinking gate fluorescence correlation spectroscopy yields equilibrium constants and separates photophysics from structural dynamics. *Proc. Natl. Acad. Sci. U.S.A.* **120**, e2211896120. doi:10.1073/pnas.2211896120 (2023).
11. Schrimpf, W., Barth, A., Hendrix, J. & Lamb, D. C. PAM: A Framework for Integrated Analysis of Imaging, Single-Molecule, and Ensemble Fluorescence Data. *Biophys. J.* **114**, 1518–1528. doi:10.1016/j.bpj.2018.02.035 (2018).

Supplementary Information for

Engineering Modular and Tunable Single Molecule Sensors by Decoupling Sensing from Signal Output

Lennart Grabenhorst¹†, Martina Pfeiffer¹†, Thea Schinkel¹, Mirjam Kümmerlin¹, Jasmin B. Maglic¹, Gereon A. Brüggenthies¹, Florian Selbach¹, Alexander T. Murr¹, Philip Tinnefeld^{1*}, and Viktorija Glembockyte^{1*}

¹Department of Chemistry and Center for NanoScience, Ludwig-Maximilians-Universität München, Butenandtstr. 5-13, 81377 München, Germany

†These authors contributed equally.

*Correspondence should be addressed to P.T. (philip.tinnefeld@cup.uni-muenchen.de) and V.G. (viktorija.glembockyte@cup.uni-muenchen.de)

Supplementary Text

Detailed DNA origami folding procedure

16 μL of unmodified staples were mixed with 4 μL of modified staples, 5 μL of FoB20 and 25 μL of p8064 scaffold (produced in-house). Modified staples consisted of the desired modified staples and the respective unmodified staples to replace the modified staples that were not desired in the respective experiment. An exemplary recipe for the modified master mix for the 2 \times 13 sample from Fig. 2 is given below:

Red and green dye strands (2 \times 1 μL)

Row 4 closing staples (4 \times 1 μL)

Row 1-3 staples without closing interactions (12 \times 1 μL)

Biotin 1-4 (4 \times 1 μL)

Stabilization staples without stabilizing interactions (4 \times 1 μL)

We used two slightly different versions of the DNA origami design. Version 1 was used in the experiments described in Fig. 3 and 4 in the main text, while Version 2 was used in the experiments described in Fig. 2. The staples needed for Version 1 of the sensor are described in Tables S1, S3, S5-S7 and the staples needed for Version 2 of the sensor are described in Tables S2, S4 and S5.

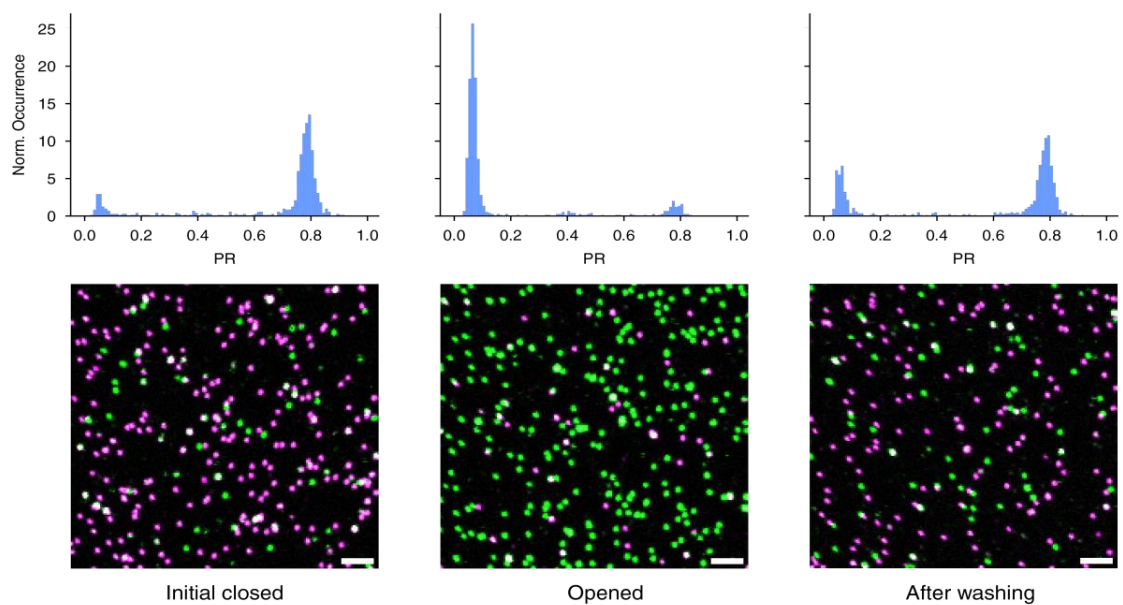
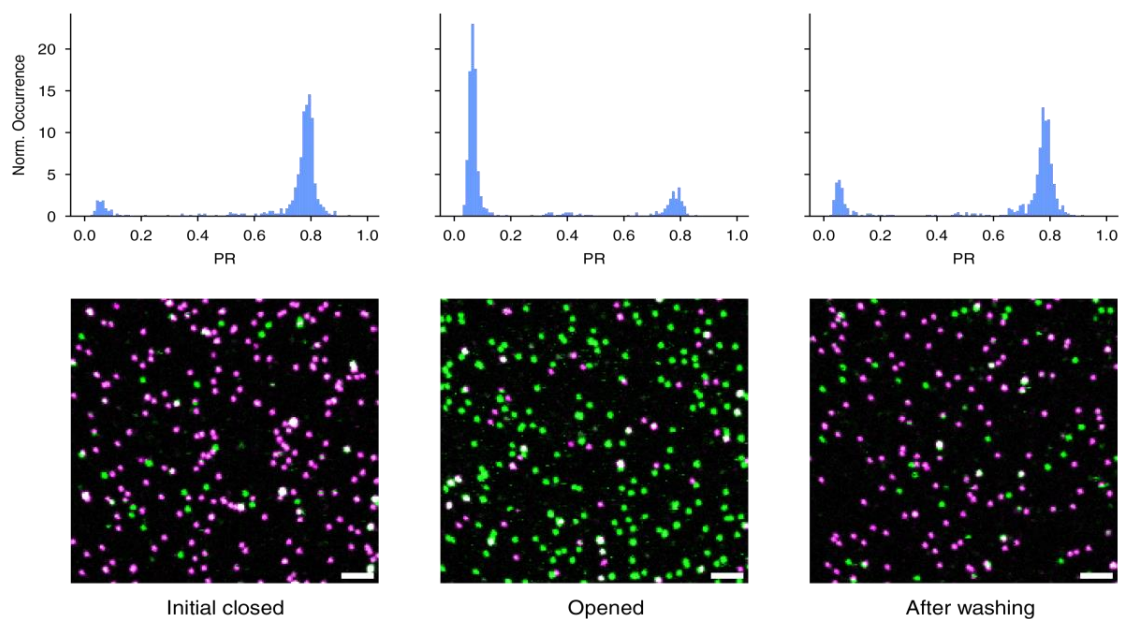
A**B**

Fig. S1. Reclosing of the hinge nanostructure with two closing interactions measured in the presence of 50 mM (**A**) and 400 mM (**B**) NaCl. Samples were opened by incubating them with 100 μ M opening strands for 1h. Afterwards, they were washed at least 10 times with the respective buffer and scans were taken after approximately 190 hours to allow for complete equilibration.

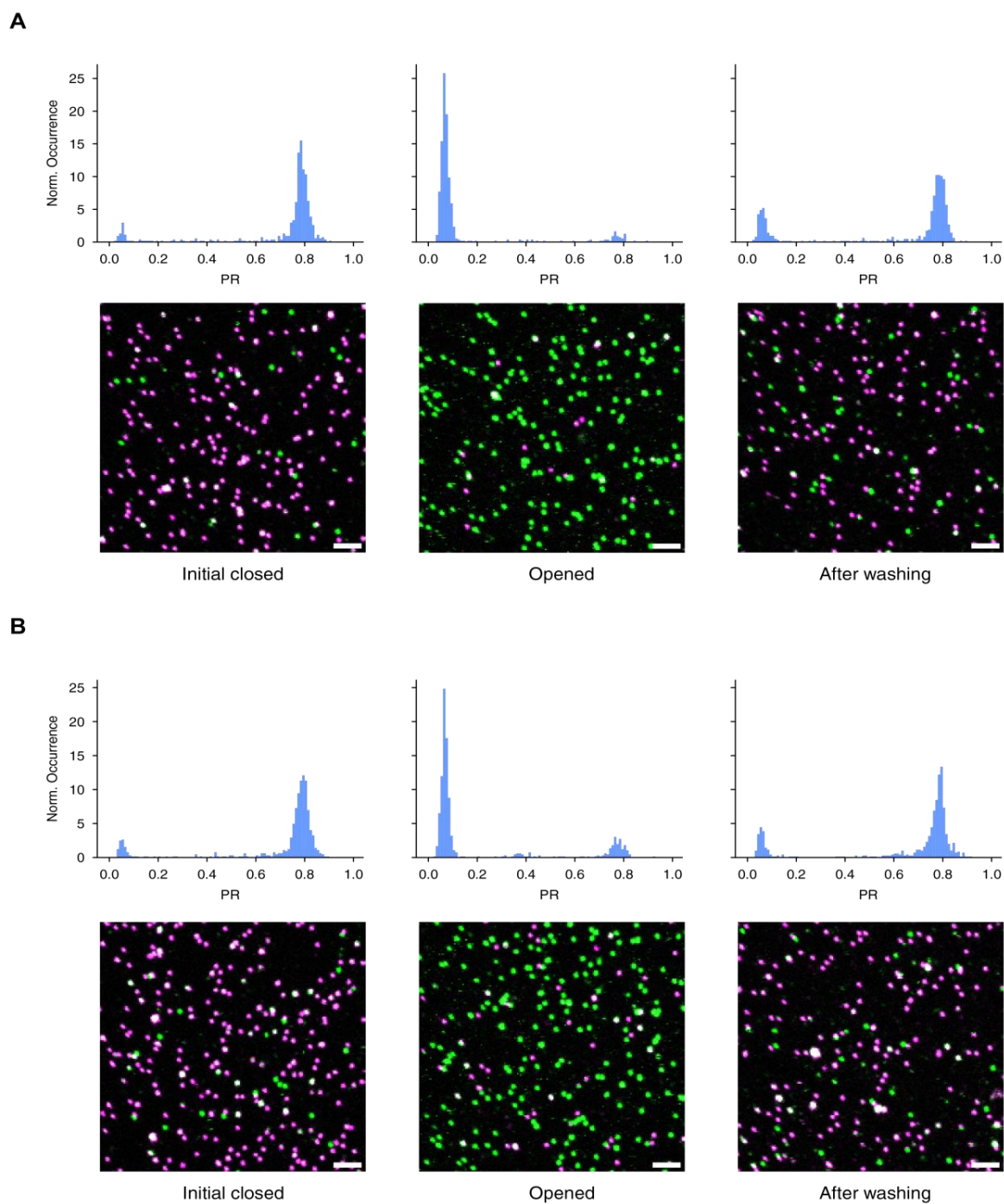
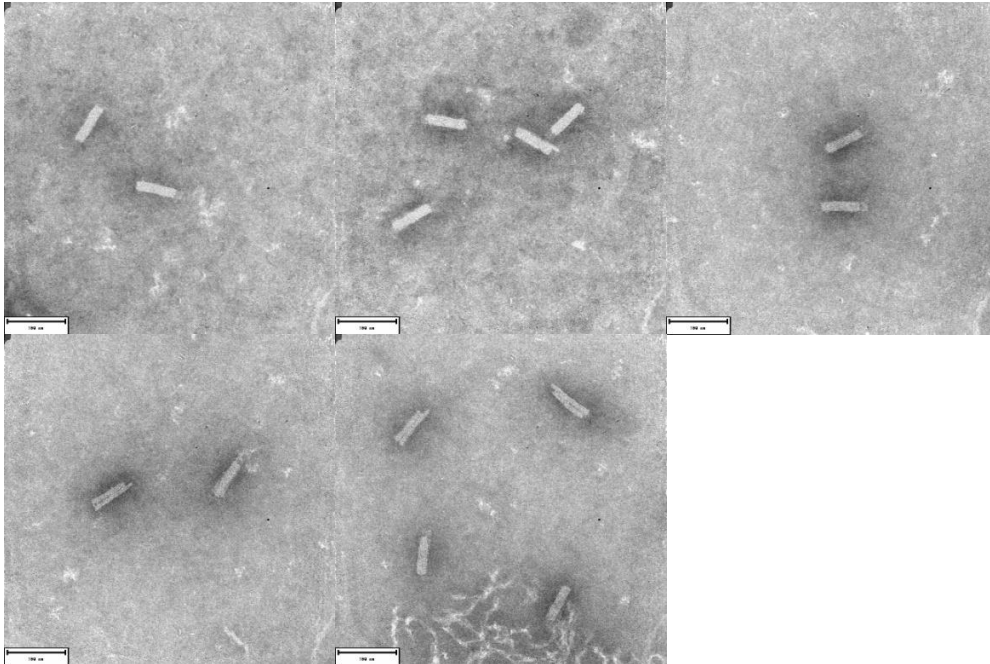


Fig. S2. Reclosing of the hinge nanostructure with four closing interactions measured in the presence of 50 mM (**A**) and 400 mM (**B**) NaCl. Samples were opened by incubating them with 100 μ M opening strands for 1h. Afterwards, they were washed at least 10 times with the respective buffer and scans were taken after approximately 190 hours to allow for complete equilibration.

Closed structures



Open structures

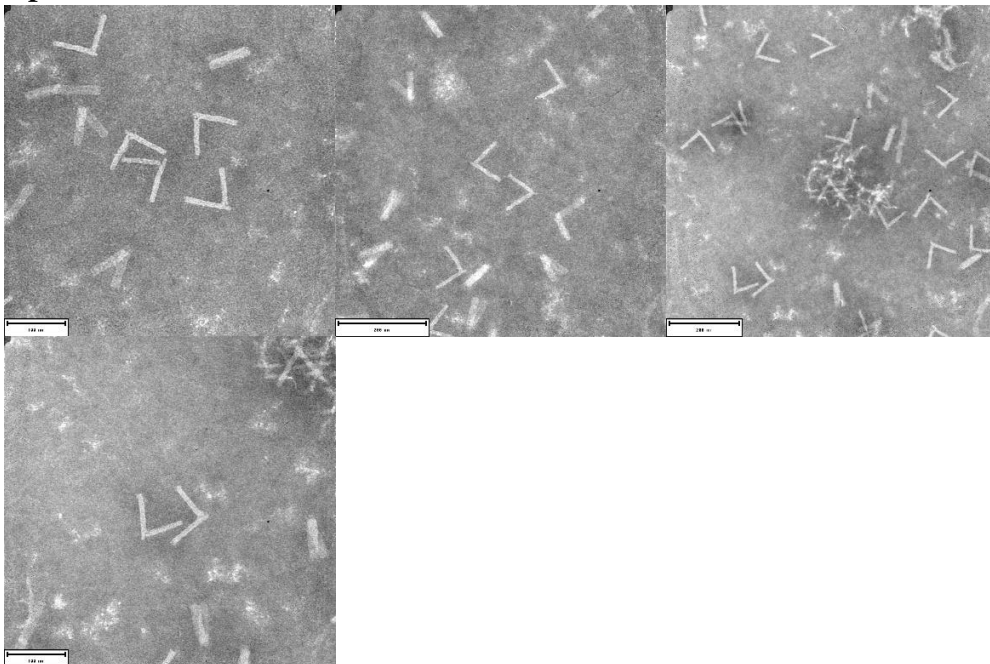


Fig. S3. Full field of view of the TEM micrographs used for the collage shown in Fig. 1B.

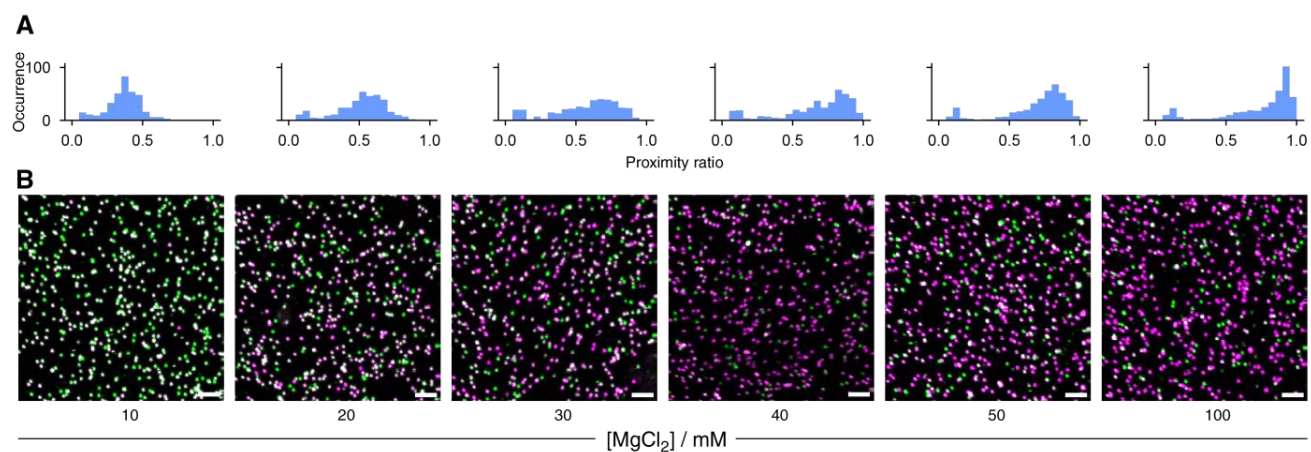


Fig. S4. FRET proximity ratios (A) and single molecule confocal scans (B) obtained for Version 1 of the nanosensor with a FRET pair consisting of ATTO532 and ATTO647N incorporated directly onto the hinge arms (Table S5) at different ionic strengths (increasing concentrations of $MgCl_2$). Scale bar: 2 μm .

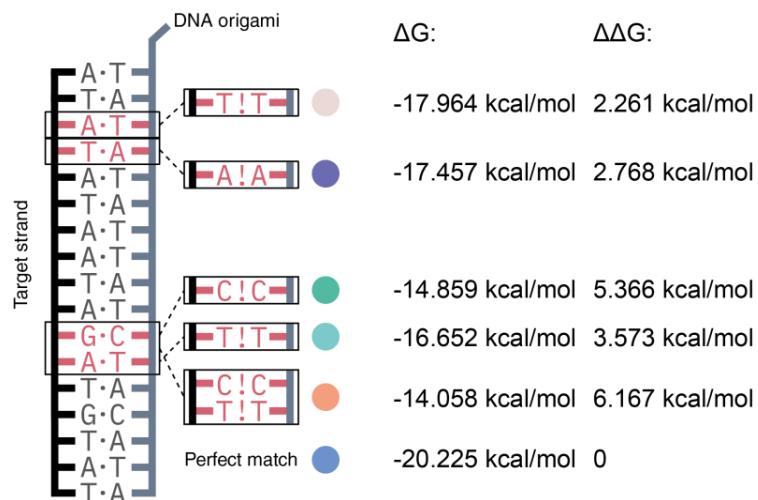


Fig. S5. Binding free energies (ΔG) for the different off-targets as well as for the perfect match as shown in Fig. 3 in the main text, as calculated by NUPACK at 25°C in a buffer containing 750 mM NaCl and 5 mM MgCl₂. $\Delta\Delta G$ is the difference in binding free energy when compared to the perfectly matched target.

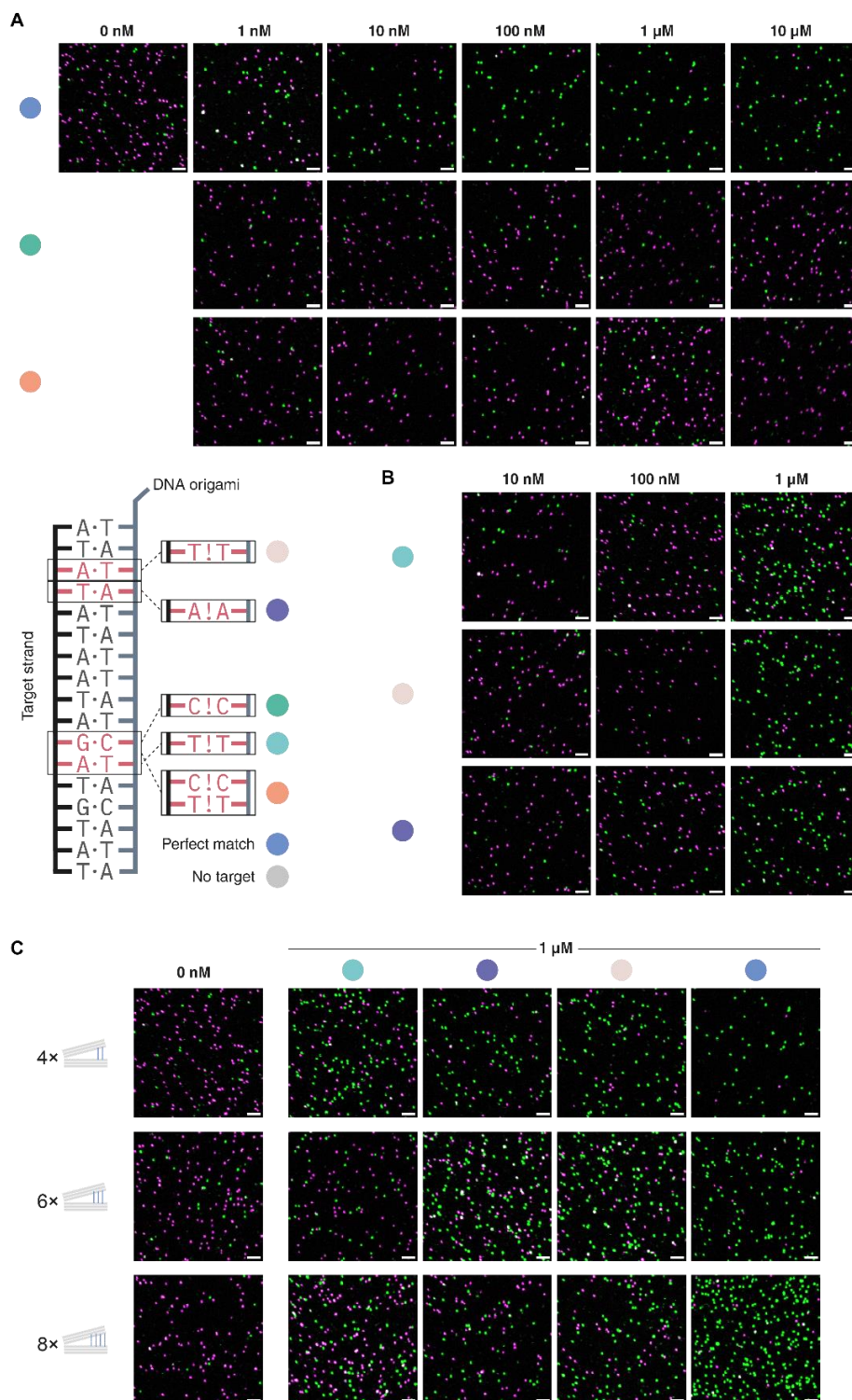


Fig. S6. Exemplary confocal microscopy scan images of the experiments shown in Fig. 3B (A), Fig. 3C (B) and Fig. 3D (C). Scale bar: 2 μm .

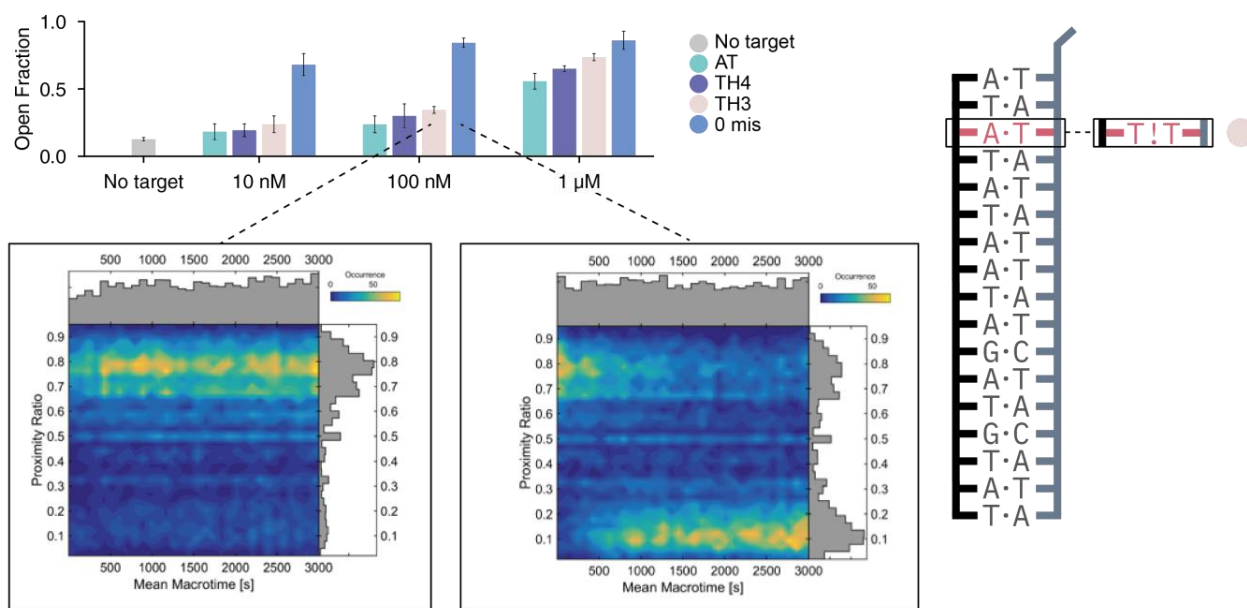


Fig. S7. Nanosensor opening kinetics (proximity ratio vs. time) obtained for 100 nM of the target containing a single nucleotide mismatch (left) and 100 nM of perfectly matched target (right) measured at 1 nM concentration of DNA origami nanosensor containing 4 closing interactions.

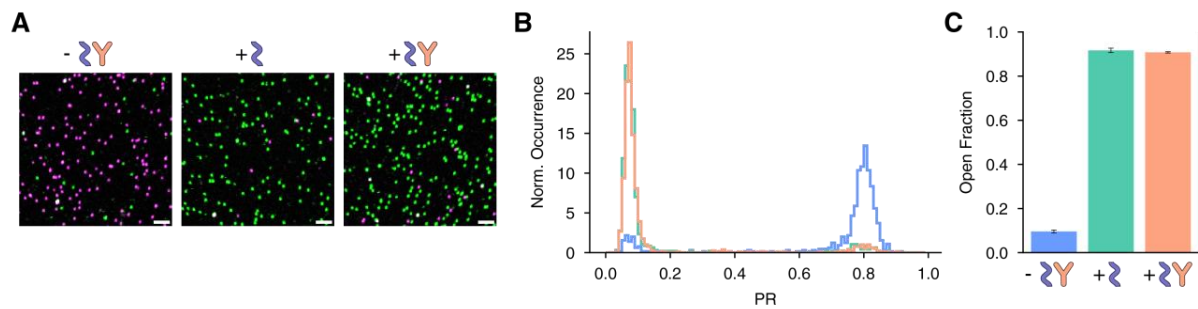


Fig. S8. Control experiment for nanosensor containing no Dig recognition elements. In this case, opening of the sensor is observed even after incubation (100 nM, 30 min) with anti-Dig antibodies. (A) Exemplary confocal microscopy scans. Scale bar: 2 μ m. (B) Proximity ratio histograms for one experiment. (C) Fraction of open sensors. Error bar represents the standard deviation obtained from three independent measurements.

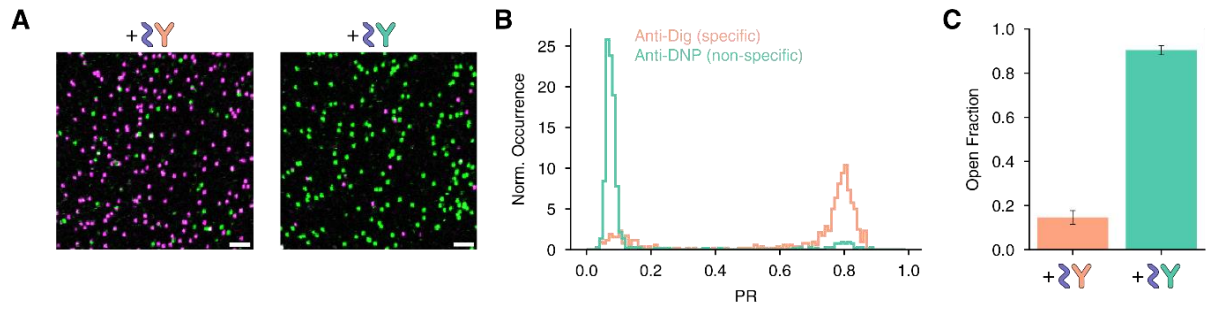


Fig. S9. Comparison of the extent of opening for sensor with Dig antigens when incubated with 100 nM of the corresponding specific antibody (Anti-Dig, orange) to 100 nM of a non-specific antibody (Anti-DNP, green). (A) Exemplary confocal microscopy scan images. Scale bar: 2 μm . (B) Proximity ratio histograms for one experiment. (C) Fraction of open sensors. Error bar represents the standard deviation obtained from three independent measurements.

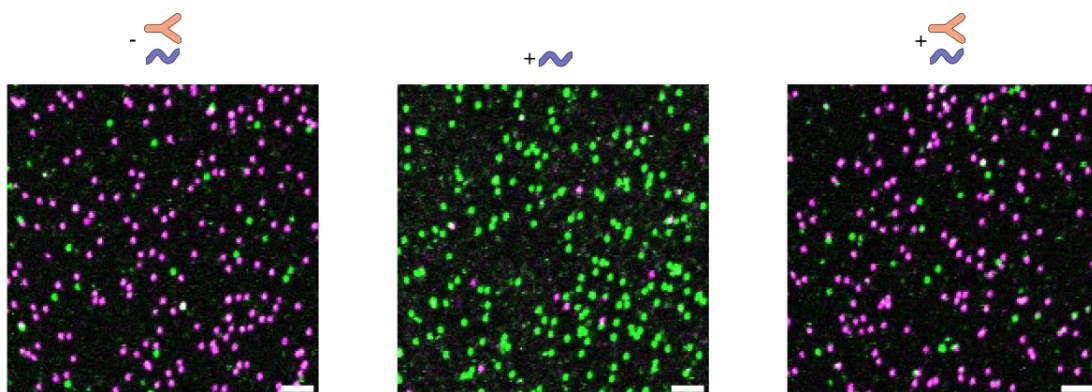


Fig. S10. Exemplary confocal microscopy scans for the data acquired for the antibody sensor (data shown in Fig. 4C before addition of the target (left), upon the addition of DNA opening strand alone (middle) and upon incubation of 100 nM antiDig antibody and addition of DNA opening strands (right) in heparin plasma. Scale bar: 2 μm .

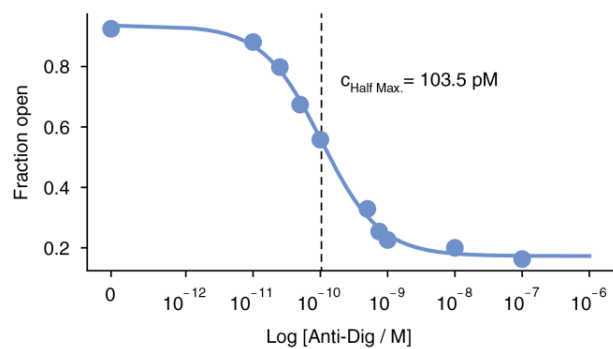


Fig S11. Estimation of the response window of the Anti-Dig antibody nanosensor. We achieve a $c_{\text{Half-Max}}$ value of 103.5 pM.

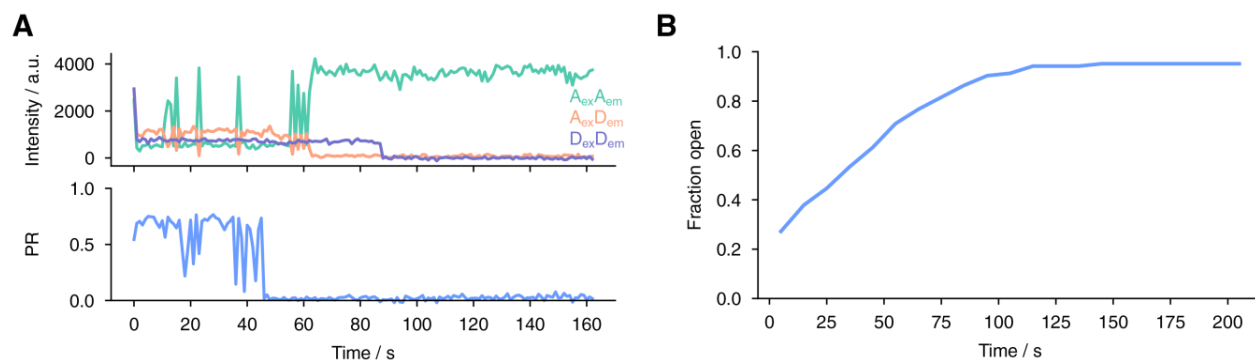


Fig. S12. Kinetics of the XhoI restriction enzyme reaction. **(A)** Exemplary single-molecule FRET trace and **(B)** Average of 103 single-molecule transients of the cleavage reaction of the closing interactions (66 units/mL XhoI, 10 min incubation) monitored by the DNA origami sensor. The FRET transients of the single DNA origami sensors were recorded on a wide-field microscope.

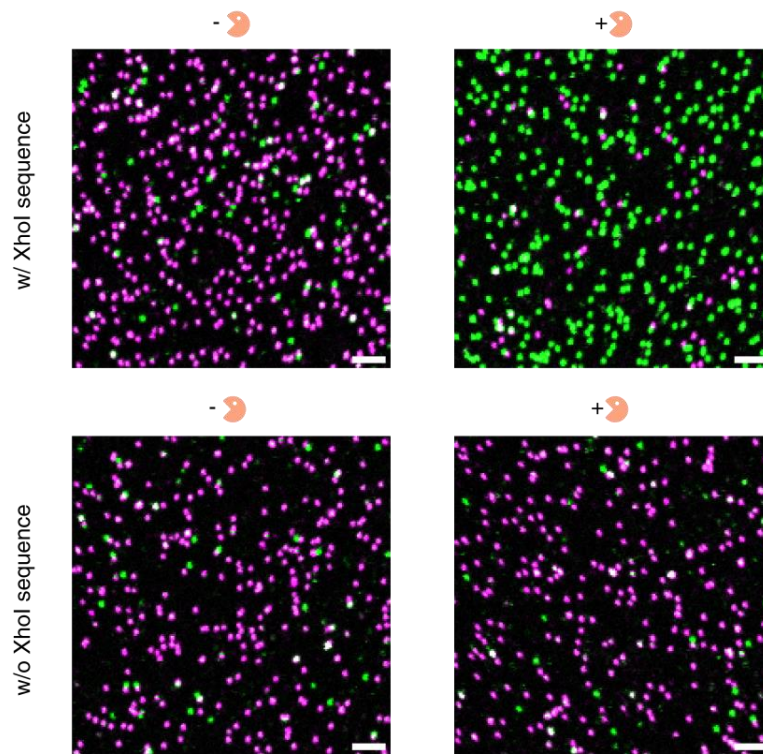


Fig. S13. Exemplary confocal microscopy scan images obtained for the nuclease nanosensor (shown in Fig. 4D-F). Scale bar: 2 μm .

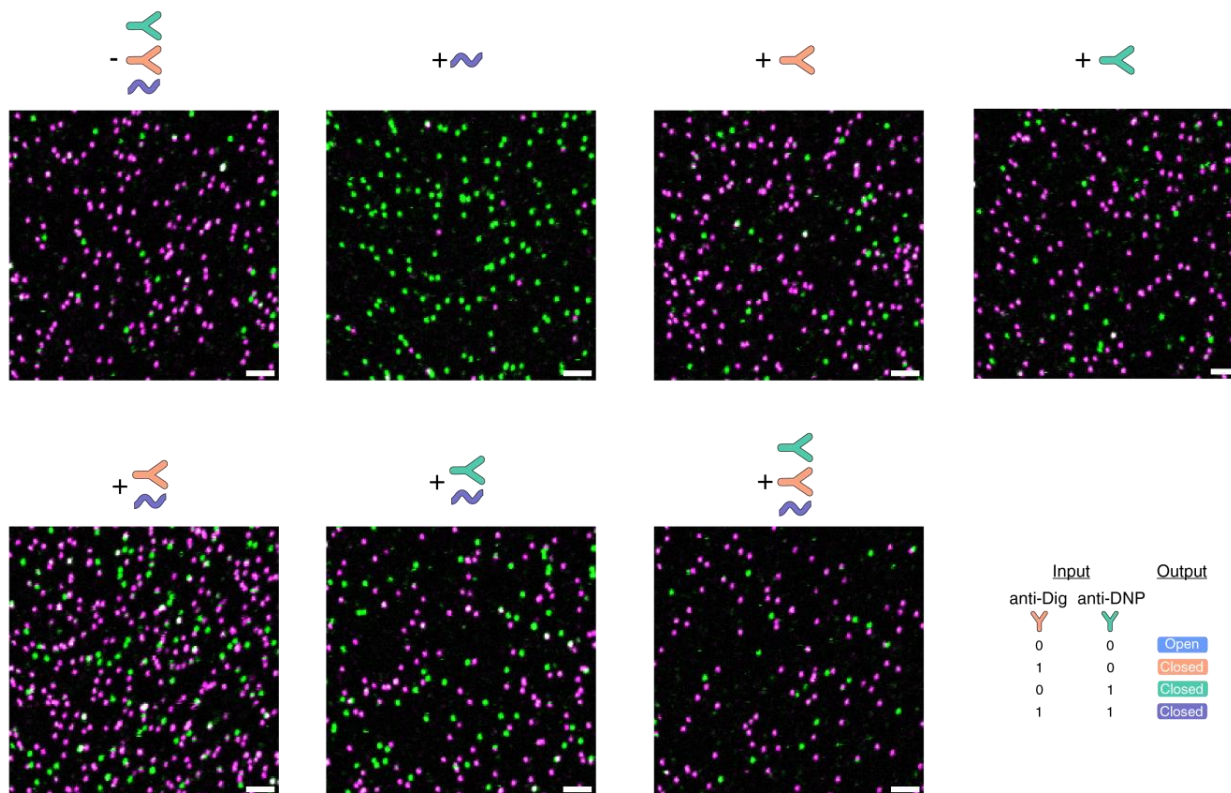


Fig. S14. Exemplary confocal microscopy scan images obtained for the multiplexed sensor for antiDig (orange) and anti-DNP (cyan) antibodies (OR gate) as shown in Fig. 4G-I. Scale bar: 2 μ m.

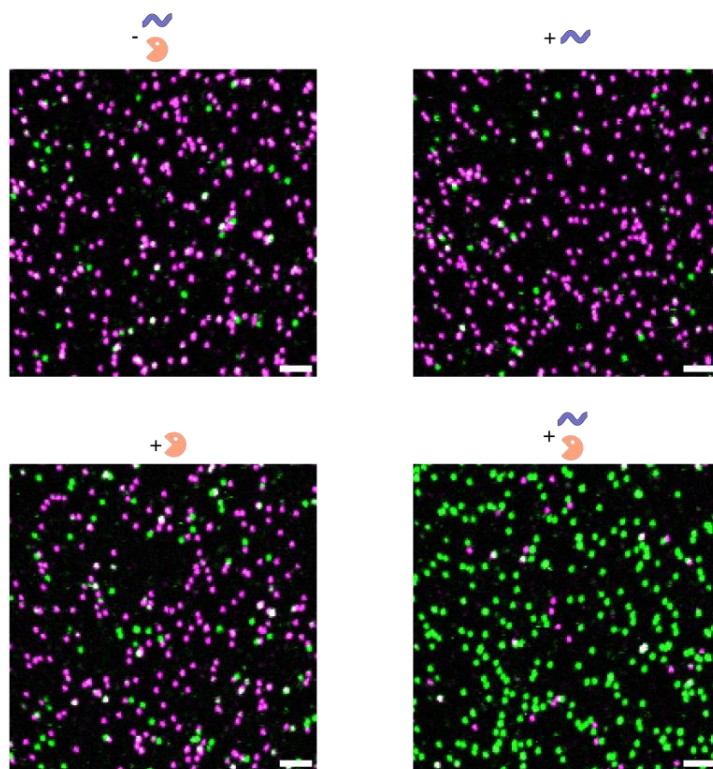


Fig. S15. Exemplary confocal microscopy scan images for the multiplexed nuclease and nucleic acid sensor (AND gate) shown in Fig. 4J-L. Scale bar: 2 μm .

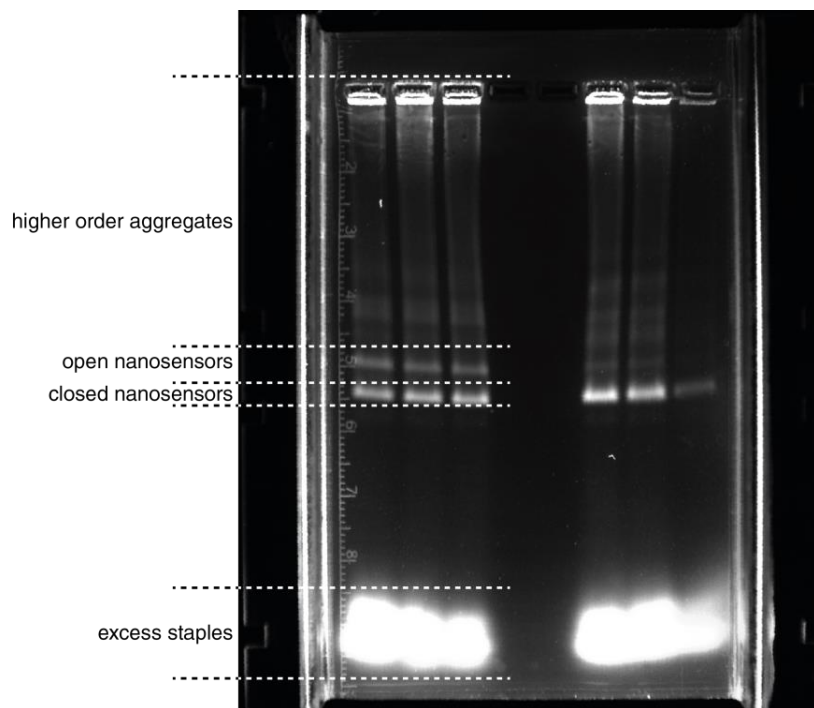


Fig. S16. Exemplary fluorescence scan of an agarose gel used for purification of the nanosensors. The respective band was then cut using a scalpel.

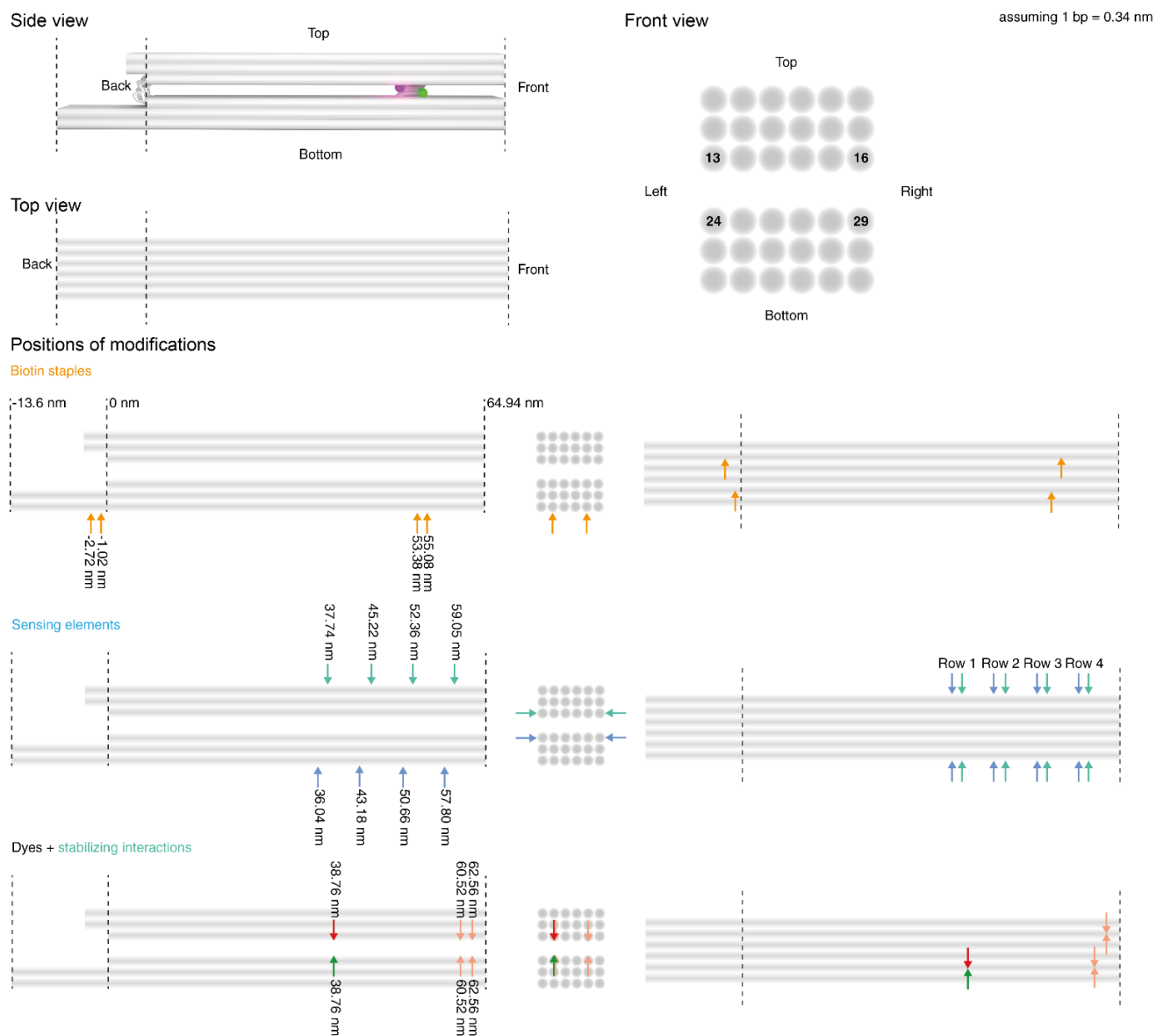


Fig. S17. Depiction of the placement of the modifications (FRET pair, sensing elements, biotin staples used for immobilization as well as stabilizing interactions) in the nanostructure. The numbering in the front view represents the helix numbering in caDNAno and are also used to indicate the positions of the sensing elements in Tables S3, S4, S6, and S7.

Table S1. Unmodified DNA origami staple sequences used for Version 1 of the nanosensor.

ID	Sequence (5'->3')
1	AAATATCCCATATGTTTCAGGCAAATCCAGTGATGACAGTTGGGCGGTTGTAAATC
2	ATATTACCAAATACCTGTAATTCTAAAACCTT
3	GCTGGGAATCAAAGAAACGTAGACGGGAGAATTAAGTAAACACCCA
4	GTCCACTAAATCCCTTTAAACCAAGGCGGGCCTGT
5	ACGTGGACTCCAACGT
6	CAAAGGGCTCAAAAATCAAGCCGTGTATGTTAGCAAAGGTGCTGCGGC
7	GAGCACGTATCCAAATTTACCGCGAACTGGCAAAGAAACGCAAAGACATTAC
8	CGTGGAACTCAAACATATCGGAAATGGATAAGAG
9	AAATTAGTAATAACATCATCACACGAATTTAGGCACCG
10	TTTACGAGCGTGGCGTTTTTATAGCCGATTTACCAGCGCCAAAAGTATC
11	AGGGCAAATTAACCGTTGGCCAACAGAGAATCGCAGAA
12	CAGCCGAAATCGGCAATTAAGA
13	CACCCAGCAGTGTTTTGAGGCCACCGAGTAAAGCGTAAGAAAGCCAAAAGCCTG
14	TATATAAATCAAAAAGAAT
15	CGCTAAACAACCCTAATTGGAAAAACGCTCATGGGCCAGCCAAGAACAAGGAAAATAG
16	TATAAACAGCCAAAAGTCA
17	CTAACTTCTTTGCAGGAGGCCGATTAAAGGGA
18	ACTCCTTAAAGCGCATATTTTTTTGTTAACGGAAAAACCCAGAACA
19	AAAGCCCAATAGCCAGTAATTATTTACAACAGAGGTGAGGCGGTGCTG
20	GCTTTTGTCAATCAATATTAG
21	CCAGCAGGCGAAAATCCTGTTTGATGGTGGTCAGAATGCGTAC
22	TCCTTTACAGAGAGAATAACATAAAAACAGGGTTACGCATTTTATTAGGT
23	AACATATTATTTATCCCAATAA
24	CGCACAGGTGCACTCTGTCGTAGAAAATACATACATAAAGAAA
25	CCATCGCCGTAAAAAAGC
26	CATTGACCTAAAAATTACCTTCAAATATAATTTTAAAAGTTTGAGTAACA
27	AGCTGTGATAACAAAATTAAGTTGGCACTCGTATT
28	ACCCACCGAAAAAGAAGGGAAGGTTGAAGTATTAGACTTTACAAACAAAACA
29	AGACGATCCAGCGCAGGTTTTTCACGGTCATAC
30	CACTGCGCGCCTCGGCCTTAATCGCAGTAAA
31	GCAACCGACAAATCATCGTAGTAATATCGTCTATCACTTTGAC
32	GAATTTTCGAGCAAGCAAAGTAGAACTTTCCTC
33	CATTCCCTTTTTAAGAAAAGTTAAGCCCATCTTACCAACGCTATAGAC
34	CTCTCTGAATAATGGAAGGGAGCGGAGAATTT
35	ATATTCACAAACAAATGTACATCGTTGCTTCTAGACAAAGCATAG
36	GCTCATTGCGCCAGAGGGTAAAGTTAAACG

37	CACCAGACGATATCAAAATTATTTGCAATCATTTTCTAAAGCA
38	GTCTCATTTGTTTAATGGAGATAAAATTGGCAGATTCACCAGCTTGCCTGTCAGA
39	TATCACCAGTAGCACCACCACG
40	TAATTTTCATTAAAGGTGAATACAAAAGGAGTAGGGCTCCCGACTTCCATCAC
41	CCGGAACACCGGAACGCTTTGAA
42	TAGTGAACAAGAAAAATAACCAATCAAACGGG
43	GTCTGAGAGACTACCTTTTAGA
44	AGATTTGAAATAGAGGCATTAAGTTTAAATAATAACGGAATACCCTG
45	ATCGGTTAAATACATATTTATCATATGGACAAAGTTACC
46	CCTAGGAATTGAATGATGAACTTTTACAGCCACCCTCAGAGCCACC
47	CGCCCCTTCTGACCTGAAAAGAGTCTGTGCGGGAGTATCCTGAAATAATA
48	CGCCTGGCCCTGAGACGCGTGCCATAGCGTCTGCTGTAGTCGAGCTTGATAAATT
49	GGGTGGAATTCGTAGCGAGAGATAACAGTCAGCAGCGTAAAGGAATTGCGAATTTTT
50	GGGGTTTCTGCCAGCAGAGTTGCAGAGTAGTA
51	TTCCAGATGCCGGGTTACGCAAACGCAACGCAAGAAAACAGGGAGAGATCTTAGGATT
52	CCGAGCTCGTTTTTCGATTTTAAAGAACTGGCAGGGAACCCATGAGGA
53	TGAAACTCGTTTATAGATTTAGTTAA
54	CGGATCCGCCGGGCGCGGTATGCCAACAAATCATAACGTC
55	TGGGGAATGCAGCATTTGGGACAA
56	GCATGCGTCCGTGAGCCTCCGCTGATTGTCAACTT
57	AAACCATTCCATGCTTTTGGACTTTTTGAACTGACCAACTTTGAA
58	GGTACGAACGAGCCAGACGAGGTAAAATACGAGGCGCAGACGGT
59	GCTGATTGCCGTTCCGCTGCAGCCGAATATAACAATA
60	TCGTGCTAAATCGTTTATGCAACTAATAGTAGCCCGAAACTACAGAGGC
61	GCCTGTAATACTATTGTAAATATGGGATCGGATAAGTGCCGTC
62	ACGTAAATCGGTCATTAAATTCTTTCCAGTATAGCCCGGAATAG
63	GGAAAAAATTCGTGTACCAGGAACAACAAGACAGCATCGGAGGAC
64	TTACCAGTATTCGCCAGACGACGACAGTATCTGATATAAGACGTTA
65	GCGAATCATTTTTAATAAAGCTTTTCACGCCGCTTTT
66	AAAACGAGCGATTAATCTCCGTGGGAACAAAGAGCCACTGA
67	CTCTGAATTTACCGTTACGCAGAAAAGCCCCAGATAAAAAATTCTA
68	GTAAGGTACTGGTAATAAGTTGAGAAGGATACAAAGG
69	ATGGCTTTCCGGCACCTGGTGAAGATATTTAATTTGCGGGTTCAA
70	CTGGCACTCCAGCCAGCTTTTGTGATAATAAGCAAGGATAGCTTTTTTCGTC
71	TCTGTAGCAATAGAACGCGACTTTCCAGGAGAGATAACCCACAAGA
72	GTGTATTTTTGAATGGCTAGGAGCACTTATTCATCCTGATTGCGCTCCC
73	CCGTGCAACCGTACTGCGTAACGATCTAAAGAAT
74	CGTCGGATGTTGGGTAACGCCA
75	CCCTGAGAGTATTAAGAG
76	TTAATGAAGATCGTGCCGGAAACCAGGCAAAGCGCCCCC
77	CAATCATAGTTACAGGAGGTTTAGTACCGCCACCCTTTGGTGTGCATC

78	AAAAACGGATAAGCAGCAACCGCAAGATGCGGTATCATTTCGCGTAA
79	TGGCACAACGCCCCACCCTCAGAACCGCCACCCTCACGGCGGATAGC
80	CAGCGCCAAGCTCCGTCGGTGGTGCCATGGCGCTTTTATATTTTATACATAATAAA
81	TAGCATGTCAATCATAAAATGCAAGTCAAATCCAGGTC
82	AGAATTAGATAGAGCCGCGCTCACAATTCACAAGCTGCATACGAACTA
83	TCTACTAACATTAAAGTAACACCACCCTCATTTTCAGGGATAG
84	AACATTTATTTTCGGTCCGTTCTCACGGAAAAAGAGCCA
85	CCCATCCAATGGCAGCATTTCAGAGGTGGAGCCGGCCAG
86	AGCCGCACTCAAAGCATAAAGTGTAAGCCCG
87	AAGAGGTCATTTTTCGCAATCCCCGGTCTTTA
88	CTGAAAGCGGAGACCTTCATCAAGAGTAATCTTGAGAG
89	GGGTAAAGTACAGCAACGGGACTTCAA
90	AACCTTGTTATCGTCACTGTTGCCCTGCTGGTGCTGAATTAAGCTAAC
91	GAGCAACCTAAATCCGCGACCTGCTCCATGTTACTAATCTACGTCAT
92	ATTCAACTTGCCTAATAGCGGGT
93	AAACATCATAAATATTCATTGGATGGCTACTC
94	AATTGGGCGGCTGGCTTTGCATCAAAAAGATTTTTTAATCTC
95	TAATCATTGACAGATGAACGGTGTA
96	ACGGAACATGTGCAAAACGAAAGAGGCAAAACGCATAACAATAA
97	AAGGCTTGCCCTGACCAAGAACCCTGACT
98	CAGACCAGGCGCATATTGAGATGAGACTGGTGTC
99	AGAGGTGAATTAGTTTTGCCGAGGATCCACTGGTGTGTTTCAGCGGCA
100	CAATCATATCATTATAACCAAAATAATCATGGAGGTTTCTTTGCTCGTCGGA
101	GAAACAAAGTACAGAGATTTA
102	CGGATATTCATTACCCAAATCAACTGCTCATCTTTAAAC
103	TTTGAACGAGGGTGGTGTCTATGACCCTCCGGCCAAGATAGACTTTCTCCGGCTT
104	TAAACAAAAGAACCTTATGCTTTTCACCAGTGAGACGGGCAACATCACAGTTAGAGG
105	AGTTTCCAGTCACCCTTGATTCCCATAAAGCTGCCGGACTCGCCATGT
106	CCACTACGTGCAGGGAGTTTGACCATTAGCAAGTCTG
107	ACACTTTGTATCATCGCCTGATAAATTGACATTATGGAATTACGAGC
108	GACCCCATTTGCGCCGGCGGAGCGCATCAAT
109	ATAAATCAGTACCTTTTTTGATTAATGTGT
110	ATATCGCGAAGAGGAAAAATGTTTGTTTAATTCCTTAC
111	GCGGGATCTTAAACGCGATAAAACCAGTCAGTTTTCGTATTGGGCGCCA
112	AGGTTGAAAATCTCCAAAAACAGCCCTAGGAACGCAGATGGGCCGGTGCG
113	TGATTTCCAGGTGAATTTCCATGTACCTGTGAGCG
114	AGGATTAGAGAAAAATCACTCAAATGTCAGTGAAT
115	CAAACCATCAATATGATATTC
116	GCTCAAAGCGAACCAGACCCAGAAGCCGGAATCGCCAGAACGCAAGCGG
117	AATGCCGGAGAGGACTAGAAGCCTGTTTTAAAAACG
118	CAGTTTCAGCGGAGTGAGATTTTCTGCG

119	AAGGTCGGTCGCTGAGGCTAAGGCACCAACACTATTAATAAATAATGAA
120	GAAAGGCAATCGATGGTAAAACACAGTTAA
121	TTCGTAAAAGGAAACAGTAGCGACCGGAAACGTCACCAATGGTG
122	TTAATCTAAAATATCTTTATTAGTCTTACTAGAAACGCTCAACGCGA
123	CTATCAGGTCAACCGTTTTTTAGAAATTGCTAGCGGTGC
124	GTAAATGAAATAGAAAAAACATTGGAAGTTTATCCCTTACCCGGGTA
125	GTCGTTTTGTTATTTGAGGGTTCAGGCTGCGCAACTG
126	GCATTCCACAGAAAAGGCTGCAA
127	GTTTCGTCACCAGCGGTTTATAGCATTAAATGTTT
128	GCTGAGACTCCTCAATTAACGGGATCAGAAACAGCGGA
129	AGCGGGGTTTTGCTCAGTAC
130	CAGGTTTGCTAAACAGTAGCTATTTTTAAGATTGTCAGGAGTCGTCATAC
131	GAGAGGGTGGCCTCAGATTTTGTGTTTTGTGAGGAGCACATCCTCATAACAT
132	GTGTATCTCTGCCAGAATCAGCACGTACAGTGTAGAACGTCAGCGGGCT
133	CTATTATTCTGAAACCCGTATAA
134	AGTCTGGAGCAAACAAGAGCGGAGACATGCCTGAG
135	CGCTGTAACCTCCATGCTGATCTAATGCAGAAC
136	AGAGTTCGCTATTATTATACTATTAAGCCAGAATGGAAAGCGCA
137	ATCAAAGCCAGCAGCAAAATGTGAGTCCTACCATTGGCCTTG
138	TCACCTTCAGTATTATTAATTTATAAAGTACATATAATGATTAAG
139	AACCTTTTTAATCAGAAATAATTGACAGGAGTTGAGGCAGGTCGTAATCAGTAC
140	TCATTACATTTTAAACGTCCACCAGAA
141	TCGCAATAGTATTATCATCATATTCCTGATTATCTTG
142	ATAAATATTTTAGACACCGCCACGCTCAATCGTCTGCCTT
143	AATCCTGAAGATGATTTAGATTAAGA
144	TTTGGAATTAATTTTCCCTTATATGTAAGGCT
145	AGAAGAATAACCACATAAAAAAATCATAGCAG
146	GCGTAGATCGTTATTCAAACCCCTCAATCAATCCAGC
147	ATACAGTTTCGACAAAATCAACAGTTGAAAAAAC
148	GTACACAAACATGTCATAGCCTTGAGCCATTGGGAAGAAAATACAACGCCATT
149	CGGATTCGTTCAATTATTCA
150	GCGTTCCAAGATAATCGGCCAGTTTGGAACAAGA
151	GACGACAAACTCATCGTTGCAACATACGAGCATGTAG
152	AAAACATTTTGTGCAACAGTGCCACGCTGAGAATAACGCGAGGTCCAGAC
153	AATCATCTTCTAGCAAGGCAGAATCAAGTTTGCCTCCGCCAGCAAGAAATT
154	TGTACCAGTAATAATACCGAACGAACCAATCTGG
155	TTCAAATATCAATATTGAAAAATGCGGAACAAAGAAACCACCAGAAGGTT
156	ACCGCAGCAAAAGCGCGTTTTTCATCGGCAGAGCCGCAGATGAAT
157	TAAAGTCACCGACCCCTTATTAGCGTTTCAGA
158	TTTAGTATGAGGCGAATAACAACACTAGCCGTCATAGATAATACATTTG

Table S2. Unmodified DNA origami staple sequences used for Version 2 of the nanosensor.

ID	Sequence (5'->3')
1	GCTGGGAATCAAAGAAACGTAGACGGGAGAATTAAGTAAACACCCA
2	TCATTACATTTTAAACGTCCACCAGAA
3	CAGCCGAAATCGGCAATTAAAGA
4	CAGTTTTGCTAAACAGTAGCTATTTTAAAGATTGTCAGGAGTCGTCATAC
5	CTCTGAATTTACCGTTACGCAGAAAAGCCCCAGATAAAAAATTCTA
6	GTACACAAACATGTCATAGCCTTGAGCCATTTGGGAAGAAAATACAACGCCATT
7	CAACATACGAGGCATAAAATGGTCCGATATATAGCCTTTAATTGTATTA
8	AAGGCTTGCCCTGACCAAGAACCCCTGACT
9	AACATTTATTTTCGGTCCGTTCTCACGGAAAAAGAGCCA
10	TTTAGTATGAGGCGAATAACAACACTAGCCGTCAATAGATAATACATTTG
11	CATTCCCTTTTTAAGAAAAGTAAGCAGAGCGAACCTTAATTGAGATAGAAGAACTGATAGC
12	CGCACAGGGTGCACCTCTGTCGTAGAAAATACATACATAAAGAAA
13	AATGGGATAGGTCACGCAGAACCCTGTA
14	GCGTAGATCGTTATTCAAACCCCTCAATCAATCCAGC
15	GCGGGATCTTAAACGCGATAAAACCAGTCA
16	TTACCAGTATTCGCCAGACGACGACAGTATCTGATATAAGACGTTA
17	GAATTTTCGAGCAAGCAAAAAGTAGAACTTTCCTC
18	GGTACGAACGAGCCAGACGAGGTAATAACGAGGCGCAGACGGT
19	ATAAATCAGTACCTTTTTTGATTAATGTGT
20	CACTGCGCGCCTCGGCCTTTAATCGCAGTAAA
21	AGTTTCCAGTCACCCTTGATTCCCATAAAGCTGCCGGACTCGCCATGT
22	GCATGCGTCCGTGAGCCTCCGCTGATTGTCAACTT
23	GCATTCCACAGAAAAGGCTGCAA
24	GAGAGGGTGGCCTCAGATTTTGTGTTTGTGAGGAGCACATCCTCATAACAT
25	CGTGGAACCTCAAACCTATCGGAAATGGATAAGAG
26	CCACTACGTGCAGGGAGTTTGACCATTAGCAAGTCTG
27	AAACATCATAAATATTCATTGGATGGCTACTC
28	AACATATTATTTATCCCAATAA
29	ATCGGTTAAATACATATTTATCATATGGACAAAGTTACC
30	GTCTGAGAGACTACCTTTTAGA
31	CCGTGCAACCGTACTGCGTAACGATCTAAAGAAT
32	CCCATCCAATGGCAGCATTGAGAGGTGGAGCCGCCAG
33	TGGCACAACGCCACCCCTCAGAACCGCCACCCTCACGGCGGATAGC
34	GTCGTTTTGTTATTTGAGGGTTCAGGCTGCGCAACTG
35	GCTTTTGTCACAATCAATATTAG
36	AACCTTGTTATCGTCACTGTTGCCCTGCTGGTGCTGAATTAAGCTAAC
37	AACCTTTTAAATCAGAAATAATTGACAGGAGGTTGAGGCAGGTCGTAATCAGTAC

38	AATGCCGGAGAGGACTAGAAAGCCTGTTTTAAAAACG
39	AGGGCAAATTAACCGTTGGCCAACAGAGAATCGCAGAA
40	AGCCTAATTTGCCAGTGAGCTA
41	AAACCATTCCATGCTTTTTGGACTTTTTGAACTGACCAACTTTGAA
42	CGGATATTCATTACCCAAATCAACTGCTCATCTTTAAAC
43	ATCAAAGCCAGCAGCAAAATGTGAGTCCTACCATTGGCCTTG
44	TCGTCGCTAAATCGTTTATGCAACTAATAGTAGCCCGAAACTACAGAGGC
45	GAAAGATTCATCAGTTACGGAGATCATCTTT
46	ACACTTTGTATCATCGCCTGATAAATTGACATTATGGAATTACGAGC
47	GCCTGTAATACTATTGTAAATATGGGATCGGATAAGTGCCGTC
48	CAATCATAGTTACAGGAGGTTTAGTACCGCCACCCTTTGGTGTCATC
49	CTCTCTGAATAATGGAAGGGAGCGGAGAATTT
50	GGGTAAAGTACAGCAACGGGACTTCAA
51	AAGAGGTCATTTTTGCGAATCCCCGGTCTTTA
52	TAGCATGTCAATCATAAAATGCAAGTCAAATCCAGGTC
53	TTTGAACGAGGGTGGTGTCTATGACCCTCCGGCCAAGATAGACTTTCTCCGGCTT
54	ACGGAACATGTCGAAAACGAAAGAGGCAAAACGCATAACAATAA
55	AGCCGCACTCAAAGCATAAAGTGTAAAGCCCG
56	CCAGCAGGCGAAAATCCTGTTTGATGGTGGTCAGAATGCGTAC
57	CAATCATATCATTATAACCAAAATAATCATGGAGGTTTCTTTGCTCGTCGGA
58	CTATCAGGTCAACCGTTTTTAGAAATTGCTAGCGGTGC
59	AGTCTGGAGCAAACAAGAGCGGAGACATGCCTGAG
60	ATTTTCGCAAGAAAAATAAGGCCATTAAAAAAGGGACAT
61	TGGGGAATGCAGCATTTGGGACAA
62	GCTGATTGCCGTTCCGCTGCAGCCGAATATAACAATA
63	ATGGCTTTCCGGCACCTGGTGAAGATATTTAATTTGCGGGTTCAA
64	GTCCACTAAATCCCTTTAAACCAAGGCGGGCCTGT
65	CACCAGACGATATCAAAATTTATTTGCAATCATTTTCTAAAGCA
66	TGAAACTCGTTTATAGATTTAGTTAA
67	ATCCAACTTGCCTAATAGCGGGGT
68	AGACGATCCAGCGCAGGTTTTACGGTCATAC
69	TTAATGAAGATCGTGCCGGAAACCAGGCAAAGCGCCCCC
70	GGGGTTTCTGCCAGCAGAGTTGCAGAGTAGTA
71	GTGTATTTTTGAATGGCTAGGAGCACTTATTCATCCTGATTGCGCTCCC
72	TCGGGAGAAACAATAAAGGAT
73	AAGGTCGGTCGCTGAGGCTAAGGCACCAACACTATTAATAAATAATGAA
74	ATATTACCAAATACCTGTAATTCTAAAACCTT
75	CGCTAAACAACCCTAATTGGAAAAACGCTCATGGGCCAGCCAAGAACAAGGAAAATAG
76	CTAACTTCTTTGCAGGAGGCCGATTAAAGGGA
77	TAAACAAAAGAACCTTATGCTTTTACCAGTGAGACGGGCAACATCACAGTTAGAGG
78	AGAATTAGATAGAGCCGCGCTCACAATTCCACA

79	TTCAAATATCAATATTGAAAAATGCGGAACAAAGAAACCACCAGAAGGTT
80	CCGGAACACCGGAACGCTTTGAA
81	CGGATTCGTTCAATTATTCA
82	TGTACCAGTAATAATACCGAACGAACCAATCTGG
83	GTCTCATTGTTTAATGGAGATAAATTGGCAGATTCACCAGCTTGCCTGTCAGA
84	CAGTTTCAGCGGAGTGAGATTTTCTGCG
85	TAGTGAACAAGAAAAATAACCAATCAAACGGG
86	GTTTCGTCAACCAGCGGTTTATAGCATTAAATGTTT
87	AGGTTGAAAATCTCCAAAAACAGCCCTAGGAACGCAGATGGGCCGGTGCG
88	CAGACCAGGCGCATATTGAGATGAGACTGGTGTTT
89	AAAGCCCAATAGCCAGTAATTATTACAACAGAGGTGAGGCGGTGCTG
90	GAGCACGTATCCAAATTTACCGCGAACTGGCAAAGAAACGCAAAGACATTAC
91	CCATCGCCGTAAAAAAGC
92	AAAACATTTTGTGCAACAGTGCCACGCTGAGAATAACGCGAGGTCCAGAC
93	CGGATCCGCCGGGCGCGGTATGCCAACAAATCATACGTC
94	GCGAATCATTTTAAATAAAGCTTTTACGCCGCTTTT
95	AGGATTAGAGAAAAATCACTCAAATGTCAGTGAAT
96	AGCGGGGTTTTGCTCAGTAC
97	AATCATCTTCTAGCAAGGCAGAATCAAGTTTGCCTCCGCCAGCAAGAAATT
98	CAAACCATCAATATGATATTC
99	GCGTTCCAAGATAATCGGCCAGTTTGGAAACAAGA
100	GAAACAAAGTACAGAGATTTA
101	CCTAGGAATTGAATGATGAACTTTTACA
102	CATTGACCTAAAAATTACCTTCAAATATAATTTTAAAAGTTTGAGTAACA
103	GCTCAAAGCGAACCCAGACCCAGAAGCCGGAATCGCCAGAACGCAAGCGG
104	AAATTAGTAATAACATCATCACACGAATTTAGGCACCG
105	ACCCACCGGAAAAAGAAGGGAAGGTTGAAGTATTAGACTTTACAAACAAAACA
106	TGATTTTCGAGGTGAATTTCCATGTACCTGTGAGCG
107	GTGTATCTCTGCCAGAATCAGCACGTACAGTGTAGAACGTCAGCGGGCT
108	GCTGAGACTCCTCAATTAACGGGATCAGAAACAGCGGA
109	GTAAGGTACTGGTAATAAGTTGAGAAGGATACAAAGG
110	GCTCATTTGCCGCCAGAGGGTAAAGTTAAACG
111	CTGGCACTCCAGCCAGCTTTTGATGATAATAAGCAAGGATAGCTTTTTTCGTC
112	CAGCGCCAAGCTCCGTCGGTGGTGCCATGGCGCTTTTATATTTTATACATAATAAA
113	GGGTGGAATTCGTAGCGAGAGATAACAGTCAGCAGCGTAAAGGAATTGCGAATTTT
114	TATAAACAGCCAAAGTCA
115	GGACGTTGGGAAGAAATAGCCGGAACGTAATG
116	AGAGTTCGCTATTATTATACTATTAAGCCAGAATGGAAAGCGCA
117	TTCGTAAAAGGAAACAGTAGCGACCGGAAACGTCACCAATGGTG
118	AGCTGTGATAACAAAATTAAGTTGGCACTCGTATT
119	CCCTGAGAGTATTAAGAG

120	AAAACGACGGCCAGTTTTTCATCAATAGTAGTCAGCTTGCCAACAACCATCGCCCAGA
121	GGAAAAAATTCGTGTACCAGGAACAACAAAGACAGCATCGGAGGAC
122	TCACCTTCAGTATTATTAATTTATAAAGTACATATAATGATTAAG
123	AGAAGAATAACCAACATAAAAAAATCATAGCAG
124	ACCGCAGCAAAGCGCGTTTTTCATCGGC
125	TCGCAATAGTATTATCATCATATTCTGATTATCTTG
126	CTGAAAGCGGAGACCTTCATCAAGAGTAATCTTGAGAG
127	ACGTGGACTCCAACGT
128	ATACAGTTTCGACAAAATCAACAGTTGAAAAAAC
129	CACCCAGCAGTGTTTTGAGGCCACCGAGTAAAGCGTAAGAAAGCCAAAAGCCTG
130	AGAGGTGAATTAGTTTTGCCGAGGATCCACTGGTGTGTTTCAGCGGCA
131	AATCCTGAAGATGATTTAGATTAAGA
132	TCCTTTACAGAGAGAATAACATAAAAAACAGGGTTACGCATTTTATTTAGGT
133	AGATTTGAAATAGAGGCATTAAGTTTAAATAATAACGGAATACCCTG
134	TTAATCTAAAATATCTTTATTAGTCTTACTAGAAACGCTCAACGCGA
135	GACCCCATTTGCGCCGGCGGAGCGCATCAAT
136	CGCCTGGCCCTGAGACGCGTGCCATAGCGTCTGCTGTAGTCGAGCTTGATAAATT
137	GAGCAACCTAAATCCGCGACCTGCTCCATGTTACTAATCTACGTCAT
138	ATATTCACAAACAAATGTACATCGTTGCTTCTAGACAAAGCATAG
139	ACGTAAATCGGTCATTAATTTCTTTCCAGTATAGCCCGGAATAG
140	CAAAGGGCTCAAAAATCAAGCCGTGTATGTTAGCAAAGGTGCTGCGGC
141	CGCCCCTTCTGACCTGAAAAGAGTCTGTGCGGGAGTATCCTGAAATAATA
142	AAATATCCCATATGTTTCAGGCAAATCCAGTGATGACAGTTGGGCGGTTGTAAATC
143	ATATCGCGAAGAGGAAAAATGTTTGTTAATTCCTTCCAC
144	CTATTATTCTGAAACCCGTATAA
145	TAAAGTCACCGACCCCTTATTAGCGTTTCAGA
146	TATATAAATCAAAAAGAAT
147	TTTACGAGCGTGCGGTTTTTATAGCCGATTTACCAGCGCCAAAAGTATC
148	TTCCAGATGCCGGGTTACGCAAACGCAACGCAAGAAAACAGGGAGAGATCTTAGGATT
149	CGCTGTAACCTCCATGCTGATCTAATGCAGAAC
150	AAAAACGGATAAGCAGCAACCGCAAGATGCGGTATCATTTCGCGTAA
151	GTAAATGAAATAGAAAAAACATTGGAAGTTTATCCCTTACCCGGGTA
152	TCTGTAGCAATAGAACGCGACTTTCCAG
153	AATTGGGCGGCTGGCTTTGCATCAAAAAGATTTTTTAATCTC
154	TAATCATTGACAGATGAACGGTGTA
155	ATAAATATTTTAGACACCGCCACGCTCAATCGTCTGCCTT
156	GCAACCGACAAATCATCGTAGTAATATCGTCTATCACTTTGAC
157	TCTACTAACATTAAGTAACACCACCCTCATTTTCAGGGATAG
158	ACTCCTTAAAGCGCATATTTTTTTGTTAACGGAAAAACCCAGAACA
159	CCGAGCTCGTTTTTCGATTTTAAAGAACTGGCAGGGAACCCATGAGGA
160	TTTGGAATTAATTTTCCCTTATATGTAAGGCT

161	TAATTCATTAAAGGTGAATACAAAAGGAGTAGGGCTCCCGACTTCCATCAC
162	GACGACAACTCATCGTTGCAACATACGAGCATGTAG
163	GAAAGGCAATCGATGGTAAAACACAGTTAA
164	TATCACCAGTAGCACCACCACG
165	CGTCGGATGTTGGGTAACGCCA
166	AAATCCTTTGCCCGAATTTTCAGGTTAACAATTAGACTG
167	GTCACCTCACCGGAAACAATCG

Table S3. Closing staples and fluorescently labelled staples used in Version 1 of the nanosensor. For the closing interactions, the number of the caDNAno helix is indicated (see Fig. S17). Yellow and Red indicate complementary sequences. Green indicates the toehold used for opening. Blue indicates additional spacer elements.

Name-HelixID	Sequence (5'->3')
Row1-top16	ATACATCTATTATATATTGAGGGTAATTGAGCGCTGAAACCGATATCCGGTAACA
Row1-top13	ATACATCTATTATATATTCCACCACCAGAGCCGTTAGC
Row1-bot24	AATAGATGTATTTATATATTGCGGGACGTTGGGAAGAAATAGCCGGAACGTAATG
Row1-bot29	AATAGATGTATTTATATATTTTGGGAAGGGCGATGCATCGTAA
Row2-top13	ATACATCTATTATATATTTTCAAGCCTAATTTGCCAGTGAGCTA
Row2-top16	ATACATCTATTATATATTTTACCCTCATTTTCGCAAGAAAAATAAGGCCCATTAATAAAGGGACAT
Row2-bot24	AATAGATGTATTTATATATTTTCGGCCAACGCGCGGGGAGAG
Row2-bot29	AATAGATGTATTTATATATTTTGGCCTCTTCGCTATTACCCACGGGAATAATTCGACAGGCAAGCCAA
Row3-top13	ATACATCTATTATATATTTTATTGAGTAAGCAGAGCGAACCTTAATTGAGATAGAAGAACTGATAGC
Row3-top16	ATACATCTATTATATATTTTACCTCGGGAGAAACAATAAAGGAT
Row3-bot24	AATAGATGTATTTATATATTTTTCGTGCCCAACATACGAGGCATAAAATGGTCCGATATATAGCCTTTAATTGTATTA
Row3-bot29	AATAGATGTATTTATATATTTTCTGAATGGGATAGGTCACGCAGAACCGTGTA
Row4-top13	ATACATCTATTATATATTTTATAGAGCAAGAAACAATGAGCTATCTAGCCTTAAACCAGTATAATAC
Row4-top16	ATACATCTATTATATATTTTTCAGAGCCGCCACCCTGCCATCTTCTTGAGCATCATAATTTAATG
Row4-bot24	AATAGATGTATTTATATATTTTCTTGAAAGATTCATCAGTTACGGGAGATCATCTTT
Row4-bot29	AATAGATGTATTTATATATTTTTCGCAAGCGGCCAGTTTTTCATCAATAGTAGTCAGCTTGCCAACAACCATCGCCCAGA
Green_dye_non_hybridizing	AATTCTCAGAGCAATTCTGATGGGTAATCATAGCTGTTTCCTGTG-[ATTO542]
Red_dye_non_hybridizing	GTTAGAATCAGAGCGGTACAAAATAGAAGGCTGGAAAC-[ATTO647N]

Red_dye_1nt_spacer	GTTAGAATCAGAGCGGTACAAAATAGAAGGCTGGAAACTCTGACGGC -[ATTO647N]
Green_dye_1nt_spacer	AATTCTCAGAGCAATTCTGATGGGTAATCATAGCTGTTTCCTGTGTGC CGTCAG-[ATTO542]

Table S4. Modified (closing, stabilization and fluorescently labelled) staples used in Version 2 of the sensor. For the closing interactions, the number of the caDNAno helix is indicated (see Fig. S17). Yellow and Red indicate complementary sequences. Green indicates the toehold used for opening. Blue indicates additional spacer elements.

Name-HelixID	Sequence (5'->3')
Row1-top13	ATATCACGAGCACATCAGTACGAGGGTAATTGAGCGCTGAAACCGATATCCG GTAACA
Row1-top16	GTGCTCGTGATATTTTTCCACCACCAGAGCCGTTAGC
Row1-bot24	GTGCTCGTGATATTTTTGCGGTTTGCCTATTGGGCGCCA
Row1-bot29	ATATCACGAGCACATCAGTACTTGGGAAGGGCGATGCATCGTAA
Row2-top13	ATATCACGAGCACATCAGTACTCAGAGAGATAACCCACAAGA
Row2-top16	GTGCTCGTGATATTTTTTTTACCCTCAGAGCCGCAGATGAAT
Row2-bot24	GTGCTCGTGATATTTTTTTTTCGGCCAACGCGCGGGGAGAG
Row2-bot29	ATATCACGAGCACATCAGTACGGCCTCTTCGCTATTACCCACGGGAATAATT CGCAGGCAAGCCAA
Row3-top13	ATATCACGAGCACATCAGTACTTATTGAGTTAAGCCCATCTTACCAACGCTA TAGAC
Row3-top16	GTGCTCGTGATATTTTTTTTTTACCGCCACCCTCAGAGCCACC
Row3-bot24	GTGCTCGTGATATTTTTTTTTTCGTGCCAGCTGCATACGAATA
Row3-bot29	ATATCACGAGCACATCAGTACTTCTGGCGAAAGGGGGATGTGC
Row4-top13	ATATCACGAGCACATCAGTACTTTAGAGCAAGAAACAATGAGCTATCTAGCC TTAAACCAGTATAATAC
Row4-top16	GTGCTCGTGATATTTTTTTTTTTTCAGAGCCGCCACCCTGCCATCTTCCTG AGCATCATAATTTAATG
Row4-bot24	GTGCTCGTGATATTTTTTTTTTTCTTTCCAGTCGGGAAACCTGT
Row4-bot29	ATATCACGAGCACATCAGTACTTTTGAAGGCGATTAATCTCCGTGGGAACA AAGAGCCACTGA
5bp_stabilisation_1	CATTGCACCCACGCAACCAGCTTGACGTTGTTTTTAGACC
5bp_stabilisation_2	TTAATTGCGTTGCGCTCACTGCCTTTTTCACAC
5bp_stabilisation_3	AACGGTACGCCAGAATCCTGAGATACAATTTGTTTTGATACCGATTTTTGTG TG
5bp_stabilisation_4	TTGAGGGAATATTGACGGAAATTACAAAATCATTTTTGGTCT

Red_dye_3nt_spacer	GTTAGAATCAGAGCGGTACAAAATAGAAGGCTGGAAACTTTCTGACGGC- [ATTO647N]
Green_dye_3nt_spacer	AATTCTCAGAGCAATTCTGATGGGTAATCATAGCTGTTTCCTGTGTTTGCCGT CAG-[ATTO542]

Table S5. Biotinylated staples for immobilization of DNA origami nanostructures used in both versions of the sensor. Blue indicates additional spacer elements.

Name	Sequence (5'->3')
Biotin1	5'Biotin- TTTATTGCCGGTTGATAGTCAGTGCCTTGAGTAACAGTGCATGAA
Biotin2	5'Biotin- TTTATTATAGTGGAAGCAATAGAGCTTACCCTCATATATTTTTGTA C
Biotin3	5'Biotin-TTTCAAACCTTCCTGTTGACCGT
Biotin4	5'Biotin-TTTATACACCGCCAAAATACAGGTA

Table S6. DNA-DNA closing interactions used for XhoI nanosensors. Shown in purple is restriction site of XhoI. The number of the caDNAno helix is indicated (see Fig. S17).

Name-HelixID	Sequence (5'->3')
Row1-top 13	ATA CTCGAGT TTATATATTGAGGGTAATTGAGCGCTGAAACCGATATCCGGTAACA A
Row1-top16	ATA CTCGAGT TTATATATT CCACCACCAGAGCCGTTAGC
Row1-bot24	AA CTCGAGT ATTTATATATTGCGGGACGTTGGGAAGAAATAGCCGGAACGTAAT G
Row1-bot29	AA CTCGAGT ATTTATATATT TTGGGAAGGGCGATGCATCGTAA
Row2-top 13	ATA CTCGAGT TTATATATTTTCAAGCCTAATTTGCCAGTGAGCTA
Row2-top16	ATA CTCGAGT TTATATATTTTACCCTCATTTTCGCAAGAAAAATAAGGCCATTAA AAAAAGGGACAT
Row2-bot24	AA CTCGAGT ATTTATATATTTTTCGGCCAACGCGCGGGGAGAG
Row2-bot29	AA CTCGAGT ATTTATATATTTTGGCCTCTTCGCTATTACCCACGGGAATAATTCGC AGGCAAGCCAA
Row3-top 13	ATA CTCGAGT TTATATATTTTATTGAGTAAGCAGAGCGAACCTTAATTGAGATAG AAGAACTGATAGC
Row3-top16	ATA CTCGAGT TTATATATTTTACCCTCGGGAGAAACAATAAAGGAT
Row3-bot24	AA CTCGAGT ATTTATATATTTTTCGTGCCAACATACGAGGCATAAAATGGTCCG ATATATAGCCTTTAATTGTATTA
Row3-bot29	AA CTCGAGT ATTTATATATTTTCTGAATGGGATAGGTCACGCAGAACCGTGTA
Row4-top 13	ATA CTCGAGT TTATATATTTTTCAGAGCCGCCACCCTGCCATCTTCCTGAGCATCA TAATTTAATG
Row4-top16	ATA CTCGAGT TTATATATTTTTCAGAGCCGCCACCCTGCCATCTTCCTGAGCATC ATAATTTAATG
Row4-bot24	AA CTCGAGT ATTTATATATTTTCTTGAAAGATTCATCAGTTACGGAGATCATCT TT
Row4-bot29	AA CTCGAGT ATTTATATATTTTTCGCAAGCGGCCAGTTTTTCATCAATAGTAGTCA GCTTGCCAACAACCATCGCCAGA

Table S7. Antigen modified staples that were used in a sensor for anti-Dig and anti-DNP antibodies. The number of the caDNAno helix is indicated (see Fig. S17). Blue indicates additional spacer element.

Name-HelixID	Sequence (5'->3')
Row1-top16	[DNP]TGAGGGTAATTGAGCGCTGAAACCGATATCCGGTAACA
Row1-top13	[DNP]TCCACCACCAGAGCCGTTAGC
Row1-bot24	[DNP]TGCGGGACGTTGGGAAGAAATAGCCGGAACGTAATG
Row1-bot29	[DNP]TTTGGGAAGGGCGATGCATCGTAA
Row4-top13	[DIG]TTTAGAGCAAGAAACAATGAGCTATCTAGCCTTAAACCAGTATAATAC
Row4-top16	[DIG]TTTTAGAGCCGCCACCCTGCCATCTTCCTGAGCATCATAATTTAATG
Row4-bot24	[DIG]TTTCTTGAAAGATTCATCAGTTACGGAGATCATCTTT
Row4-bot29	[DIG]TTTTGCAAGCGGCCAGTTTTCATCAATAGTAGTCAGCTTGCCAACAACCA TCGCCCAGA

Table S8. Sequences of opening strands used in different sensor constructs. Red indicates the mismatch.

Name	Sequence (5'->3')
15 bp interaction	ACTGATGTGCTCGTG
17 bp interaction	ATATATAATAGATGTAT
17 bp mismatch GC	ATATATAATACATGTAT
17 bp mismatch AT	ATATATAATAGTTGTAT
17 bp mismatch GC+AT	ATATATAATACTTGTAT
17 bp mismatch Toehold AT	ATTTATAATAGATGTAT
17 bp mismatch Toehold TA	ATAATAATAGATGTAT

Table S9. Fit results as well as buffer compositions for the titration data shown in Fig. 2.

Sample	Buffer	K_{1/2}	n_H
2x13	10 mM Tris, 10 mM MgCl ₂ , 50 mM NaCl	100.08 ± 10.43 nM	0.9782 ± 0.084
2x13	10 mM Tris, 10 mM MgCl ₂ , 200 mM NaCl	195.05 ± 12.36 nM	0.8709 ± 0.041
2x13	10 mM Tris, 10 mM MgCl ₂ , 400 mM NaCl	601.19 ± 19.57 nM	0.8075 ± 0.019
2x13 stabilized	10 mM Tris, 10 mM MgCl ₂ , 50 mM NaCl	704.97 ± 64.84 nM	0.7997 ± 0.049
4x13	10 mM Tris, 10 mM MgCl ₂ , 50 mM NaCl	1087.31 ± 85.60 nM	1.5459 ± 0.1524
6x13	10 mM Tris, 10 mM MgCl ₂ , 50 mM NaCl	2025.14 ± 102.35 nM	1.7335 ± 0.1255